Universidad
Carlos III de Madrid
www.uc3m.es

TESIS DOCTORAL

Elastoplastic solids subjected to dynamic tension: New experimental and computational insights

Autor:

Álvaro Vaz-Romero Santero

Directores:

José Antonio Rodríguez Martínez

Ángel Arias Hernández

DEPARTAMENTO DE MECÁNICA DE MEDIOS CONTINUOS Y TEORÍA DE ESTRUCTURAS

Leganés, Septiembre 2015

[This page is intentionally left blank]

Universidad
Carlos III de Madrid
www.uc3m.es

TESIS DOCTORAL

ELASTOPLASTIC SOLIDS SUBJECTED TO DYNAMIC TENSION: NEW EXPERIMENTAL AND COMPUTATIONAL INSIGHTS

Autor: *Álvaro Vaz-Romero Santero*

Directores: **José Antonio Rodríguez Martínez**
Ángel Arias Hernández

Firma del Tribunal Calificador:

Firma

Presidente:

Vocal:

Secretario:

Calificación:

Leganés, de de

[This page is intentionally left blank]

“Al fin y al cabo, somos lo que hacemos para cambiar lo que somos.”

Eduardo Galeano

[This page is intentionally left blank]

Agradecimientos

Son muchas las personas que han participado, de manera directa o indirecta, en la elaboración de este trabajo y a quienes quiero expresar mi gratitud por el ánimo y el apoyo que me han prestado de forma desinteresada.

En primer lugar, quisiera dedicar unas palabras a mis directores de tesis, José Antonio Rodríguez Martínez y Ángel Arias Hernández, sin los cuales no hubiera sido posible completar este trabajo. A José, no puedo sentirme más afortunado por haber tenido la oportunidad de trabajar contigo. Gracias por transmitirme una ínfima parte de tus conocimientos, por el constante apoyo e implicación, por el tiempo dedicado y por tus consejos, tanto desde el punto de vista académico como personal. A Ángel, por el respaldo y el apoyo que me has brindado en todo momento, profesional y personalmente.

También quisiera agradecer al Departamento de Mecánica de Medios Continuos, en especial a Guadalupe Vadillo, por su inestimable participación activa y altruista, no sólo en forma de aportación de ideas y discusión científica, sino además por sus constantes palabras de aliento. A Jorge Zahr por sus continuas y esclarecedoras enseñanzas, así como a Ramón Zaera Polo y a José Fernández Sáez, por sus consejos y aportaciones. A los técnicos de laboratorio Sergio y David por su colaboración, su disposición y, principalmente, por su amistad.

Un sincero agradecimiento a Daniel Rittel, por su generosa hospitalidad y amabilidad, y por abrirme las puertas de su laboratorio para futuras colaboraciones. Otra mención especial a Sébastien Mercier y Alain Molinari, no sólo por su exquisito trato personal sino por brindarme la posibilidad (y la suerte) de poder trabajar con ellos en un futuro próximo.

A mis padres y a mi hermana. Esta tesis es fruto de vuestra inquebrantable fe en mí. Sin vuestro apoyo incondicional, sin vuestro sacrificio, no hubiera sido posible. Por entender el esfuerzo que implica escribir una tesis y por ser los primeros en prestarse para ayudarme en todo aquello que estuviera a su alcance. Por quererme a pesar de mi inagotable lista de defectos.

A Estefanía. Has sido el pilar fundamental sobre el que se ha erigido un proyecto que significaba mucho para mí, un proyecto que no es sólo mío sino tuyo también. Tú has sido la inspiración en muchos momentos; el consuelo, el ánimo, el sostén y el cariño en muchos otros. No tengo palabras para describir lo que ha significado tu comprensión, tu eterna paciencia, y el orgullo y el respeto que me has transmitido por todo el trabajo realizado. Gracias por empujarme a crecer y a ser mejor persona. Somos un gran equipo.

No puedo olvidar a los que, por méritos propios, se han convertido en estos años en algo más que compañeros de despacho, en verdaderos amigos. Gracias Jesús y José. Por todo los momentos que hemos vivido juntos, por las risas y las conversaciones sobre política regadas con buena cerveza. Espero que continúen durante muchos años.

A Patricia, por tu amistad, por tus continuos e incansables mensajes de ánimo. Por haber estado en los momentos malos, por haberme sacado una sonrisa cuando más lo necesitaba sin pedir nada a cambio; y porque al fin y al cabo, somos unos espartanos. A Elena, por el apoyo y la confianza depositada en mí, sin los que no me hubiera animado a emprender este largo camino. Gracias por ayudarme en los duros inicios. A Ismael, por ser como un hermano, y porque nos quedan muchas cervezas y barbacoas para celebrar nuestros éxitos. A Claudio, por ayudarme a evolucionar como persona.

Finalmente, agradecer al Ministerio de Ciencia e Innovación de España por el soporte financiero necesario para la consecución de este trabajo a través del proyecto DPI/2011-24068.

En definitiva, a todos aquellos, citados o no; sin los que este trabajo no hubiera visto la luz. Gracias de corazón.

Álvaro Vaz-Romero Santero
Septiembre 2015

A mis padres y hermana.
A Estefanía.

[This page is intentionally left blank]

Abstract

This Doctoral Thesis provides new insights into the mechanisms which control flow localization in elastoplastic solids subjected to dynamic tension. For that task, we have a developed a methodology which combines experiments and numerical calculations. Dynamic tension tests have been performed in a high-speed testing machine using specimens with six different gauge lengths, ranging from 20 mm to 140 mm, that have been tested within a wide spectrum of loading velocities from 1 m/s to 7.5 m/s. The experiments show that variations in the applied velocity and the gauge length of the samples lead to the systematic motion of the fracture location along the specimen. A key outcome is that we have provided experimental evidences of the deterministic nature of the flow localization in dynamic tensile specimens. Finite element calculations have been conducted in ABAQUS/Explicit in order to complement our experimental findings. The finite elements predict, in agreement with the experiments, the interplay between fracture location, impact velocity and gauge length. Moreover, we have explored the role played by initial and boundary conditions in plastic flow localization. A salient feature is that we have demonstrated that the intervention of stress waves within the specimen is a limiting factor for the sample ductility. On the one hand we have observed that the strain to failure, instead of being a material property, is strongly dependent on the specimen size. On the other hand, we have shown that the topology of the localization pattern is closely connected to the post-uniform elongation of the specimen. Finite difference calculations have been conducted in MATLAB in order to rationalize the experimental and finite element outcomes. For that task, we have developed a simple one-dimensional model within a finite deformation framework. The key point of our finite difference computations is that, unlike the finite element calculations, we solved the kinematics, and thus obtained a complete control of the problem. We show that the intervention of wave propagation phenomena within the specimen is responsible for the interplay between flow localization, impact velocity and gauge length. Moreover, we have explored the role of selected material properties in the kinetics of flow localization. A key outcome is that we have shown that material flaws (may) play a secondary role within the mechanisms which govern plastic localization in dynamic tensile specimens. All in all, we have developed a comprehensive and innovative research to establish: (1) the deterministic nature of flow localization and (2) the material properties and the initial and boundary conditions which control the process at hand.

[This page is intentionally left blank]

Contents

[This page is intentionally left blank]

List of Figures

[This page is intentionally left blank]

List of Tables

[This page is intentionally left blank]

1

Introduction

In this chapter we state the theme of this Doctoral Thesis and place it within the framework of Solid Mechanics. We point out the works that have inspired this investigation and present the salient features of our research. The outline is as follows: in section 1.1 we develop a critical, and chronological, assessment of the seminal works published in the field during the last century. Within this context, we establish the central goal of our investigation and a methodology to accomplish this objective. In section 1.2 we detail the structure of this document and explain the process that we have followed to build our research from the fundamental basis of the Continuum Mechanics theory. In section 1.3 we provide a brief summary of the main scientific achievements of this investigation.

1.1 Introduction, objective and methodology

In this Doctoral Research we provide new insights into the fundamental problem of elastoplastic solids subjected to dynamic tension. Namely, we have focused our attention on the plastic localization process which is precursor of fracture in ductile solids subjected to high strain rates. For that task, we have developed a combined experimental-numerical research that shows the deterministic nature of the flow localization in the dynamic tension test. We have uncovered the critical roles played by specimens dimensions, initial and boundary conditions, stress wave phenomena, material properties and material flaws in the fracture of the tensile samples.

The investigation of flow localization in ductile specimens started with the work of Considère [4] who proposed the well-known load maximum criterion: necking begins when the increment of strain hardening becomes equal to the geometric softening in a simple tension test. Note that, despite the enormous popularity that this criterion has achieved, it is only applicable to strain rate and temperature insensitive materials tested under quasi-static loading conditions. For several decades, the latter constraint hampered the study of necking in all of kinds applications where the role of inertial forces is not negligible. For instance, in the 40's, a series of celebrated papers published by Nadai and Manjoine [5], De Forest et al. [6], Clark [7], Parker and Ferguson [8] and Manjoine [9] showed that the well-established concepts of failure under static loading no longer apply in the dynamic regime. The experiments revealed that the deformation behaviour of metallic specimens subjected to impact loading is controlled, to a large extent, by the intervention of strain propagation phenomena within the sample. It was acknowledged, for the first time, that the performance of some materials under dynamic loading is different from that observed under static conditions. These works, that were motivated by the seminal papers of Mann [10, 11], definitely showed that high velocity tests are essential to reveal the true dynamic properties of materials. The effect of velocity on the capacity of metallic materials to absorb energy was demonstrated.

Within this context, special mention requires the thorough experimental investigation conducted in the Guggenheim Aeronautical Laboratory of the California Institute of Technology (directed at that time by Theodore Von Kármán) with the aim of evaluating the ultimate strength and ductility of different metals used in aircraft construction [12–15]. Note that this extensive experimental research was directly driven by industrial concerns. In Beardsley and Coates [13] words *"with the current improvements in aircraft structural design methods, resulting in more efficient structures in which the material is worked at higher stresses, it is becoming increasingly more necessary to consider the effects of dynamic loading on the structure"*. During the following years, with the continuous support of the aeronautical sector, the efforts were focused on rationalizing (within the framework of Continuum Mechanics) these experimental findings. Thus, Clark and co-workers published a series of papers [16–19] in which the theory of the elastic and plastic strain propagation developed by Von Kármán and others [20–24] was used to interpret the experimental data. A key outcome of these theoretical investigations was to show that the strain rate in impact tests varies from point to point along the specimen, and for a given point it is also dependent upon time [18]. This behaviour, which is accentuated as the impact velocity increases, was identified as the main problem of the tension impact test to study the influence of the rate of strain on the deformation and failure of metals. The following decades, especially after the development of the tension version of the Hopkinson-bar technique in the early 60's [25], were very much focused on overcoming this drawback. The belief that the use of very short specimens minimizes the importance of the inertia loads and allows to neglect the intervention of strain propagation phenomena within the specimen became widely accepted [26, 27] and the dynamic stress-strain characteristics of different metallic materials were published, see for instance the works of Nicholas [28, 29, 30].

Nevertheless, it took a long time to build a reliable theoretical framework to describe flow localization under dynamic tension. In the 80's, Fressengeas and Molinari [31, 32], based on previous works of Hill and Hutchinson [33] and Hutchinson et al. [34], developed a linear stability analysis which uncovered the critical mechanisms controlling the flow localization under dynamic tensile loading. These authors showed that inertia and stress multiaxiality effects stabilize the material behaviour and delay plastic localization. The later works of Shenoy and Freund [35], Mercier and Molinari [36, 37] and Zhou et al. [38] confirmed the findings of Fressengeas and Molinari [31, 32]. It is apparent that the analytical solutions obtained from the linear stability analyses provide important information on the localization behaviour of uniformly strained solids. However, they fall short of describing the localization process in specimens subjected to wave propagation phenomena. In the dynamic tensile test, due to the strongly non-linear nature of the problem, a full numerical solution of the field equations is required. For instance, the works of Lubliner [39] and Botte et al. [40, 41] strengthened the idea that the essential character of the tensile impact test is the non-uniformity in time and space of the state variables of the material. The critical field variables (stress, strain and particle velocity) assume different values in the different sections of the specimen, and they change with time. Botte et al. [40] explicitly stated that numerical analysis becomes indispensable to investigate the spatial-temporal variation of the field variables in detail.

Thus, the advent of computational mechanics gave new impetus to the analysis and understanding of the failure process in tensile specimens subjected to impact loading. The numerical studies on the dynamic flow localization started in the late 80's and early 90's with the pioneering works of Regazzoni et al. [42], Needleman and co-workers [43–45] and Nemes and Eftis [46]. One advantage of the numerical calculations is that, unlike the linear stability analyses, they allow to investigate the spatio-temporal development of the instability. For two decades the numerical methods have been the most common tool to analyze dynamic problems which involve localization of plastic deformations. For instance, the papers of Noor et al. [47], Sørensen and Freund [48], Glema et al. [49], Guduru and Freund [50], Xue et al. [51] and Rotbaum et al. [52] studied the evolution of the field variables in viscoplastic specimens subjected to dynamic tension. These works suggested that the multidimensional character of the stress, strain and strain rate fields which develop inside a localized region control, to a large extent, the post-uniform behaviour of the specimen. The numerical calculations indicated that material inertia introduces a length scale so that the specimen ductility is a function of the specimen size. It was shown that the inception and evolution of dynamic tensile instabilities depend on structural aspects such as loading and boundary conditions as much as on the properties of the material.

Specifically, the finite element method has been widely used over the last years in the design of tensile specimens suitable to extract the true dynamic properties of metallic materials [53–55]. Within this context, it has to be highlighted the work of Rusinek et al. [56] who reviewed the performance of six different specimen geometries loaded in impact tension. Driven by the earlier work of Nemes and Eftis [46], Rusinek et al. [56] paid special attention to the interplay between flow localization, impact velocity and specimen geometry. They showed that, as soon as the impact velocity is such that the strain propagation effects become relevant, the necking moves away from the central point of the sample (where it locates under quasi-static conditions). This observation, which agrees with previous experimental results published by Wood [57], suggests that the necking inception in the dynamic tensile test is a deterministic process. Nevertheless, whether the nature of the flow localization is deterministic or random is still a controversial (and fundamental) issue debated in a significant number of recent papers published by different research groups, see for instance the works of Besnard et al. [58], Mirone [55], Rodríguez-Martínez et al. [59], Osovski et al. [60] and Rittel et al. [61].

With the aim of clarifying this controversial (and fundamental) issue, in this Doctoral Thesis we have developed a combined experimental-numerical research that leaves no doubt about the deterministic nature of the plastic localization process in the dynamic tensile test. We have carried out dynamic tensile experiments using steel sheet specimens with six different gauge lengths (20 mm, 40 mm, 60 mm, 80 mm, 100 mm and 140 mm) for seven impact velocities (1 m/s, 1.75 m/s, 2.5 m/s, 3.75 m/s, 5 m/s, 6.25 m/s and 7.5 m/s). Similarly to the experiments reported by Wood [57], we have observed that the fracture location moves systematically from side to side of the sample with the variations in impact velocity and gauge length. Further, for each combination of gauge length and applied velocity several repeats are performed which show an extremely high repeatability in the failure location. A key, and very unusual, experimental finding of this work is the multiple, and largely regular, localization patterns that have been observed in a significant number of the shortest samples tested. We have complemented our experimental findings with finite element simulations performed in ABAQUS/-Explicit [62]. In agreement with the experiments, the computations have shown that variations in the applied velocity and gauge length lead to the systematic motion of the plastic localization along the gauge. Our numerical calculations served to prove that the emergence of multiple localization patterns is associated to equilibrated specimens with low slenderness ratios and *hardly* subjected to the influence of stress waves. Further, we have developed an original 1D finite difference model that has provided new insights into the critical role played by the stress propagation phenomena in the flow localization process. Relying on this simple one-dimensional approach, we have rationalized the secondary role played by material defects in the failure location of the dynamic tensile specimens. In addition, we have specified the main material properties that control flow localization in the dynamic tension test.

1.2 Thesis structure

This Thesis Dissertation is divided into 10 Chapters:

- **Chapter 1**. This introductory section defines the central objective of our research. The seminal works which served as a basis to develop this investigation are pointed out. The methodology followed in this research is summarized. In addition, the critical scientific achievements of this Doctoral Thesis are highlighted.
- **Chapter 2**. We introduce the basic concepts associated to the kinematics of deformable bodies and derive the main strain measures. Moreover, the frame indifference principle is presented and the conditions of objectivity discussed. We summarize the principal objective stress rates.
- **Chapter 3**. We derive the Balance Laws which define the rates of change of mass, momentum and energy. These general principles are presented in Lagrangian and Eulerian forms.
- **Chapter 4**. We develop constitutive equations to model the mechanical behaviour of hypoelastic-plastic and hyperelastic-plastic solids within the framework of Huber-Mises plasticity. We present two specific procedures to integrate both constitutive formulations. In addition, a consistent thermodynamic scheme is derived.
- **Chapter 5**. We formulate, on the basis of the fundamental equations of the Continuum Mechanics derived in chapters 2, 3 and 4, the initial boundary value problem addressed in this Doctoral Thesis.
- **Chapter 6**: We carry out an experimental campaign to show the deterministic nature of the fracture location in the dynamic tensile testing of elastoplastic solids. We provide evidences of the role played by wave propagation on the specimens failure.
- **Chapter 7**: We develop a 3D finite element approach to model flow localization and failure in elastoplastic solids subjected to dynamic tension. We uncover the key mechanisms which determine the fracture location. In addition, we show the critical role played by the initial and boundary conditions in the failure pattern of tensile specimens.

- **Chapter 8**: We develop a 1D finite difference approach to model the flow localization of ductile solids subjected to dynamic tension. We provide critical information about the role played by wave propagation in the failure of the sample. We show that, at high strain rates, material flaws may not dictate the fracture location.
- **Chapter 9**: We summarize the main scientific achievements of this doctoral research. We highlight that our combined experimental-numerical approach reveals the deterministic nature of the flow localization in elastoplastic solids submitted to dynamic tensile loading.
- **Chapter 10**: The concluding section proposes future work that shall be conducted within the framework of the dynamic stretching of elastoplastic solids. The research plan presented in this section devises new experimental and numerical developments to approach the problem at hand.

The idea which resides behind this structure is to build a self-contained Doctoral Dissertation in which an initial boundary value problem is identified, formulated and approached using the fundamental principles of the Continuum Mechanics specifically derived here for that task.

In addition, we have included 6 appendixes in order to help readers to follow some mathematical developments presented in the document:

- **Appendix A**. We detail the main mathematical operations required to build the Continuum Mechanics theory reported in chapters 2, 3 and 4.
- **Appendix B**. We discuss the main physical and mathematical concepts associated to the Lagrangian and Eulerian descriptions used in chapters 2, 3 and 4.
- **Appendix C**. We introduce various stress tensors, and the associated work conjugacy concept, used in the theoretical developments of chapters 2, 3 and 4.
- **Appendix D**. We discuss some specific features of the integration algorithm used for the hyperelastic-plastic model developed in chapter 4.

- **Appendix E**. We show the complete set of the dynamic tensile experiments discussed in 6.
- **Appendix F**. We introduce the basic concepts of the finite difference method, with emphasis in the mathematical operations used in the one-dimensional scheme developed in chapter 8.

1.3 Original contributions

We highlight the main scientific achievements of this Doctoral research. The key outcomes coming from experiments, finite elements and finite differences are presented below:

- **Experiments**. We have carried out a comprehensive experimental campaign which leaves no doubt about the deterministic nature of the fracture location in the dynamic tensile test.
- **Finite elements**. We have conducted 3D finite element computations which uncover the critical role played by the initial and boundary conditions in the failure pattern of dynamic tensile specimens.
- **Finite differences**. We have developed a 1D finite difference scheme which shows that the stress waves phenomena determine the fracture location in tensile samples tested at high strain rates.

All in all, we have developed an integral approach to the problem of elastopasltic specimens subjected to dynamic tension using experiments, finite elements and finite differences. This methodology has allowed to provide new experimental and computational insights into the role played by stress waves in the fracture of the samples.

2

Kinematics and objectivity

In this chapter we introduce the basic concepts associated to two fundamental pillars of the Continuum Mechanics framework: the kinematics and the objectivity. A complete understanding of the physics and mathematics which reside behind these subjects is essential to pose, develop and solve any boundary value problem within the framework of the Continuum Theory. The outline is as follows: in section 2.1 we develop the main kinematic concepts and measures (scalars, vectors and tensors) in both Lagrangian and Eulerian descriptions. In section 2.2 we introduce the fundamental concept of frame indifference, show the conditions of objectivity and summarize the main objective stress rates.

2.1 Kinematics

This section is adapted from Holzapfel [1] and Hashiguchi and Yamakawa [63].

2.1.1 Configurations and motions of continuum bodies

Let us consider the body $\mathcal{B}$ and a particle $\mathrm{P} \in \mathcal{B}$ in the Euclidean space at time t, and consider the rectangular reference coordinate system at a fixed origin O and a basis of orthonormal vectors $(\mathbf{e}_1, \mathbf{e}_2, \mathbf{e}_3)$. During its motion the body changes its position from the reference one Ω_0 to the current one Ω, both named as configurations of $\mathcal{B}$ at time t.

The **reference** or **undeformed** configuration Ω_0 coincides with the initial configuration at time $t = 0$. As time evolves, the body moves from region Ω_0 to Ω at time $t > 0$. Point P is located now by position vector $\mathbf{x}$, see Fig. 2.1. Components (X_1, X_2, X_3) and (x_1, x_2, x_3) are the **material** and **spatial** coordinates of point X and x, respectively.

As shown in Fig. 2.1, the map $\mathbf{X} = \boldsymbol{\kappa}_0 (\mathrm{P}, t)$ establishes a biunivocal relation between the point $\mathrm{P} \in \mathcal{B}$ and the point $\mathbf{X} \in \Omega_0$ in the reference configuration at time $t = 0$. By analogy, the map $\boldsymbol{\kappa}$ describes the correspondence between point $\mathrm{P} \in \mathcal{B}$ and point $\mathbf{x} \in \Omega$. The mathematical description is as follows:

$$\mathbf{x} = \boldsymbol{\kappa} \left[\boldsymbol{\kappa}_0^{-1} (\mathbf{X}, t) \right] = \boldsymbol{\chi} (\mathbf{X}, t) \tag{2.1}$$

in which the vector field $\boldsymbol{\chi}$ is the **motion** of body $\mathcal{B}$, and transform the position of points $\mathbf{X}$ in Ω_0 into points $\mathbf{x}$ in the configuration Ω. Assuming that the mapping $\boldsymbol{\chi}$ is invertible, it is possible to refer the position of point $\mathbf{X}$ linked to the spatial point $\mathbf{x}$ at time t with the **inverse motion** denoted by $\boldsymbol{\chi}^{-1}$:

$$\mathbf{X} = \boldsymbol{\chi}^{-1} (\mathbf{x}, t) \tag{2.2}$$

2.1.1.1 Material and spatial descriptions

In the finite deformation analysis, it is mandatory to specify the coordinate system (description) selected to describe the behaviour of the body under the motion $\mathbf{x} = \chi (\mathbf{X}, t)$, see Bonet and Wood [64].

The **material** or **Lagrangian description** is the representation of the main variables during a motion with respect to the material coordinates (X_1, X_2, X_3) and time t. In this description, we focus on the behaviour of a particle while moving. By contrast, the **spatial** or **Eulerian description** is the representation in terms of the spatial coordinates (x_1, x_2, x_3) and time t. Regarding the material description, the attention is focused on a point in space, analysing its evolution as times evolves.

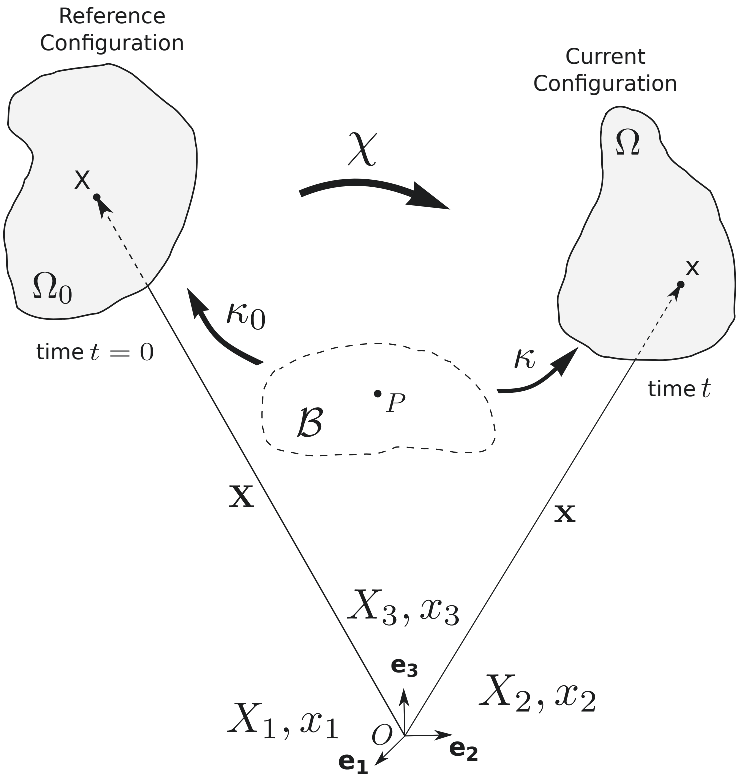

Figure 2.1: Configuration and motion in a Continuum Body, adapted from Holzapfel [1].

Remark 2.1. In solid mechanics the material description is used to approach most boundary value problems. This is (basically) because at some stage of the formulation (see section 4), we have to consider the constitutive behaviour of the material which (usually) involves the material description.

2.1.2 Displacement, velocity and acceleration fields

2.1.2.1 Displacement field

The displacement $\mathbf{U}$ represents the displacement field of a particle in the **material description** (or Lagrangian form) and it is a function of the reference position $\mathbf{X}$ and time t. It is computed as follows:

$$\mathbf{U}(\mathbf{X}, t) = \mathbf{x}(\mathbf{X}, t) - \mathbf{X} \tag{2.3}$$

The displacement $\mathbf{u}$ in the **spatial description** (or Eulerian form) is a function of the current position $\mathbf{x}$ and time t:

$$\mathbf{u}(\mathbf{x}, t) = \mathbf{x} - \mathbf{X}(\mathbf{x}, t) \tag{2.4}$$

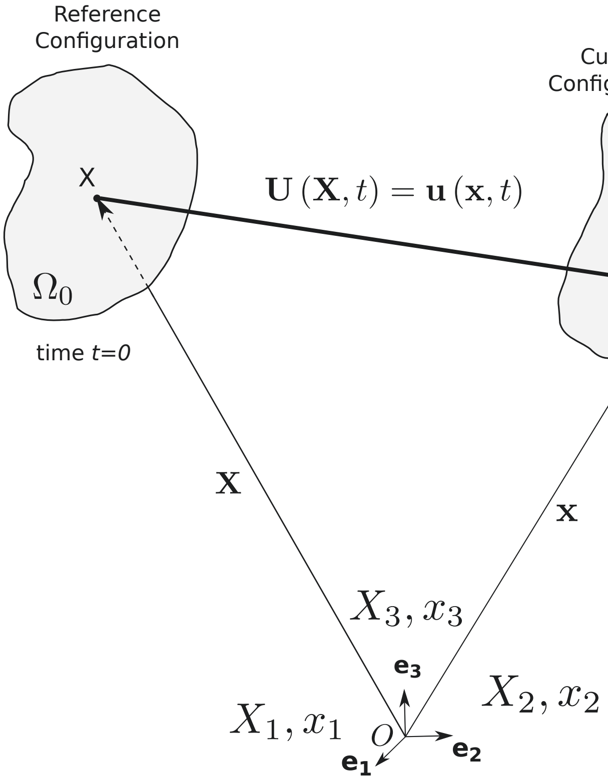

Figure 2.2: Displacement field $\mathbf{u}$ and $\mathbf{U}$ of a particle, adapted from Holzapfel [1].

A map that can describe the positions of the material particles in a body is called a *configuration*. Let us assume a scalar-valued or tensor-valued physical quantity υ and time t, the distribution of this quantity in space can be described by $\upsilon(\mathbf{X}, t)$ or $\upsilon(\mathbf{x}, t)$ in the reference configuration $\mathbf{X}$ or the current configuration $\mathbf{x}$. The mapping from $\mathbf{x}$ to $\mathbf{X}$ is described as follows:

$$\mathbf{x} = \boldsymbol{\chi}(\mathbf{X}, t), \quad \mathbf{X} = \boldsymbol{\chi}^{-1}(\mathbf{x}, t) \tag{2.5}$$

which describes the motion of the material particle. The particle displacement in both descriptions is related by the motion $\mathbf{x}$ as follows:

$$\mathbf{U}(\mathbf{X},t)=\mathbf{U}\left[\boldsymbol{\chi}^{-1}(\mathbf{x},t),t\right]=\mathbf{u}(\mathbf{x},t) \tag{2.6}$$

In previous expression we show that both displacements have the same value (see Fig. 2.2).

2.1.2.2 Velocity and acceleration fields

The **velocity** field in material description can be computed using the first derivative of the motion $\boldsymbol{\chi}$ with respect to time t:

$$\mathbf{V}(\mathbf{X},t)=\frac{\partial\boldsymbol{\chi}(\mathbf{X},t)}{\partial t} \tag{2.7}$$

or in spatial description:

$$\mathbf{V}(\mathbf{X},t)=\mathbf{V}\left[\boldsymbol{\chi}^{-1}(\mathbf{x},t),t\right]=\mathbf{v}(\mathbf{x},t) \tag{2.8}$$

The **acceleration** field in material description is given by the second derivative of the particle's motion:

$$\mathbf{A}(\mathbf{X},t)=\frac{\partial\mathbf{V}(\mathbf{X},t)}{\partial t}=\frac{\partial^2\boldsymbol{\chi}(\mathbf{X},t)}{\partial t^2} \tag{2.9}$$

or its equivalent in Eulerian description:

$$\mathbf{A}(\mathbf{X},t)=\mathbf{A}\left[\boldsymbol{\chi}^{-1}(\mathbf{x},t),t\right]=\mathbf{a}(\mathbf{x},t) \tag{2.10}$$

2.1.3 Measures of total deformation

Let us focus on the variations of size and shape of a body under the deformation from a reference configuration Ω_0 to the current configuration Ω.

2.1.3.1 Deformation gradient

The relation between the current infinitesimal line element $\mathrm{d}\mathbf{x}$ to the initial infinitesimal line element $\mathrm{d}\mathbf{X}$ is given by:

$$\mathrm{d}\mathbf{x} = \mathbf{F}\left(\mathbf{X}, t\right)\mathrm{d}\mathbf{X} \tag{2.11}$$

where the quantity $\mathbf{F}$, referred to as the **deformation gradient**, is defined as follows

$$\mathbf{F}\left(\mathbf{X}, t\right) = \frac{\partial \mathbf{x}}{\partial \mathbf{X}} = \frac{\partial \boldsymbol{\chi}\left(\mathbf{X}, t\right)}{\partial \mathbf{X}} = \mathrm{grad}\mathbf{x}\left(\mathbf{X}, t\right) \tag{2.12}$$

The deformation gradient it is the primary measure of deformation, and it establishes a linear transformation which generates a vector $\mathrm{d}\mathbf{x}$ in the spatial description by the action of the tensor $\mathbf{F}$ on the vector $\mathrm{d}\mathbf{X}$.

Since the map $\boldsymbol{\chi}$ is assumed to be uniquely invertible, we can carry out the inverse of the deformation gradient such that:

$$\mathbf{F}^{-1}\left(\mathbf{x}, t\right) = \frac{\partial \boldsymbol{\chi}^{-1}\left(\mathbf{x}, t\right)}{\partial \mathbf{x}} = \mathrm{grad}\mathbf{X}\left(\mathbf{x}, t\right) \tag{2.13}$$

This inversion carries the spatial line element $\mathrm{d}\mathbf{x}$ into the material line element $\mathrm{d}\mathbf{X}$ using the following relation:

$$\mathrm{d}\mathbf{X} = \mathbf{F}^{-1}\left(\mathbf{x}, t\right)\mathrm{d}\mathbf{x} \tag{2.14}$$

Remark 2.2. Variations of line elements can be computed using the deformation gradient $\mathbf{F}$. However, this relation via $\mathbf{F}$ does not apply to map an infinitesimal material surface element $\mathrm{d}S$ to the corresponding infinitesimal spatial surface element $\mathrm{d}s$. In the same manner, variations of volume elements cannot be computed applying directly the deformation gradient.

The current and the reference infinitesimal volume elements $\mathrm{d}v$ and $\mathrm{d}V$ formed by the infinitesimal line elements $\mathrm{d}\mathbf{x}$ and $\mathrm{d}\mathbf{X}$ are related by:

$$\mathrm{d}v = J\left(\mathbf{X}, t\right)\mathrm{d}V \tag{2.15}$$

where

$$J\left(\mathbf{X}, t\right) = \det\mathbf{F}\left(\mathbf{X}, t\right) > 0 \tag{2.16}$$

where J is the determinant of the deformation gradient and is called the *Jacobian* or Jacobian determinant.

Assuming that $\mathbf{F}$ is invertible, then $J\left(\mathbf{X}, t\right) = \det\mathbf{F}\left(\mathbf{X}, t\right) \neq 0$. In addition, because volume cannot be negative, it derives that $J\left(\mathbf{X}, t\right) > 0$ and so on the inverse $J^{-1} = \det\mathbf{F}^{-1}\left(\mathbf{x}, t\right) > 0$.

Surface vectors in material and spatial description can be expressed as follows:

$$\mathrm{d}\mathbf{s} = \mathbf{n} \cdot \mathrm{d}s, \quad \mathrm{d}\mathbf{S} = \mathbf{N} \cdot \mathrm{d}S \tag{2.17}$$

If we define the infinitesimal spatial volume as the following dot product:

$$\mathrm{d}v = \mathrm{d}\mathbf{s} \cdot \mathrm{d}\mathbf{x} = J\mathrm{d}\mathbf{S} \cdot \mathrm{d}\mathbf{X} \tag{2.18}$$

we can apply equations (2.11) and (2.15) leading to

$$\mathrm{d}\mathbf{s} = J\mathbf{F}^{-T}\mathrm{d}\mathbf{S} \tag{2.19}$$

Previous expression is known as **Nanson's formula**.

2.1.3.2 Strain tensors

In previous section we showed that the deformation gradient is a quantitative measure of changes in material elements during motion. Anyway, strain can be measured by different tensors that are defined in various manners. Firstly, we focus on the most common strain tensors in the **material description**.

The length of the material line element d$\mathbf{X}$ at point $\mathbf{X}$ and time $t = 0$ changes from $\mathrm{d}\varepsilon$ to $\lambda \mathrm{d}\varepsilon$ at time t (see **Fig.** 2.3). The quantity λ is called the **stretch ratio** or **stretch**, and it can be defined as the length $\lambda = \mid \boldsymbol{\lambda}_{\mathbf{a}_0} \mid$ of the stretch vector $\boldsymbol{\lambda}_{\mathbf{a}_0}$ in the direction of the unit vector $\mathbf{a}_0$:

$$\boldsymbol{\lambda}_{\mathbf{a}_0}(\mathbf{X}, t) = \mathbf{F}(\mathbf{X}, t)\,\mathbf{a}_0 \tag{2.20}$$

The stretch λ is a quantitative measure of the magnitude of vector $\mathbf{a}_0$ and its sign provides information about the nature of the stretching, considering that it has been extended, unstretched or compressed if $\lambda > 1$, $\lambda = 1$ or $\lambda < 1$, respectively.

Taking the square of λ and using definition (2.20) we have that:

$$\lambda^2 = \lambda_{\mathbf{a}_0} \cdot \lambda_{\mathbf{a}_0} = \mathbf{F}\mathbf{a}_0 \cdot \mathbf{F}\mathbf{a}_0 = \mathbf{a}_0 \cdot \mathbf{F}^T\mathbf{F}\mathbf{a}_0 = \mathbf{a}_0 \cdot \mathbf{C}\mathbf{a}_0 \tag{2.21}$$

where

$$\mathbf{C} = \mathbf{F}^T\mathbf{F} \tag{2.22}$$

Tensor $\mathbf{C}$ is the **right Cauchy-Green** tensor, a strain measure in material coordinates. The inverse of the right Cauchy-Green tensor, denoted by $\mathbf{B}$, is the so-called **Piola deformation tensor**.

The change in vector's squared lengths is an alternative strain measure known as tensor $\mathbf{E}$ or **Green-Lagrange strain tensor**

$$\frac{1}{2}\left[(\lambda \mathrm{d}\varepsilon)^2 - \mathrm{d}\varepsilon^2\right] = \mathrm{d}\mathbf{X} \cdot \mathbf{E}\mathrm{d}\mathbf{X} \tag{2.23}$$

where

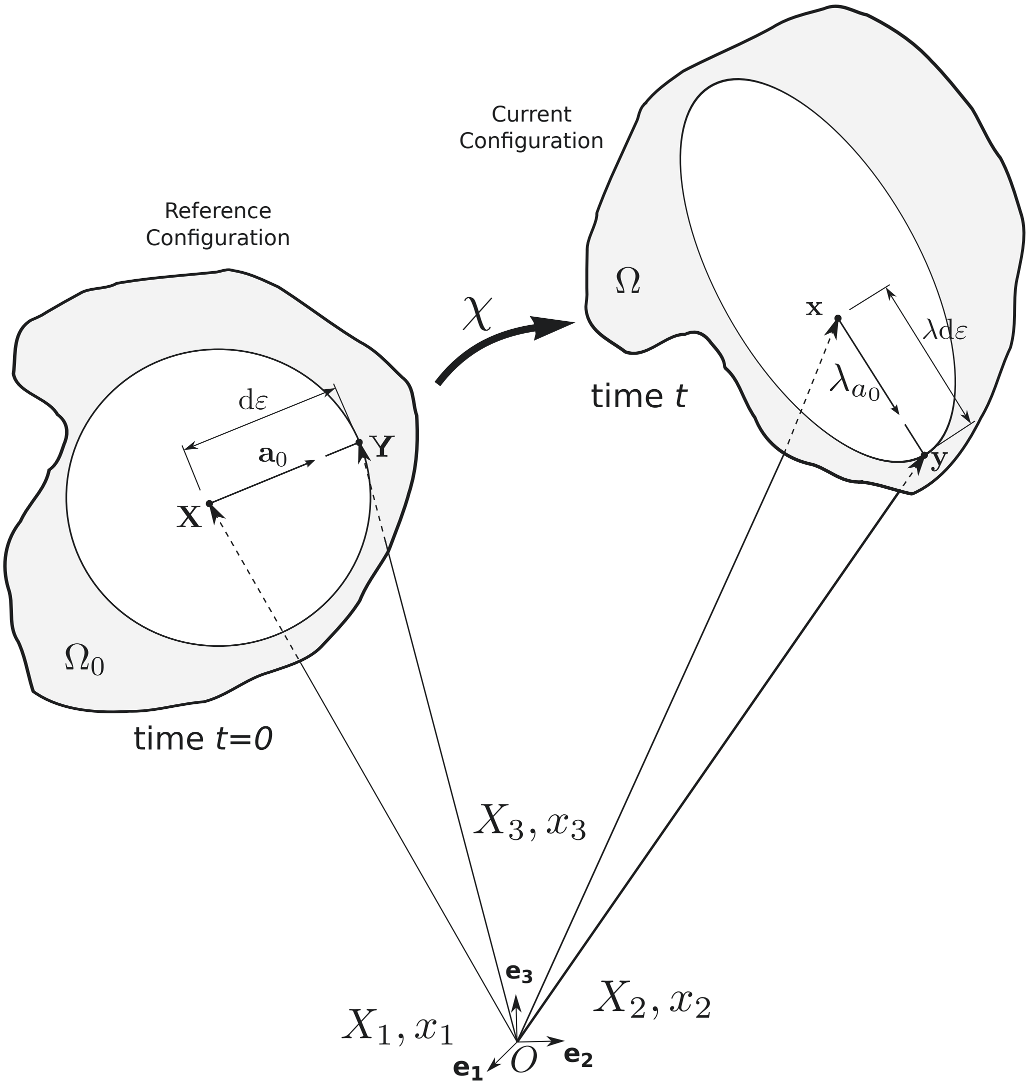

Figure 2.3: Deformation of a material line element in **material** description, adapted from Holzapfel [1].

$$\mathbf{E} = \frac{1}{2}\left(\mathbf{F}^T\mathbf{F} - \mathbf{I}\right) = \frac{1}{2}\left(\mathbf{C} - \mathbf{I}\right) \tag{2.24}$$

Alternatively, all those strain tensors can be defined in the spatial description if all quantities are referred to the current configuration, as it is shown in **Fig.** 2.4.

In this case, the **stretch vector $\boldsymbol{\lambda}_\mathbf{a}$** in the direction of the unit vector **a** is:

$$\boldsymbol{\lambda}_\mathbf{a}^{-1}(\mathbf{x}, t) = \mathbf{F}^{-1}(\mathbf{x}, t)\,\mathbf{a} \tag{2.25}$$

where the length of the inverse stretch vector $\boldsymbol{\lambda}_\mathbf{a}^{-1}$ is the **inverse stretch ratio** λ^{-1}. Following the same procedure as in the material description, the square of

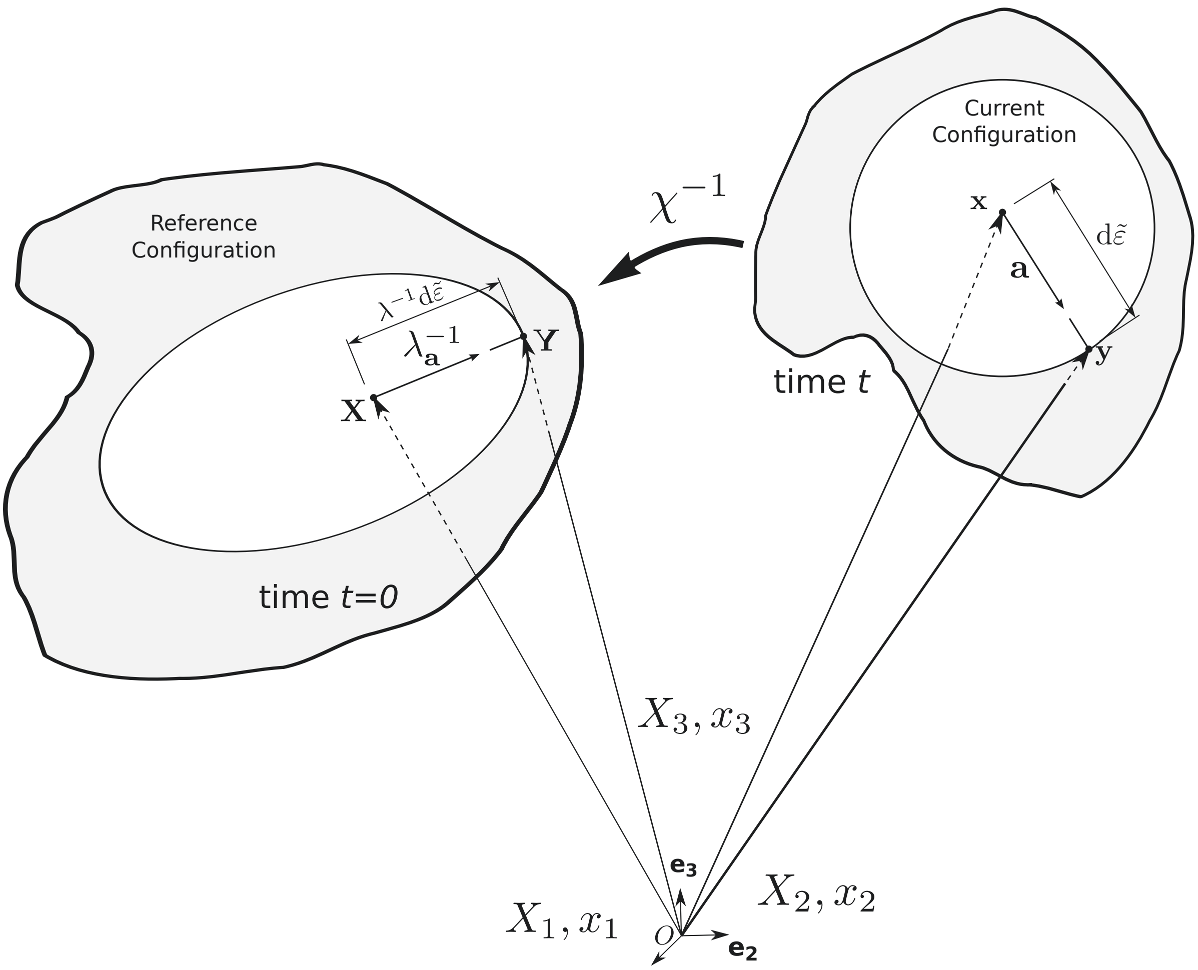

Figure 2.4: Deformation of a material line element in **spatial** description, adapted from Holzapfel [1].

the inverse stretch ratio is:

$$\lambda^{-2} = \boldsymbol{\lambda}_{\mathbf{a}}^{-1} \cdot \boldsymbol{\lambda}_{\mathbf{a}}^{-1} = \mathbf{F}^{-1}\mathbf{a} \cdot \mathbf{F}^{-1}\mathbf{a} = \mathbf{a} \cdot \mathbf{F}^{-T}\mathbf{F}^{-1}\mathbf{a} = \mathbf{a} \cdot \mathbf{b}^{-1}\mathbf{a} \tag{2.26}$$

where $\mathbf{b}^{-1} = \mathbf{F}^{-T}\mathbf{F}^{-1}$ is the inverse of the **left Cauchy-Green tensor b** defined by:

$$\mathbf{b} = \mathbf{F}\mathbf{F}^{T} \tag{2.27}$$

or also known as **Finger deformation tensor**.

Moreover, computing the change in the squared lengths in spatial description (see Fig. 2.4), we obtain:

$$\frac{1}{2}\left[\mathrm{d}\tilde{\varepsilon}^2 - \left(\lambda^{-1}\mathrm{d}\tilde{\varepsilon}\right)^2\right] = \mathrm{d}\mathbf{x}\cdot\mathbf{e}\mathrm{d}\mathbf{x} \tag{2.28}$$

where

$$\mathbf{e} = \frac{1}{2}\left(\mathbf{I} - \mathbf{F}^{-T}\mathbf{F}^{-1}\right) \tag{2.29}$$

Tensor **e** is a symmetric strain tensor referred to as the **Euler-Almansi strain tensor**.

Other useful measure of strain is the so-called **Hencky strain tensor**. The **material** or **right Hencky strain tensor**, $\mathbf{E}^{(0)}$ can be defined by the right stretch tensor **U** or the right Cauchy-Green tensor **C** as follows:

$$\mathbf{E}^{(0)} = \ln\mathbf{U} = \frac{1}{2}\ln\mathbf{C} \tag{2.30}$$

The **spatial** or **left Hencky strain tensor**, $\mathbf{e}^{(0)}$ is described using the left stretch tensor **V** or the left Cauchy-Green tensor b, that is,

$$\mathbf{e}^{(0)} = \ln\mathbf{V} = \frac{1}{2}\ln\mathbf{b} \tag{2.31}$$

$\mathbf{E}^{(0)}$ and $\mathbf{e}^{(0)}$ are mutually related as follows

$$\mathbf{E}^{(0)} = \mathbf{R}^T\mathbf{e}^{(0)}\mathbf{R} \tag{2.32}$$

$$\mathbf{e}^{(0)} = \mathbf{R}\mathbf{E}^{(0)}\mathbf{R}^T \tag{2.33}$$

2.1.4 Rotation and stretch tensors

Any motion can be decomposed into two separate contributions, i.e., a pure **stretching** and a pure **rotation**. From a purely mathematical point of view, this means that the deformation gradient tensor **F** can be expressed as the product of a rotation tensor times a stretch tensor to define the so-called **polar decomposition**:

$$\mathbf{F} = \mathbf{R}\mathbf{U} = \mathbf{v}\mathbf{R} \tag{2.34}$$

in which $\mathbf{R}^T\mathbf{R} = \mathbf{I}$ because $\mathbf{R}$ is an orthogonal tensor. Tensors $\mathbf{U}$ and $\mathbf{v}$ or **right** or **material stretch tensor** and **left** or **spatial** stretch tensor respectively are unique, positive definite and symmetric, i.e. $\mathbf{U} = \mathbf{U}^T$ and $\mathbf{v} = \mathbf{v}^T$. They are defined in the reference of current configuration so they are a quantitative measure of local changes in shape.

Moreover, we have that:

$$\mathbf{U}^2 = \mathbf{U}\mathbf{U} = \mathbf{C}, \qquad \mathbf{v}^2 = \mathbf{v}\mathbf{v} = \mathbf{b} \tag{2.35}$$

and

$$\det\mathbf{U} = \det\mathbf{v} = J > 0 \tag{2.36}$$

2.1.5 The rate of deformation tensors

In Continuum Mechanics is mandatory to define the rate of fields that describe changes of shape, position or orientation in a body during a motion.

Firstly, we introduce the spatial and material velocity gradient. For that task we take the gradient of a spatial velocity field $\mathbf{v}(\mathbf{x}, t)$ in the spatial description:

$$\mathbf{l}(\mathbf{x}, t) = \frac{\partial \mathbf{v}(\mathbf{x}, t)}{\partial \mathbf{x}} = \mathrm{grad}\mathbf{v}(\mathbf{x}, t) \tag{2.37}$$

The second-order and non-symmetric tensor $\mathbf{l}$ is called **spatial velocity gradient**. Now the operation can be repeated in the material description to obtain the **material velocity gradient**. If we take the material time derivative of the deformation gradient $\mathbf{F}$ we have that:

$$\begin{aligned}\dot{\mathbf{F}}\left(\mathbf{X},t\right) &= \frac{\partial}{\partial t}\left(\frac{\partial \boldsymbol{\chi}\left(\mathbf{X},t\right)}{\partial \mathbf{X}}\right) = \frac{\partial}{\partial \mathbf{X}}\left(\frac{\partial \boldsymbol{\chi}\left(\mathbf{X},t\right)}{\partial t}\right) = \\ &= \frac{\partial \mathbf{V}\left(\mathbf{X},t\right)}{\partial \mathbf{X}} = \mathrm{Grad}\mathbf{V}\left(\mathbf{X},t\right) \qquad (2.38)\end{aligned}$$

Using Eqs. (2.7), (2.8) and (2.37), the spatial velocity gradient $\mathbf{l}$ is rewritten as follows:

$$\mathbf{l} = \frac{\partial \mathbf{v}}{\partial \mathbf{x}} = \frac{\partial \dot{\boldsymbol{\chi}}\left(\mathbf{X},t\right)}{\partial \mathbf{X}}\frac{\partial \mathbf{X}}{\partial \mathbf{x}} = \dot{\mathbf{F}}\mathbf{F}^{-1} \qquad (2.39)$$

Remark 2.3. The material time derivative of $\mathbf{F}^{-1}$ and $\mathbf{F}^{-T}$ are computed below for further calculations.

Using the property $\mathbf{F}^{-1}\mathbf{F} = \mathbf{I}$, the product rule and the relation $\mathbf{l} = \dot{\mathbf{F}}\mathbf{F}^{-1}$ we have that:

$$\begin{aligned}\mathbf{F}^{-1}\mathbf{F} = \mathbf{I} \Longrightarrow \dot{\overline{\mathbf{F}^{-1}\mathbf{F}}} = 0 \Longrightarrow \dot{\overline{\mathbf{F}^{-1}}}\mathbf{F} = -\mathbf{F}^{-1}\dot{\mathbf{F}} \Longrightarrow \\ \Longrightarrow \dot{\overline{\mathbf{F}^{-1}}} = -\mathbf{F}^{-1}\dot{\mathbf{F}}\mathbf{F}^{-1} = -\mathbf{F}^{-1}\mathbf{l} \qquad (2.40)\end{aligned}$$

and

$$\begin{aligned}\mathbf{F}^{-T}\mathbf{F}^{T} = \mathbf{I} \Longrightarrow \dot{\overline{\mathbf{F}^{-T}\mathbf{F}^{T}}} = 0 \Longrightarrow \dot{\overline{\mathbf{F}^{-T}}}\mathbf{F}^{T} = -\mathbf{F}^{-T}\dot{\overline{\mathbf{F}^{T}}} \\ \dot{\overline{\mathbf{F}}} = -\mathbf{F}^{-T}\dot{\overline{\mathbf{F}}}\mathbf{F}^{-T} = -\mathbf{l}^{T}\mathbf{F}^{-T} \qquad (2.41)\end{aligned}$$

Previous expressions allow to obtain the following relations:

$$\dot{\overline{\mathbf{F}^{-1}}} = -\mathbf{F}^{-1}\mathbf{l} \tag{2.42}$$

$$\dot{\overline{\mathbf{F}^{-T}}} = -\mathbf{l}^{T}\mathbf{F}^{-T} \tag{2.43}$$

Moreover, spatial velocity gradient can be decomposed into a symmetric and skew symmetric part in order to obtain:

$$\mathbf{l}\left(\mathbf{x},t\right) = \mathbf{d}\left(\mathbf{x},t\right) + \mathbf{w}\left(\mathbf{x},t\right) \tag{2.44}$$

where

$$\mathbf{d} = \frac{1}{2}\left(\mathbf{l} + \mathbf{l}^{T}\right) = \frac{1}{2}\left(\mathrm{grad}\mathbf{v} + \mathrm{grad}^{T}\mathbf{v}\right) = \mathbf{d}^{T} \tag{2.45}$$

$$\mathbf{w} = \frac{1}{2}\left(\mathbf{l} - \mathbf{l}^{T}\right) = \frac{1}{2}\left(\mathrm{grad}\mathbf{v} - \mathrm{grad}^{T}\mathbf{v}\right) = -\mathbf{w}^{T} \tag{2.46}$$

The symmetric part of the spatial velocity gradient **l** is the covariant second-order **rate of deformation tensor d** and the skew symmetric part of **l** is the covariant second-order **spin tensor w**.

Moreover, we can define the spatial velocity gradient in terms of the right stretch tensor **U** or its material time derivative $\dot{\mathbf{U}}$. Using Eqs. (2.39),(2.34) and (A.49) we have that:

$$\mathbf{l} = \left(\dot{\mathbf{R}}\mathbf{U}\right)\mathbf{F}^{-1} + \left(\mathbf{R}\dot{\mathbf{U}}\right)\mathbf{F}^{-1} = \dot{\mathbf{R}}\mathbf{R}^{T} + \mathbf{R}\left(\dot{\mathbf{U}}\mathbf{U}^{-1}\right)\mathbf{R}^{T} \tag{2.47}$$

In addition, the decomposition of the spatial velocity gradient into the rate of deformation tensor **d** and the spin tensor **w** leads to:

$$\mathbf{d} = \mathbf{R}\mathrm{sym}\left(\dot{\mathbf{U}}\mathbf{U}^{-1}\right)\mathbf{R}^{T}, \quad \mathbf{w} = \dot{\mathbf{R}}\mathbf{R}^{T} + \mathbf{R}\mathrm{skew}\left(\dot{\mathbf{U}}\mathbf{U}^{-1}\right)\mathbf{R}^{T} \tag{2.48}$$

2.1.5.1 Material time derivatives of strain tensors

The material time derivative of the Green-Lagrange strain tensor is computed as:

$$\dot{\mathbf{E}} = \mathbf{F}^T \mathbf{d} \mathbf{F} \tag{2.49}$$

The time rate of change of the rigth Cauchy-Green tensor $\mathbf{C}$ is:

$$\dot{\mathbf{C}} = 2\dot{\mathbf{E}} = 2\mathbf{F}^T \mathbf{d} \mathbf{F} \tag{2.50}$$

The material time derivative of the left Cauchy-Green tensor $\mathbf{b}$ is computed as follows:

$$\dot{\mathbf{b}} = \dot{\overline{\mathbf{F}\mathbf{F}^T}} = \left(\dot{\mathbf{F}}\mathbf{F}^{-1}\right)\mathbf{F}\mathbf{F}^T + \left(\mathbf{F}\mathbf{F}^T\right)\mathbf{F}^{-T}\dot{\overline{\mathbf{F}^T}} = \mathbf{l}\mathbf{b} + \mathbf{b}\mathbf{l}^T \tag{2.51}$$

The time rate of change of the Euler-Almansi strain tensor $\mathbf{e}$ is:

$$\dot{\mathbf{e}} = -\frac{1}{2}\dot{\overline{\mathbf{F}^{-T}\mathbf{F}^{-1}}} = \mathbf{d} - \mathbf{l}^T\mathbf{e} - \mathbf{e}\mathbf{l} \tag{2.52}$$

If we consider that the principal directions of $\mathbf{C}$ and $\mathbf{b}$ are fixed, then the following equation holds:

$$\left[\mathbf{E}^{(0)}\right]_i = \left[\mathbf{e}^{(0)}\right]_i = \ln\lambda_i = \ln\frac{\partial \mathbf{x}_i}{\partial \mathbf{X}_i} \tag{2.53}$$

with i the diagonal terms in the tensor. Then, the time rate of change of Hencky strain tensors is:

$$\left\{\left[\mathbf{E}^{(0)}\right]_i\right\}^{\bullet} = \left\{\left[\mathbf{e}^{(0)}\right]_i\right\}^{\bullet} = [\ln\lambda_i]^{\bullet} = \left(\frac{\partial \mathbf{x}_i}{\partial \mathbf{X}_i}\right)^{\bullet} \Big/ \left(\frac{\partial \mathbf{x}_i}{\partial \mathbf{X}_i}\right) = \frac{\partial \dot{\mathbf{x}}_i}{\partial \mathbf{X}_i} = \mathbf{d}_i \tag{2.54}$$

where $\mathbf{d}_i$ (no sum) is the normal component in the strain rate tensor $\mathbf{d}$.

2.1.5.2 Material time derivatives of spatial line, surface and volume elements

Considering the spatial and material line elements d$\mathbf{x}$ and d$\mathbf{X}$, the material time derivative of d$\mathbf{x}$ is:

$$\dot{\overline{\mathrm{d}\mathbf{x}}} = \dot{\mathbf{F}}\mathrm{d}\mathbf{X} = \dot{\mathbf{F}}\mathbf{F}^{-1}\mathrm{d}\mathbf{x} = \mathbf{l}\mathrm{d}\mathbf{x} \tag{2.55}$$

To compute the material time derivative of the spatial surface and volume elements, it is necessary to obtain the material time derivative of the Jacobian, i.e: $J = \det\mathbf{F}$. Using the chain rule we have that:

$$\dot{J} = \frac{\partial J}{\partial \mathbf{F}} : \dot{\mathbf{F}} \tag{2.56}$$

The first term in the right-hand side of the equation can be simplified using expression (A.94) that allows to compute the gradient of the determinant of a second order tensor $\mathbf{A}$, i.e:

$$\frac{\partial J}{\partial \mathbf{F}} = J\mathbf{F}^{-T} \tag{2.57}$$

Using the trace and double contraction operator's properties, and the time derivative of the deformation gradient $\dot{\mathbf{F}} = \mathbf{l}\mathbf{F}$ we have that:

$$\dot{J} = J\mathrm{div}\mathbf{v} \tag{2.58}$$

An alternative (equivalent) expression deduced from the additive decomposition of the spatial gradient velocity $\mathbf{l} = \mathrm{grad}\mathbf{v} = \mathbf{d} + \mathbf{w}$ is:

$$\dot{J} = J\mathrm{tr}\mathbf{d} \tag{2.59}$$

Once the value of $\dot{J}$ is known, we can perform the material time derivative of an infinitesimal surface in spatial description using Eqs. (2.19), (2.43) and (2.58):

$$\dot{\overline{\mathrm{d}\mathbf{s}}} = \left(\dot{J}\mathbf{F}^{-T} + J\dot{\overline{\mathbf{F}^{-T}}}\right)\mathrm{d}\mathbf{S} = \mathrm{div}\mathbf{v}\mathrm{d}\mathbf{s} - \mathbf{l}^T\mathrm{d}\mathbf{s} \tag{2.60}$$

The material time derivative of the spatial volume element $\mathrm{d}v = J\mathrm{d}V$ is:

$$\dot{\overline{\mathrm{d}v}} = \dot{J}\mathrm{d}V = \mathrm{div}\mathbf{v}\mathrm{d}v \tag{2.61}$$

2.2 Objectivity

This section is adapted from Holzapfel [1], Hashiguchi and Yamakawa [63] and Sumelka [65].

2.2.1 The concept of objectivity

Objectivity is one of the key points in the description of deformation behaviour of materials. The essential meaning of the objectivity principle, advocated by Oldroyd (1950) and also referred to as the *principle of material-frame indifference*; is that constitutive properties of materials, including deformation, are independent of the observer. This means that any constitutive equation has to be formulated such that it is not influenced by the superposition of rigid-body rotation [63]. Mathematically, the principle of material frame-indifference can be stated as the invariance of constitutive equation under any change of frame [66]. Therefore, its formulation has to be independent of the coordinate system. The tensors included in the formulation must obey a common coordinate transformation rule. A tensor that obeys this common transformation rule, even if there is a relative motion between the coordinate systems (this means that a rigid-body rotation is superposed on material), is referred to as an *objective tensor*; and the rule is called the *objective transformation rule* [63]. The order of the tensor, or in other words, the number of the base vectors to which the tensor is based on; does not affect to this transformation rule.

Physically, objectivity can be explained in terms of how a tensor describing a physical quantity included in a material is observed from the outside of the material.

This leads to the use of a coordinate system different than the convected (or material) one for examination of objectivity. Usually, orthogonal coordinate systems are used.

2.2.2 Dependence on observer

Let us consider that two different observers are recording an arbitrary event in the Euclidean space by means of the position in space and time. For instance, they are registering the deformation of a solid in time. This deformation can be described by each observer using kinematic variables as displacement, velocity, strain and so on. However, the observers can not record the same value for these variables, since they have different perspectives [2].

An observer is someone who can measure relative positions in space and instants of time. An event is the physical world, i.e, a material particle, that the observer is measuring at a particular point in space and time. Imagine that one specific event is recorded by an observer O as the pair $(\mathbf{x}, t)$ and the same event is measured by the observer O^* as the different pair $(\mathbf{x}^*, t^*)$. An observer O records that the distance between the points in the first pair of points is $\mid \mathbf{x} - \mathbf{x}_0 \mid$ and $\mid \mathbf{x}_1 - \mathbf{x}_0 \mid$ in the second pair, and the time interval is $\mid t - t_0 \mid$ in both cases. The observer O^* registers the distances $\mid \mathbf{x}^* - \mathbf{x}_0^* \mid$ and $\mid \mathbf{x}_1^* - \mathbf{x}_0^* \mid$ in the same time interval $\mid t - t_0 \mid$. A spatial map that satisfies the requirement of preserving distance is the following transformation equation:

$$\mathbf{x}^* - \mathbf{x}_0^* = \mathbf{Q}\,(\mathbf{x} - \mathbf{x}_0) \tag{2.62}$$

Application of this transformation to the case illustrated in Fig. 2.5 leads to:

$$(\mathbf{x}_1^* - \mathbf{x}_0^*) \cdot (\mathbf{x}^* - \mathbf{x}_0^*) = \mathbf{Q} \cdot (\mathbf{x}_1 - \mathbf{x}_0) \cdot \mathbf{Q} \cdot (\mathbf{x} - \mathbf{x}_0) = (\mathbf{x}_1 - \mathbf{x}_0) \cdot (\mathbf{x} - \mathbf{x}_0) \tag{2.63}$$

The tensor $\mathbf{Q}$ is a proper orthogonal tensor (see section A.2.4), to preserve lengths, angles and orientation. Furthermore, its dependency on time reflects the movement between observers in time.

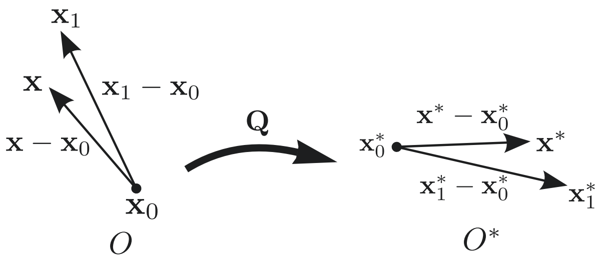

Figure 2.5: Map of three points preserving distance and time interval [2].

Observers must also agree on time intervals between events, so if observer O records an event at time t and observer O^* at time t^*, then the relation between times is given by a constant α as follows [2]:

$$t^* = t + \alpha \tag{2.64}$$

In addition, if we consider a origin of coordinate system for each observer, i.e o and o^*, then we may write the following mathematical expression:

$$\mathbf{x}^* = \mathbf{c}\,(t) + \mathbf{Q}\,(t)\,\mathbf{x} \tag{2.65}$$

where the vector $\mathbf{c}\,(t)$ is a continuous differentiable function defined as:

$$\mathbf{c}\,(t) = \mathbf{x}_0^* - \mathbf{Q}\,(t)\,\mathbf{x}_0 \tag{2.66}$$

2.2.3 Objective vectors and tensors

We have to ensure that any physical quantity must be invariant relative to a particular change of observer. A physical quantity is **objective** if it is independent of the observer.

Any spatial vector field $\mathbf{u}$ is an **objective spatial vector**, or it is said to be **frame-indifferent**, if it fulfils the following transformation:

$$\mathbf{u}^* = \mathbf{Q}\mathbf{u} \tag{2.67}$$

As previously mentioned, observers can move relative to each other, as it is included in the time dependency of $\mathbf{c}(t)$ and $\mathbf{Q}(t)$. Let us consider the motion $\mathbf{x} = \boldsymbol{\chi}(\mathbf{X}, t)$ recorded by one observer O and $\mathbf{x}^* = \boldsymbol{\chi}(\mathbf{X}, t^*)$ by a second observer:

$$\boldsymbol{\chi}^*(\mathbf{X}, t^*) = \mathbf{Q}(t)\,\boldsymbol{\chi}(\mathbf{X}, t) + \mathbf{c}(t), \quad t^* = t + \alpha \tag{2.68}$$

We show in previous expression that the motion is not an objective vector [2]. Taking the derivative of this motion we can obtain the velocity under the observer transformation:

$$\dot{\mathbf{x}}^* = \dot{\mathbf{Q}}\mathbf{x} + \mathbf{Q}\dot{\mathbf{x}} + \dot{\mathbf{c}} \tag{2.69}$$

We show in previous expression that the velocity field is not an objective vector. This expression can be rewritten as follows:

$$\dot{\mathbf{x}}^* - \mathbf{Q}\dot{\mathbf{x}} = \Omega_0(\mathbf{x}^* - \mathbf{c}) + \dot{\mathbf{c}} \tag{2.70}$$

where $\Omega_0 = \dot{\mathbf{Q}}\mathbf{Q}^T$ is a skew symmetric tensor that represents the rigid body angular velocity between the observers.

It can be obtained the following transformation for the acceleration [2]:

$$\ddot{\mathbf{x}}^* - \mathbf{Q}\ddot{\mathbf{x}} = \dot{\boldsymbol{\Omega}}_{\mathbf{Q}}(\mathbf{x}^* - \mathbf{c}) - \boldsymbol{\Omega}_{\mathbf{Q}}^2(\mathbf{x}^* - \mathbf{c}) + 2\boldsymbol{\Omega}_{\mathbf{Q}}(\dot{\mathbf{x}} - \dot{\mathbf{c}}) + \ddot{\mathbf{c}} \tag{2.71}$$

The first three terms on the right-hand side of the equation are the so-called **Euler acceleration**, **centrifugal acceleration** and the **Coriolis acceleration**, respectively.

Remark 2.4. In general, velocity and acceleration of motion are not objective.

An **objective (spatial) tensor** is defined to be one which transforms and objective vector into an objective vector [2]. Consider two tensors corresponding to two different observers $\mathbf{T}$ and $\mathbf{T}^*$, and two objective vector $\mathbf{v}$ and $\mathbf{v}^*$. Consider also vectors $\mathbf{u} = \mathbf{T}\mathbf{v}$ and $\mathbf{u}^* = \mathbf{T}^*\mathbf{v}^*$. Then, to assure that $\mathbf{u}$ is objective:

$$\mathbf{u}^* = \mathbf{Q}\mathbf{u} = \mathbf{Q}\mathbf{T}\mathbf{v} = \mathbf{Q}\mathbf{T}\mathbf{Q}^T\mathbf{v}^* \tag{2.72}$$

so the tensor is **objective** if it fulfills the expression:

$$\mathbf{T}^* = \mathbf{Q}\mathbf{T}\mathbf{Q}^T \tag{2.73}$$

and the following properties arise [2]:

$$(\mathbf{a} + \mathbf{b})^* = \mathbf{a}^* + \mathbf{b}^* \tag{2.74}$$

$$(\mathbf{a} \otimes \mathbf{b})^* = \mathbf{a}^* \otimes \mathbf{b}^* \tag{2.75}$$

$$(\mathbf{a} \cdot \mathbf{b})^* = \mathbf{a}^* \cdot \mathbf{b}^* \tag{2.76}$$

$$(\mathbf{A}\mathbf{b})^* = \mathbf{A}^*\mathbf{b}^* \tag{2.77}$$

$$(\mathbf{A}\mathbf{B})^* = \mathbf{A}^*\mathbf{B}^* \tag{2.78}$$

$$\left(\mathbf{A}^{-1}\right)^* = (\mathbf{A}^*)^{-1} \tag{2.79}$$

$$(\mathbf{A} : \mathbf{B})^* = \mathbf{A}^* : \mathbf{B}^* \tag{2.80}$$

A **two-point tensor** is objective if it transforms an objective material tensor into an objective spatial tensor. Consider two tensors $\mathbf{T}$ and $\mathbf{T}^*$ recorded by two different observers. If we take objective material vectors $\mathbf{v}$ and $\mathbf{v}^*$ and use them to obtain vectors $\mathbf{u} = \mathbf{T}\mathbf{v}$ and $\mathbf{u}^* = \mathbf{T}^*\mathbf{v}^*$, then the material vector is objective if it is unaffected by and observer transformation [2]:

$$\mathbf{u}^* = \mathbf{Q}\mathbf{u} = \mathbf{Q}\mathbf{T}\mathbf{v} = \mathbf{Q}\mathbf{T}\mathbf{v}^* \tag{2.81}$$

so the tensor is objective and

$$\mathbf{T}^* = \mathbf{Q}\mathbf{T} \tag{2.82}$$

is the objectivity requirement for a two-point tensor.

2.2.4 Objective rates

In order to formulate constitutive equations, it is mandatory that all fields in the structure of the model will be objective. In addition, if the model has a rate type structure, it is essential to fulfill the objectivity in all the rate fields. In this regard, one should note that the material time rate is not enough to assure the objectivity of all the field variables, for instance the stress fields. Deriving objective stress rates can be conducted in several ways, each of these ways leading to a different stress rate tensor.

The material time derivatives of an objective vector field $\mathbf{u} = \mathbf{u}\left(\mathbf{x}, t\right)$ and an objective second-order tensor field $\mathbf{A} = \mathbf{A}\left(\mathbf{x}, t\right)$ are given by:

$$\dot{\mathbf{u}}^* = \mathbf{Q}\dot{\mathbf{u}} + \dot{\mathbf{Q}}\mathbf{u}, \qquad \dot{\mathbf{A}}^* = \dot{\mathbf{Q}}\mathbf{A}\mathbf{Q}^T + \mathbf{Q}\dot{\mathbf{A}}\mathbf{Q}^T + \mathbf{Q}\mathbf{A}\dot{\overline{\mathbf{Q}^T}} \tag{2.83}$$

and they are not objectives quantities because they do not fulfil the objectivity condition $\dot{\mathbf{u}}^* \neq \mathbf{Q}\dot{\mathbf{u}}$ and $\dot{\mathbf{A}}^* \neq \dot{\mathbf{Q}}\mathbf{A}\mathbf{Q}^T$.

Manipulation of the material time derivative allows to obtain an objective rate. Using properties of orthogonal tensors (see section A.2.4) and spin tensor property $\mathbf{w} = -\mathbf{w}^T$, we have that:

$$\dot{\mathbf{Q}} = \mathbf{w}^*\mathbf{Q} - \mathbf{Q}\mathbf{w}, \quad \dot{\overline{\mathbf{Q}^T}} = -\mathbf{Q}^T\mathbf{w}^* + \mathbf{w}\mathbf{Q}^T \tag{2.84}$$

Convenient rewriting of Eqs. (2.83) leads to:

$$\left(\dot{\mathbf{u}} - \mathbf{w}\mathbf{u}\right)^* = \mathbf{Q}\left(\dot{u} - \mathbf{w}\mathbf{u}\right) \tag{2.85}$$

Using the corotational rate of the vector field $\mathbf{u}$, i.e. $\mathring{\mathbf{u}} = \dot{\mathbf{u}} - \mathbf{w}\mathbf{u}$, we have that:

$$\left(\mathring{\mathbf{u}}\right)^* = \mathbf{Q}\mathring{\mathbf{u}} \tag{2.86}$$

The same procedure is developed for the second-order tensor $\mathbf{A}$ following the steps in section 2.2.3

$$\left(\dot{\mathbf{A}} - \mathbf{wA} + \mathbf{Aw}\right)^* = \mathbf{Q}\left(\dot{\mathbf{A}} - \mathbf{wA} + \mathbf{Aw}\right)\mathbf{Q}^T \tag{2.87}$$

Using the equation in the corotational rate form we have that:

$$\left(\mathring{\mathbf{A}}\right)^* = \mathbf{Q}\mathring{\mathbf{A}}\mathbf{Q}^T \tag{2.88}$$

where the objective rate expression

$$\mathring{\mathbf{A}} = \dot{\mathbf{A}} - \mathbf{wA} + \mathbf{Aw} \tag{2.89}$$

is the **Jaumann-Zaremba rate**.

In addition, we can be define the **convected rates** of **u** and **A** as:

$$\mathbf{u}^{(\mathrm{C})^\circ} = \dot{\mathbf{u}} + \mathbf{l}^T\mathbf{u} \tag{2.90}$$

and

$$\mathbf{A}^{(\mathrm{C})^\circ} = \dot{\mathbf{A}} + \mathbf{l}^T\mathbf{A} + \mathbf{A}\mathbf{l} \tag{2.91}$$

where $\mathbf{A}^{(\mathrm{C})^\circ}$ is the **Cotter-Rivlin rate**.

2.2.5 Objective stress rates

Following the notation of Sumelka [65], we provide below a brief summary of the main objectives rates:

- **Oldroyd or Lie rate**: The **Oldroyd stress rate** of a spatial stress field is defined by means of the Lie time derivative of that field. It is a contravariant convected rate of the Cauchy stress σ (or first Kirchhoff stress), given by:

$$\mathcal{L}_v\boldsymbol{\sigma} = \boldsymbol{\sigma}^{(O)^\circ} = \dot{\boldsymbol{\sigma}} - \boldsymbol{\sigma}\cdot\mathbf{l}^T - \mathbf{l}\cdot\boldsymbol{\sigma} \tag{2.92}$$

- **Truesdell rate**: The **Truesdell stress rate** of the Cauchy stress is defined as the Piola transformation of $\dot{\mathbf{S}}$:

$$\boldsymbol{\sigma}^{(T)^\circ} = J^{-1}\mathbf{F}\dot{\mathbf{S}}\mathbf{F}^T \tag{2.93}$$

  It can be given in its convected form, as a function of the spatial velocity gradient $\mathbf{l}$:

$$\boldsymbol{\sigma}^{(T)^\circ} = \dot{\boldsymbol{\sigma}} - \boldsymbol{\sigma} \cdot \mathbf{l}^T - \mathbf{l} \cdot \boldsymbol{\sigma} + \boldsymbol{\sigma}\mathrm{tr}\mathbf{d} \tag{2.94}$$

  We can see that there is a relation between the Oldroyd and the Truesdell stress rate such that:

$$\boldsymbol{\sigma}^{(O)^\circ} = \boldsymbol{\sigma}^{(T)^\circ} - \boldsymbol{\sigma}\mathrm{tr}\mathbf{d} \tag{2.95}$$

  or in terms of the Kirchhoff stress:

$$\boldsymbol{\tau}^{(O)^\circ} = J\boldsymbol{\tau}^{(T)^\circ} \tag{2.96}$$

- **Cotter-Rivlin rate**: The covariant convected rate of the Cauchy stress is given by:

$$\boldsymbol{\sigma}^{(C)^\circ} = \dot{\boldsymbol{\sigma}} + \boldsymbol{\sigma} \cdot \mathbf{l}^T + \mathbf{l} \cdot \boldsymbol{\sigma} \tag{2.97}$$

- **Zaremba-Jaumann rate** is:

$$\boldsymbol{\sigma}^{(J)^\circ} = \dot{\boldsymbol{\sigma}} + \boldsymbol{\sigma} \cdot \Omega^{(J)} - \Omega^{(J)} \cdot \boldsymbol{\sigma} \tag{2.98}$$

- **Polar or Green-Naghdi rate** is:

$$\boldsymbol{\sigma}^{(R)^\circ} = \dot{\boldsymbol{\sigma}} + \boldsymbol{\sigma} \cdot \Omega^{(R)} - \Omega^{(R)} \cdot \boldsymbol{\sigma} \tag{2.99}$$

  Note that both the **Zaremba-Jaumann** and **Green-Naghdi** stress rates are particular cases of the **Oldroyd** Cauchy stress rate, because $\boldsymbol{\sigma}^{(R)^\circ}$ is the Lie time derivative in which the deformation gradient $\mathbf{F}$ has been replaced by the rotation tensor $\mathbf{R}$. Furthermore, $\boldsymbol{\sigma}^{(J)^\circ}$ is the Lie time derivative with the rate of deformation tensor $\mathbf{d}$ set to zero [1].

- **Logarithmic rate** is defined as:

$$\boldsymbol{\sigma}^{(R)^\circ} = \dot{\boldsymbol{\sigma}} + \boldsymbol{\sigma} \cdot \Omega^{(L)} - \Omega^{(L)} \cdot \boldsymbol{\sigma} \tag{2.100}$$

In previous expressions $(\ldots)^{(\ldots)^\circ}$ denotes an objective time derivative and $\boldsymbol{\Omega}^{(\ldots)}$ is:

$$\boldsymbol{\Omega}^{(J)} = \mathbf{w}, \tag{2.101}$$

$$\boldsymbol{\Omega}^{(G-N)} = \dot{\mathbf{R}} \cdot \mathbf{R}^T \tag{2.102}$$

Objective stress rates can be classified into **corotational** and **non-corotational** stress rates. **Corotational** stress rates like the Zaremba-Jaumann, Green-Naghdi and Logarithmic stress rates use the spin tensor $\boldsymbol{\Omega}$. On the other hand **non-corotational** stress rates, also known as **convected**, like the Truesdell, Oldroyd and Cotter-Rivlin have different mathematical structure.

We conclude that the general definition of an objective stress rate is:

$$\boldsymbol{\Lambda}^\circ = \dot{\boldsymbol{\Lambda}} + \boldsymbol{\Lambda} \cdot \boldsymbol{A} + \boldsymbol{A}^T \cdot \boldsymbol{\Lambda} \tag{2.103}$$

in which $\boldsymbol{\Lambda}^\circ$ is a corotational rate if tensor $\mathbf{A}$ is skew symmetric, i.e: $\mathbf{A}^T = -\mathbf{A}$. If this tensor is non-skewsymmetric, i.e: $\mathbf{A}^T \neq -\mathbf{A}$, the stress rate is non-corotational [65].

[This page is intentionally left blank]

3

Balance principles

In this chapter we introduce the Balance Laws. These are general principles common to all materials. The Balance Principles, within the framework of Continuum Mechanics, define the rates of change of mass, momentum and energy. The proper derivation and understanding of the Balance Laws is a non-trivial issue that needs to be addressed in order to solve any Solid Mechanics problem. The outline is as follows: in section 3.1 we develop the conservation of mass, in section 3.2 the momentum balance principles, in section 3.3 the balance of energy and in section 3.4 the entropy inequality principle. All the Balance Laws are derived in Lagrangian and Eulerian form.

3.1 Conservation of mass

This section is adapted from Holzapfel [1]. From a non-relativistic point of view, mass cannot be produced or destroyed. So, if there are neither mass sources nor mass sinks, the mass m of a body is a conserved quantity. Considering a closed system, previous statement can be mathematically expressed as follows:

$$\mathrm{d}m(\mathbf{X}) = \mathrm{d}m(\mathbf{x}, t) > 0 \tag{3.1}$$

with the infinitesimal **mass element** $\mathrm{d}m$. Considering the scalar fields: **reference mass density** $\rho_0 = \rho_0(\mathbf{X}) > 0$ and the **spatial mass density** $\rho = \rho(\mathbf{x}, t) > 0$, the following relationship holds for an infinitesimal volume:

$$\rho_0(\mathbf{X})dV = \rho(\mathbf{x},t)dv > 0 \tag{3.2}$$

which means that the volume increases when density decreases. The reference mass density ρ_0 is independent of time and space and it depends only on the position $\mathbf{X}$ in the initial configuration. The spatial mass density ρ during a motion $\mathbf{x} = \chi(\mathbf{X},t)$ depends both on the spatial location $\mathbf{x}$ and time t.

We integrate Eq. (3.2) all over the entire closed region to obtain:

$$m = \int_{\Omega_0} \rho_0(\mathbf{X})dV = \int_{\Omega} \rho(\mathbf{x},t)dv = \text{const} > 0 \tag{3.3}$$

The, we can be derive that:

$$\dot{m} = \frac{\mathrm{D}m}{\mathrm{D}t} = \frac{\mathrm{D}}{\mathrm{D}t}\int_{\Omega} \rho(\mathbf{x},t)\,\mathrm{d}v = \frac{\mathrm{D}}{\mathrm{D}t}\int_{\Omega_0} \rho_0(\mathbf{X})\,\mathrm{d}V = 0 \tag{3.4}$$

in which Ω_0 and Ω are the boundary surfaces of the solid in the reference and current configurations.

3.1.1 Continuity mass equation

Using the definition of the Jacobian determinant described in section 2.1.3.1: $\mathrm{d}v = J(\mathbf{X},t)\,\mathrm{d}V,\ J = \det\mathbf{F}(\mathbf{X},t) > 0$, we obtain a relationship between the reference $\rho_0(\mathbf{X})$ and current mass density $\rho(\mathbf{x},t)$, changing the variable of integration from $\mathbf{x} = \chi(\mathbf{X},t)$ to $\mathbf{X}$:

$$\int_{\Omega_0} [\rho_0(\mathbf{X}) - \rho(\boldsymbol{\chi}(\mathbf{X},t),t)J(\mathbf{X},t)]\,\mathrm{d}V = 0 \tag{3.5}$$

Taking into account that V is a generic volume of the solid, previous equation must be fulfilled everywhere, leading to the so-called **continuity mass equation** in the **material or Lagrangian description**:

$$\rho_0(\mathbf{X}) = \rho(\boldsymbol{\chi}(\mathbf{X},t),t)J(\mathbf{X},t) \tag{3.6}$$

The local form of equation:

$$\dot{m} = \frac{\mathrm{D}m}{\mathrm{D}t} = \frac{\mathrm{D}}{\mathrm{D}t} \int_{\Omega_0} \rho_0 \left(\mathbf{X}\right) \mathrm{d}V = 0 \tag{3.7}$$

is written in its rate form as:

$$\frac{\partial \rho_0(\mathbf{X})}{\partial t} = \dot{\rho_0}(\mathbf{X}) = 0 \tag{3.8}$$

describing that the reference density ρ_0 is independent of time.

We can express the continuity equation in the local form using the spatial description and the Reynolds transportation theorem (see Eq. (A.5.2)):

$$\dot{\rho} \left(\mathbf{x}, t\right) + \rho \left(\mathbf{x}, t\right) \mathrm{div}\mathbf{v} \left(\mathbf{x}, t\right) = 0 \tag{3.9}$$

Alternative forms of previous equations are:

$$\frac{\partial \rho \left(\mathbf{x}, t\right)}{\partial t} + \mathrm{grad}\rho \left(\mathbf{x}, t\right) \cdot \mathbf{v} \left(\mathbf{x}, t\right) + \rho \left(\mathbf{x}, t\right) \mathrm{div}\mathbf{v} \left(\mathbf{x}, t\right) = 0, \tag{3.10}$$

$$\frac{\partial \rho \left(\mathbf{x}, t\right)}{\partial t} + \mathrm{div} \left[\rho \left(\mathbf{x}, t\right) \mathbf{v} \left(\mathbf{x}, t\right)\right] = 0 \tag{3.11}$$

Previous expressions describe the evolution of spatial mass density ρ as time evolves. It represents the continuity mass equation in the spatial framework.

3.2 Momentum balance principles

This section is based on the works of Holzapfel [1] and Hashiguchi and Yamakawa [63]. We introduce the balance of linear and angular momentum in a closed system. In addition, the Cauchy's first and second equations of motion are developed.

3.2.1 Conservation law of linear momentum

Consider a body occupying a region Ω whith boundary surface $\partial\Omega$ at time t. If the motion is $\mathbf{x} = \boldsymbol{\chi}(\mathbf{X}, t)$, the mass density is $\rho = \rho(\mathbf{x}, t)$ and the spatial velocity is $\mathbf{v} = \mathbf{v}(\mathbf{x}, t)$, the total **Linear momentum L** can be defined as follows:

$$\mathbf{L}(t) = \int_{\Omega} \rho(\mathbf{x}, t)\mathbf{v}(\mathbf{x}, t)\mathrm{d}v = \int_{\Omega_0} \rho_0(\mathbf{X})\,\mathbf{V}(\mathbf{X}, t)\,\mathrm{d}V \tag{3.12}$$

in which the vector-valued function is also expressed in the reference configuration ρ_0, $\mathbf{V}$ and $\mathrm{d}V$.

If the material time derivative of linear momentum is taken, then the fundamental balance of linear momentum arises:

$$\dot{\mathbf{L}}(t) = \frac{\mathrm{D}}{\mathrm{D}t}\int_{\Omega} \rho\mathbf{v}\mathrm{d}v = \frac{\mathrm{D}}{\mathrm{D}t}\int_{\Omega_0} \rho_0\mathbf{V}\mathrm{d}V = \mathbf{F}(t) \tag{3.13}$$

where $\mathbf{F}(t)$ is the **resultant force**. Using the Reynolds transportation theorem (see Eq. (A.5.2)), last equation can be rewritten as follows:

$$\dot{\mathbf{L}}(t) = \int_{\Omega} \rho\dot{\mathbf{v}}\mathrm{d}v = \int_{\Omega_0} \rho_0\dot{\mathbf{V}}\mathrm{d}V = \mathbf{F}(t) \tag{3.14}$$

In previous expression we introduce the concepts of spatial and material acceleration $\dot{\mathbf{v}}$ and $\dot{\mathbf{V}}$, respectively. Furthermore, the inertia forces per unit current and reference volume emerge when the terms $\rho\dot{v}$ and $\rho_0\dot{V}$ are considered. The **change of the momentum of the body is equal the sum of the forces that act on this body**. This equation is also known as **Euler's first law of motion** in the spatial description.

Let us consider now the Cauchy traction vector $\mathbf{t} = \mathbf{t}\left(\mathbf{x}, t, \mathbf{n}\right)$ acting on the boundary surface $\partial\Omega$ of the solid. Note that $\mathbf{n}$ is the normal vector pointing outwards. In addition, if we consider the body force vector $\mathbf{b} = \mathbf{b}\left(\mathbf{x}, t\right)$ in the spatial configuration, then the resultant force $\mathbf{F}$ can be decomposed into the following expression:

$$\mathbf{F}(t) = \int_{\partial\Omega} \mathbf{t} ds + \int_{\Omega} \mathbf{b} dv \tag{3.15}$$

so the global form of the balance of linear momentum in the spatial description is:

$$\frac{D}{Dt}\int_{\Omega} \rho\mathbf{v}\mathrm{d}v = \int_{\partial\Omega} \mathbf{t}\mathrm{d}s + \int_{\Omega} \mathbf{b}\mathrm{d}v \tag{3.16}$$

An alternative form of previous expression, using Eq. (3.14), is:

$$\frac{D}{Dt}\int_{\Omega} \rho\mathbf{v}\mathrm{d}v = \int_{\Omega} \rho\dot{\mathbf{v}}\mathrm{d}v = \int_{\partial\Omega} \mathbf{t}\mathrm{d}s + \int_{\Omega} \mathbf{b}\mathrm{d}v \tag{3.17}$$

The global form of this balance can be expressed in the material description if we consider the reference body force $\mathbf{B} = \mathbf{B}\left(\mathbf{X}, t\right)$ in the reference position $\mathbf{X}$ and the first Piola-Kirchhoff traction vector $\mathbf{T} = \mathbf{T}\left(\mathbf{X}, t, \mathbf{N}\right)$:

$$\frac{\mathrm{D}}{\mathrm{D}t}\int_{\Omega_0} \rho_0\mathbf{V}\mathrm{d}V = \int_{\partial\Omega_0} \mathbf{T}\mathrm{d}S + \int_{\Omega_0} \mathbf{B}\mathrm{d}V \tag{3.18}$$

3.2.2 Conservation law of angular momentum

In this section we develop the balance of angular momentum. The total angular momentum $\mathbf{J}$ for an arbitrary point $\mathbf{x}_0$ defined by the position vector $\mathbf{r}(\mathbf{x}) = \mathbf{x} - \mathbf{x}_0 = \boldsymbol{\chi}\left(\mathbf{X}, t\right) - \mathbf{x}_0$ is:

$$\mathbf{J}(t) = \int_{\Omega} \left[\mathbf{r} \times \rho(\mathbf{x}, t)\mathbf{v}(\mathbf{x}, t)\right] \mathrm{d}v = \int_{\Omega_0} \left[\mathbf{r} \times \rho_0\left(\mathbf{X}\right)\mathbf{V}\left(\mathbf{X}, t\right)\right] \mathrm{d}V \tag{3.19}$$

in which $\mathbf{r} \equiv \mathbf{r}(\mathbf{x})$. This balance is also known in the literature as the **balance of moment of momentum**, or the **second Cauchy law of motion**, or rotational momentum.

We take the material derivative and obtain the following formula:

$$\dot{\mathbf{J}}(t) = \frac{\mathrm{D}}{\mathrm{D}t}\int_{\Omega} (\mathbf{r} \times \rho \mathbf{v})\,\mathrm{d}v = \frac{\mathrm{D}}{\mathrm{D}t}\int_{\Omega_0} (\mathbf{r} \times \rho_0 \mathbf{V})\,\mathrm{d}V = \mathbf{M}(t) \tag{3.20}$$

in which $\mathbf{M}(t)$ is the **resultant moment**, that is, the moment of $\mathbf{F}$ about $\mathbf{x}_0$. This equation can be reduced to the following one:

$$\dot{\mathbf{J}}(t) = \int_{\Omega} (\mathbf{r} \times \rho \dot{\mathbf{v}})\,\mathrm{d}v = \int_{\Omega_0} \left(\mathbf{r} \times \rho_0 \dot{\mathbf{V}}\right)\mathrm{d}V = \mathbf{M}(t) \tag{3.21}$$

considering that $\dot{\overline{\mathbf{r} \times \mathbf{v}}} = \mathbf{r} \times \dot{\mathbf{v}}$, since $\dot{\mathbf{r}} = \dot{\mathbf{x}} = \mathbf{v}$ and $\dot{\mathbf{r}} \times \mathbf{v} = \mathbf{v} \times \mathbf{v} = 0$.

The resultant moment $\mathbf{M}\,(t)$ in the spatial description can be computed using the spatial Cauchy traction vector $\mathbf{t}$ and the body force $\mathbf{b}$:

$$\mathbf{M}(t) = \int_{\partial\Omega} (\mathbf{r} \times \mathbf{t})\,\mathrm{d}s + \int_{\Omega} (\mathbf{r} \times \mathbf{b})\,\mathrm{d}v \tag{3.22}$$

The global form of the balance of angular momentum in the spatial description is:

$$\frac{D}{Dt}\int_{\Omega} (\mathbf{r} \times \rho \mathbf{v})\,\mathrm{d}v = \int_{\partial\Omega} (\mathbf{r} \times \mathbf{t})\,\mathrm{d}s + \int_{\Omega} (\mathbf{r} \times \mathbf{b})\,\mathrm{d}v \tag{3.23}$$

The equivalent form of previous expression in the material description is:

$$\frac{\mathrm{D}}{\mathrm{D}t}\int_{\Omega_0} (\mathbf{r} \times \rho_0 \mathbf{V})\,\mathrm{d}\mathbf{V} = \int_{\partial\Omega_0} (\mathbf{r} \times \mathbf{T})\,\mathrm{d}S + \int_{\Omega_0} (\mathbf{r} \times \mathbf{B})\,\mathrm{d}V \tag{3.24}$$

3.2.3 Equation of motion in spatial and material description

The existence of a spatial tensor field σ such as $\mathbf{t}\,(\mathbf{x}, t, \mathbf{n}) = \sigma\,(\mathbf{x}, t)\,\mathbf{n}$ has to be fulfilled. This means that the Cauchy's stress theorem (see section C.1.1 in Appendix C) holds and it can be used along with the divergence theorem (see section A.5.1 in Appendix A) to rearrange Eq. (3.14) and obtain:

$$\int_{\partial\Omega} \mathbf{t}(\mathbf{x}, t, \mathbf{n})\mathrm{d}s = \int_{\partial\Omega} \boldsymbol{\sigma}(\mathbf{x}, t)\mathbf{n}\mathrm{d}s = \int_{\Omega} \mathrm{div}\boldsymbol{\sigma}(\mathbf{x}, t)\mathrm{d}v \tag{3.25}$$

where $\boldsymbol{\sigma}$ is the symmetric Cauchy stress tensor. We replace this last expression into Eq. (3.17) and show that $\boldsymbol{\sigma}$ fulfils the **Cauchy's first equation of motion**:

$$\begin{aligned} \frac{D}{Dt}\int_{\Omega} \rho \mathbf{v} \mathrm{d}v = \int_{\Omega} \rho \dot{\mathbf{v}} \mathrm{d}v = \int_{\Omega} \left(\mathrm{div}\boldsymbol{\sigma}(\mathbf{x}, t) + \mathbf{b}\right) \mathrm{d}v = 0 \\ \int_{\Omega} \left(\mathrm{div}\boldsymbol{\sigma} + \mathbf{b} - \rho\dot{\mathbf{v}}\right) \mathrm{d}v = 0 \end{aligned} \tag{3.26}$$

This relation holds for any volume so it can be rewritten in the local form:

$$\mathrm{div}\boldsymbol{\sigma} + \mathbf{b} = \rho\dot{\mathbf{v}} \tag{3.27}$$

An alternative form of previous formula, using the Kirchoff stres tensor $\boldsymbol{\tau} = J\boldsymbol{\sigma}$ (see section C.1.2 in Appendix C), is:

$$\mathrm{div}\left(\frac{\boldsymbol{\tau}}{J}\right) + \mathbf{b} = \rho\dot{\mathbf{v}} \tag{3.28}$$

Moreover, we can obtain the material **Cauchy's first equation of motion** in the global form:

$$\int_{\Omega_0} \left(\mathrm{Div}\mathbf{P} + \mathbf{B} - \rho_0\dot{\mathbf{V}}\right) \mathrm{d}V = 0 \tag{3.29}$$

and the local form:

$$\mathrm{Div}\mathbf{P} + \mathbf{B} = \rho_0\dot{\mathbf{V}} \tag{3.30}$$

where $\mathbf{P}$ is the first Piola-Kirchhoff stress tensor in material coordinates (see section C.1.1 in Appendix C).

3.2.4 Symmetry of the cauchy stress tensor

In order to verify the symmetry of the Cauchy stress tensor, we rely on the balance of angular momentum and take advantage of the properties of the divergence theorem (see section A.5.1 in Appendix A) and the Cauchy's stress theorem (see section C.1.1 in Appendix C).

$$\int_{\partial\Omega} (\mathbf{r} \times \mathbf{t})\, \mathrm{d}s = \int_{\partial\Omega} (\mathbf{r} \times \boldsymbol{\sigma}\mathbf{n})\, \mathrm{d}s = \int_{\Omega} \left(\mathbf{r} \times \mathrm{div}\boldsymbol{\sigma} + \boldsymbol{\mathcal{E}} : \boldsymbol{\sigma}^T\right) \mathrm{d}v \tag{3.31}$$

where $\boldsymbol{\mathcal{E}}$ is a third-order permutation tensor such as $\boldsymbol{\mathcal{E}} : (\mathbf{u} \times \mathbf{v}) = \mathbf{v} \times \mathbf{u}$, i.e. equation (A.48). Using previous expression together with Eq. (3.21), we can rewrite Eq. (3.23) as:

$$\left.\begin{array}{l} \frac{\mathrm{D}}{\mathrm{D}t} \int_{\Omega} (\mathbf{r} \times \rho\mathbf{v})\, \mathrm{d}v = \int_{\Omega} \left(\mathbf{r} \times \mathrm{div}\boldsymbol{\sigma} + \boldsymbol{\mathcal{E}} : \boldsymbol{\sigma}^T\right) \mathrm{d}v + \int_{\Omega} (\mathbf{r} \times \mathbf{b})\, \mathrm{d}v \\ \frac{\mathrm{D}}{\mathrm{D}t} \int_{\Omega} (\mathbf{r} \times \rho\mathbf{v})\, \mathrm{d}v = \int_{\Omega} \mathbf{r} \times \rho\dot{\mathbf{v}} \mathrm{d}v \end{array}\right\} \Longrightarrow$$

$$\int_{\Omega} \left[\mathbf{r} \times \rho\dot{\mathbf{v}} - \mathbf{r} \times \mathrm{div}\boldsymbol{\sigma} - \mathbf{r} \times \mathbf{b} - \boldsymbol{\mathcal{E}} : \boldsymbol{\sigma}^T\right] \mathrm{d}v = 0 \tag{3.32}$$

or in its equivalent form:

$$\int_{\Omega} \mathbf{r} \times (\rho\dot{\mathbf{v}} - \mathbf{b} - \mathrm{div}\boldsymbol{\sigma}]\, \mathrm{d}v = \int_{\Omega} \left(\boldsymbol{\mathcal{E}} : \boldsymbol{\sigma}^T\right) \mathrm{d}v \tag{3.33}$$

Using the equation of motion $\rho\dot{\mathbf{v}} - \mathbf{b} - \mathrm{div}\boldsymbol{\sigma} = 0$, and relying on the fact that the current volume v may be any volume, we conclude that:

$$\boldsymbol{\mathcal{E}} : \boldsymbol{\sigma}^T = 0 \tag{3.34}$$

This operation leads to a vector in which all components must be zero, so we get that:

$$\sigma_{32} - \sigma_{23} = 0 \qquad \sigma_{13} - \sigma_{31} = 0 \qquad \sigma_{21} - \sigma_{12} = 0$$

This relation implies that the Cauchy stress tensor $\boldsymbol{\sigma}$ must be symmetric:

$$\boldsymbol{\sigma} = \boldsymbol{\sigma}^T \tag{3.35}$$

Remark 3.1. Both Kirchhoff stress tensor $\boldsymbol{\tau}$ and second Piola-Kirchhoff stress tensor $\mathbf{S}$ are symmetric. However, the first Piola-Kirchhoff stress tensor $\mathbf{P}$ is not symmetric in general (see section C.1 in Appendix C).

3.3 Balance of energy in continuum thermodynamics

This section is partially adapted from Holzapfel [1]. We introduce the balance of energy considering both mechanical and thermal energies. Note that, if we disregard the effect of thermal energy, the total balance of energy can be derived from the Cauchy's first equation of motion without any additional consideration. However, within a thermodynamic context, we must add the balance of energy and the entropy inequality law to the conservation of mass and the momentum balance principles introduced in previous sections.

We take the scalar product of the velocity $\mathbf{v}$ in the Cauchy's first equation of motion:

$$\mathbf{v}\cdot\mathrm{div}\boldsymbol{\sigma}+\mathbf{v}\cdot\mathbf{b}=\rho\mathbf{v}\cdot\dot{\mathbf{v}} \tag{3.36}$$

Using the relations $\mathrm{div}\left(\mathbf{v}\boldsymbol{\sigma}\right)=\boldsymbol{\sigma}:\mathrm{grad}\mathbf{v}+\mathbf{v}\cdot\mathrm{div}\boldsymbol{\sigma}$ and $\boldsymbol{\sigma}:\mathrm{grad}\mathbf{v}=\boldsymbol{\sigma}:\mathbf{l}=\boldsymbol{\sigma}:\mathbf{d}$, Eq. (3.36) leads to:

$$\boldsymbol{\sigma}:\mathbf{d}=\mathrm{div}\left(\mathbf{v}\boldsymbol{\sigma}\right)+\mathbf{v}\cdot\mathbf{b}-\rho\left(\frac{1}{2}\mathbf{v}\cdot\mathbf{v}\right)^{\bullet} \tag{3.37}$$

We integrate the first term on the right-hand side of previous expression over the current volume using the divergence theorem developed in Eq. (A.5.1), the Cauchy theorem (see section C.1.1 from Appendix C) and Eq. (A.6) to obtain:

$$\int_{\Omega}\mathrm{div}\left(\mathbf{v}\boldsymbol{\sigma}\right)\mathrm{d}v=\int_{\partial\Omega}\left(\mathbf{v}\boldsymbol{\sigma}\right)\cdot\mathbf{n}\mathrm{d}s=\int_{\partial\Omega}\mathbf{v}\cdot\left(\boldsymbol{\sigma}\mathbf{n}\right)\mathrm{d}s=\int_{\partial\Omega}\mathbf{v}\cdot\mathbf{t}\mathrm{d}s \tag{3.38}$$

Now, we can integrate Eq. (3.37):

$$\int_{\Omega} (\boldsymbol{\sigma} : \mathbf{d}) \,\mathrm{d}v = \int_{\partial\Omega} (\mathbf{t} \cdot \mathbf{v}) \,\mathrm{d}s + \int_{\Omega} \mathbf{b} \cdot \mathbf{v} \mathrm{d}v - \left[\int_{\Omega} \left(\frac{1}{2} \rho \mathbf{v} \cdot \mathbf{v} \right) \mathrm{d}v \right]^{\bullet} \tag{3.39}$$

We define the **stress power** or the **rate of internal mechanical work** as:

$$\mathcal{P}_{int}(t) = \int_{\Omega} (\boldsymbol{\sigma} : \mathbf{d}) \,\mathrm{d}v = \int_{\Omega} \operatorname{tr}\left(\boldsymbol{\sigma}^T \mathbf{d}\right) \mathrm{d}v \tag{3.40}$$

The **external mechanical power** or the **rate of external mechanical work** $\mathcal{P}_{ext}$ is defined as the power done by the system of forces $(\mathbf{t}, \mathbf{d})$:

$$\mathcal{P}_{ext}(t) = \int_{\partial\Omega} (\mathbf{t} \cdot \mathbf{v}) \,\mathrm{d}s + \int_{\Omega} (\mathbf{b} \cdot \mathbf{v}) \,\mathrm{d}v \tag{3.41}$$

The **kinetic energy** $\mathcal{K}$ is given by:

$$\mathcal{K}(t) = \int_{\Omega} \left(\frac{1}{2} \rho \mathbf{v} \cdot \mathbf{v} \right) \mathrm{d}v \tag{3.42}$$

Let us now introduce the concept of **internal energy** $\mathcal{E}$. It is a thermodynamic state variable that can be integrated over current volume as follows:

$$\mathcal{E}(t) = \int_{\Omega} e(\mathbf{x}, t) \,\mathrm{d}v \tag{3.43}$$

where e is the internal energy defined per unit current volume.

The thermal energy is formulated to compute the transference between a system and its surroundings by virtue of a temperature gradient. The thermal power or the rate of thermal work is defined by:

$$\mathcal{Q}(t) = \int_{\partial\Omega} q_n \mathrm{d}s + \int_{\Omega} r \mathrm{d}v \tag{3.44}$$

where q_n denotes the heat flux across the body per current surface area and $r = r(\mathbf{x}, t)$ is the heat source per unit time and per unit current volume. Using the **Stoke's heat flux theorem** (see section A.6 in Appendix A) in thermodynamics, the heat flux q_n can be computed as:

$$q_n\left(\mathbf{x}, t, \mathbf{n}\right) = -\mathbf{q}\left(\mathbf{x}, t\right) \cdot \mathbf{n} \tag{3.45}$$

Since the unit vector $\mathbf{n}$ is outward normal, in previous expression the negative sign is necessary to express the inward nature of the heat flux across the body surface.

The so-called balance of thermal energy states that the rate of work done on the body in terms of the internal mechanical work $\mathcal{P}_{int}$ and the rate of thermal work $\mathcal{Q}$ equals the rate of internal energy $\mathcal{E}$. This leads to:

$$\mathcal{P}_{int}\left(t\right) + \mathcal{Q}\left(t\right) = \frac{\mathrm{D}}{\mathrm{D}t}\mathcal{E}\left(t\right) \tag{3.46}$$

We replace last equation into the following balance of mechanical energy:

$$\frac{\mathrm{D}}{\mathrm{D}t}\mathcal{K}\left(t\right) + \mathcal{P}_{int}\left(t\right) = \mathcal{P}_{ext}\left(t\right) \tag{3.47}$$

in order to obtain the balance of total energy:

$$\frac{\mathrm{D}}{\mathrm{D}t}\mathcal{K}\left(t\right) + \frac{\mathrm{D}}{\mathrm{D}t}\mathcal{E}\left(t\right) = \mathcal{P}_{ext}\left(t\right) + \mathcal{Q}\left(t\right) \tag{3.48}$$

The alternative global form in the spatial description is:

$$\frac{\mathrm{D}}{\mathrm{D}t}\int_{\Omega}\left(\frac{1}{2}\rho\mathbf{v}^2 + e\right)\mathrm{d}v = \int_{\partial\Omega}\left(\mathbf{t}\cdot\mathbf{v} - \mathbf{q}\cdot\mathbf{n}\right)\mathrm{d}s + \int_{\Omega}\left(\mathbf{b}\cdot\mathbf{v} + r\right)\mathrm{d}v \tag{3.49}$$

Using the continuity equation, previous expression can be rearranged to obtain:

$$\frac{\mathrm{D}}{\mathrm{D}t}\int_{\Omega} e\mathrm{d}v = \int_{\Omega}\left(\boldsymbol{\sigma} : \mathbf{d} - \mathrm{div}\mathbf{q} + r\right)\mathrm{d}v \tag{3.50}$$

Thus, we obtain the conservation law of energy in the local form:

$$\rho\dot{e} = \boldsymbol{\sigma} : \mathbf{d} + r - \mathrm{div}\mathbf{q} \tag{3.51}$$

Each term in Eq. (3.48) can be described in the reference or material configuration. Thus, the external power can be rewritten as:

$$\mathcal{P}_{ext}\left(t\right)=\int_{\partial\Omega_0}\left(\mathbf{T}\cdot\mathbf{V}\right)\mathrm{d}S+\int_{\Omega_0}\left(\mathbf{B}\cdot\mathbf{V}\right)\mathrm{d}V \tag{3.52}$$

the kinetic energy as:

$$\mathcal{K}\left(t\right)=\int_{\Omega_0}\left(\frac{1}{2}\rho_0\mathbf{V}\cdot\mathbf{V}\right)\mathrm{d}V \tag{3.53}$$

and the rate of internal mechanical work (stress-power) as:

$$\mathcal{P}_{int}\left(t\right)=\int_{\Omega_0}\left(\mathbf{P}:\dot{\mathbf{F}}\right)\mathrm{d}V=\int_{\Omega_0}\left(\mathbf{S}:\dot{\mathbf{E}}\right)\mathrm{d}V \tag{3.54}$$

where the stress power has been formulated using the conjugated pairs: first Piola-Kirhchoff stress tensor **P** and the rate of deformation gradient $\dot{\mathbf{F}}$ and second Piola-Kirchhoff stress tensor **S** and the material strain rate tensor $\dot{\mathbf{E}}$ (see work conjugacy in section C.2 in Appendix C).

Further, using the transformation $e_0\left(\mathbf{X},t\right)=J\left(\mathbf{X},t\right)e\left(\mathbf{x},t\right)$, the internal energy can be formulated in the material description as follows:

$$\mathcal{E}\left(t\right)=\int_{\Omega_0}e_0\left(\mathbf{X},t\right)\mathrm{d}V \tag{3.55}$$

The thermal power can be defined in material description as:

$$\mathcal{Q}\left(t\right)=\int_{\partial\Omega_0}Q_N\mathrm{d}S+\int_{\Omega_0}R\mathrm{d}V \tag{3.56}$$

where Q_N is the heat flux per unit time and per unit reference surface area and $R=R\left(\mathbf{X},t\right)$ is the **heat source** per unit time and per unit reference volume. Using the **Stoke's heat flux theorem**, i.e $Q_N\left(\mathbf{X},t,\mathbf{N}\right)=-\mathbf{Q}\left(\mathbf{X},t\right)\cdot\mathbf{N}$, the rate of thermal work is:

$$\mathcal{Q}\left(t\right)=-\int_{\partial\Omega_0}\mathbf{Q}\cdot\mathbf{N}\mathrm{d}S \tag{3.57}$$

Using Nanson's formula, Eq. (2.19), the following relation between heat flux in the current and material description can be derived:

$$\mathbf{Q} = J\mathbf{F}^{-1}\mathbf{q} \tag{3.58}$$

Thus, the first law of thermodynamics in the material description reads:

$$\frac{\mathrm{D}}{\mathrm{D}t}\int_{\Omega_0}\left(\frac{1}{2}\rho_0\mathbf{V}^2 + e_0\right)\mathrm{d}V = \int_{\partial\Omega_0}(\mathbf{T}\cdot\mathbf{V} - \mathbf{Q}\cdot\mathbf{N})\,\mathrm{d}S + \int_{\Omega_0}(\mathbf{B}\cdot\mathbf{V} + R)\,\mathrm{d}V \tag{3.59}$$

Moreover, Eq. (3.59) can be reduced to:

$$\frac{\mathrm{D}}{\mathrm{D}t}\int_{\Omega_0} e_0\mathrm{d}V = \int_{\Omega_0}\left(\mathbf{P} : \dot{\mathbf{F}} - \mathrm{div}\mathbf{Q} + R\right)\mathrm{d}V \tag{3.60}$$

where the work conjugacy pair $\mathbf{P}$-$\dot{\mathbf{F}}$ has been considered.

Next, we use that $\frac{\mathrm{D}}{\mathrm{D}t}\int_{\Omega_0} e\mathrm{d}V = \int_{\Omega_0}\dot{e}\mathrm{d}V$ (because the reference V is independent of time) in order to write the local form of the balance of energy in the material description:

$$\dot{e}_0 = \mathbf{P} : \dot{\mathbf{F}} - \mathrm{Div}\mathbf{Q} + R \tag{3.61}$$

3.4 Entropy inequality principle

This section is adapted from Holzapfel [1]. We derive the entropy inequality principle which states that for all possible thermodynamic processes, the rate of entropy is non negative [65]. The first law of thermodynamics governs the energy transfer within a thermodynamic process, but says nothing about the direction of the energy transfer. In order to consider that heat flows from the warmer to the colder region of a body, we have to introduce the second law of thermodynamics. This evolution law determines the direction of an energy transfer process.

The entropy, defined as a measure of microscopic randomness and disorder, of a continuum body is:

$$\mathcal{S}(t) = \int_{\Omega}\eta(\mathbf{x}, t)dv = \int_{\Omega_0}\eta_0\left(\mathbf{X}, t\right)\mathrm{d}V \tag{3.62}$$

with $\eta_c = \eta_c(\mathbf{x}, t)$ the entropy per unit current volume in the spatial description and $\eta = \eta(\mathbf{X}, t)$ in the material description.

We compute the **rate of entropy input** $\tilde{\mathcal{Q}}(t)$ into a certain region of a continuum body as the value of entropy transferred across its boundary surface and the entropy generated (or destroyed) inside that region:

$$\tilde{\mathcal{Q}}(t) = -\int_{\partial\Omega} \mathbf{h} \cdot \mathbf{n} \mathrm{d}s + \int_{\Omega} \tilde{r} \mathrm{d}s = -\int_{\partial\Omega_0} (\mathbf{H} \cdot \mathbf{N}) \, \mathrm{d}S + \int_{\Omega_0} \tilde{R} \mathrm{d}V \tag{3.63}$$

where $\tilde{r} = \tilde{r}(\mathbf{x}, t)$ and $\tilde{R} = \tilde{R}(\mathbf{X}, t)$ denote entropy source per unit time and per unit current volume and reference volume, respectively. The **Cauchy entropy flux** $\mathbf{h} = \mathbf{h}(\mathbf{x}, t)$ is the entropy flux per unit reference surface area Ω and $\mathbf{H} = \mathbf{H}(\mathbf{X}, t)$ is the **Piola-Kirchhoff** entropy flux defined in the reference configuration Ω_0. Moreover, $\mathbf{n}$ and $\mathbf{N}$ are the outward normals to $\partial\Omega$ and $\partial\Omega_0$, respectively.

The total production of entropy per unit time, $\Gamma(t)$, can be expressed as the difference between the rate of change of entropy $\dot{\mathcal{S}}$ and the rate of entropy input $\tilde{\mathcal{Q}}$ into a body:

$$\Gamma(t) = \frac{\mathrm{D}}{\mathrm{D}t} \mathcal{S}(t) - \tilde{\mathcal{Q}}(t) \geq 0 \tag{3.64}$$

This inequality is the entropy inequality principle, also known as the **second law of thermodynamics**. The global form in the spatial description of this inequality is given by:

$$\Gamma(t) = \frac{\mathrm{D}}{\mathrm{D}t} \int_{\Omega} \eta(\mathbf{x}, t) \mathrm{d}v + \int_{\partial\Omega} (\mathbf{h} \cdot \mathbf{n}) \, \mathrm{d}s - \int_{\Omega} \tilde{r} \mathrm{d}v \geq 0 \tag{3.65}$$

Remark 3.2. A thermodynamic process is irreversible if the strict inequality holds and reversible if there is no entropy production, i.e. $\Gamma = 0$.

3.4.1 Clausius-Duhem inequality

We assume that both entropy fluxes $\mathbf{h}$, $\mathbf{H}$ and entropy sources $\tilde{r}$, $\tilde{R}$ are related to the heat fluxes $\mathbf{q}$, $\mathbf{Q}$ and heat sources r, R respectively by the absolute temperature T:

$$\mathbf{h} = \frac{\mathbf{q}}{T}, \qquad \tilde{r} = \frac{r}{T}, \qquad \mathbf{H} = \frac{\mathbf{Q}}{T}, \qquad \tilde{R} = \frac{R}{T} \tag{3.66}$$

where T is a time-dependent scalar field. Using these relations the second law of thermodynamics can be rewritten as follows:

$$\Gamma(t) = \frac{\mathrm{D}}{\mathrm{D}t}\int_{\Omega} \eta(\mathbf{x},t)\mathrm{d}v + \int_{\partial\Omega} \frac{\mathbf{q}}{T}\cdot\mathbf{n}\mathrm{d}s - \int_{\Omega}\frac{r}{T}\mathrm{d}v \geq 0 \tag{3.67}$$

$$\Gamma(t) = \frac{\mathrm{D}}{\mathrm{D}t}\int_{\Omega_0} \eta_0(\mathbf{X},t)\mathrm{d}V + \int_{\partial\Omega_0} \frac{\mathbf{Q}}{T}\cdot\mathbf{N}\mathrm{d}S - \int_{\Omega}\frac{R}{T}\mathrm{d}V \geq 0 \tag{3.68}$$

Previous expression are the **Clausius-Duhem inequality** in the spatial and material descriptions.

The local form of the aforementioned inequality can be obtained, in its spatial form, considering that $\mathrm{d}v = J\mathrm{d}V$ and $\frac{\mathrm{D}}{\mathrm{D}t}\left(J\eta(\mathbf{x},t)\right) = \frac{\mathrm{D}}{\mathrm{D}t}\left(\eta_0\right) = \dot{\overline{J\eta}} = \dot{J}\eta + J\dot{\eta} = J\left(\eta\cdot\mathrm{div}\mathbf{v} + \dot{\eta}\right) = J\dot{\eta}$. Thus, we obtain:

$$\begin{aligned}\frac{\mathrm{D}}{\mathrm{D}t}\int_{\Omega}\eta(\mathbf{x},t)\mathrm{d}v &= \frac{\mathrm{D}}{\mathrm{D}t}\int_{\Omega_0} J\eta(\mathbf{x},t)\mathrm{d}V = \int_{\Omega_0}\frac{\mathrm{D}}{\mathrm{D}t}\left(J\eta(\mathbf{x},t)\right)\mathrm{d}V = \\ &= \int_{\Omega_0}\frac{\mathrm{D}}{\mathrm{D}t}\left(\eta_0\right)\mathrm{d}V = \int_{\Omega_0} J\dot{\eta}\mathrm{d}V\end{aligned} \tag{3.69}$$

The second term in the Clausius-Duhem inequality can be simplified using the divergence theorem (see section A.5.1) and the divergence property, Eq. (A.105), in order to obtain:

$$\int_{\partial\Omega}\left(\frac{\mathbf{q}}{T}\cdot\mathbf{n}\right)\mathrm{d}s = \int_{\Omega}\mathrm{div}\left(\frac{\mathbf{q}}{T}\right)\mathrm{d}v = \int_{\Omega}\left(\frac{1}{T}\mathrm{div}\mathbf{q} - \frac{1}{T^2}\mathbf{q}\cdot\mathrm{grad}T\right)\mathrm{d}v \tag{3.70}$$

Next, we can rearrange the inequality in spatial description as follows:

$$\int_{\Omega_0} J\dot{\eta}\mathrm{d}V + \int_{\Omega_0} J\left(\frac{1}{T}\mathrm{div}\mathbf{q} - \frac{1}{T^2}\mathbf{q}\cdot\mathrm{grad}T - \frac{\mathbf{r}}{T}\right)\mathrm{d}V \geq 0 \tag{3.71}$$

Considering that the above integral is independent of the current volume, using the entropy per unit current mass instead of per unit current volume and taking into account that $J \geq 0$, we obtain:

$$\rho\dot{\eta} + \frac{1}{T}\mathrm{div}\mathbf{q} - \frac{1}{T^2}\mathbf{q} \cdot \mathrm{grad}T - \frac{r}{T} \geq 0 \tag{3.72}$$

Furthermore, since $T > 0$ we have that:

$$\rho\dot{\eta}T + \mathrm{div}\mathbf{q} - \frac{1}{T}\mathbf{q} \cdot \mathrm{grad}T - r \geq 0 \tag{3.73}$$

Following the same procedure in the material description we obtain the local form of the Clausius-Duhem expression:

$$\rho_0\dot{\eta}_0 T + \mathrm{div}\mathbf{Q} - \frac{1}{T}\mathbf{Q} \cdot \mathrm{grad}T - R \geq 0 \tag{3.74}$$

4

Elastoplastic constitutive equations

In this chapter we develop a thermo-viscoplastic constitutive framework to describe the mechanical behaviour of metallic materials. The outline is as follows: in section 4.1 we provide a brief review of the features which characterize the hypoelastic- and hyperelastic-plastic constitutive models frequently applied to describe the mechanical response of metallic materials. In section 4.2 we develop a general three dimensional hypoelastic-plastic model and describe a procedure used to integrate the constitutive equations. In section 4.3 we develop a general three dimensional hyper-elastoplastic approach, alternative to the hypoelastic-plastic models, and describe a procedure to integrate the constitutive equations. Finally, in section 4.4 we provide a thermodynamic framework for both constitutive approaches.

4.1 Finite strain elastoplasticity

Infinitesimal theories are adopted to model the behaviour of inelastic solids whenever the strains and rotations remain sufficiently small. However, as soon as the deformation process involves large strains and rotations, to use the finite strain elastoplasticity becomes mandatory. The first developments in elastoplastic models were based in the hypoelastic-plastic constitutive formulations. In this approach the infinitesimal elastoplasticity model is extended to the finite strain range using objective stress rates. However, over the years, some inherent drawbacks of the hypoelastic-plastic formulations have been raised by several authors [67], namely:

- The constitutive behaviour of the solid is not derived from a free-energy potential.
- Thermodynamic inconsistencies may lead to spurious dissipative effects in the elastic range [67, 68].
- Objective stress rates must be used to ensure the objectivity (frame-invariance) of the constitutive laws [67, 69].
- Constitutive formulations based on the Jaumann stress rate may yield non-physical results in simple shear [70].

In order to overcome such problems, hyperelastic-plastic formulations of finite plasticity were developed in the 80's [71, 72]. Using an hyperelastic description for the reversible behaviour, and assuming the multiplicative elastoplastic decomposition of the deformation gradient tensor, the dissipative-response problem can be solved. Further, the objectivity of the constitutive equations is naturally fulfilled. In addition, whether the Hencky logarithmic strain is used, the classical return mapping algorithm, widely applied for the integration of the hypoelastic-plastic constitutive models, is retrieved.

4.2 General hypoelastic-plastic model

Despite of the inconveniences of the hypoelastic-plastic approach described above, this type of models have been extensively used (e.g. they are implemented in most commercial finite element codes) due to the simple algorithms that are required to integrate the resulting constitutive equations. Thus, the formulation of a three-dimensional hypoelastic-plastic constitutive structure, which follows the standard principles of Huber-Mises plasticity, is developed below.

4.2.1 Constitutive equations: Hypoelastic-plastic model

- The evolution equation for the Kirchhoff stress is:

$$\boldsymbol{\tau}^{\nabla} = \mathcal{L} : \mathbf{d}^{\mathrm{e}} \tag{4.1}$$

where $\boldsymbol{\tau}^{\nabla}$ is the Eulerian Green-Naghdi stress rate (see section 2.2.5). The fourth order isotropic elasticity tensor $\mathcal{I}$ and the elastic rate of deformation tensor $\mathbf{d}^e$ are defined as:

$$\mathcal{L} = 2G\mathcal{I} + \varrho\mathbf{I} \otimes \mathbf{I} \tag{4.2}$$

$$\mathbf{d}^e = \mathbf{d} - \mathbf{d}^p \tag{4.3}$$

where G and ϱ are the Lamé's constants, $\mathcal{I}$ is the fourth order identity tensor and $\mathbf{I}$ is the second order identity tensor. $\mathbf{d}$ and $\mathbf{d}^p$ are the total and plastic rate of deformation tensors, respectively.

The Kirchhoff stress is the most directly available stress measure when an elastic reference state is considered. Note also that the Kirchhoff stress is used by most of the commercial finite element codes (including the code ABAQUS/Explicit used in the finite element calculations conducted in this Thesis, see chapter 7) in the development of finite deformation constitutive models. On the other hand, using the Kirchhoff stress tensor in the model implies that, in order to preserve the pair stress-strain conjugacy [1, 65], the strain rate measure has to be the rate of deformation tensor.

- The yield function Ψ is written as:

$$\Psi = \bar{\tau} - \sigma_Y = 0 \tag{4.4}$$

where σ_Y is the yield stress and $\bar{\tau}$ is the equivalent effective stress defined by:

$$\bar{\tau} = \sqrt{\frac{3}{2}\left(\mathbf{s} : \mathbf{s}\right)} \tag{4.5}$$

where $\mathbf{s}$ is the deviatoric part of the Kirchhoff stress:

$$\mathbf{s} = \boldsymbol{\tau} - \frac{1}{3}\left(\boldsymbol{\tau} : \mathbf{I}\right)\mathbf{I} \tag{4.6}$$

- The yield stress σ_Y is given as a function of the equivalent plastic strain $\bar{\varepsilon}^p$, the equivalent plastic strain rate $\dot{\bar{\varepsilon}}^p$ and the temperature T through the following power-type relation:

$$\sigma_Y = A + B\left(\bar{\varepsilon}^p\right)^n \left(\frac{\dot{\bar{\varepsilon}}^p}{\dot{\bar{\varepsilon}}_{ref}}\right)^m \left(\frac{T}{T_{ref}}\right)^{-\mu} \tag{4.7}$$

  where A, B, n, m and μ are material parameters. On the other hand, $\dot{\bar{\varepsilon}}_{ref}$ and T_{ref} are the reference strain rate and temperature.

- The equivalent plastic strain rate $\dot{\bar{\varepsilon}}^p$ is defined as:

$$\dot{\bar{\varepsilon}}^p = \sqrt{\frac{2}{3}\left(\mathbf{d}^p : \mathbf{d}^p\right)} \tag{4.8}$$

  and the accumulated or equivalent plastic strain $\bar{\varepsilon}^p$ is defined by:

$$\bar{\varepsilon}^p = \int_0^t \dot{\bar{\varepsilon}}^p\left(\xi\right) \mathrm{d}\xi \tag{4.9}$$

- Assuming an associative plastic flow rule, the plastic component of the rate of deformation tensor $\mathbf{d}^p$ is given by:

$$\mathbf{d}^p = \frac{\partial \Psi}{\partial \boldsymbol{\tau}} \dot{\bar{\varepsilon}}^p = \frac{3}{2} \frac{\mathbf{s}}{\bar{\tau}} \dot{\bar{\varepsilon}}^p \tag{4.10}$$

- The formulation of the model is completed by introducing the Kuhn-Tucker loading/unloading complementary conditions:

$$\dot{\bar{\varepsilon}}^p \geq 0, \quad \Psi \leq 0, \quad \Psi \dot{\bar{\varepsilon}}^p = 0 \tag{4.11}$$

  and the consistency condition during plastic loading:

$$\dot{\Psi} = 0 \tag{4.12}$$

4.2.2 Numerical integration: Hypoelastic-plastic model

We develop a procedure to integrate the set of constitutive equations given in section 4.2.1. This procedure, based on the work of Zaera and Fernández-Sáez [73], may be used to implement the constitutive model into a finite element code (e.g. ABAQUS/Explicit) through a user subroutine. Note that the numerical integration has to be done in such way that it ensures the material objectivity, leading to a so-called *incrementally objective algorithm*. The methodology is to map the original rate-type constitutive equations into a rotation-neutralised local configuration, usually defined by the polar rotation tensor, and then perform the time discretisation [74, 75]. Several authors [74, 75] showed that the optimal framework for hypoelastic-plastic formulations that use rotational objective rates, such as the Green-Naghdi derivative we use here, is the so-called *corotated coordinate* system. Following this approach, the structure of the classical radial return algorithm (characteristic of the inifinitesimal J_2 flow theory) is maintained. Thus, the integration algorithm is formulated in the rotated configuration and after the variables (in the local configuration) are pushed forward to the spatial configuration.

- We define the Lagrangian version of Eq. (4.1):

  $$\overset{\circ}{\mathbf{\Sigma}} = \mathcal{L} : \tilde{\mathbf{D}}^{e} \tag{4.13}$$

  where $\overset{\circ}{\mathbf{\Sigma}}$ is the Lagrangian rate of the rotated Kirchhoff stress tensor $\mathbf{\Sigma}$ defined as:

  $$\mathbf{\Sigma} = \mathbf{\Lambda}^{T} \boldsymbol{\tau} \mathbf{\Lambda} \tag{4.14}$$

  and $\tilde{\mathbf{D}}^{e}$ is the rotated stretching tensor defined as:

  $$\tilde{\mathbf{D}}^{e} = \mathbf{\Lambda}^{T} \mathbf{D}^{e} \mathbf{\Lambda} \tag{4.15}$$

  where $\mathbf{\Lambda}$ is the rotation tensor that solves the following initial value problem:

  $$\begin{cases} \dot{\mathbf{\Lambda}} = \tilde{\boldsymbol{\omega}} \mathbf{\Lambda} \\ \mathbf{\Lambda} \mid_{t=0} = \mathbf{I} \end{cases} \tag{4.16}$$

and $\tilde{\boldsymbol{\omega}}$ is a second order (skew-symmetric) spin tensor [67].

- The rotated Kirchhoff stress rate is:

$$\dot{\boldsymbol{\Sigma}} = \boldsymbol{\Lambda}^T \overset{\circ}{\boldsymbol{\Sigma}} \boldsymbol{\Lambda} \tag{4.17}$$

- Following Simó and Hughes [74] and de Souza Neto et al. [67], the discretization is conducted applying the generalized midpoint rule (with α defining the integration algorithm equals to $\alpha = 1/2$) to the rotation-insensitive equation (4.17):

$$\boldsymbol{\Sigma}^{n+1} - \boldsymbol{\Sigma}^{n} = \Delta t \dot{\boldsymbol{\Sigma}}^{n+1/2} = \Delta t \boldsymbol{\mathcal{L}} : (\tilde{\mathbf{D}}^e)^{n+1/2} \tag{4.18}$$

where the rotated stretch tensor $(\tilde{\mathbf{D}}^e)^{n+1}$ is computed as:

$$(\tilde{\mathbf{D}}^e)^{n+1/2} = (\boldsymbol{\Lambda}^T)^{n+1/2} (\mathbf{D}^e)^{n+1/2} \boldsymbol{\Lambda}^{n+1/2} \tag{4.19}$$

Remark 4.1. The rotation tensor is obtained through the numerical integration of the initial value problem defined by Eq. (4.16), as it will be explained later.

- The Kirchhoff stress tensor $\boldsymbol{\tau}^{n+1}$ is obtained rotating back to the spatial configuration the updated rotated Kirchhoff stress tensor $\boldsymbol{\Sigma}$ computed in Eq. (4.18):

$$\boldsymbol{\tau}^{n+1} = \boldsymbol{\Lambda}^{n+1} \boldsymbol{\Sigma}^{n+1} (\boldsymbol{\Lambda}^T)^{n+1} \tag{4.20}$$

where $\boldsymbol{\Lambda}^{n+1}$ is solved numerically using the initial value problem defined by Eq. (4.16). The objective generalized midpoint rule conveniently rewritten is:

$$\boldsymbol{\tau}^{n+1} = \boldsymbol{\Lambda}_{\triangle} \boldsymbol{\tau}^{n} \boldsymbol{\Lambda}_{\triangle}^T + \boldsymbol{\mathcal{L}} : \boldsymbol{\Lambda}_{\delta} \Delta t (\mathbf{D}^e)^{n+1/2} \boldsymbol{\Lambda}_{\delta}^T \tag{4.21}$$

where

$$\boldsymbol{\Sigma}^n = \boldsymbol{\Lambda}^T \boldsymbol{\tau}^n \boldsymbol{\Lambda} \tag{4.22}$$

and

$$\boldsymbol{\Lambda}_{\triangle} \equiv \boldsymbol{\Lambda}^{n+1} (\boldsymbol{\Lambda}^T)^n \tag{4.23}$$

$$\boldsymbol{\Lambda}_{\delta} \equiv \boldsymbol{\Lambda}^{n+1} (\boldsymbol{\Lambda}^T)^{n+1/2} \tag{4.24}$$

- The rotation tensor $\boldsymbol{\Lambda}$ is the solution of the initial problem defined by Eq. (4.16). Taking into account the Green-Naghdi stress rate, this evolution problem turns into:

  $$\begin{cases} \dot{\boldsymbol{\Lambda}} = \boldsymbol{\Omega}\boldsymbol{\Lambda} \\ \boldsymbol{\Lambda} \mid_{t=0} = \mathbf{I} \end{cases} \tag{4.25}$$

  The exact solution of previous problem is:

  $$\boldsymbol{\Lambda} = \mathbf{R} \tag{4.26}$$

  Therefore the incremental rotation tensor $\boldsymbol{\Lambda}_{\triangle}$ and $\boldsymbol{\Lambda}_{\delta}$ can be defined as:

  $$\boldsymbol{\Lambda}_{\triangle} \equiv \mathbf{R}_{\triangle} = \mathbf{R}^{n+1} \mathbf{R}_n^T \tag{4.27}$$

  $$\boldsymbol{\Lambda}_{\delta} \equiv \mathbf{R}_{\delta} = \mathbf{R}^{n+1} (\mathbf{R}^T)^{n+1/2} \tag{4.28}$$

  where the rotations $\mathbf{R}^n$, $\mathbf{R}^{n+1}$ and $\mathbf{R}^{n+1/2}$ are computed using the polar decomposition of deformation gradient at times n and $n+1$, and the average value for the deformation gradient at the midpoint configuration.

Now, the classical radial return algorithm, originally developed for the infinitesimal J_2 theory, is performed in the $n+1$ configuration in order to update the stress state.

- Using the additive decomposition of the rate of deformation tensor, Eq. (4.18) takes the form:

$$\boldsymbol{\Sigma}^{n+1} = \boldsymbol{\Sigma}^{n} + \mathcal{L} : \Delta t \left[\tilde{\mathbf{D}}^{n+1/2} - (\tilde{\mathbf{D}}^{p})^{n+1/2}\right] \tag{4.29}$$

- Taking advantage of the properties of the return mapping algorithm, we obtain the equivalent expression:

$$\boldsymbol{\Sigma}^{n+1} = \boldsymbol{\Sigma}^{n+1}_{\text{trial}} - 3G\Delta\bar{\varepsilon}^{p}\frac{\mathbf{S}^{n+1}}{\bar{\Sigma}^{n+1}} \tag{4.30}$$

  where $\mathbf{S}^{n+1}$ is the deviatoric part of the Kirchhoff stress in the rotated configuration.

  The rotated trial stress is defined as:

$$\boldsymbol{\Sigma}^{n+1}_{\text{trial}} = \boldsymbol{\Sigma}^{n} + \mathcal{L} : \Delta t\tilde{\mathbf{D}}^{n+1/2} = \boldsymbol{\Sigma}^{n} + \mathcal{L} : \Delta\boldsymbol{\varepsilon} \tag{4.31}$$

  where $\Delta\boldsymbol{\varepsilon}$ is the strain increment.

  According to the properties of radial return, the equivalent Kirchhoff stress in the rotated configuration may be updated as:

$$\bar{\Sigma}^{n+1} = \bar{\Sigma}^{n+1}_{\text{trial}} - 3G\Delta\bar{\varepsilon}^{p} \tag{4.32}$$

  Therefore, the terms in Eq. (4.30) are known once the plastic strain increment $\Delta\bar{\varepsilon}^{p}$ is obtained by imposing the consistency condition.

- For that task, according to Zaera and Fernández-Sáez [73], we rewrite the consistency condition as follows:

$$\Psi^{n+1} = \Psi\left(\bar{\Sigma}^{n+1}, (\bar{\varepsilon}^{p})^{n+1}, (\dot{\bar{\varepsilon}}^{p})^{n+1}, T^{n+1}\right) = 0 \tag{4.33}$$

  where $\dot{\bar{\varepsilon}}^{p}$ can be approximated as:

$$\dot{\bar{\varepsilon}}^{p} = \frac{\Delta\bar{\varepsilon}^{p}}{\Delta t} \tag{4.34}$$

- If the yield condition is expressed in terms of the equivalent plastic strain, a non-linear algebraic equation in the variable $\bar{\varepsilon}^{p}$ arises:

$$\Psi^{n+1} = \Psi\left(\bar{\Sigma}^{n+1}_{\text{trial}} - 3G\Delta\bar{\varepsilon}^p, (\bar{\varepsilon}^p)^n + \Delta\bar{\varepsilon}^p, \frac{\Delta\bar{\varepsilon}^p}{\Delta t}, T^n + \Delta T\left(\Delta\bar{\varepsilon}^p\right)\right) = 0 \quad (4.35)$$

Previous expression can be linearised in order to implement an iterative Newton-Raphson procedure such that:

$$\begin{aligned}\Psi^{(r+1)} \approx\ & \Psi^{(r)} - 3G\delta\bar{\varepsilon}^{p(r)} - H^{(r)}\delta\bar{\varepsilon}^{p(r)} - M^{(r)}\frac{\delta\bar{\varepsilon}^{p(r)}}{\Delta t} - \\ & - P^{(r)}\frac{\beta}{\rho C_p}\left(\bar{\tau}^{n+1}_{\text{trial}}\delta\bar{\varepsilon}^{p(r)} - 6G\Delta\bar{\varepsilon}^{p(r)}\delta\bar{\varepsilon}^{p(r)}\right) = 0 \end{aligned} \quad (4.36)$$

where r is the iteration index, $H = -\frac{\partial\Psi}{\partial\bar{\varepsilon}^p}$ is the plastic modulus, $M = -\frac{\partial\Psi}{\partial\dot{\bar{\varepsilon}}^p}$ is the viscoplastic modulus and $P = -\frac{\partial\Psi}{\partial T}$ is the temperature sensitivity. Note that the linearised term arising from $\Delta T\left(\Delta\bar{\varepsilon}^p\right)$ (last term in previous equation) can be calculated because it entirely comes from the heat generated due to plastic deformation (see Eq. 4.93 in section 4.4.1 of this chapter).

- Thus, we can obtain $\delta\bar{\varepsilon}^p$ as:

$$\delta\bar{\varepsilon}^{p(r)} = \frac{\Psi^{(r)}}{3G + H^{(r)} + \frac{M^{(r)}}{\Delta t} + P^{(r)}\frac{\beta}{\rho C_p}\left(\bar{\tau}^{n+1}_{\text{trial}} - 6G\Delta\bar{\varepsilon}^{p(r)}\right)} \quad (4.37)$$

- The plastic strain increment $\Delta\bar{\varepsilon}^p$ is updated at the end of the iteration procedure such that:

$$\Delta\bar{\varepsilon}^{p(r+1)} = \Delta\bar{\varepsilon}^{p(r)} + \delta\bar{\varepsilon}^{p(r)} \quad (4.38)$$

Finally, the rotated stress is pushed forward to the spatial configuration using Eq. (4.21). The rest of variables can be updated once $\Delta\bar{\varepsilon}^p$ is known.

4.3 General hyperelastic-plastic model

A suitable alternative to the hypoelastic-plastic models are the hyperelastic-plastic constitutive descriptions. As previously mentioned, the hyperelastic-plastic models overcome some of the inherent drawbacks of the hypoelastic-plastic approaches.

Based on the hyperelastic description of the reversible behaviour, combined with the multiplicative elastoplastic split of the deformation gradient, we can by-pass the dissipative response in the elastic range and the requirement of *incremental objectivity* (frame invariance in the constitutive integration rule). In addition, using the Hencky's logarithmic strain and an exponential map-based integrator for the plastic flow equation (see Appendix D), we retrieve the elastic predictor-return mapping algorithm described in section 4.2.2 [67].

4.3.1 Constitutive equations: Hyperelastic-plastic model

- The constitutive equation for the Kirchhoff stress is expressed as:

$$\boldsymbol{\tau} = \mathcal{L} : \varepsilon^e \tag{4.39}$$

  where

$$\varepsilon^e = \ln\left(\mathbf{V}^e\right) = \frac{1}{2}\ln\left(\mathbf{B}^e\right) \tag{4.40}$$

  This linear stress-strain constitutive equation which relates the Kirchhoff stress and the logarithm of the left stretch tensor of the elastic part of the deformation gradient allows us to extend the classical Hooke's law for infinitesimal isotropic elasticity to finite deformation [76–78].

- We rely on the multiplicative decomposition of the deformation gradient $\mathbf{F}$ into elastic and plastic parts [79] to obtain:

$$\mathbf{F} = \mathbf{F}^e\mathbf{F}^p \tag{4.41}$$

  This decomposition assumes the existence of a local unstressed intermediate configuration defined by the plastic deformation gradient $\mathbf{F}^p$, in such a way that a purely elastic unloading of the deformed configuration is obtained using the inverse of $\mathbf{F}^e$, see [67].

Using the polar decomposition

$$\mathbf{F}^e = \mathbf{R}^e\mathbf{U}^e = \mathbf{V}^e\mathbf{R}^e \tag{4.42}$$

$$\mathbf{F}^p = \mathbf{R}^p\mathbf{U}^p = \mathbf{V}^p\mathbf{R}^p \tag{4.43}$$

we obtain the elastic and plastic right stretch tensors $\mathbf{U}^e$ and $\mathbf{U}^p$, the elastic and plastic left tensors $\mathbf{V}^e$ and $\mathbf{V}^p$ and the elastic and plastic rotation tensors $\mathbf{R}^e$ and $\mathbf{R}^p$, see de Souza Neto et al. [67].

The velocity gradient $\mathbf{L}$ is defined by:

$$\mathbf{L} = \dot{\mathbf{F}}\mathbf{F}^{-1} \tag{4.44}$$

We insert into previous expression the multiplicative decomposition of $\mathbf{F}$ using the product rule in order to obtain:

$$\mathbf{L} = \mathbf{L}^e + \mathbf{F}^e\mathbf{L}^p\left(\mathbf{F}^e\right)^{-1} \tag{4.45}$$

where the elastic and plastic components of the velocity gradient are:

$$\mathbf{L}^e \equiv \dot{\mathbf{F}}^e\left(\mathbf{F}^e\right)^{-1}, \quad \mathbf{L}^p \equiv \dot{\mathbf{F}}^p\left(\mathbf{F}^p\right)^{-1} \tag{4.46}$$

- In order to derive the plastic flow rule, we define the rate of plastic deformation and the plastic spin tensors as [67]:

$$\mathbf{D}^p \equiv \mathrm{sym}\left(\mathbf{L}^p\right), \quad \mathbf{W}^p \equiv \mathrm{skew}\left(\mathbf{L}^p\right) \tag{4.47}$$

- A procedure similar to the rotation-neutralised configuration in the hypoelastic model is developed here. The finite multiplicative plasticity constitutive model is described in the so-called *spatially rotated* configuration, which corresponds to the unstressed intermediate configuration defined by the elastic unloading. For that task, according to Gomaa [78], the following rotated plastic velocity gradient tensor is used:

$$\tilde{\mathbf{L}}^p = \mathbf{R}^e\left(\dot{\mathbf{F}}^p\left(\mathbf{F}^p\right)^{-1}\right)\left(\mathbf{R}^e\right)^T \tag{4.48}$$

This tensor is decomposed into symmetric and skew-symmetric parts:

$$\tilde{\mathbf{L}}^p = \tilde{\mathbf{D}}^p + \tilde{\mathbf{W}}^p \tag{4.49}$$

where

$$\tilde{\mathbf{D}}^p = \frac{1}{2}\left(\tilde{\mathbf{L}}^p + \left(\tilde{\mathbf{L}}^p\right)^T\right) = \mathbf{R}^e\mathbf{D}^p(\mathbf{R}^e)^T = \mathbf{R}^e\mathrm{sym}\left[\dot{\mathbf{F}}^p(\mathbf{F}^p)^{-1}\right](\mathbf{R}^e)^T \tag{4.50}$$

and

$$\tilde{\mathbf{W}}^p = \frac{1}{2}\left(\tilde{\mathbf{L}}^p - \left(\tilde{\mathbf{L}}^p\right)^T\right) = \mathbf{R}^e\mathbf{W}^p(\mathbf{R}^e)^T = \mathbf{R}^e\mathrm{skew}\left[\dot{\mathbf{F}}^p(\mathbf{F}^p)^{-1}\right](\mathbf{R}^e)^T \tag{4.51}$$

- The formalism applied in the hypoelastic-plastic based model is used to describe the yield function Ψ in terms of the equivalent effective Kirchhoff stress $\bar{\tau}$ and the yield stress σ_Y (further details are given in section 4.2).
- Assuming an associative plastic flow rule, the evolution of the plastic deformation gradient is defined by the following constitutive equation for the rotated plastic stretching [67]:

$$\tilde{\mathbf{D}}^p = \frac{\partial\Psi}{\partial\boldsymbol{\tau}}\dot{\bar{\varepsilon}}^p \tag{4.52}$$

complemented with the assumption of zero plastic spin

$$\tilde{\mathbf{W}}^p = 0 \tag{4.53}$$

Let us note that, using equations (4.48), (4.49) and (4.50), together with above definition of plastic flow, equation (4.52), an alternative plastic flow rule for the plastic deformation gradient is obtained:

$$\tilde{\mathbf{D}}^p \equiv \tilde{\mathbf{L}}^p = \mathbf{R}^e\left(\dot{\mathbf{F}}^p\left(\mathbf{F}^p\right)^{-1}\right)\left(\mathbf{R}^e\right)^T = \frac{\partial\Psi}{\partial\boldsymbol{\tau}}\dot{\bar{\varepsilon}}^p \tag{4.54}$$

or equivalently, in the current configuration

$$\mathbf{L}^p \equiv \dot{\mathbf{F}}^p\left(\mathbf{F}^p\right)^{-1} = \dot{\bar{\varepsilon}}^p\left(\mathbf{R}^e\right)^T\frac{\partial\Psi}{\partial\boldsymbol{\tau}}\mathbf{R}^e \tag{4.55}$$

- The formulation of the model is completed using the Kuhn-Tucker loading/unloading complementary conditions and the consistency condition during plastic loading, see section 4.2.1.

4.3.2 Numerical integration: Hyperelastic-plastic model

The integration algorithm presented in this section assumes *elastoplastic isotropy* and a specific *implicit exponential approximation* to discretise the plastic flow rule. Recall that the logarithmic strain is used to measure deformation. To adopt this scheme simplifies the numerical scheme and allow us to retrieve the integration procedure developed for the hypoelastic case described in section 4.2.2.

Thus, the elastic predictor and return-mapping algorithm in J_2 theory is used to update the stress and the internal variables in the spatially rotated configuration, following the procedure described in de Souza Neto et al. [67] and Gomaa [78]. Additional details about the integration scheme are provided in Appendix D.

Given the set of field variables at time t_n and the deformation gradient $\mathbf{F}^{n+1}$ at the time t^{n+1}, the integration algorithm should allow us to update the whole set of field variables.

- We start with the following trial elastic deformation gradient given by:

$$\mathbf{F}^{e^{n+1}}_{\text{trial}} = \mathbf{F}_{\Delta}\mathbf{F}^{e^{n}} \tag{4.56}$$

where $\mathbf{F}_{\Delta}$ is the incremental deformation gradient updated at time t_{n+1}:

$$\mathbf{F}_{\Delta} \equiv \mathbf{F}^{n+1}\left(\mathbf{F}^{n}\right)^{-1} \tag{4.57}$$

Note that we can obtain an equivalent expression for the trial elastic deformation gradient in terms of the plastic deformation gradient at time t_n as follows:

$$\mathbf{F}^{e^{n+1}}_{\text{trial}} = \mathbf{F}_{\triangle}\mathbf{F}^{e^{n}} \equiv \mathbf{F}^{n+1}\left(\mathbf{F}^{n}\right)^{-1}\mathbf{F}^{e^{n}} \equiv \mathbf{F}^{n+1}\left(\mathbf{F}^{p^{n}}\right)^{-1} \tag{4.58}$$

The deformation gradient can be decomposed using the polar rotation to obtain the trial elastic left stretch tensor $\mathbf{V}^{e}_{\text{trial}}$:

$$\mathbf{F}^{e^{n+1}}_{\text{trial}} = \mathbf{R}^{e^{n+1}}_{\text{trial}} \mathbf{U}^{e^{n+1}}_{\text{trial}} = \mathbf{V}^{e^{n+1}}_{\text{trial}} \mathbf{R}^{e^{n+1}}_{\text{trial}} \tag{4.59}$$

and finally we can compute the trial logarithmic as:

$$\varepsilon^{e^{n+1}}_{\text{trial}} = \ln\left(\mathbf{V}^{e^{n+1}}_{\text{trial}}\right) = \frac{1}{2}\ln\left(\mathbf{B}^{e^{n+1}}_{\text{trial}}\right) \tag{4.60}$$

- Once we know $\varepsilon^{e^{n+1}}_{\text{trial}}$, we can compute the trial Kirchchoff stress as follows:

$$\boldsymbol{\tau}^{n+1}_{\text{trial}} = \mathcal{L} : \varepsilon^{e^{n+1}}_{\text{trial}} \tag{4.61}$$

- We can proceed in the integration procedure using the return mapping algorithm, as we explained in section 4.2.2, to update stress $\boldsymbol{\tau}$ and plastic strain $\bar{\varepsilon}^{p}$. Note that the Cauchy stress can be updated as in the hypoelastic using:

$$\boldsymbol{\sigma}^{n+1} = \det\left[\mathbf{F}^{n+1}\right]^{-1} \boldsymbol{\tau} = J^{-1}\boldsymbol{\tau} \tag{4.62}$$

4.4 Thermodynamic framework

In this section we derive a thermodynamic framework for the constitutive models presented in sections 4.2.1 and 4.3.1. We have to point out that the second law of thermodynamics impose restrictions to the constitutive equations of dissipative materials. We formulate a thermodynamic framework based on the *Clausius-Duhem inequality* and the *principle of maximum dissipation* (or plastic work). Moreover, we adopt the so-called *thermodynamics with internal variables* approach.

The thermodynamics with internal variables approach assumes that the thermodynamic state at a given material point is fully determined by a finite number of state variables. The thermodynamic state depends only on the *instantaneous* value of the state variables. In other words, the thermodynamic state does not take into account the past history of the state variables, see de Souza Neto et al. [67]. In the context of thermodynamics with internal variables, we need to define the so-called **thermodynamic potential**, which characterizes (all) the thermodynamic properties of a system and the **heat flux vector** describing heat transfer. Based on such a thermodynamic framework, we obtain an evolution equation for the temperature.

Remark 4.2. Firstly we develop the thermodynamic framework for the hyperelastic-plastic model since this constitutive formulation is thermodynamically (fully) consistent, while the hypoelastic-plastic model is not.

4.4.1 Thermodynamic framework: Hyperelastic-plastic model

Following Perzyna [80] and Sumelka [65], we assume the following postulates :

1. Existence of a *free energy potential*, from which the hyperelastic law is derived. This free energy is expressed as follows:

$$\psi = \widehat{\psi}\left(\mathbf{e}, T; \boldsymbol{\mu}\right) \tag{4.63}$$

This potential is expressed as a function of the logarithmic strain $\mathbf{e}$, the temperature T and a generic set of internal variables associated with dissipative mechanisms: $\boldsymbol{\mu} \equiv \{\mu_1, \mu_2, \ldots, \mu_k\}$. The current thermodynamic state of materials that involve dissipation can be determined by a finite number of so-called internal variables (or even hidden variables [1]). These thermodynamic state variables describe aspects of the internal structure of materials associated with irreversible effects. The strain (or stress) and temperature (or entropy) depend on these internal variables, see Holzapfel [1].

The evolution of the internal variables gives the background of the deformation history, and their nature in the current framework is phenomenological. In our analysis, the internal state vector depends on a single variable:

$$\boldsymbol{\mu} = \bar{\varepsilon}^p, \tag{4.64}$$

such that the equivalent plastic strain describes (all) dissipative effects generated by viscoplastic deformation.

2. The *axiom of entropy production.* The constitutive equations must fulfil the following dissipation inequality (see section 3.4), which is developed from the first and second laws of thermodynamics, see section 3.4.1:

$$\frac{1}{\rho_0}\tau : \mathbf{d} - \left(\eta \dot{T} + \dot{\psi}\right) - \frac{1}{\rho T}\mathbf{q} \cdot \mathrm{grad} T \geq 0 \tag{4.65}$$

   This expression defines the thermodynamic admissibility of the constitutive equations, Holzapfel [1].

3. Existence of a *yield function* Ψ which defines the onset of plastic yielding.

4. Existence of a *dissipation potential* ψ which determines the plastic flow rule and the evolution laws for the internal variables.

   Remark 4.3. In contrast to the above described family of hyperelastic-plastic based models, hypoelastic-plastic theories *do not rely on the assumption of the existence of a free-energy potential to model the reversible behaviour* [1].

Based on previous postulates, we combine the first law of thermodynamics in its local spatial form, Eq. (3.51):

$$\rho \dot{e}_0 = \frac{\rho}{\rho_0}\tau : \mathbf{d} - \text{div}\mathbf{q} + \mathbf{r} \tag{4.66}$$

and the inequality entropy production, Eq. (3.73):

$$\rho \dot{\eta} T + \text{div}\mathbf{q} - \frac{1}{T}\mathbf{q} \cdot \text{grad}T - r \geq 0 \tag{4.67}$$

to obtain an alternative form of the Clausius-Duhem inequality such that:

$$\begin{gathered} \rho \dot{\eta} T + \frac{\rho}{\rho_0}\tau : \mathbf{d} - \rho \dot{e}_0 - \frac{1}{T}\mathbf{q} \cdot \text{grad}T \geq 0 \Longrightarrow \\ \Longrightarrow \dot{\eta} T + \frac{1}{\rho_0}\tau : \mathbf{d} - \dot{e}_0 - \frac{1}{\rho T}\mathbf{q} \cdot \text{grad}T \geq 0 \end{gathered} \tag{4.68}$$

Now, relying on the Legendre transformation, we obtain the Helmholtz free energy ψ in terms of the entropy η and the associated thermodynamic potential e_0.

$$\psi = e_0 - T\eta \tag{4.69}$$

Previous expression is usually known as the **caloric equation of state**.

Remark 4.4. The thermodynamic potential e_0 should not be confused with the measure of strain defined by the tensor $\mathbf{e}$.

The material time differentiation of the Helmholtz free energy provides the variation of the thermodynamic state:

$$\dot{\psi} = \dot{e}_0 - \dot{T}\eta - T\dot{\eta} \tag{4.70}$$

Then, we replace previous expression in the first law of thermodynamics to obtain:

$$\rho \dot{e}_0 + \mathrm{div}\mathbf{q} = \frac{\rho}{\rho_0}\tau : \mathbf{d} + \mathbf{r} \Longrightarrow \rho\left(\dot{\psi} + \dot{T}\eta + T\dot{\eta}\right) + \mathrm{div}\mathbf{q} = \frac{\rho}{\rho_0}\tau : \mathbf{d} + \mathbf{r}$$

such that the Clausius-Duhem inequality now reads:

$$\frac{1}{\rho_0}\tau : \mathbf{d} - \left(\dot{\psi} + \dot{T}\eta\right) - \frac{1}{\rho T}\mathbf{q}\cdot \mathrm{grad}T \geq 0 \tag{4.71}$$

Based on physical observations, we know that heat flows from the warmer to the colder region of a body, so the entropy production by conduction of heat must be positive, that is, the last term in previous expression is:

$$\mathbf{q}\cdot \mathrm{grad}T \leq 0 \longrightarrow -\frac{1}{\rho T}\mathbf{q}\cdot \mathrm{grad}T \geq 0 \tag{4.72}$$

Previous expression points out that the heat flows against a temperature gradient.

According to this restriction, the **Clausius-Duhem inequality** in the form of equation (4.71) turns into an alternative expression of the second law of thermodynamics, the **Clausius-Planck inequality**:

$$D_{int} = \frac{1}{\rho_0}\tau : \mathbf{d} - \left(\dot{\psi} + \dot{T}\eta\right) \geq 0 \tag{4.73}$$

Now we take the material time rate of the free energy function $\psi = \widehat{\psi}\left(\mathbf{e}, T; \boldsymbol{\mu}\right)$ such that:

$$\begin{aligned} \dot{\psi} &= \frac{\partial\widehat{\psi}}{\partial\mathbf{e}} : \dot{\mathbf{e}} + \frac{\partial\widehat{\psi}}{\partial T}\dot{T} + \frac{\partial\widehat{\psi}}{\partial\mu}\dot{\boldsymbol{\mu}} \\ &= \frac{\partial\widehat{\psi}}{\partial\mathbf{e}} : \mathbf{d} + \frac{\partial\widehat{\psi}}{\partial T}\dot{T} + \frac{\partial\widehat{\psi}}{\partial\boldsymbol{\mu}}\dot{\boldsymbol{\mu}} \end{aligned} \tag{4.74}$$

where we have taken into account that the derivative of logarithmic strain $\dot{\mathbf{e}}$ ($\dot{\mathbf{e}} \equiv \dot{\mathbf{e}}^{(0)}$, see Eq. (2.31)) is the rate of deformation tensor $\mathbf{d}$. Next, we insert previous expression into the entropy inequality, Eq. (4.71), to obtain:

$$\left(\frac{1}{\rho_0}\tau - \frac{\partial\widehat{\psi}}{\partial\mathbf{e}}\right) : \mathbf{d} - \left(\eta + \frac{\partial\widehat{\psi}}{\partial T}\right)\dot{T} - \frac{\partial\widehat{\psi}}{\partial\boldsymbol{\mu}}\dot{\boldsymbol{\mu}} - \frac{1}{\rho T}\mathbf{q}\cdot\mathrm{grad}T \geq 0 \tag{4.75}$$

Remark 4.5. The principle of thermodynamic determinism requires that the constitutive equations must be such that the above inequality holds for any thermokinetic process [67].

Thus, Eq. (4.75) must remain valid for any pair of functions $\left\{\mathbf{d}, \dot{T}\right\}$. This implies the following constitutive equations:

$$\tau = \rho_0\frac{\partial\widehat{\psi}}{\partial\mathbf{e}} \tag{4.76}$$

$$\eta = -\frac{\partial\widehat{\psi}}{\partial T} \tag{4.77}$$

$$D_{int} = -\frac{\partial\widehat{\psi}}{\partial\boldsymbol{\mu}}\dot{\boldsymbol{\mu}} \tag{4.78}$$

Therefore, Eq. (4.75) reduces to:

$$-\frac{\partial\widehat{\psi}}{\partial\boldsymbol{\mu}}\dot{\boldsymbol{\mu}} - \frac{1}{\rho T}\mathbf{q}\cdot\mathrm{grad}T \geq 0 \tag{4.79}$$

where the first term defines the rate of internal dissipation.

Using the Clausius-Planck inequality, an alternative rate of dissipation is derived:

$$\mathrm{D}_{int} \equiv \frac{\partial\widehat{\psi}}{\partial\boldsymbol{\mu}}\dot{\boldsymbol{\mu}} = \dot{\psi} + \dot{T}\eta - \frac{1}{\rho_0}\tau : \mathbf{d} \tag{4.80}$$

Now, using Legendre transformation, we rewrite Eq. (3.51) to obtain:

$$\begin{aligned}
\rho\dot{e}_0 &= \frac{\rho}{\rho_0}\tau : \mathbf{d} - \mathrm{div}\mathbf{q} + \mathbf{r} \Longrightarrow \\
&\Longrightarrow \rho\left(\dot{\psi} + \dot{T}\eta + T\dot{\eta}\right) = \frac{\rho}{\rho_0}\tau : \mathbf{d} - \mathrm{div}\mathbf{q} + \mathbf{r} \\
&\Longrightarrow \rho T\dot{\eta} + \rho\left(\dot{\psi} + \dot{T}\eta\right) + \mathrm{div}\mathbf{q} = \frac{\rho}{\rho_0}\tau : \mathbf{d} + \mathbf{r} \\
&\Longrightarrow \rho T\dot{\eta} + \rho\left(\dot{\psi} + \dot{T}\eta - \frac{1}{\rho_0}\tau : \mathbf{d}\right) + \mathrm{div}\mathbf{q} = \mathbf{r} \qquad (4.81)
\end{aligned}$$

We combine Eqs. (4.80) and (4.81) to obtain:

$$\rho T\dot{\eta} = -\mathrm{div}\mathbf{q} - \rho\frac{\partial\widehat{\psi}}{\partial\boldsymbol{\mu}}\dot{\boldsymbol{\mu}} + \mathbf{r} \qquad (4.82)$$

We take the time derivative of Eq. (4.77), taking into account that $\psi = \widehat{\psi}\left(\mathbf{e}, T; \bar{\varepsilon}^p\right)$, to obtain:

$$\dot{\eta} = -\frac{\partial^2\widehat{\psi}}{\partial T^2}\dot{T} - \frac{\partial^2\widehat{\psi}}{\partial T\partial\mathbf{e}} : \dot{\mathbf{e}} - \frac{\partial^2\widehat{\psi}}{\partial T\partial\bar{\varepsilon}^p}\dot{\bar{\varepsilon}}^p \qquad (4.83)$$

Next, we insert previous expression into Eq. (4.82) to get:

$$\rho T\left(-\frac{\partial^2\widehat{\psi}}{\partial T^2}\dot{T} - \frac{\partial^2\widehat{\psi}}{\partial T\partial\mathbf{e}} : \dot{\mathbf{e}} - \frac{\partial^2\widehat{\psi}}{\partial T\partial\bar{\varepsilon}^p}\dot{\bar{\varepsilon}}^p\right) = -\mathrm{div}\mathbf{q} - \rho\frac{\partial\widehat{\psi}}{\partial\boldsymbol{\mu}}\dot{\boldsymbol{\mu}} + \mathbf{r} \qquad (4.84)$$

Considering that the only internal variable is the equivalent plastic strain we obtain that:

$$\boldsymbol{\mu} = \boldsymbol{\mu}\left(\bar{\varepsilon}^p\right) \Longrightarrow \frac{\partial\widehat{\psi}}{\partial\boldsymbol{\mu}}\dot{\boldsymbol{\mu}} = \frac{\partial\widehat{\psi}}{\partial\bar{\varepsilon}^p}\dot{\bar{\varepsilon}}^p \qquad (4.85)$$

Therefore, Eq. (4.84) yields:

$$\rho T\left(-\frac{\partial^2\widehat{\psi}}{\partial T^2}\dot{T}-\frac{\partial^2\widehat{\psi}}{\partial T\partial \mathbf{e}}:\dot{\mathbf{e}}-\frac{\partial^2\widehat{\psi}}{\partial T\partial\bar{\varepsilon}^p}\dot{\bar{\varepsilon}}^p\right)=-\mathrm{div}\mathbf{q}-\rho\frac{\partial\widehat{\psi}}{\partial\bar{\varepsilon}^p}\dot{\bar{\varepsilon}}^p+\mathbf{r}\Longrightarrow$$

$$-\rho T\frac{\partial^2\widehat{\psi}}{\partial T^2}\dot{T}=-\mathrm{div}\mathbf{q}+\rho T\frac{\partial^2\widehat{\psi}}{\partial T\partial \mathbf{e}}:\dot{\mathbf{e}}+\rho T\frac{\partial^2\widehat{\psi}}{\partial T\partial\bar{\varepsilon}^p}\dot{\bar{\varepsilon}}^p-\rho\frac{\partial\widehat{\psi}}{\partial\bar{\varepsilon}^p}\dot{\bar{\varepsilon}}^p+\mathbf{r}$$

Taking into account that $\dot{\mathbf{e}}=\mathbf{d}$, and recalling the term $c_p=-T\frac{\partial^2\widehat{\psi}}{\partial T^2}$, we can rewrite the above equation as follows:

$$\rho c_p\dot{T}=-\mathrm{div}\mathbf{q}+\rho T\frac{\partial^2\widehat{\psi}}{\partial T\partial \mathbf{e}}:\mathbf{d}-\rho\left(\frac{\partial\widehat{\psi}}{\partial\bar{\varepsilon}^p}-T\frac{\partial^2\widehat{\psi}}{\partial T\partial\bar{\varepsilon}^p}\right)\dot{\bar{\varepsilon}}^p+\mathbf{r} \tag{4.86}$$

Next, we take the partial differentiation of Eq. (4.76):

$$\tau=\rho_0\frac{\partial\widehat{\psi}}{\partial\mathbf{e}}\Longrightarrow\frac{\partial\tau}{\partial T}=\rho_0\frac{\partial^2\widehat{\psi}}{\partial T\partial\mathbf{e}} \tag{4.87}$$

and insert this expression into Eq. (4.86) to obtain:

$$\rho c_p\dot{T}=-\mathrm{div}\mathbf{q}+\frac{\rho}{\rho_0}T\frac{\partial\tau}{\partial T}:\mathbf{d}+\left(-\rho\frac{\dot{\bar{\varepsilon}}^p}{\tau:\mathbf{d}^p}\left(\frac{\partial\widehat{\psi}}{\partial\bar{\varepsilon}^p}-T\frac{\partial^2\widehat{\psi}}{\partial T\partial\bar{\varepsilon}^p}\right)\right)(\tau:\mathbf{d}^p)+\mathbf{r} \tag{4.88}$$

Where the third term in the right hand side of previous formula has been multiplied and divided by the term $\tau:\mathbf{d}^p$. We rename this term as the irreversibility coefficient χ^*:

$$\chi^*=-\rho\frac{\dot{\bar{\varepsilon}}^p}{\tau:\mathbf{d}^p}\left(\frac{\partial\widehat{\psi}}{\partial\bar{\varepsilon}^p}-T\frac{\partial^2\widehat{\psi}}{\partial T\partial\bar{\varepsilon}^p}\right) \tag{4.89}$$

Using the relation between the equivalent plastic strain and the plastic rate of deformation tensor we rewrite the irreversibility coefficient as follows:

$$\chi^*=-\rho\sqrt{\frac{2}{3}}\frac{\sqrt{\mathbf{d}^p:\mathbf{d}^p}}{\tau:\mathbf{d}^p}\left(\frac{\partial\widehat{\psi}}{\partial\bar{\varepsilon}^p}-T\frac{\partial^2\widehat{\psi}}{\partial T\partial\bar{\varepsilon}^p}\right) \tag{4.90}$$

Thus, we can obtain the energy balance equation in *temperature form*:

$$\rho c_p \dot{T} = -\mathrm{div}\mathbf{q} + \frac{\rho}{\rho_0} T \frac{\partial \tau}{\partial T} : \mathbf{d} + \chi^* \left(\tau : \mathbf{d}^p\right) + \mathbf{r} \tag{4.91}$$

The evolution of the temperature T is influenced by the divergence of the heat flux $\mathbf{q}$, the structural thermoelastic heating, the structural inelastic dissipation and the heat source $\mathbf{r}$.

Two important issues must be addressed:

- The procedure to obtain the temperature evolution equation in material coordinates is identical. In material coordinates, Eq. (4.91) depends on the material divergence Div$\mathbf{Q}$, the Piola-Kirchhoff, the heat flux $\mathbf{Q}$ and the material heat source $\mathbf{R}$.
- From this point on, we neglect the thermo-elastic effects since the temperature variation in the elastic range is negligible in most metals [65]. We also consider that there is no heat source $\mathbf{r}$ in the body.

Under such premises, the equation of temperature evolution takes the form:

$$\rho c_p \dot{T} = -\mathrm{div}\mathbf{q} + \chi^* \left(\tau : \mathbf{d}^p\right) \tag{4.92}$$

where, for our purposes, the irreversibility coefficient χ^* is the so-called Taylor-Quinney coefficient β.

Using the Fourier law of heat conduction in the spatial configuration we can rewrite previous expression to be a function of the temperature only, such that:

$$\rho c_p \dot{T} = k \nabla^2 T + \beta \left(\boldsymbol{\tau} : \mathbf{d}^p\right) \tag{4.93}$$

4.4.2 Thermodynamic framework: Hypoelastic-plastic model

The equations of hypoelasticity were introduced for the first time in 1955 by Truesdell [81]. These equations, as it was explained previously, were a generalization of infinitesimal strain elasticity to finite strain through a rate theory in which the material shows no time dependence.

Noll [82] showed that every Cauchy-elastic material for which the stress-strain relations are invertible is also hypoelastic[1] [83]. It appears that hypoelastic materials are, in a sense, more general than elastic materials.

In 1958 Ericksen [84] obtained conditions under which there exists a function of stress for hypoelasticity which plays a role similar to the strain energy of a hyperelastic material, called *hypo-elastic potentials* [83]. In 1960, Bernstein [85] established conditions for a hypoelastic material to be elastic, and later suggested a dynamic formulation for a set of unified equations for elasticity and plasticity [86]. Though these equations were expressed in a infinitesimal strain framework, they assumed a generalization to a specific set of hypoelastic equations.

Following this idea, Olsen and Bernstein [87] constructed these hypoelastic equations and showed that they did indeed lead to a thermodynamic theory [83]. However, Bernstein [85] showed that this thermodynamic hypoelastic theory was not a theory of an elastic material. Nevertheless it satisfied the first and second laws of thermodynamics [83].

Olsen and Bernstein [87] found the general conditions for which a hypoelastic material is consistent with thermodynamics and they constructed a thermodynamic theory based on the thermodynamic potential named as a modified Gibbs function. The assignment of such a function does not determine the stress-rate of strain relation of hypoelasticity, but leaves it greatly undetermined. Nevertheless, the theory is internally consistent and the laws of thermodynamics are obeyed [83].

As a summary we have that:

1. It is unreasonable to expect to be able to construct a thermodynamic theory without a thermodynamic potential (Hemholtz, Gibbs, etc.) in which a free

---

[1] The Cauchy-elstic materials are sometimes called elastic materials (there need be no strain energy function). Should there be a strain energy function, then the material is called Green-elastic or hyperelastic. [83]

strain energy is not embedded. At least in appearance, only the hyperelastic theory allows for a thermodynamic theory.

2. However, several researchers have shown that it is possible to construct a thermodynamic framework for hypoelastic materials which fulfils the first and second laws. However, this theory is not based on a free energy function from which the stress-rate of strain relation can be derived.

Based on such premises, in this work we have considered for the hypoelastic-plastic materials the same thermodynamic framework derived in section 4.4.1 for the hyperelastic-plastic solids. This practice, which has motivated fundamental discussions in the Continuum Mechanics community over the last decades, is widely accepted in the literature. Nevertheless, we acknowledge that the application of the evolution equation for the temperature derived in section 4.4.1 to hypoelastic-plastic materials presents serious theoretical drawbacks.

5

Initial boundary value problem: Elastoplastic solids subjected to dynamic tension

In this chapter we define the initial boundary value problem that will be investigated experimentally and numerically in forthcoming sections of this Thesis. Now (and only now) that we have posed the kinematics of finite strains, the frame indifference principle, the balance laws and the constitutive equations of elastoplastic solids, we can properly define an initial boundary value problem. Namely, in this Thesis we address the problem of flow localization in metallic specimens subjected to dynamic loading. We specify here the kinematic relation, the balance principles and the constitutive equations which define the problem at hand. At such, this episode of the Thesis is the required transition between the theoretical foundations of the Continuum Mechanics elaborated in chapters 2, 3 and 4, and the practical resolution of the dynamic tensile test conducted in chapters 6, 7 and 8.

5.1 Initial boundary value problem: Elastoplastic solids subjected to dynamic tension

We pose the kinematic relation, governing equations, initial conditions and boundary conditions which define the mechanical response of elastoplastic solids subjected to dynamic tension. This framework is based on the theoretical developments elaborated in chapters 2, 3 and 4. The problem is formulated in the Lagrangian configuration using a Cartesian coordinate system. Nevertheless, it could be easily posed in an Eulerian framework relying on the mathematical structures developed in chapters 2, 3 and 4.

1. Kinematic relation: using Eqs. (2.3) and (2.7) from chapter 2 we have

$$\mathbf{V} = \frac{\partial \boldsymbol{\chi}}{\partial t} = \frac{\partial \mathbf{U}}{\partial t} \tag{5.1}$$

   Remark 5.1. The displacement field $\mathbf{U}$ in the material description should not be confused with the right (or material) stretch tensor from the polar decomposition of the deformation gradient $\mathbf{F}$.

2. Balance equations

   - Balance of mass or continuity equation: see Eq. (3.6) in chapter 3

$$\rho_0 = \rho J \tag{5.2}$$

   - Balance of linear momentum: see Eq. (3.30) in chapter 3

$$\rho_0 \dot{\mathbf{V}} = \mathrm{Div}\left(\frac{1}{J}\boldsymbol{\tau}\right) \tag{5.3}$$

3. Constitutive equations: following the standard principles of Huber-Mises plasticity

   - Hypoelastic-based model: see Eq. (4.1) in chapter 4

$$\boldsymbol{\tau}^{\nabla} = \mathcal{L} : \mathbf{d}^{\mathrm{e}} \tag{5.4}$$

   - Hyperelastic-based model: see Eq. (5.5) in chapter 4

$$\boldsymbol{\tau} = \mathcal{L} : \boldsymbol{\varepsilon}^{e} \tag{5.5}$$

4. Thermodynamic framework: see Eq. (4.93) in chapter 4

$$\rho_0 C_p \dot{T} = k \nabla^2 T + \beta \boldsymbol{\tau} : \mathbf{d}^{p} \tag{5.6}$$

5. Initial conditions: the solid is initially at rest and unloaded unless otherwise noted

$$\begin{aligned}
&\mathbf{U}(X,Y,Z,0)=0 \quad \mathbf{V}(X,Y,Z,0)=0 \quad \boldsymbol{\tau}(X,Y,Z,0)=0 \\
&\rho(X,Y,Z,0)=\rho_0 \quad T(X,Y,Z,0)=T_0
\end{aligned} \tag{5.7}$$

6. Boundary conditions: the domain of the solid is $-h/2 \leq X \leq h/2$, $-W/2 \leq Y \leq W/2$ and $0 \leq Z \leq L_0$ unless otherwise noted

   - Mechanical boundary conditions:

$$\mathbf{U}(X,Y,0,t)=0 \quad \mathbf{V}(X,Y,L_0,t)=\mathbf{V}^{\mathrm{inp}} \tag{5.8}$$

   - Thermal boundary conditions:

$$\begin{aligned}
&\mathbf{Q}(\pm h/2,Y,Z,t)\cdot\mathbf{n}(\pm h/2,Y,Z,t)=0 \\
&\mathbf{Q}(X,\pm W/2,Z,t)\cdot\mathbf{n}(X,\pm W/2,Z,t)=0 \\
&\mathbf{Q}(X,Y,L_0,t)\cdot\mathbf{n}(X,Y,L_0,t)=0
\end{aligned} \tag{5.9}$$

This is the set of equations which define the (baseline) initial boundary value problem investigated in this Thesis. In chapter 6 we will develop an experimental methodology to analyse the flow localization in metallic specimens subjected to dynamic tension. In 7 we will conduct a finite element study to uncover the key mechanics which control the fracture location, with emphasis on the role played by the initial and boundary conditions in the sample ductility and failure pattern. In section 8 we develop a finite difference scheme to investigate the role of material properties and material flaws in the failure of the dynamic specimens.

[This page is intentionally left blank]

6

Analysis and results: Experiments

In this chapter we develop an experimental approach to uncover the deterministic nature of the fracture location in the dynamic tensile testing of metallic materials. The goal is to obtain experimental evidences of the role played by wave propagation on the specimens failure. The outline of this chapter is as follows: in section 6.1 we carry out the mechanical characterization of the steel AISI 430 that we have used in this investigation. Quasi-static and dynamic tensile experiments have been conducted for different loading rates and temperatures. We have observed that this material shows isotropic behaviour with mild yield stress, moderate strain hardening and significant ductility. In section 6.2 we carry out dynamic tensile experiments using samples with six different gauge lengths, ranging from 20 mm to 140 mm, that have been tested within a wide spectrum of loading velocities from 1 m/s to 7.5 m/s. The dynamic tensile tests revealed that variations in the applied velocity and the gauge length alter the processes of reflection and interaction of waves taking place in the sample during the test, which leads to the systematic motion of the fracture location along the sample gauge. In section 6.3 we summarize and discuss the main outcomes of the experimental investigation. Part of this chapter has been published in Vaz-Romero et al. [88].

6.1 Experimental setup and mechanical characterization

In this section we describe the set-ups and the specimens used in the experiments, and carry out the mechanical characterization of the material. The dependences of the material flow stress on strain, strain rate and temperature are discussed.

6.1.1 Material and specimens

The material of this study is annealed AISI 430 stainless steel. Its chemical composition is given in Table 6.1.

Fe	**C**	**Mn**	**P**	**S**	**Si**	**C**	**Ni**
Balance	0.12 max.	1.00 max.	0.04 max.	0.03 max.	1.00 max.	16.00 - 18.00	0.5 max.

Table 6.1: Chemical composition of the AISI 430 stainless steel (wt %) as taken from AK steel corporation [3].

The AISI 430 is one of the most widely used ferritic stainless steels. It shows excellent stress corrosion cracking resistance and good resistance to pitting and crevice corrosion in chloride environments. Typical consumer product applications include automotive trim and molding and furnace combustion chambers. Industrial and commercial applications range from interior architectural applications to nitric acid plant equipment and oil refinery equipment [3].

The material is supplied in plates of thickness $h = 1\ mm$ from which tensile specimens are machined. The specimens' geometry and dimensions are shown in Fig. 6.1. The impacted side is the right side of the specimen in the figure (and therefore the clamped side is the left side). We distinguish between samples used in the quasi-static tests and samples used in the dynamic tests. The quasi-static specimens, identical to those used by Rodríguez-Martínez et al. [89], have a gauge length of 20 mm. Note that the quasi-static tests are a requisite to characterize the mechanical response of the material rather than a specific goal of this investigation. The dynamic samples are machined with six different gauge lengths: type 1 with 20 mm, type 2 with 40 mm, type 3 with 60 mm, type 4 with 80 mm, type 5 with 100 mm and type 6 with 140 mm. The dynamic tests are performed in order to uncover the interplay between specimen gauge length, the impact velocity and the fracture location, as further discussed in section 6.2. Whether it is a quasi-static or dynamic experiment, at least three repeats are conducted.

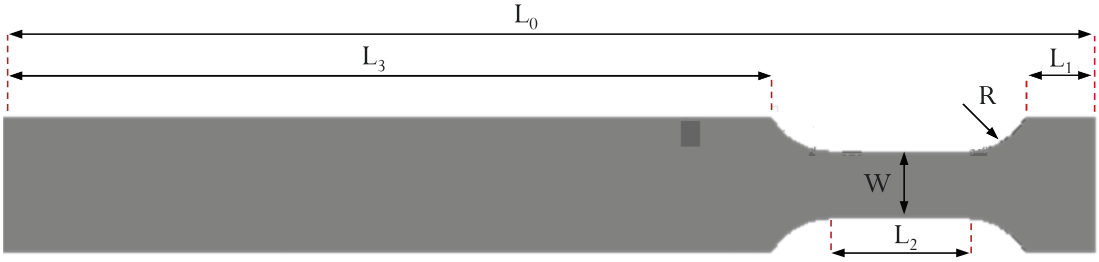

Static specimens

L_0	L_1	L_2 (gauge length)	L_3	W	R
120	41.34	**20**	41.34	10	10

Dynamic specimens

	L_0	L_1	L_2 (gauge length)	L_3	W	R
Type 1	500	41.34	**20**	421.34	10	10
Type 2			**40**	401.34		
Type 3			**60**	381.34		
Type 4			**80**	361.34		
Type 5			**100**	341.34		
Type 6			**140**	301.34		

Figure 6.1: Geometry and dimensions of the specimens used in the static and dynamic experiments (all dimensions in millimeters).

6.1.2 Quasi-static testing

The quasi-static experiments at room temperature were conducted using a servo-hydraulic testing machine INSTRON 8516 100kN under displacement control. We tested specimens whose loading direction formed angles of 0° (parallel), 45° and 90° (perpendicular) with the rolling direction of the plate. The goal was to investigate whether the material displays anisotropy caused by the rolling of the plate. Experiments were conducted for three nominal (initial) strain rates: $\dot{\varepsilon}_0 = 10^{-3}\ s^{-1}$, $\dot{\varepsilon}_0 = 10^{-2}\ s^{-1}$ and $\dot{\varepsilon}_0 = 10^{-1}\ s^{-1}$. In all the experiments the axial strain in the specimen is calculated relying on the cross-head displacement of the machine which has been corrected with knowledge of the elastic modulus of the material.

Fig. 6.2 shows stress-strain curves obtained from specimens tested at $10^{-3}\ s^{-1}$, that have been cut following the three different orientations (0°, 45°, 90°) investigated. It is shown that the orientation plays a minor role in the material behaviour since the three curves (practically) overlap. The yield stress and the strain hardening of the material are mild, and the static necking strain is ~ 0.23.

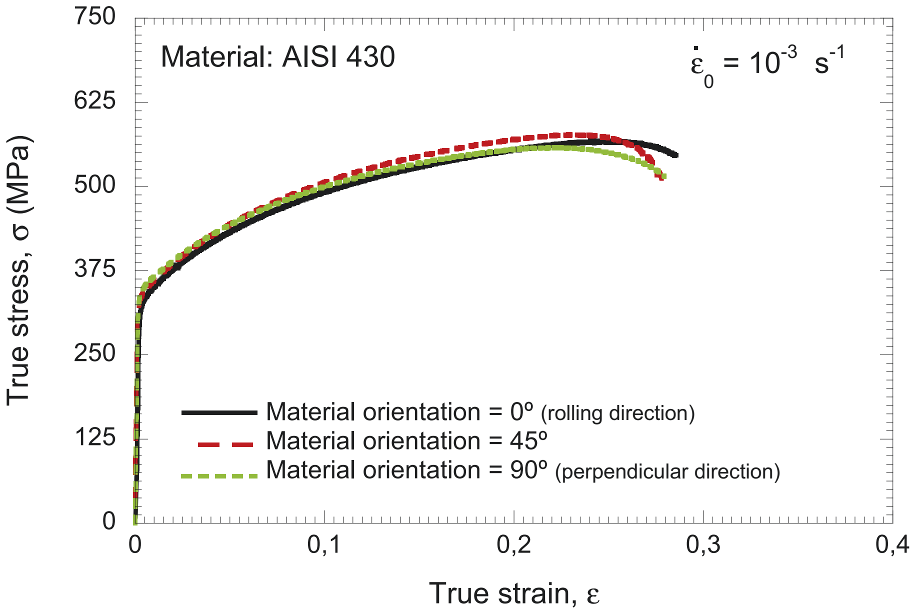

Figure 6.2: Experimental stress-strain curves for AISI 430 at $T_0 = 300\ K$ and $\dot{\varepsilon}_0 = 10^{-3}\ s^{-1}$.

Similarly, we have observed that for $10^{-2}\ s^{-1}$ and $10^{-1}\ s^{-1}$ the orientation barely affects the stress-strain characteristics of the material. Relying on these observations we assume that the in-plane mechanical behaviour can be considered isotropic. From now on, all other experimental results we show are obtained from specimens taken parallel to the rolling direction.

Additionally to quasi-static room temperature tests, we conducted experiments at elevated temperatures $T_0 = 375\ K$, $T_0 = 425\ K$ and $T_0 = 475\ K$. For that task, a heating furnace SERVOSIS Split was installed on a servo-hydraulic testing machine INSTRON 8516 100kN. The experiments were conducted under displacement control. For all these tests, the (initial) strain rate was $10^{-2}\ s^{-1}$. Fig. 6.3 shows that the stress-strain characteristic is slightly shifted downwards as the testing temperature increases, revealing the temperature sensitivity of the material within the range of testing temperatures considered.

6.1.3 Dynamic testing

Dynamic tensile tests at room temperature are conducted using a high-speed testing machine Instron VHS within the range of impact velocities $1\ m/s \leq$

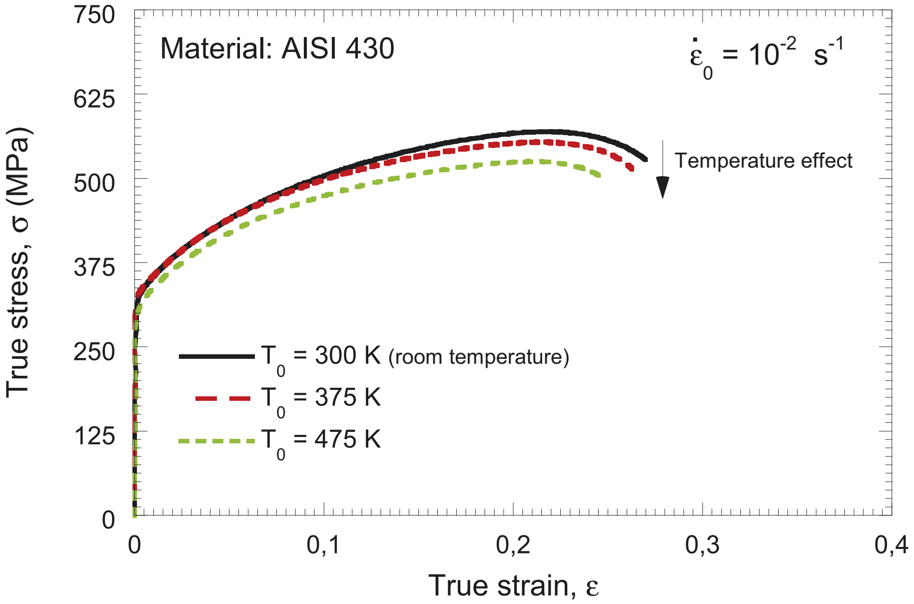

Figure 6.3: Experimental stress-strain curves for AISI 430 at $10^{-2}\ s^{-1}$ and three different testing temperatures $T_0 = 300\ K$, $T_0 = 375\ K$ and $T_0 = 475\ K$.

$V^{inp} \leq\ 7.5\ m/s$. For the dynamic samples shown in Fig. 6.1, this set of impact velocities leads to a wide range of nominal strain rates $7.15\ s^{-1}\ \leq \dot{\varepsilon}_0 \leq\ 375\ s^{-1}$.

The gripping system incorporated in the Instron VHS is the so-called Fast Jaw System. This system relies on two gripping faces being initially held apart by a pair of angled wedges. The actuator initially accelerates downwards with the specimen passing freely between the grips. At the desired location the wedges are knocked out by a set of adjustable rods. This action releases the force of four pretensioned bolts, so causing a set of grips to clamp onto the specimen surface, applying the high velocity loading. This explanation, and further details on the operation mode of the Instron VHS machine, can be found in the work of Battams [90].

Note that the ringing period of the raw data registered from the machine is $\sim 157\ \mu s$. This value corresponds to an eigenfrequency of the piezoelectric load cell of $\sim 6.4\ kHz$, as further verified using the Welch's Power Spectral Density estimation preimplemented in MATLAB. A band-pass Butterworth IIR Filter with a zero-phase forward and reverse procedure (to correct the associated delay of the signal) has been designed in MATLAB to filter the raw stress-strain curves. As further discussed by Rusinek et al. [53], this type of filtering process is usually applied to analyse the stress-strain characteristics obtained from dynamic tensile experiments performed using fast servo-hydraulic machines.

Fig. 6.4 shows stress-strain curves obtained for different loading rates using specimens with gauge length $L_2 = 20\ mm$. Dynamic (filtered) experimental curves for $\dot{\varepsilon}_0 = 87.5\ s^{-1}$ and $\dot{\varepsilon}_0 = 250\ s^{-1}$ are compared with the stress-strain characteristic obtained for $\dot{\varepsilon}_0 = 10^{-3}\ s^{-1}$. The material shows significant strain rate sensitivity within the range of strain rates tested.

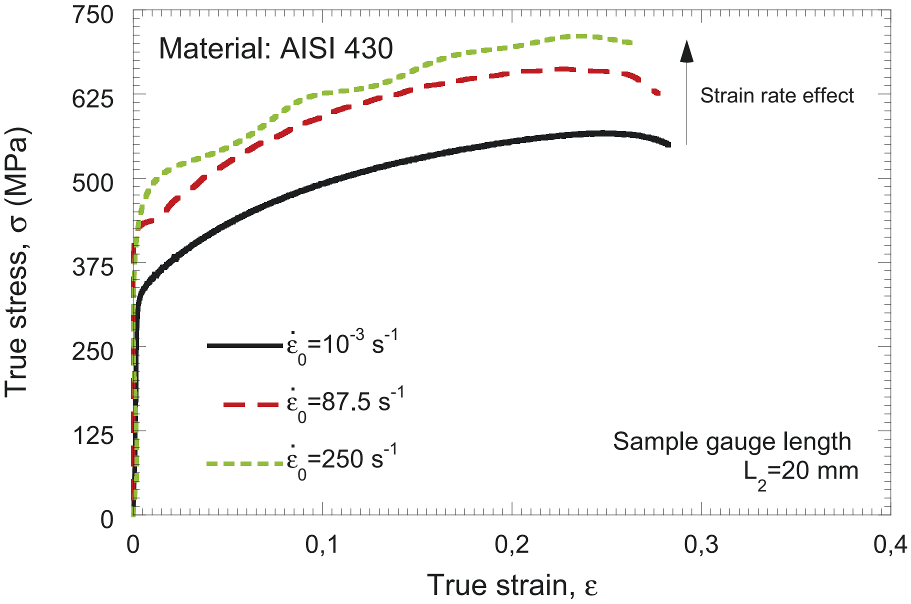

Figure 6.4: Experimental stress-strain curves for AISI 430 at $T_0 = 300\ K$ and three different initial strain rates: $\dot{\varepsilon}_0 = 10^{-3}\ s^{-1}$, $\dot{\varepsilon}_0 = 87.5\ s^{-1}$ and $\dot{\varepsilon}_0 = 250\ s^{-1}$.

6.2 Analysis and results

In this section we show selected dynamic experiments for different gauge lengths and impact velocities. The complete set of dynamic experiments that we have carried out is shown in Appendix E.

Fig. 6.5 shows three post-mortem samples with gauge length $L_2 = 100\ mm$ tested at $V^{inp} = 5\ m/s$. It has to be highlighted that, in the three repeats conducted of this test, we have obtained the same failure location. The specimen fails close to the clamped (opposite) side. According to Rodríguez-Martínez et al. [59], the fact that the failure is located away from the middle of the gauge indicates that the specimen is not in (complete) equilibrium during loading. As discussed in the introductory section, the lack of equilibrium in dynamic testing of long tensile samples was reported, for instance, by Lubliner [39] and Botte et al. [40, 41]. Moreover, note that plastic localization develops by the intersection of a pair of necking bands that, in agreement with the theoretical and numerical predictions reported for instance by Storen and Rice [91] and Zhang and Ravi-Chandar [92], are aligned with the directions of zero stretch rate. One of these two bands, the one which develops faster, leads to the final fracture of the specimen. Note that, there is (relatively) little reduction of the samples-width within the area surrounding the failure location. The width-reduction of the samples is largely uniform along the gauge.

The repeatability in the failure location of the dynamic samples is further illustrated in Fig. 6.6 where we show three post-mortem samples with gauge length $L_2 = 140\ mm$ tested at $V^{inp} = 1.75\ m/s$. The failure of the sample always occurs close to the middle of the gauge. This does not necessarily imply that the sample is in equilibrium, but it simply exposes that the failure location depends on the applied velocity and the gauge length, as further discussed in sections 6.2.1 and 6.2.2. In other words: (1) if the failure locus is located away from the middle of the gauge we know that the sample is not in equilibrium but (2) the fact that the failure locus is located in the middle of the gauge does not ensure that the sample is in equilibrium, see Rodríguez-Martínez et al. [59] for details. Moreover, it has to be noted that, in comparison with the results shown in Fig. 6.5, now there is larger width-reduction of the gauge in the vicinity of the fracture point. The pair

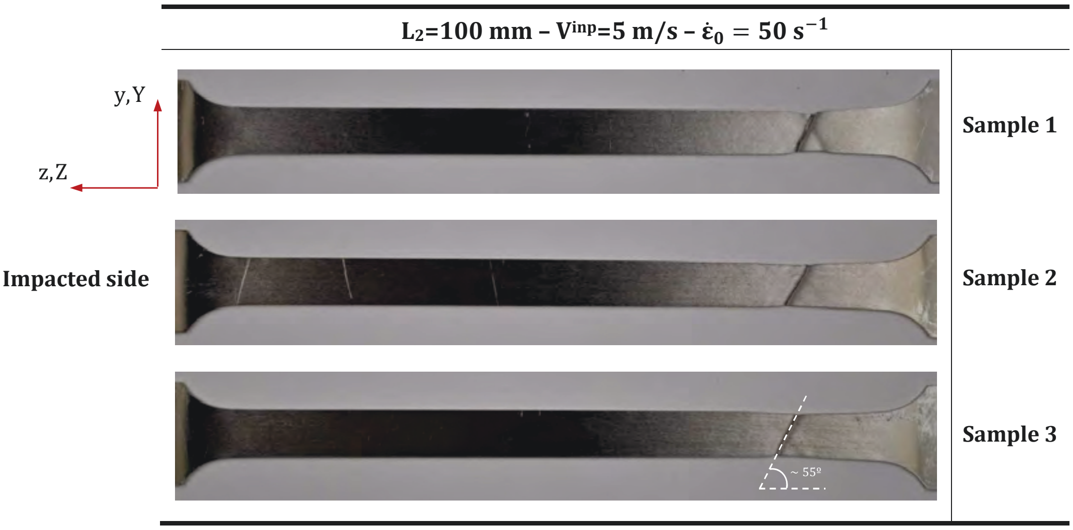

Figure 6.5: Three post-mortem samples with gauge length $L_2 = 100\ mm$ tested at $V^{inp} = 5\ m/s$.

of localization bands are located inside a necked region in the $\{Y, Z\}$ plane. The width-reduction is not uniform along the gauge. The aspect ratio of the specimen gauge seems to play a strong role in the failure location and in the failure pattern, as further discussed in the following sections of this chapter.

To be noted that, as detailed in Table (E.1) of Appendix E, we have obtained very high repeatability in the failure location for all the gauge lengths explored and within the whole range of impact velocities tested. This indicates that, rather than being random, the position where the flow localization occurs is deterministic. Exceptions occurred in few cases for which one of the three repeats programmed showed different failure location than the other two. In these selected cases we decided to perform an additional test after which we always had three (of four) samples with the same failure location. This failure location was assumed to be the representative of such sample geometry and loading conditions. The fact that one of the tests is not providing the same fracture location than the other three is simply attributed to the inherent uncertainties surrounding experimentation. Our belief is that slight variations in (1) the pressure applied by the jaws to fix the samples during testing and/or (2) the actual velocity applied by the machine are responsible for the small scatter that we have registered in the fracture location.

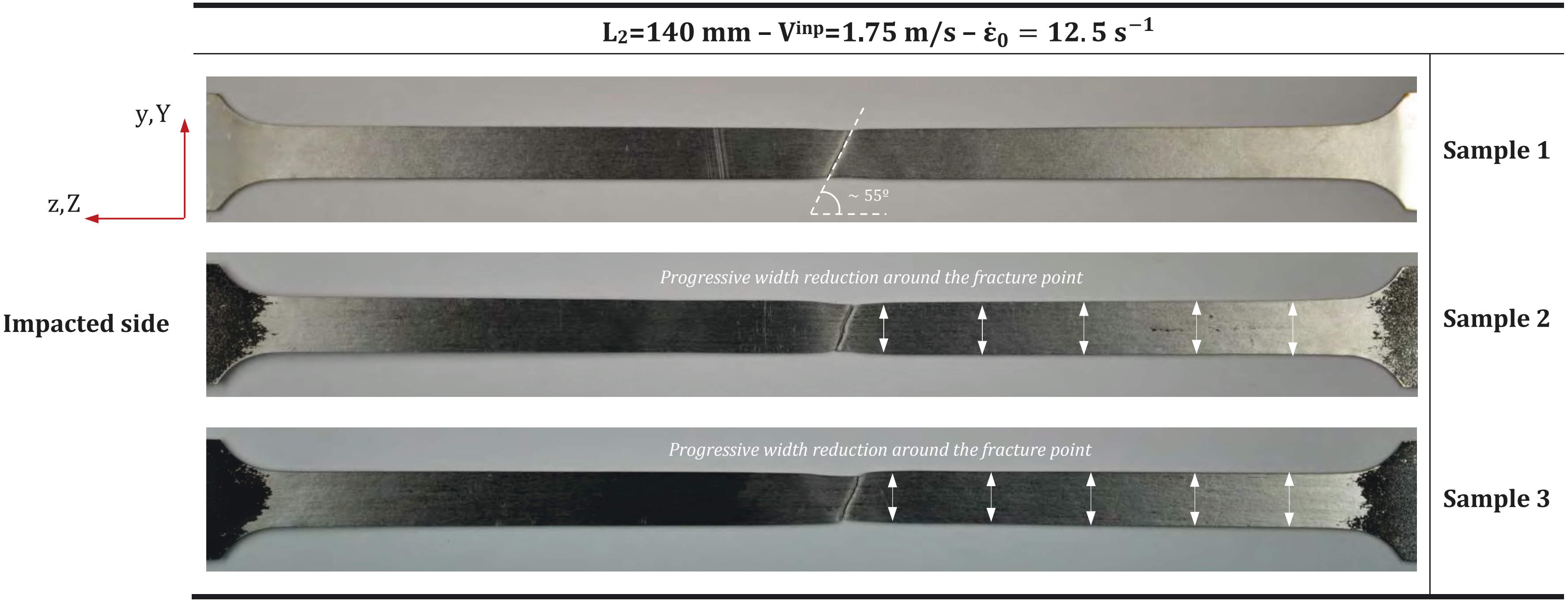

Figure 6.6: Three post-mortem samples with gauge length $L_2 = 140\ mm$ tested at $V^{inp} = 1.75\ m/s$.

6.2.1 Influence of loading velocity on the location of flow localization

In this section we analyse the influence of loading velocity on the fracture location. Fig. 6.7 shows seven samples with gauge length $L_2 = 60\ mm$ tested at different velocities. For the smallest impact velocity that we have explored $V^{inp} = 1\ m/s$ the failure location occurs close to the impacted side. Increasing the impact velocity changes the place where the failure occurs. Thus, for $V^{inp} = 1.75\ m/s$, $V^{inp} = 2.5\ m/s$, $V^{inp} = 3.75\ m/s$, $V^{inp} = 5\ m/s$ and $V^{inp} = 6.25\ m/s$, we have that the sample breaks near the clamped side. Finally, for the highest velocity tested $V^{inp} = 7.5\ m/s$ the fracture location moves again to the impacted side. Note that such a strong interplay between impact velocity and failure location has been found for the largest sample gauge lengths investigated. These experimental results bear a definite resemblance to those recently reported by Osovski et al. [60], Rittel et al. [61] and Rotbaum et al. [52] using cylindrical samples, and confirm the numerical predictions reported by Rusinek et al. [56] and Rodríguez-Martínez et al. [93] using flat samples who claimed that the failure location in the dynamic tensile test is very much controlled by the impact velocity. Since the sample is initially at rest, the fact that the fracture location is controlled by the impact velocity means that the dynamic effects (stress waves and inertia) dictate the fracture location.

6.2.2 Influence of specimen gauge length on the location of flow localization

Relying on the experimental results shown above, we expect that the gauge length will play a role in the fracture location. For different gauge lengths the stress waves need different times to go over the entire gauge, which alters the processes of reflection and interaction of waves taking place in the sample during the test. Further, we expect that the gauge length will affect the fracture pattern. The gauge length determines the aspect ratio (slenderness) of the gauge which, on the basis of the results shown in Figs. 6.5 and 6.6, plays a role in the failure mode.

Fig. 6.8 shows six specimens with different gauge lengths tested at $V^{inp} = 5\ m/s$. In the case of $L_2 = 20\ mm$ the failure occurs in the middle of the gauge with negligible (localized) width-reduction near the fracture location. To be noted that, instead of having a single localization point which leads to fracture as in the

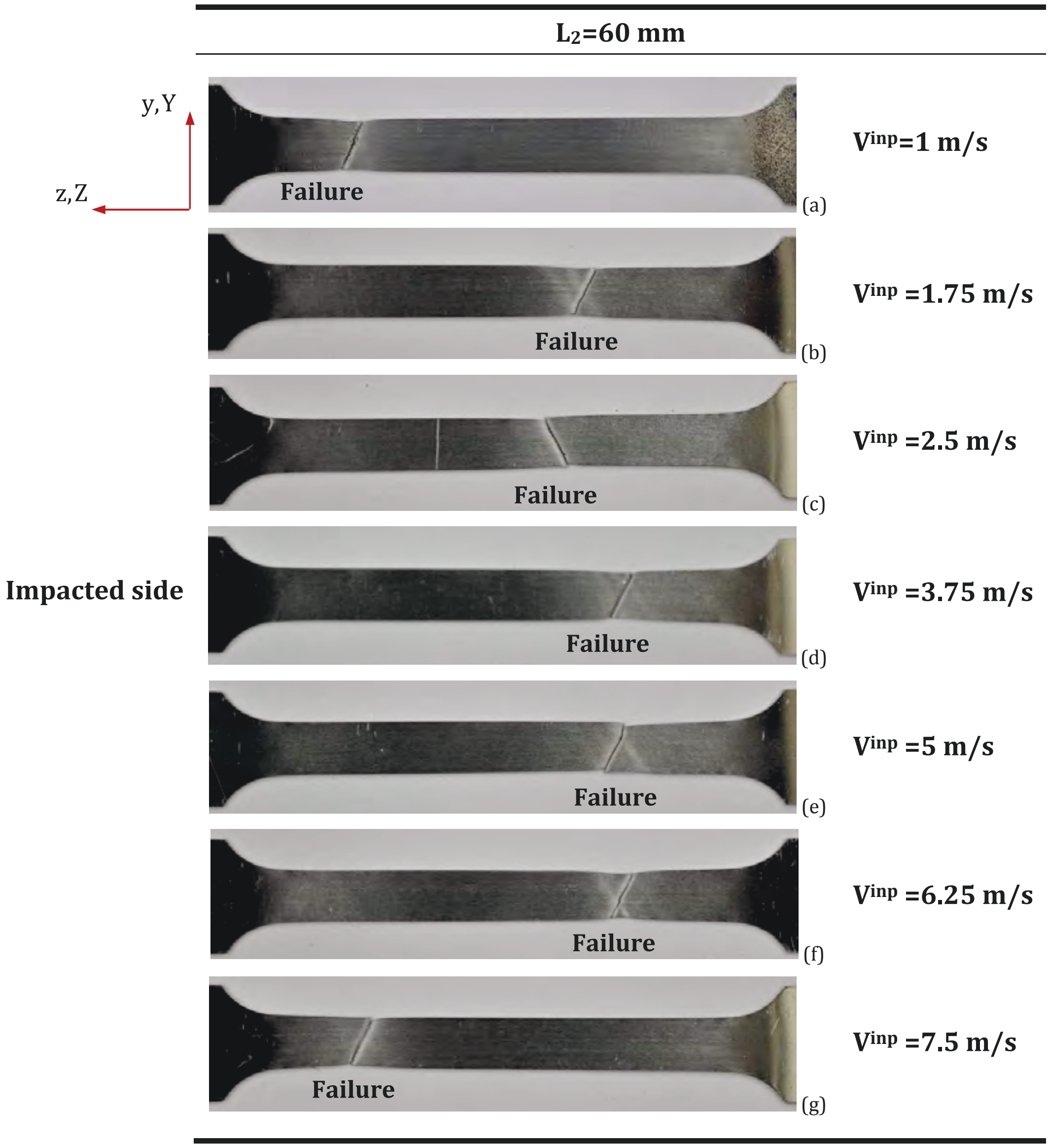

Figure 6.7: Seven post-mortem samples with gauge length $L_2 = 60\ mm$ tested at: (a) $V^{inp} = 1\ m/s$, (b) $V^{inp} = 1.75\ m/s$, (c) $V^{inp} = 2.5\ m/s$, (d) $V^{inp} = 3.75\ m/s$, (e) $V^{inp} = 5\ m/s$, (f) $V^{inp} = 6.25\ m/s$, (g) $V^{inp} = 7.5\ m/s$.

specimens shown in Figs. 6.5, 6.6 and 6.7, there are traces of multiple localization bands all along the gauge. This key (and very uncommon) finding will be discussed in detail in the next section. By now, we just focus on the role played by the gauge length in the fracture location. It is observed that for $L_2 = 40\ mm$ the failure is no longer in the middle of the gauge but close to the impacted side, whereas for $L_2 = 60\ mm$, $L_2 = 80\ mm$ and $L_2 = 100\ mm$ the fracture is located near the clamped side. Surrounding the failure point, the thinning of the sample along the Y direction increases with the gauge length. Finally, for the greatest gauge length $L_2 = 140\ mm$ the fracture location is located in the middle of the gauge. There is a significant reduction of the width of the gauge around the fracture point. The sample straining is not uniform along the gauge.

A close relation between gauge length, failure location and failure pattern has been found for all the impact velocities tested, which confirms the control that dynamic effects (stress waves and inertia) have over the failure location and failure mode of the sample. Further, we claim that the extensive experimental campaign that we have conducted in this investigation strengthens the idea that the failure location in the dynamic tensile test is deterministic. Instead of being controlled by random-type effects as intrinsic material defects, the failure location seems to be governed to a large extent by dynamic phenomena.

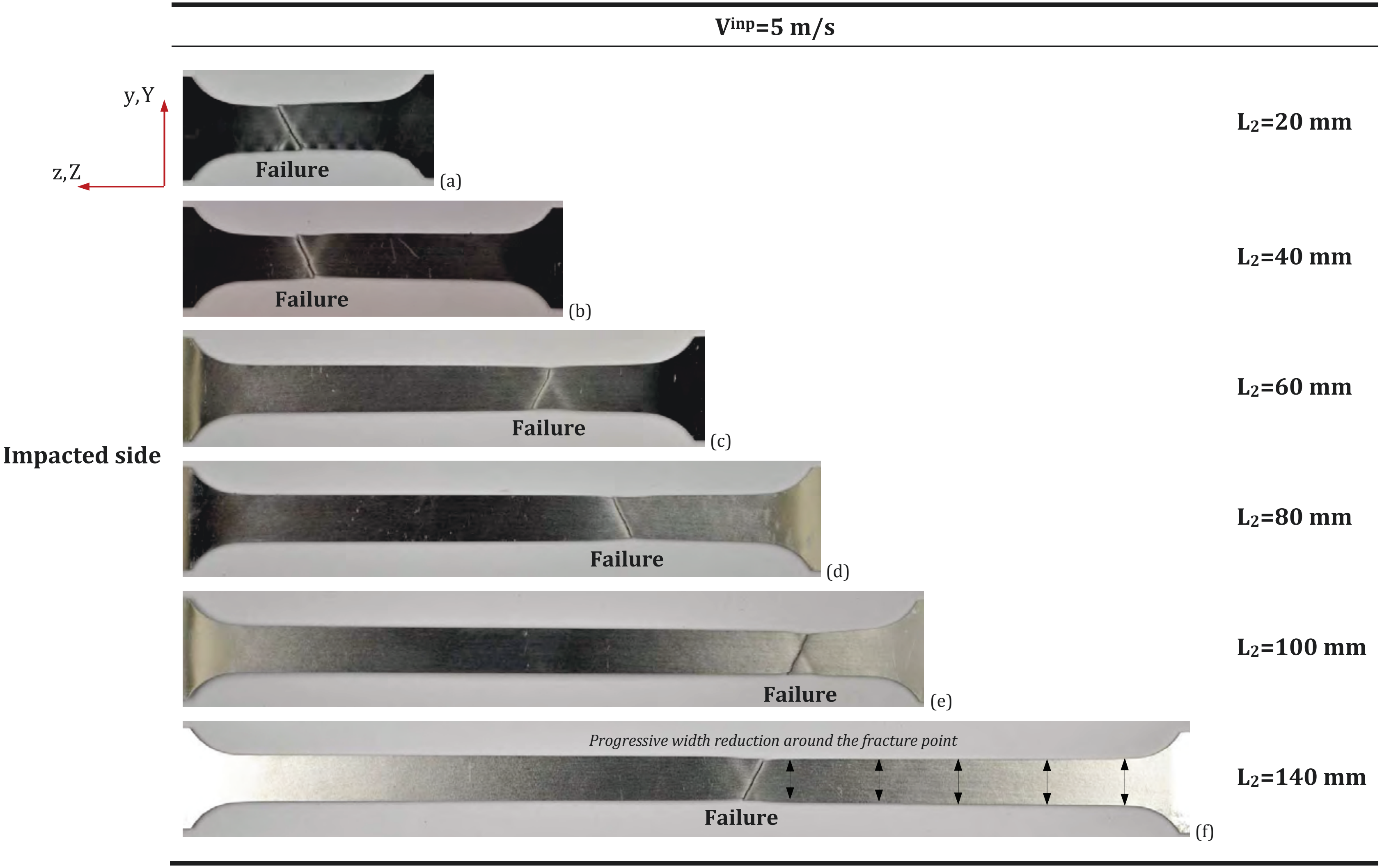

Figure 6.8: Six post-mortem samples with different gauge lengths tested at $V^{inp} = 5\ m/s$: (a) $L_2 = 20\ mm$, (b) $L_2 = 40\ mm$, (c) $L_2 = 60\ mm$, (d) $L_2 = 80\ mm$, (e) $L_2 = 100\ mm$, (f) $L_2 = 140\ mm$.

6.2.3 Multiple localization pattern

Multiple, and largely regular, localization patterns have been observed in a significant number of the experiments performed using the samples with the shorter gauge lengths. Four of these samples are shown in Fig. 6.9. For $L_2 = 20\ mm$ we have found multiple necking bands in $\sim 45\%$ of the samples tested at velocities larger than $V^{inp} = 3.75\ m/s$. For $L_2 = 40\ mm$ the multiple localization pattern is observed in $\sim 35\%$ of the experiments. For $L_2 = 60\ mm$ we only have observed multiple necking bands in two samples tested at $V^{inp} = 1.75\ m/s$ and $V^{inp} = 5\ m/s$. For all the samples with $L_2 = 80\ mm$, $L_2 = 100\ mm$ and $L_2 = 140\ mm$ only a pair of necking bands are formed, these being responsible for the specimen fracture. It follows from previous results that short samples tested at high impact velocities are more prone to develop multiple localization bands. This behaviour may be explained based on the following premises: (1) the shortest samples (shortest aspect ratios L_2/W in Fig. 6.1) are the most equilibrated during testing [26, 41, 94], develop the most uniform strain distribution along the gauge and do not show (localized) width-reduction near the fracture point; (2) increasing impact velocity boosts the role played by inertia in the material response [31, 32, 95].

1. A tensile sample with constant cross section tested under *perfect* mechanical equilibrium shall develop uniform strain distribution along the gauge (i.e. constant width-reduction along the gauge) leading to regular and symmetric localization and failure patterns (in the absence of significant material defects). In the absence of *perfect* equilibrium, the specimen is susceptible to show variability in the strain field along the gauge (i.e. variable width-reduction along the gauge) leading to irregular and unsymmetrical localization and failure patterns. On these basis, it is reasonable to assume that a specimen tested under conditions close to equilibrium is more likely to develop regular and symmetric localization and failure patterns than a sample tested under loading conditions which are far from mechanical equilibrium.

   One the one hand, these arguments explain that almost all the specimens that we have tested under (quasi)static loading, and therefore under loading conditions very close to mechanical equilibrium, failed in the middle of the sample, i.e. they have shown a symmetric failure pattern. One the other hand, these arguments also explain that most of the shortest samples (shortest aspect ratio L_2/W) tested under dynamic loading show symmetric localization and failure patterns. Note that in these samples (1) the localization pattern is repetitive and largely symmetric with the respect to the longitudinal and transversal axes of the specimens and (2) the samples fail in (approximately) the middle of the gauge.

2. An equilibrated tensile specimen tested under dynamic loading is prone to develop multiple localization points. This behaviour is frequently observed in the radial expansion of axially symmetric structures like rings [96–101], tubes [102, 103] and hemispheres [104]. The symmetry of these structures nearly eliminates the effects of wave propagation before the onset of plastic localization, the specimen being tested under loading conditions close to equilibrium. All these experimental works reported that the number of localization points increases with the loading velocity. This experimental finding has been explained by several authors [36, 37, 95, 105] who claimed that inertia, via strain rate, is the main responsible for the development of multiple localization patterns in samples tested under dynamic loading. These arguments explain that we have observed multiple necking bands mostly in those samples that we have tested at the higher strain rates.

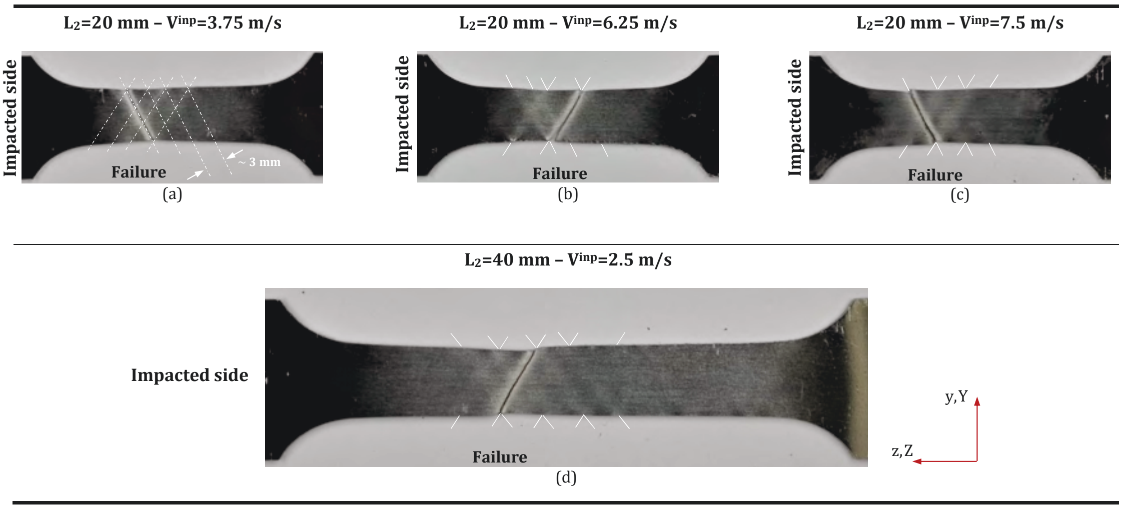

Figure 6.9: Four post-mortem samples with different gauge lengths tested at different velocities. Multiple localization bands are observed in all of them. (a) $L_2 = 20\ mm$ and $V^{inp} = 3.75\ m/s$, (b) $L_2 = 20\ mm$ and $V^{inp} = 6.25\ m/s$, (c) $L_2 = 20\ mm$ and $V^{inp} = 7.5\ m/s$ and (d) $L_2 = 40\ mm$ and $V^{inp} = 2.5\ m/s$.

6.3 Discussion and conclusions

In this chapter we have investigated the nature of the fracture location in the dynamic tensile testing of steel sheets. For that purpose we have conducted a comprehensive experimental campaign in which a large number of specimens with different gauge lengths have been tested at various velocities. For each combination of sample-length/applied-velocity we have carried out several repeats which have revealed an extremely high repeatability in the fracture location. This is a key experimental finding that shows that the fracture location is not random but deterministic.

Moreover, we claim that the deterministic character of the fracture location is directly connected with the intervention of dynamic effects (stress waves and inertia) during the test. We further investigate this statement paying specific attention to the role played by the applied velocity and the gauge length, since these factors control to a large extent the processes of reflection and interaction of waves taking place in the sample during the test. For different impact velocities we have different magnitudes of the stress waves induced in this specimen, while for different gauge lengths the stress waves need different times to go over the gauge. Thus, we claim that the systematic motion from side to side of the sample that shows the fracture location with the variations in impact velocity and gauge length is an additional proof of the deterministic character of the strain localization process.

Nevertheless, it is not only the failure location which depends on the applied velocity and the gauge length, but the failure pattern also does. While short samples tested at high velocities are prone to develop multiple and highly regular localization bands, large samples tested at low velocities use to develop a single pair of bands inside a necked region. We conclude that the emergence of multiple localization bands is favoured in those samples with low slenderness for which the strain field along the gauge is kept highly uniform during the loading process.

7

Analysis and results: Finite elements

In this chapter we develop a 3D finite element approach in ABAQUS/-Explicit to model, relying on the experiments presented in previous chapter, the flow localization and failure of tensile specimens subjected to dynamic testing. We focus our attention on the key mechanisms which determine the fracture location and discuss the initial and boundary conditions which lead to the formation of the multiple localization patterns. The outline of this chapter is as follows: in section 7.1 we describe the main features of the two finite element models that we have developed. These models are specifically devised to uncover the effect of the initial and boundary conditions in the plastic localization process. In section 7.2 we carry out calculations using specimens with different gauge lengths subjected to a wide spectrum of loading velocities. The computations show, in agreement with the experimental evidence, the role played by dynamic effects (wave propagation and inertia) in flow localization. In addition, we show the interplay between the boundary conditions and the emergence of multiple localization patters. In section 7.3 we summarize and discuss the salient features of the finite element investigation. Part of this chapter has been published in Vaz-Romero et al. [88].

7.1 3D Finite element model

This section describes the features of the 3D finite element models developed to simulate plastic strain localization in AISI 430 steel sheets subjected to dynamic tension. The numerical analyses are carried out using the finite element code ABAQUS/Explicit [62]. We model the mechanical behaviour of the material using the constitutive equations for hypoelastic-plastic solids derived in section 4.2. We have implemented the constitutive model in the finite element code through a user subroutine VUMAT following the integration scheme described in section 4.2.2. The thermodynamic framework developed in section 4.4 is considered.

Remark 7.1. For the sake of brevity, we only show numerical calculations conducted with the hypoelastic-plastic model. Finite element calculations using the hyperelastic-plastic model are not shown in this document.

The identification of the yield stress parameters (see Eq. 4.7) is conducted by a numerical regression based on experimental data obtained (only) with the samples of gauge length 20 mm at different strain rates and temperatures. We have checked that these specimens reach *equilibrium* (we are aware that, strictly speaking, under dynamic loading there is no equilibrium) during the experiments. This result agrees with previous observations reported by Rusinek et al. [56] and Klepaczko [106]. Conventional material constants, elastic parameters and parameters related to the yield stress for AISI 430 steel are given in Table 7.1.

The goal of the numerical calculations is not to mimic the experimental tests but to provide new insights into the role played by dynamic effects (inertia and wave disturbances) and boundary conditions in the deterministic character of the plastic flow localization. For that purpose is enough to use simple geometrical models which solely consider the gauge of the sample, as further demonstrated in section 7.2. This greatly simplifies the interpretation of the finite element results and reduces the computational cost. Thus, our problem setting is a strip with thickness $h = 1\ mm$, width $W = 10\ mm$ (unless otherwise stated, see section 7.2.3) and six different lengths L_2, according to the six gauge lengths used in the dynamic samples described in Fig. 6.1 of chapter 6. On these geometrical basis, two different types of finite element models are developed. The idea is that the comparison between the results obtained with these two models which are described below will allow to explore the respective influence of dynamic effects and boundary conditions on flow localization. Note that $\{x, y, z\}$ denotes the Eulerian coordinate system while $\{X, Y, Z\}$ refers to the Lagrangian.

Symbol	**Property and units**	**Value**
ρ_o	Initial density (kg/m^3)	7740
C_p	Specific heat (J/kgK), Eq. (4.93)	460
k	Thermal conductivity (W/mK), Eq. (4.93)	26.1
E	Young modulus (GPa)	200
ν	Poisson ratio	0.33
A	Initial yield stress (MPa), Eq. (4.7)	175.67
B	Work hardening modulus (MPa), Eq. (4.7)	530.13
n	Work hardening exponent, Eq. (4.7)	0.167
$\dot{\varepsilon}_{ref}$	Reference strain rate (s^{-1}), Eq. (4.7)	0.01
m	Strain rate sensitivity exponent, Eq. (4.7)	0.0118
T_{ref}	Reference temperature (K), Eq. (4.7)	300
μ	Temperature sensitivity exponent, Eq. (4.7)	0.51
β	Taylor-Quinney coefficient, Eq. (4.93)	0.9

Table 7.1: Physical material constants, elastic parameters and parameters related to the yield stress for AISI 430 steel.

- **Model A: No-field configuration**. The solid is initially at rest. The loading conditions are $V_Z(X, Y, L_2, t) = V^{inp} = \dot{\varepsilon}_0 L_2$ and $V_Z(X, Y, 0, t) = 0$ (see the Lagrangian coordinate system defined in the figure). Application of these loading conditions leads to the propagation of stress waves along the sample [44, 51], precluding –full/complete– mechanical equilibrium. Within model A we distinguish 2 configurations:
  - **Model A-1**. No additional constraints are imposed to the displacements of the nodes of the model. This configuration is representative of a typical experimental test.
  - **Model A-2**. The nodes of the workpiece located at the surfaces $\{X, \pm\frac{W}{2}, Z\}$ have identical displacement along the Y axis during the calculation. Using Hencky strain as our strain measure, and relying on the incompressibility of the plastic flow, we set $U_Y(X, \pm W/2, Z, t) = \mp\frac{W}{2}\left(\frac{1}{\sqrt{\dot{\varepsilon}_0 t+1}} - 1\right)$. This configuration tries to emulate an infinitely long sample along the Y axis.

  Note that, due to the symmetry of the model, only the $\{X > 0, Y > 0\}$ quarter of the specimen has been analysed (see Fig. 7.1).

- **Model B: Field configuration**. The initial condition corresponds to an equilibrium configuration which *virtually* prevents the generation of stress waves during the loading process. We say *virtually* because, due to the discretization of the workpiece and the explicit integration scheme used by the FE code, slight disturbances in the field variables are generated during the simulations. These little perturbations are required to trigger plastic flow localization as shown by Rusinek and Zaera [107]. Nevertheless, we claim that in comparison with the *no-field* condition, now the role played by the stress waves in the sample's response is significantly reduced [59, 105]. The loading conditions are $V_Z(X, Y, \pm\frac{L_2}{2}, t) = \pm\frac{V^{inp}}{2} = \pm\dot{\varepsilon}_0\frac{L_2}{2}$ (see the Lagrangian coordinate system defined in the figure). The initial equilibrium state is obtained by initializing the velocity, stress, strain and displacement fields in the sample. The initial conditions in velocity, formulated based on Zaera et al. [105], are $V_X(X, Y, Z, 0) = -\nu\dot{\varepsilon}_0 X$, $V_Y(X, Y, Z, 0) = -\nu\dot{\varepsilon}_0 Y$ and $V_Z(X, Y, Z, 0) = \dot{\varepsilon}_0 Z$. The initial conditions in stress are $\tau_X(X, Y, Z, 0) = 0$, $\tau_Y(X, Y, Z, 0) = 0$ and $\tau_Z(X, Y, Z, 0) = \rho_0 \mathrm{c}_0 \dot{\varepsilon}_0 \frac{L_2}{2}$, where $\mathrm{c}_0 = \sqrt{E/\rho_0}$ is the longitudinal elastic wave speed referred to the initial material density. Note that this procedure for initializing the stress field has to be limited to the cases for which $\rho_0 \mathrm{c}_0 \dot{\varepsilon}_0 \frac{L_2}{2} < A$, where it has to be recalled that A in Eq. (4.7) defines the initial yield stress of the material. Previous expression implies that the maximum loading velocity V^{inp} that can be investigated using this procedure is 8.92 m/s. With the knowledge of the initial stress field, and relying on the Hooke's law, we calculate the initial strains as $\varepsilon_X(X, Y, Z, 0) = -\frac{\nu\rho_0 \mathrm{c}_0 \dot{\varepsilon}_0 L_2}{2E}$, $\varepsilon_Y(X, Y, Z, 0) = -\frac{\nu\rho_0 \mathrm{c}_0 \dot{\varepsilon}_0 L_2}{2E}$ and $\varepsilon_Z(X, Y, Z, 0) = \frac{\rho_0 \mathrm{c}_0 \dot{\varepsilon}_0 L_2}{2E}$. Using Hencky strain we calculate the initial displacements as $U_X(X, Y, Z, 0) = -\frac{X}{2}\left(\exp^{-\frac{\nu\rho_0 \mathrm{c}_0 \dot{\varepsilon}_0 L_2}{2E}} - 1\right)$, $U_Y(X, Y, Z, 0) = -\frac{Y}{2}\left(\exp^{-\frac{\nu\rho_0 \mathrm{c}_0 \dot{\varepsilon}_0 L_2}{2E}} - 1\right)$ and $U_Z(X, Y, Z, 0) = Z\left(\exp^{\frac{\rho_0 \mathrm{c}_0 \dot{\varepsilon}_0 L_2}{2E}} - 1\right)$. It is worth mentioning that this *initialization methodology* is an original contribution of this work since it significantly improves the procedure proposed by Rodríguez-Martínez et al. [59], where only the velocity along the loading direction was initialized in the so-called field configuration. As for model A, we also distinguish 2 configurations for model B:

- **Model B-1**. No additional constraints are imposed to the displacements of the nodes of the model.
- **Model B-2**. The displacement of the nodes located at the surfaces $\{X, \pm W/2, Z\}$ is prescribed as $U_Y(X, \pm W/2, Z, t) = \mp\frac{W}{2}\left(\exp^{-\frac{\nu\rho_0 \mathrm{c}_0 \dot{\varepsilon}_0 L_2}{2E}} + + \frac{1}{\sqrt{\dot{\varepsilon}_0 t + 1}} - 2\right)$. The first term inside the parenthesis refers to the displacement due to the initialization of the field variables while the second

term corresponds to the time dependent displacement calculated based on the incompressibility of the plastic flow, as previously described for model A-2.

Note that, due to the symmetry of the model, only the $\{X > 0, Y > 0, Z > 0\}$ eight of the specimen has been analysed (see Fig. 7.1).

Models A-2 and B-2 will serve to explain the role played by boundary conditions in the post-uniform elongation of the sample and, specifically, in the failure pattern. Further, the fact that the boundary condition $U_Y(X, \pm W/2, Z, t)$ imposed to the models A-2 and B-2 emulates an infinitely long sample in the Y axis will serve to highlight the influence of the sample slenderness on the formation of multiple localization patterns.

The models are meshed using eight node coupled displacement-temperature solid elements, with reduced integration and hourglass control ($C3D8RT$ in ABAQUS notation). The elements have an initial aspect ratio 1 : 2 : 1 with dimensions $0.166 \times 0.333 \times 0.166\ mm^3$ for all the models that we have built. We have checked that, with the increase of plastic deformation in the workpiece, the shape of the elements evolves, approaching an aspect ratio closer to 1 : 1 : 1 at the time of flow localization. According to Zukas and Scheffer [108], such an element shape is optimal for describing dynamic events like high rate flow localization. Further, a mesh convergence study has been performed, and the time evolution of different critical output variables, namely stress, strain and necking inception, were compared against a measure of mesh density until the results converged satisfactorily. Note that, in our modelling, viscosity, inertia and thermal conductivity act as potent regularization factors that help to the well-possessedness of the problem at hand [109, 110]. We hold that this minimizes the spurious influence of the mesh in the solution of the boundary value problem.

7.2 Analysis and results

In this section we show and analyse the finite element results in order to rationalize the experimental findings reported in chapter 6.

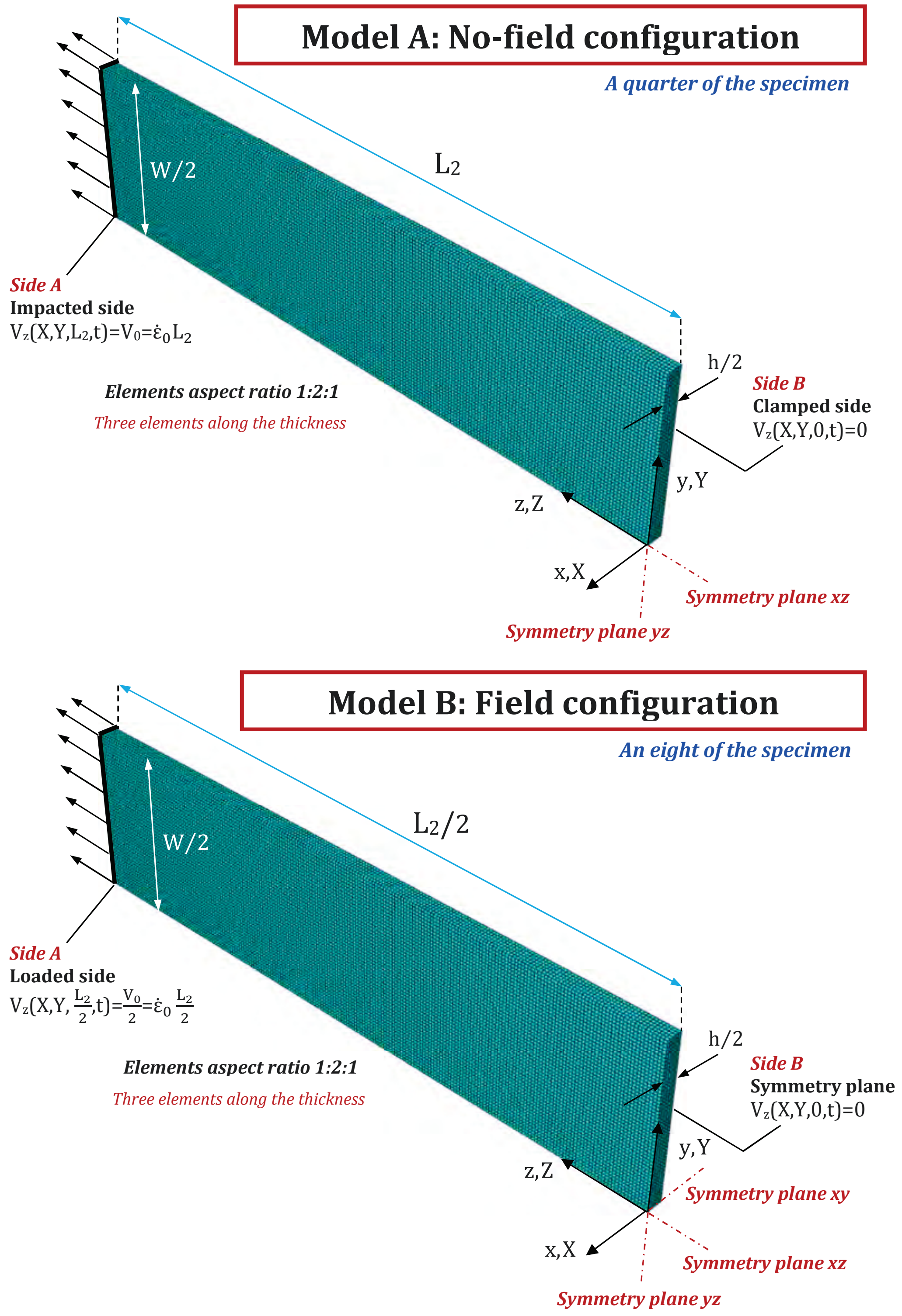

Finite element models

L_2 (mm)					
Type 1	Type 2	Type 3	Type 4	Type 5	Type 6
20	40	60	80	100	140

Figure 7.1: 3D finite element models. Mesh, dimensions, boundary conditions and loading conditions of models A and B.

7.2.1 Influence of loading velocity on the location of flow localization

With the aim of providing further insights into the interplay between the impact velocity and the location of flow localization, we rely on finite element simulations conducted using the model A-1. As described in section 7.1, within the models built in this work, the A-1 is the most similar to a typical experimental arrangement in terms of initial, loading and boundary conditions. Fig. 7.2 shows contours of equivalent plastic strain $\bar{\varepsilon}^p$ in the Lagrangian configuration (undeformed shape) for $L_2 = 60\ mm$ and various loading velocities. The range of loading velocities analysed in the calculations is wider than the range covered by the experiments in order to reveal, to the full extent, how the point of localization varies sequentially from side to side of the sample with the increase of the loading velocity. Note that, irrespective of the loading velocity, the plastic strain localization takes the form of a pair of necking bands that follow the directions of zero stretch rate, as shown in the experimental results of chapter 6.

In the case of $V^{inp} = 0.125\ m/s$, the smallest velocity explored, the localization of plastic deformation is located at the clamped end. The increase in applied velocity moves the localization point towards the impacted side, where it remains until reaching $V^{inp} = 7.5\ m/s$. Then, plastic localization occurs near the clamped end. For $V^{inp} = 10\ m/s$ the localization point is back to the impacted side while for $V^{inp} = 15\ m/s$ it takes place, again, near the clamped end. Such a systematic motion of the localization point along the sample continues taking place if we keep increasing the applied speed, until the critical impact velocity (CIV) is attained for $V^{inp} \approx 80\ m/s$. When the CIV is reached the applied velocity is such that it generates a plastic wave which induces *(instantaneous)* flow localization [51]. Thus, for velocities above the CIV the localization of plastic deformation inevitably occurs *(instantaneously)* at the impacted side, as shown by Klepaczko [111] and Rusinek et al. [56]. Note that such a strong influence of the impact velocity on the location of flow localization has been found for all the gauge lengths investigated, the so-called types 1-6 in Fig. 7.1.

Note that the specific locations of flow localization predicted by the numerical calculations do not agree with their experimental counterparts shown in Fig. 6.7 of chapter 6. While we highlight the qualitative agreement between numerical calculations and experiments, we acknowledge the lack of quantitative agreement.

Besides the simplified geometry that we have analysed, we think that there are some other factors, that can hardly be overcome, responsible for this disagreement (quantitative, but not qualitative, disagreement). For instance, there are *uncertainties* intrinsic to the experimental setup related to the loading condition (the actual applied velocity is surely not a *perfect* step-function) and the boundary conditions (the system used to attach the sample does not ensures a *perfect* embedding). We hold that these *uncertainties* make virtually impossible to build a finite element model to mimic the experiments with the accuracy required to predict the specific location of flow localization. Moreover, while in the experiments the stress waves may be transmitted to the machine through the jaws, we do not consider this scenario in our modelling. Nevertheless, we hold that our (simple) calculations are in qualitative agreement with the experiments and show the interplay between the fracture location and the loading velocity. Further, these calculations provide an additional proof of the deterministic character of location of plastic strain localization in the dynamic tensile test.

7.2.2 Influence of specimen gauge length on the location of flow localization

This section aims at further deepen into the relationship between the sample gauge length and the location of flow localization that was revealed in chapter 6. For that purpose we rely on finite element simulations conducted using the model A-1. Fig. 7.3 illustrates contours of equivalent plastic strain $\bar{\varepsilon}^p$ in the Lagrangian configuration (undeformed shape) for $V^{inp} = 5\ m/s$ and various gauge lengths. Note that, irrespective of the sample length, the plastic strain localization takes the form of a pair of necking bands.

In the case of $L_2 = 20\ mm$, the shortest gauge length explored, the localization of plastic deformation is located roughly at the center of the sample. The increase of the gauge length affects the location of flow localization which occurs at the impacted end for $L_2 = 40\ mm$, $L_2 = 60\ mm$ and $L_2 = 80\ mm$. For $L_2 = 100\ mm$ two localization points are detected. The main one (the most developed) takes place at the impacted end, while the secondary one appears at the clamped site. For $L_2 = 140\ mm$ a single localization point appears at the clamped site. Such a systematic motion of the localization point along the sample continues taking place if we keep increasing the sample gauge length. Note that such a strong influence

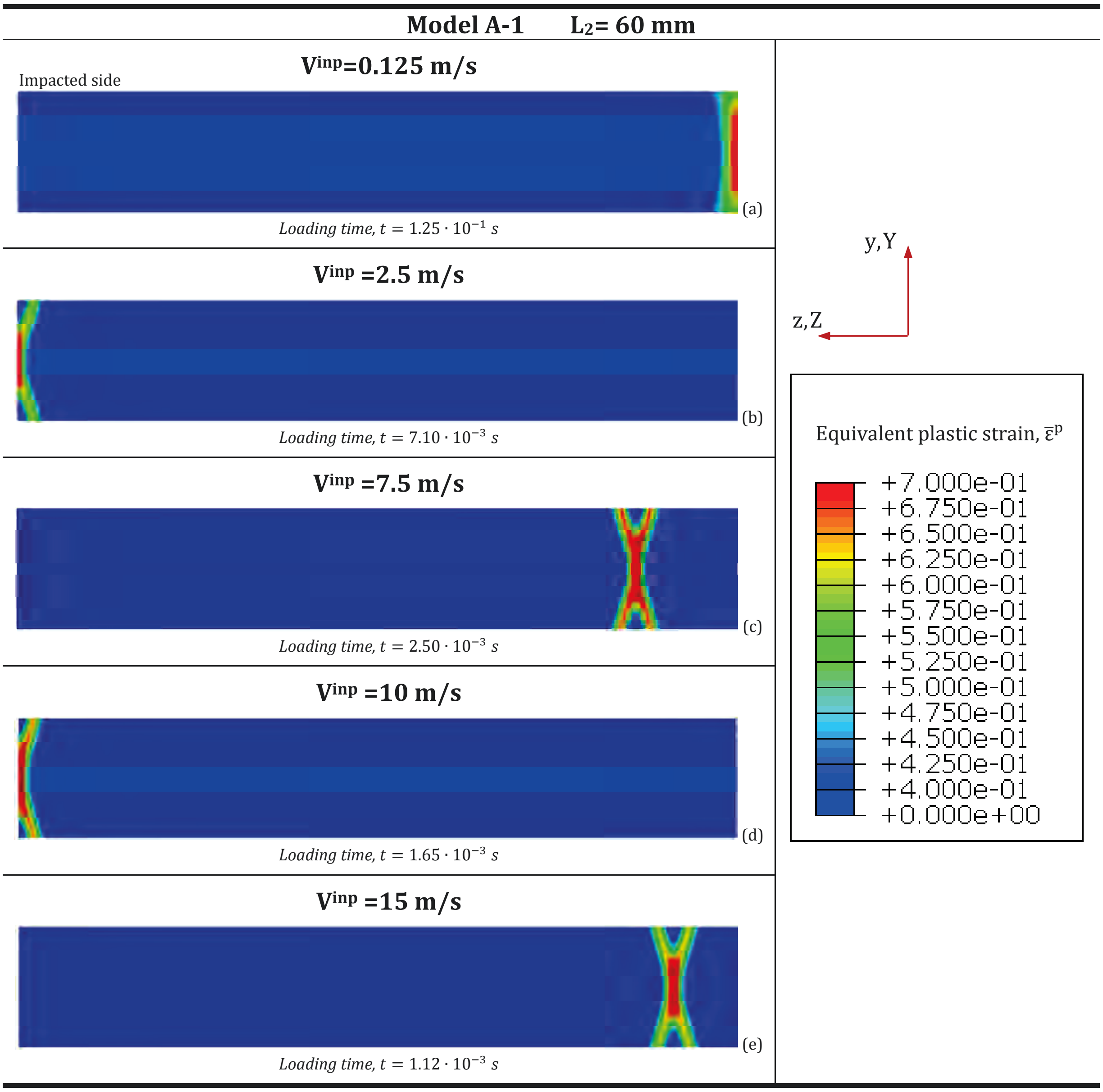

Figure 7.2: Finite element results. Model A-1. Contours of equivalent plastic strain $\bar{\varepsilon}^p$ in the Lagrangian configuration (undeformed shape) for $L_2 = 60\ mm$ and various impact velocities. (a) $V^{inp} = 0.125\ m/s$, (b) $V^{inp} = 2.5\ m/s$, (c) $V^{inp} = 7.5\ m/s$, (d) $V^{inp} = 10\ m/s$ and (e) $V^{inp} = 15\ m/s$.

of the gauge length on the location of flow localization has been found for all the applied velocities investigated within the range $0.125\ m/s \lesssim V^{inp} \lesssim 80\ m/s$ (below the CIV).

Moreover, it has to be highlighted that the case $L_2 = 100\ mm$ shown in Fig. 7.3 is a transient state, halfway between the localization pattern of $L_2 = 80\ mm$ and $L_2 = 140\, mm$. As such, it reveals the nature of the role played by the sample length in the location of flow localization. We recall here that the gauge length determines the time required by the elastic strains to travel over the whole gauge and, as such, it controls the processes of reflection and interaction of stress waves which dictates the locations where the build up of plastic deformation occurs. These results shall be understood as an additional proof of the deterministic character of the flow localization in the dynamic tensile test.

It is a fact that, because of a number of reasons already discussed in previous section, our calculations do not predict the specific location of flow localization observed in the experiments (qualitative agreement, quantitative disagreement), see Fig. 6.8 in chapter 6. Nevertheless, we hold that they help to provide a proper interpretation of our experimental findings and contribute to reveal the key mechanisms which reside behind the interplay between the gauge length and the fracture location.

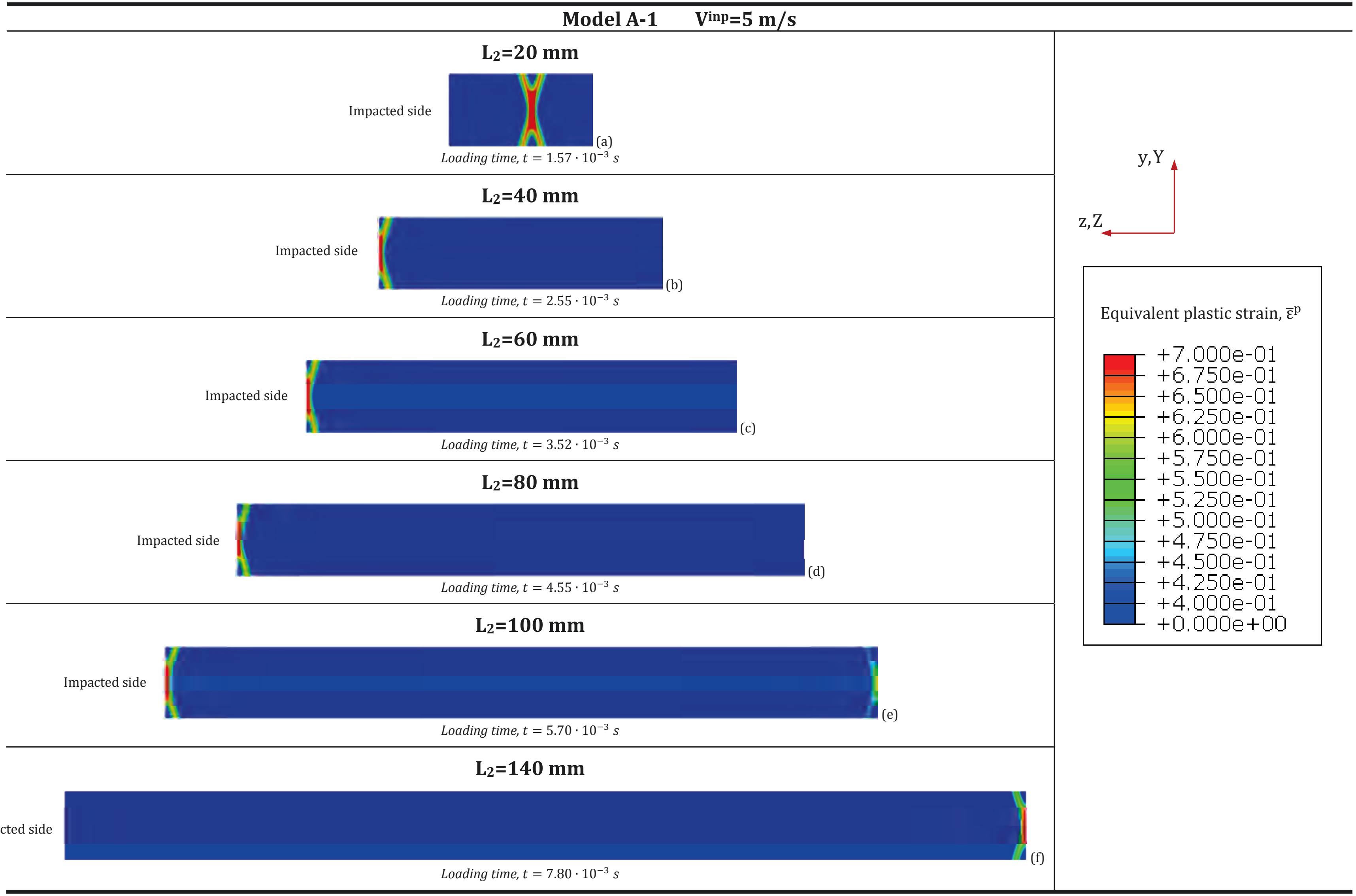

Figure 7.3: Finite element results. Model A-1. Contours of equivalent plastic strain $\bar{\varepsilon}^p$ in the Lagrangian configuration (undeformed shape) for $V^{inp} = 5 m/s$ and various gauge lengths. (a) $L_2 = 20\ mm$, (b) $L_2 = 40\ mm$, (c) $L_2 = 60\ mm$, (d) $L_2 = 80\ mm$, (e) $L_2 = 100\ mm$ and (f) $L_2 = 140\ mm$.

7.2.3 Multiple localization pattern

In this section we aim at uncovering the role played by the initial conditions, the boundary conditions and the sample slenderness on the formation of multiple localization patterns. The way in which these factors either favour or preclude the emergence of multiple necking bands has been hardly investigated in the literature [112], thus we intend to give some indications about it here.

Fig. 7.4 shows contours of equivalent strain rate in Eulerian (deformed shape) configuration for $V^{inp} = 5\ m/s$ and $L_2 = 20\ mm$. The results for model A-1 are depicted in Fig. 7.4(a) while the results of model B-1 are illustrated in Fig. 7.4(b). We have determined the localization strain $\bar{\varepsilon}_l^p$ in the calculations following the procedure reported elsewhere [51, 113]. The localization strain is assumed as given by the condition $\frac{d\bar{\varepsilon}^p}{dt} = 0$, where $\bar{\varepsilon}^p$ is measured within the unloading zone which surrounds the localized region. The localization strain obtained for model A-1 is $\bar{\varepsilon}_l^p \approx 0.25$ while for model B-1 is $\bar{\varepsilon}_l^p \approx 0.34$. The retardation of flow localization registered for model B-1 is caused by the initialization of the field variables (see section 7.1) which minimizes the stress propagation phenomena, boosting mechanical equilibrium and delaying plastic localization [105]. This observation agrees with the theoretical and numerical results presented by different authors [112, 114] who showed that the stress waves disturbances represent a limiting factor for the specimen ductility.

Note that in Fig. 7.4 we show the deformed shape in order to have a clear perception of the straining of the samples during the process of plastic localization. Thus, we point out that the development of the pair of localization bands is accompanied by a substantial reduction of the width of the sample near the localization area. As shown in Fig. 6.8, such kind of localization pattern with a single pair of bands inside a necked region (local width reduction) is representative of the largest samples tested. However, it does not find correlation with the experimental failure pattern observed for $V^{inp} = 5\ m/s$ and $L_2 = 20\ mm$, for which multiple localization bands and little width reduction near the fracture location were observed (see Fig. 6.8). This mismatch between the numerical calculation and the experimental counterpart is mostly attributed to the simplicity of our finite element model which only takes into account the gauge of the sample. In the experimental sample, the fillets and the gripping sections increase the momentum of inertia of the cross section (along the Y direction). We assume that this opposes to the local width reduction near the failure point, enhancing the formation of multiple necking bands. This statement is confirmed with Fig. 7.5, where we show contours of equivalent strain rate for model A-2 in Fig. 7.5(a) and model B-2 in Fig. 7.5(b). As for Fig. 7.4, the loading velocity is $V^{inp} = 5\ m/s$ and the sample length is $L_2 = 20\ mm$. The Eulerian (deformed shape) configuration is depicted. The localization strain corresponding to model A-2 is $\bar{\varepsilon}_l^p \approx 0.85$ while for model B-2 the specimen never reaches the condition of full localization. Thus, we have:

- Because of the difference in the initial conditions, model A-2 shows lower ductility than model B-2.
- Because of the difference in the boundary conditions, model A-2 shows larger ductility than model A-1 and model B-2 shows larger ductility than model B-1.

Since the effect of the initial conditions in the material ductility was already discussed above, we analyse here the role played by the boundary conditions. It has to be recalled that, as described in section 7.1, the boundary conditions applied to models A-2 and B-2 are such that all the nodes located at the surfaces $\{X, \pm\frac{W}{2}, Y\}$ have identical displacement along the Y axis during the calculation (thus impeding the local width reduction of the sample). The application of such boundary conditions, which try to emulate an infinite plate along the Y direction (see section 7.1), delays flow localization and promotes the emergence of multiple localization bands. These results suggest that:

- If the metallic sheet has a large slenderness L_2/W such that it mostly behaves like a rod then: (1) flow localization is promoted and (2) a single pair of necking bands contained in the $\{X, Z\}$ plane are formed inside a necked region contained in the $\{Y, Z\}$ plane.
- If the metallic sheet shows a short slenderness L_2/W such that it mostly behaves like a plate then: (1) flow localization is delayed and (2) multiple necking bands contained in the $\{X, Z\}$ plane are formed.

In order to deepen into the previous two observations, we carry out additional numerical calculations for models A-1 and A-2 in which different values of W have

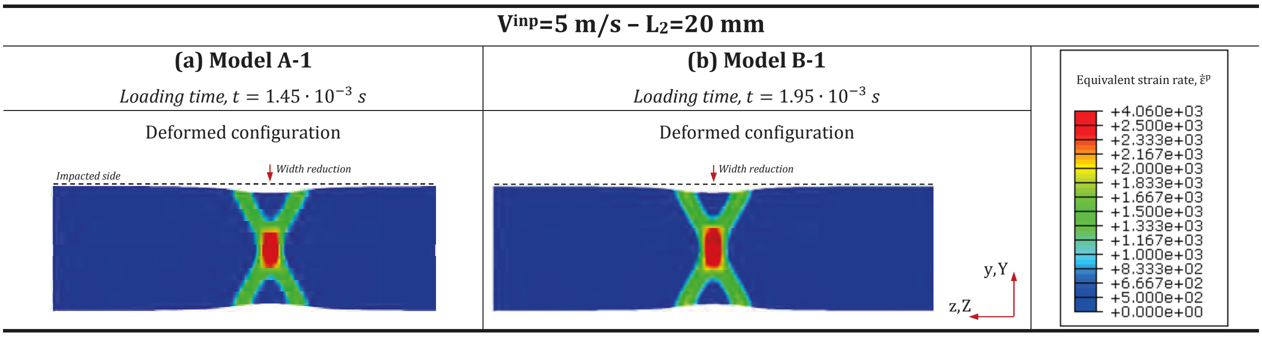

Figure 7.4: Finite element results. Contours of equivalent strain rate $\dot{\bar{\varepsilon}}^p$ in Eulerian (deformed shape) configuration for $V^{inp} = 5\ m/s$ and $L_2 = 20\ mm$. (a) Model A-1, loading time $t = 1.45 \cdot 10^{-3}\ s$. (b) Model B-1, loading time $t = 1.95 \cdot 10^{-3}\ s$.

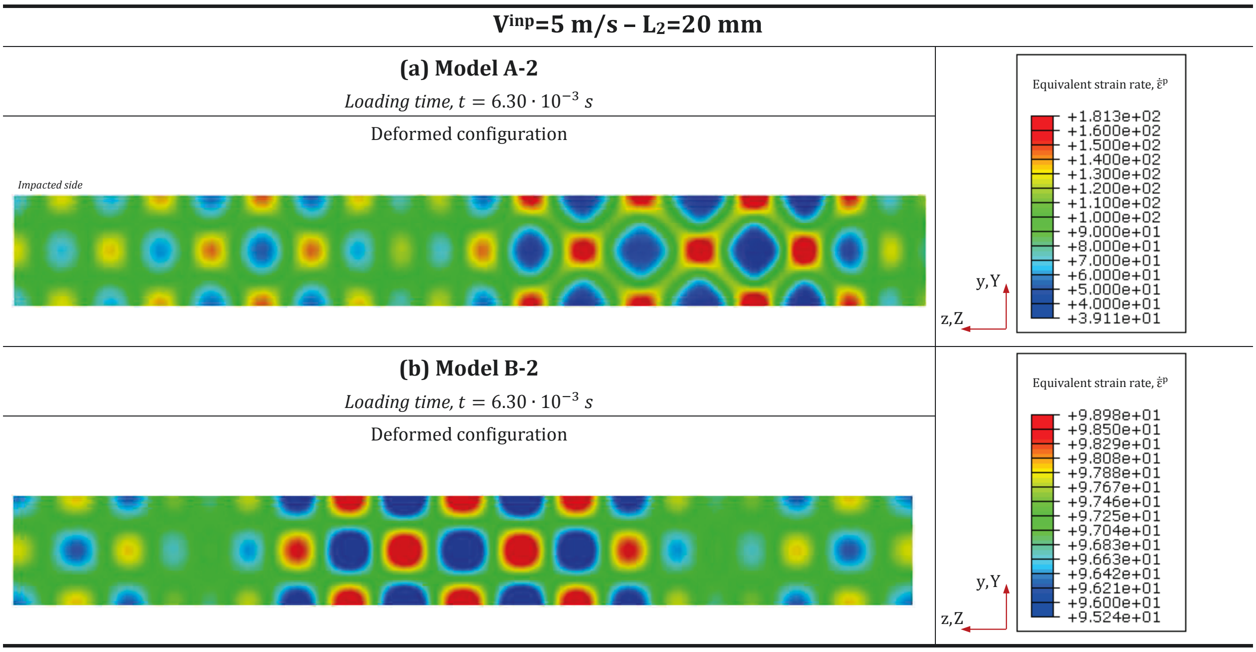

Figure 7.5: Finite element results. Contours of equivalent strain rate $\dot{\bar{\varepsilon}}^p$ in Eulerian (deformed shape) configuration for $V^{inp} = 5\ m/s$ and $L_2 = 20\ mm$. (a) Model A-2, loading time $t = 6.30 \cdot 10^{-3}\ s$. (b) Model B-2, loading time $t = 6.30 \cdot 10^{-3}\ s$.

been explored: 2 mm, 10 mm (reference width as shown in Fig. 7.1), 30 mm, 40 mm, 80 mm, 140 mm, 280 mm, 560 mm and 600 mm. In order to maintain the longitudinal inertial resistance to motion of the specimen we have used for all the computations the same applied velocity $V^{inp} = 5\ m/s$ and sample length $L_2 = 20\ mm$. Recall that for model A-1 the surfaces $\{X, \pm\frac{W}{2}, Z\}$ are free of constrains (in such a sense this configuration is representative of an experimental test) whereas for model A-2 all the nodes of the surfaces $\{X, \pm\frac{W}{2}, Z\}$ undergo the same displacement along the Y direction. Fig. 7.6 shows the localization strain

$\bar{\varepsilon}_l^p$ versus the sample slenderness L_2/W.

- Model A-1: there is a significant increase of the localization strain with the decrease of sample slenderness within the greatest values of L_2/W considered. Nevertheless, the rise of $\bar{\varepsilon}_l^p$ becomes gradually reduced as L_2/W decreases, such that within the range $L_2/W < 0.1$ the localization strain tends asymptotically to ~ 0.39. We have observed that the localization pattern evolves from a single pair of bands inside a necked region for large values of L_2/W to multiple necking bands for short values of L_2/W. This interplay between the specimen slenderness and the failure pattern finds good correlation (qualitative agreement) with the experimental trends shown in Fig. 6.8 of chapter 6.

  Note that, irrespective of the ratio L_2/W, the sample is subjected to uniaxial tension during the process of homogeneous deformation. It is only after the perturbation of the fundamental solution, within the post-uniform deformation regime (after the diffuse localization and prior to the full localization [38, 95, 115]), when samples with different aspect ratios L_2/W may behave in a different manner due to the development of stress gradients along the Y direction.

- Model A-2: the localization strain tends to infinity for the greatest values of L_2/W studied. The imposed boundary condition in the sample-surfaces $\{X, \pm\frac{W}{2}, Z\}$ does not allow to develop a necked region contained in the $\{Y, Z\}$ plane (the natural localization pattern of the samples that mostly behave like a rod, see Fig. 7.4) and the specimen ductility *virtually* tends to infinity. Finite values of the localization strain are found for $L_2/W < 2$. For this range of the ratio L_2/W the localization strain decreases non-linearly with the decrease of the sample slenderness. This drop is slowed down as L_2/W decreases, such that within the range $L_2/W < 0.1$ the localization strain tends asymptotically to ~ 0.39.

  Within the range $0.1 < L_2/W < 2$ flow localization is reached but, in comparison with the model A-1, the process requires the investment of a greater amount of external work. The sample undergoes localization but, due to the imposed boundary conditions, without following the natural pattern of the specimen. For $L_2/W < 0.1$ the imposed boundary conditions do not affect the localization process, thus models A-1 and A-2 provide very similar localization strain and failure pattern. Then, the samples with aspect ratio $L_2/W < 0.1$ can be considered, for all purposes, as infinite plates. This is further illustrated in Fig. 7.7 where, for models A-1 and A-2, we show contours of equivalent plastic strain $\bar{\varepsilon}^p$ in the Eulerian configuration (deformed shape) for $L_2 = 20\ mm$ and $W = 280\ mm$ ($L_2/W = 0.0714$). We observe that the failure pattern is now characterized, irrespective of the model selected (either A-1 or A-2), by the emergence of various necking bands contained in the $\{X, Z\}$ plane.

The finite element calculations presented in this section explain the experimental observations previously reported in section 6.2.3 of chapter 6, and illustrate the effect that the specimen slenderness and the boundary conditions have on the emergence of multiple localization patterns.

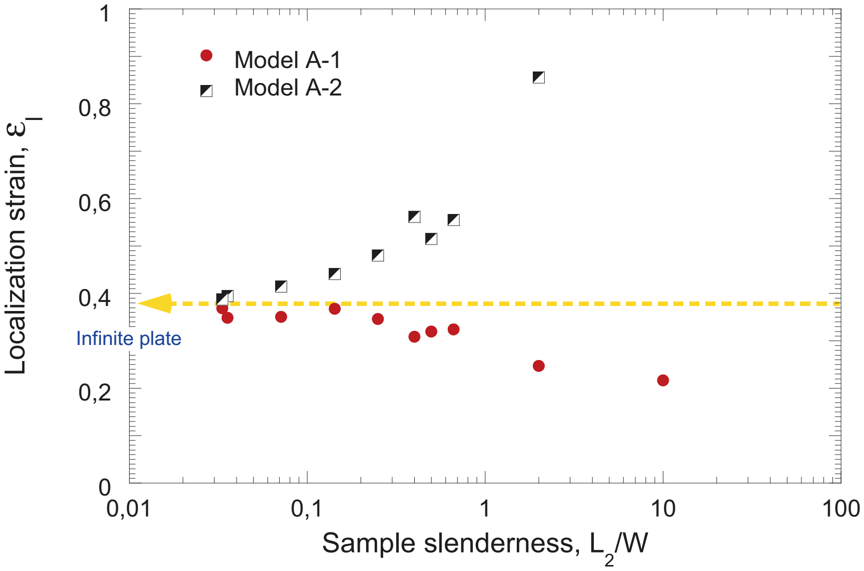

Figure 7.6: Finite element results. Models A-1 and A-2. Localization strain $\bar{\varepsilon}^p_l$ versus sample slenderness L_2/W.

Note that, while our simple geometrical models neglect the influences of the shoulders of the specimen as well as possible wave transmissions and reflections from/to the machine in the location of flow localization, they capture the essential features of the interplay between fracture location, loading velocity and sample size observed in the experiments.

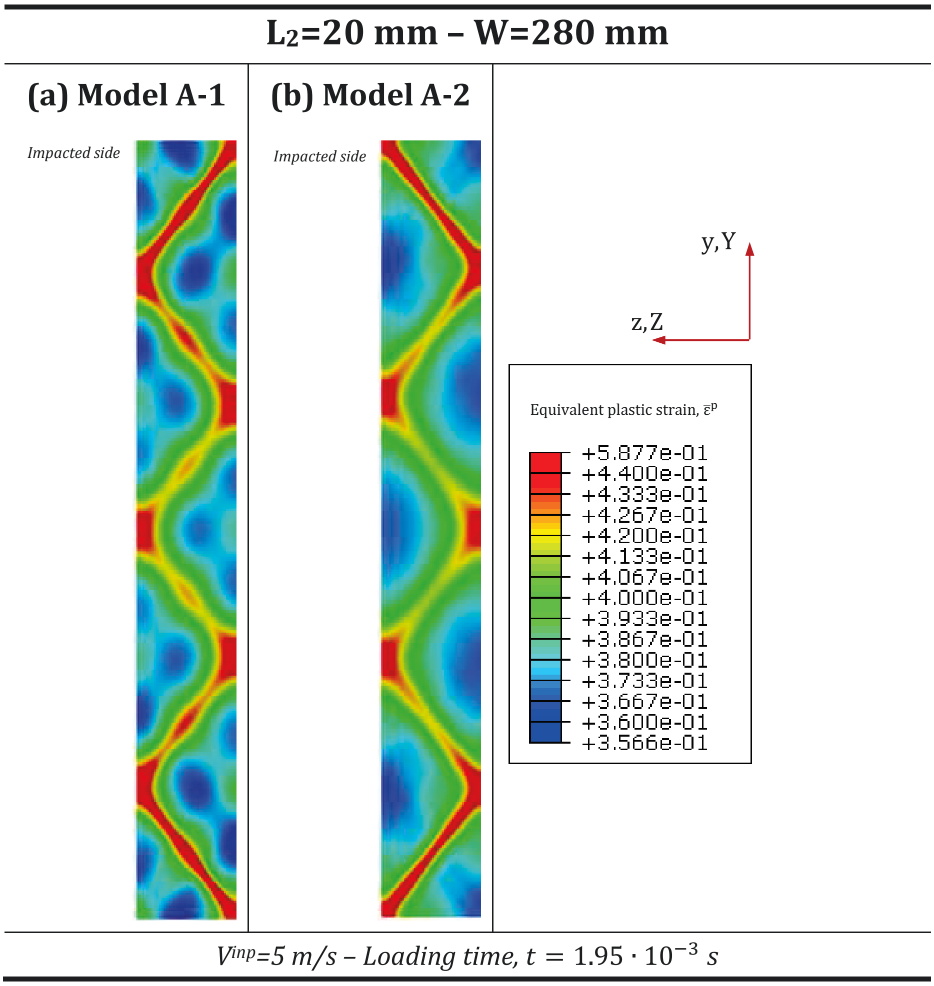

Figure 7.7: Finite element results. Contours of equivalent plastic strain $\bar{\varepsilon}^p$ in the Eulerian configuration (deformed shape) for $L_2 = 20\ mm$ and $W = 280\ mm$, i.e. $L_2/W = 0.0714$. Applied velocity $V^{inp} = 5\ m/s$, loading time $t = 1.95 \cdot 10^{-3}\ s$. (a) Model A-1. (b) Model A-2.

7.3 Discussion and conclusions

In this chapter we have carried out finite element calculations using ABAQUS/Explicit in order to rationalize the experimental findings reported in chapter 6. For that purpose, we have considered simple geometrical models which solely accounts for the gauge of the sample. Different initial and boundary conditions have been used in our modelling, leading to four distinctive numerical configurations named in section 7.1 as models A-1, A-2, B-1 and B-2.

Model A-1, for which the initial and boundary conditions are representative of a typical experimental test, has been used to check the interplay between the location of plastic strain localization, the applied velocity and the gauge length.

In qualitative agreement with the experiments, the computations predict that the location of plastic localization changes with variations in the impact velocity and the slenderness of the sample. This reinforces the idea that stress waves and inertia are main factors which control flow localization.

Moreover, the confrontation of the results obtained from models A-1, A-2, B-1 and B-2 allowed to point out two key issues. The first one refers to the increased ductility registered in the calculations for which the field variables (velocity, stress, strain and displacement) have been initialized. In agreement with different works available in the literature, we have shown that the stress waves, under specific loading conditions, may represent a limiting factor for the sample ductility. The second key issue refers to the role played by the boundary conditions in the specimen ductility and localization pattern. We have shown that the application of boundary conditions representative of an infinite plate (infinite width) to a sheet with finite width may lead to a substantial increase of the sample ductility and a strong modification of the localization pattern which (always) takes the form of multiple necking bands. From previous statement we have derived two relevant conclusions:

1. If the metallic sheet has a large slenderness such that it mostly behaves like a rod then flow localization is promoted and a single pair of necking bands contained inside a necked region are formed.
2. If the metallic sheet shows a short slenderness such that it mostly behaves like a plate then flow localization is delayed (and slow down) and multiple necking bands are formed.

8

Analysis and results: Finite differences

In this chapter we develop a simple 1D finite difference approach in MATLAB to model, relying on the experiments and finite elements presented in chapters 6 and 7, the flow localization in tensile specimens subjected to dynamic testing. The computations illustrate the intervention of wave propagation phenomena within the specimen which is responsible for the interplay between necking location, impact velocity and gauge length. We provide new computational insights into the kinetics of flow localization. In addition, we have assessed the role played by material properties, materials flaws and initial conditions in the inception of dynamic necks. The outline of the chapter is as follows: in section 8.1 we present the finite difference model and the discretization of the governing equations. In section 8.2 we carry out calculations in order to uncover the role played by stress waves disturbances in the kinetics of flow localization. For that task, we develop a comprehensive parametric analysis in which impact velocity, gauge length and material properties have been systematically varied. In addition, we assess the influence of material defects and initial conditions in the inception of dynamic necks. We show that material defects may play a secondary role in flow localization. Moreover, an specific analysis has been developed to point out the constitutive sensitivity of the dynamic tensile problem. In section 8.3 we summarize and discuss the salient features of the finite difference investigation.

8.1 1D finite difference model

We consider a cylindrical rod of length L_0 and cross-section diameter Φ subjected to dynamic stretching. Note that the experimental and finite element specimens used in chapters 6 and 7 have rectangular cross-sections. We acknowledge that the mismatch in the geometry of the cross-sections affects the post-uniform behaviour of the sample. Nevertheless, the purpose of the 1D finite difference model is not to mimic the experiments and the finite elements. Our goal is to illustrate the stress wave propagation within the sample and the kinetics of flow localization. To accomplish this objective, our 1D approach is a reliable and simple choice, as shown in section 8.2 of this chapter.

Remark 8.1. Let us point that the length L_0 of the cylindrical rod is equivalent to the specimen gauge length L_2 as it was defined in chapter 7.

8.1.1 Problem formulation

The problem is formulated in the Lagrangian configuration, using the 1D form of the initial boundary value problem posed in chapter 5. The relation between the Eulerian z and the Lagrangian coordinate Z ($0 \leq Z \leq L_0$) is given by:

$$z = Z + U_Z \tag{8.1}$$

For simplicity, from this point on the displacement along the axial direction U_Z will be denoted by U. The logarithmic strain and strain rate along the axial direction are given by:

$$\varepsilon_Z = \ln\left(\lambda_Z\right) = \ln\left(1 + \frac{\partial U}{\partial Z}\right) \tag{8.2}$$

$$\dot{\varepsilon}_Z = \frac{\partial \varepsilon}{\partial t} \tag{8.3}$$

where $\lambda_Z = \frac{\partial z}{\partial Z}$ is the axial stretch.

The fundamental equations, formulated in Lagrangian coordinates, which govern the loading process are given below.

1. Kinematic relation
$$V = \frac{\partial U}{\partial t} \tag{8.4}$$
where $V = V_Z$ is the axial velocity of the material particles.
2. Balance equations
   - Balance of mass or continuity equation:
$$\rho_0 = \rho J \tag{8.5}$$
   - Balance of linear momentum:
$$\rho_0 \Lambda_0 \frac{\partial^2 U}{\partial t^2} = \frac{\partial}{\partial Z}\left(\frac{\Lambda}{\mathrm{J}}\tau_Z\right) \tag{8.6}$$
     where Λ_0 and Λ are the reference and current cross-section areas of the bar and τ_Z is the Kirchhoff stress along the axial direction. Hereinafter τ_Z will be denoted by τ.
3. Thermodynamic framework:
$$\rho C_p \frac{\partial T}{\partial t} = k \frac{\partial^2 T}{\partial Z^2} + \beta \tau d_Z^p \tag{8.7}$$
4. Constitutive equations: hypoelastic and hyperelastic-based models are considered.
   - Hypoelastic-based model:
$$\dot{\tau} = \varrho \left[\dot{\varepsilon}_Z + 2\dot{\varepsilon}_R\right] + 2\mathrm{G}\dot{\varepsilon}_Z \tag{8.8}$$
   - Hyperelastic-based model:
$$\tau = \varrho \left[\varepsilon_Z + 2\varepsilon_R\right] + 2\mathrm{G}\varepsilon_Z \tag{8.9}$$
     where ε_R and $\dot{\varepsilon}_R$ are the radial strain and strain rate, respectively.

5. Initial conditions: the solid is initially at rest and unloaded, unless otherwise noted, see section 8.2.5

$$
\begin{aligned}
&U(Z,0)=0 \quad V(Z,0)=0 \quad \tau(Z,0)=0 \\
&\rho(Z,0)=\rho_0 \quad T(Z,0)=T_0
\end{aligned} \tag{8.10}
$$

6. Boundary conditions: note that the domain of the solid is $0 \leq Z \leq L_0$
   - Mechanical boundary conditions:

$$
U(0,t)=0 \quad V(L_0,t)=V^{\mathrm{inp}} \tag{8.11}
$$

   - Thermal boundary conditions:

$$
\frac{\partial T\,(0,t)}{\partial Z}=\frac{\partial T\,(L_0,t)}{\partial Z}=0 \tag{8.12}
$$

8.1.2 Numerical scheme

Relying on the seminal work of Regazzoni et al. [42], we develop a simple finite difference model to solve the set of equations presented above. Our explicit numerical approach lies within the spirit of the scheme recently developed by Kudryashov et al. [116] to investigate the onset and development of shear bands in metallic solids subjected to dynamic loading. In order to construct our numerical solution, we introduce the rectangular grid depicted in Fig. 8.1 such that $\Pi=\{Z_j=j\Delta Z,\ t^n=n\Delta t\}$, where $j=0,\ldots,M$ and $n=0,\ldots,N$. The integration space and time steps are $\Delta Z=L_0/M$ and Δt respectively. Further details about the finite difference scheme are provided in Appendix F.

We introduce the following notations of functions in the grid nodes $g\,(Z_j,t^n)=g_j^n$. For the first derivative of the functions g with respect to the Lagrangian coordinate Z we have used a central difference discretization which leads to the following second order accuracy approximation:

$$
\frac{\partial g}{\partial Z}=\frac{g_{j+1}^n-g_{j-1}^n}{2\Delta Z} \tag{8.13}
$$

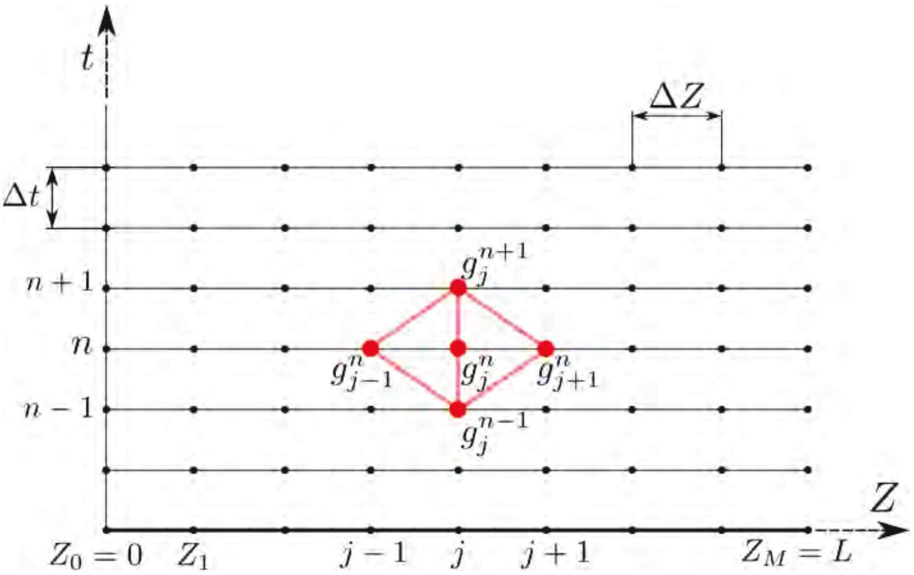

Figure 8.1: Finite difference model. Grid on time-space domain.

Then, the second derivative with respect to the coordinate Z is given by:

$$\frac{\partial^2 g}{\partial Z^2} = \frac{g_{j+1}^n - 2g_j^n + g_{j-1}^n}{\Delta Z^2} \tag{8.14}$$

For the first order derivative of the functions g with respect to the time t we have used a classical forward difference discretization which leads to the following first order accuracy approximation:

$$\frac{\partial g}{\partial t} = \frac{g_j^{n+1} - g_j^n}{\Delta t} \tag{8.15}$$

Thus, the second derivative with respect to time t is given by:

$$\frac{\partial^2 g}{\partial t^2} = \frac{g_j^{n+1} - 2g_j^n + g_j^{n-1}}{\Delta t^2} \tag{8.16}$$

Fig. 8.2 shows a flow chart which illustrates the numerical scheme. The goal is to express the balance principles in terms of the axial displacement of the material particles U. For that task, we carry out the spatio-temporal discretization of the governing equations and apply the initial and boundary conditions. The discretized problem is solved explicitly. The updated displacement field along the bar U^{n+1} is obtained using the current (known) values U^n. Once the displacement field is computed we calculate the updated strain and strain increment tensors. The strain increment tensor is the field variable which connects the kinematics with the constitutive equations. Once the strain increment tensor is computed, we apply the radial return algorithm to update the stress.

Remark 8.2. The key point of the finite difference model is that we solve the kinematics of the problem. This gives us a complete understanding of the physical mechanisms which control the deformation of dynamic tensile specimens. This is a salient feature of this Doctoral Research and a major advantage over the commercial numerical codes.

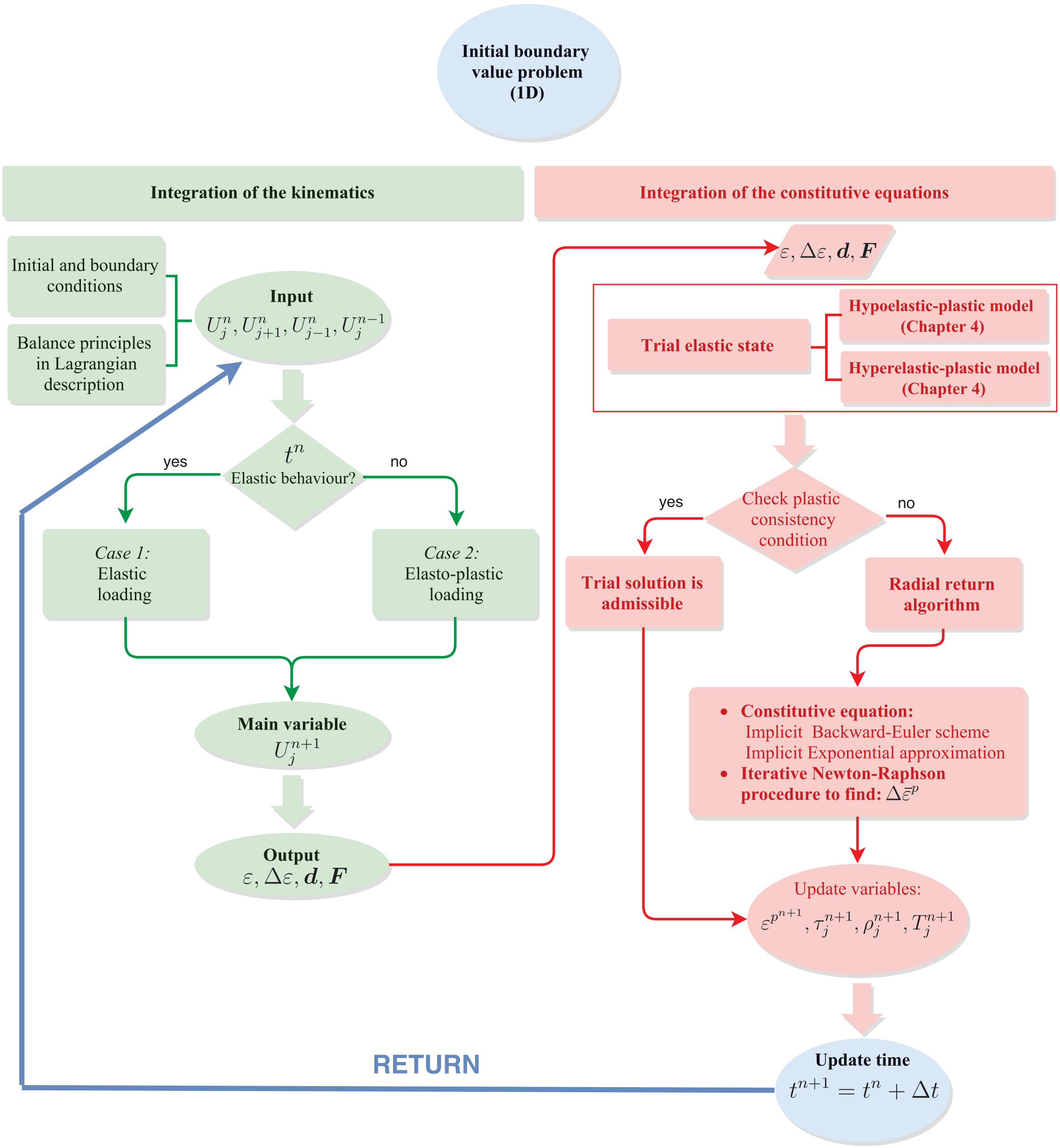

Figure 8.2: Flow chart which illustrates the numerical scheme.

Integration of the kinematics

We rewrite Eq. (8.6) using the divergence properties in the right hand side of the expression to obtain:

$$\rho_0 \Lambda_0 \frac{\partial^2 U}{\partial t^2} = \mathrm{Div}\left(\frac{\Lambda}{J}\tau\right) = \mathrm{Div}\left(\frac{\rho}{\rho_0}\Lambda\tau\right) = \frac{1}{\rho_0}\mathrm{Div}\left(\rho\Lambda\tau\right) \tag{8.17}$$

where Eq. (8.5) has been used. Moreover, application of the chain rule properties gives:

$$\begin{aligned}&\frac{1}{\rho_0}\mathrm{Div}\left(\rho\Lambda\tau\right)=\frac{1}{\rho_0}\left[\rho\mathrm{Div}\left(\Lambda\tau\right)+\Lambda\tau\mathrm{Grad}\left(\rho\right)\right]\\&=\frac{1}{\rho_0}\left[\rho\tau\mathrm{Grad}\left(\Lambda\right)+\rho\Lambda\mathrm{Div}\left(\tau\right)+\Lambda\tau\mathrm{Grad}\left(\rho\right)\right]\end{aligned}\tag{8.18}$$

Previous expression is inserted into Eq. (8.17) to obtain:

$$\frac{\partial^2 U}{\partial t^2}=\frac{1}{\rho_0}\left[\frac{\rho}{\rho_0}\tau\frac{\mathrm{Grad}\Lambda}{\Lambda_0}+\frac{\rho}{\rho_0}\frac{\Lambda}{\Lambda_0}\mathrm{Div}\tau+\frac{\Lambda}{\Lambda_0}\frac{\mathrm{Grad}\rho}{\rho_0}\tau\right]\tag{8.19}$$

Where, in a one-dimensional approach, we have that:

$$\mathrm{Grad}\Lambda=\frac{\partial\Lambda}{\partial Z},\quad \mathrm{Grad}\rho=\frac{\partial\rho}{\partial Z},\quad \mathrm{Div}\tau=\frac{\partial\tau}{\partial Z}$$

In order to proceed with the discretization, we need to consider two different scenarios in the displacements update: (1) In the previous time step the material showed purely elastic behaviour and (2) in the previous time step the material deformed elasto-plastically.

1. **Case 1: Elastic loading**

   The current area Λ is calculated as a function of the Lagrangian coordinate Z assuming that the solid is subjected to elastic loading:

   $$\Lambda=\Lambda_0\left(1+\frac{\partial U}{\partial Z}\right)^{-2\nu}\tag{8.20}$$

   Moreover, the one-dimensional Hencky's elastic law is:

$$\begin{aligned}\tau &= \mathrm{E}\cdot\ln\left(\lambda_Z\right) = \mathrm{E}\cdot\ln\left(\lambda_Z^e\lambda_Z^p\right) = \\ &= \mathrm{E}\left[\ln\left(\lambda_Z\right) - \ln\left(\lambda_Z^p\right)\right] = \mathrm{E}\left[\ln\left(1+\frac{\partial U}{\partial Z}\right) - \varepsilon_Z^p\right] \qquad (8.21)\end{aligned}$$

where we have considered the multiplicative decomposition of the axial stretch into the elastic and plastic components. While this assumption is typical of hyperelastic approaches, it is not contrary to any postulate of the hypoelastic-based models. In fact, the multiplicative decomposition of the stretch can be derived from the *standard* additive decomposition of the rate of deformation tensor **d**.

Then, Eqs. (8.20) and (8.21) are inserted into Eq. (8.19) to obtain the following expression:

$$\begin{aligned}\frac{\partial^2 U}{\partial t^2} = \mathrm{c}_0^2\cdot\left[1+\frac{\partial U}{\partial Z}\right]^{-2\nu}\cdot\left[\frac{\rho}{\rho_0}\left[\left[\frac{\frac{\partial^2 U}{\partial Z^2}}{1+\frac{\partial U}{\partial Z}}\right]\left[1-2\nu\left[\ln\left(1+\frac{\partial U}{\partial Z}\right)-\varepsilon_Z^p\right]\right]-\right.\right. \\ \left.\left. -\frac{\partial \varepsilon_Z^p}{\partial Z}\right] + \left[\ln\left(1+\frac{\partial U}{\partial Z}\right)-\varepsilon_Z^p\right]\frac{1}{\rho_0}\frac{\partial \rho}{\partial Z}\right] \qquad (8.22)\end{aligned}$$

where $\mathrm{c}_0 = \sqrt{\dfrac{E}{\rho_0}}$ is the one-dimensional elastic wave speed expressed as a function of the initial density.

Following the discretization scheme defined by Eqs. (8.13)–(8.16), Eq. (8.22) leads to an expression which allows to calculate the updated axial displacement as follows:

$$\begin{aligned}U_j^{n+1} = {} & [\mathrm{c}_0 \Delta t]^2 \left[\frac{2\Delta Z + U^n_{j+1} - U^n_{j-1}}{2\Delta Z}\right]^{-2\nu} \Bigg[\frac{\rho^n_j}{\rho_0} \Bigg[\Bigg[\frac{2\left(U^n_{j+1} - 2U^n_j + U^n_{j-1}\right)}{\Delta Z\left(2\Delta Z + U^n_{j+1} - U^n_{j-1}\right)}\Bigg] \Bigg[1- \\ & -2\nu \Bigg[\ln\left(\frac{2\Delta Z + U^n_{j+1} - U^n_{j-1}}{2\Delta Z}\right) - (\varepsilon^p_Z)^n_j\Bigg]\Bigg] - \left(\frac{(\varepsilon^p_Z)^n_{j+1} - (\varepsilon^p_Z)^n_{j-1}}{2\Delta Z}\right)\Bigg] + \\ & + \frac{1}{\rho_0}\left(\frac{\rho^n_{j+1} - \rho^n_{j-1}}{2\Delta Z}\right)\Bigg[\ln\left(\frac{2\Delta Z + U^n_{j+1} - U^n_{j-1}}{2\Delta Z}\right) - (\varepsilon^p_Z)^n_j\Bigg]\Bigg] + \\ & + 2U^n_j - U^{n-1}_j \end{aligned} \tag{8.23}$$

2. **Case 2: Elasto-plastic loading**

   Relying on the incompressibility of the plastic flow, we can express the relation between the current area Λ and the Lagrangian coordinate Z as:

$$\Lambda = \Lambda_0 \left(1 + \frac{\partial U}{\partial Z}\right)^{-1} \tag{8.24}$$

   Then, Eqs. (8.21) and (8.24) are inserted into Eq. (8.19) to obtain the following expression:

$$\begin{aligned}\frac{\partial^2 U}{\partial t^2} = {} & \mathrm{c}_0^2 \cdot \left[1 + \frac{\partial U}{\partial Z}\right]^{-1} \cdot \Bigg[\frac{\rho}{\rho_0}\Bigg[\Bigg[\frac{\frac{\partial^2 U}{\partial Z^2}}{1 + \frac{\partial U}{\partial Z}}\Bigg]\Bigg[1 - \Bigg[\ln\left(1 + \frac{\partial U}{\partial Z}\right) - \varepsilon^p_Z\Bigg]\Bigg] - \\ & - \frac{\partial \varepsilon^p_Z}{\partial Z}\Bigg] + \Bigg[\ln\left(1 + \frac{\partial U}{\partial Z}\right) - \varepsilon^p_Z\Bigg] \frac{1}{\rho_0}\frac{\partial \rho}{\partial Z}\Bigg]\end{aligned} \tag{8.25}$$

   Following the discretization scheme defined by Eqs. (8.13)–(8.16), expression (8.25) leads to an equation which allows to calculate the updated axial displacement as follows:

$$\begin{aligned} U_j^{n+1} = {} & [\mathrm{c}_0 \Delta t]^2 \left[\frac{2\Delta Z + U_{j+1}^n - U_{j-1}^n}{2\Delta Z}\right]^{-1} \left[\frac{\rho_j^n}{\rho_0} \left[\left[\frac{2\left(U_{j+1}^n - 2U_j^n + U_{j-1}^n\right)}{\Delta Z\left(2\Delta Z + U_{j+1}^n - U_{j-1}^n\right)}\right] \left[1 - \right.\right.\right. \\ & \left.\left. - \left[\ln\left(\frac{2\Delta Z + U_{j+1}^n - U_{j-1}^n}{2\Delta Z}\right) - (\varepsilon_Z^p)_j^n\right]\right] - \left(\frac{(\varepsilon_Z^p)_{j+1}^n - (\varepsilon_Z^p)_{j-1}^n}{2\Delta Z}\right)\right] + \\ & \left. + \frac{1}{\rho_0}\left(\frac{\rho_{j+1}^n - \rho_{j-1}^n}{2\Delta Z}\right)\left[\ln\left(\frac{2\Delta Z + U_{j+1}^n - U_{j-1}^n}{2\Delta Z}\right) - (\varepsilon_Z^p)_j^n\right]\right] + \\ & + 2U_j^n - U_j^{n-1} \end{aligned} \tag{8.26}$$

Whether the case I or the case II is selected for the first time step depends on the applied velocity V^{inp}. If $\rho_0 c_0 V^{inp} < A$, the impact initially induces only elastic strains in the bar (note that A defines the initial yield stress of the material in Eq. (4.7)) and the case I is selected. If $\rho_0 c_0 V^{inp} \geq A$ the applied velocity induces instantaneous plastic strains in the solid and we take the case II. Moreover, the distinction between cases 1 and 2 is critical to capture the unloading behaviour in the bar.

The stability of the integration procedure is determined by Eqs. (8.23) and (8.26). According to Kudryashov et al. [116], the numerical scheme is sustainable under the Courant-Friedrisch-Lewy condition:

$$\Delta t \leq \min\left(\frac{\Delta Z}{c_0}\right) \tag{8.27}$$

Integration of the constitutive equations

Next, we show the integration procedure of the constitutive equation. We use 1D forms of the schemes detailed in sections 4.2.2 and 4.3.2 for hypoelastic-based and hyperelastic-based materials, respectively.

- Hypoelastic-plastic model

  Within a one-dimensional framework the rotation tensor R turns into the identity matrix and the spin tensor is $\boldsymbol{\Omega} = 0$. Thus, the Green-Naghdi stress rate turns into a simple time derivative:

  $$\boldsymbol{\tau}^{\nabla} = \dot{\tau} \tag{8.28}$$

The stress is updated as follows:

$$\tau^{n+1} = \tau_{\text{trial}}^{n+1} - 2\text{G}\Delta\bar{\varepsilon}^{p} \tag{8.29}$$

where the trial stress is:

$$\tau_{\text{trial}}^{n+1} = \tau^{n} + \varrho\left[\Delta\varepsilon_Z + 2\Delta\varepsilon_R\right] + 2\text{G}\Delta\varepsilon_Z \tag{8.30}$$

where $\Delta\varepsilon_Z$ and $\Delta\varepsilon_R$ are the longitudinal and radial strain increments, respectively. Moreover, the updated equivalent stress takes the form:

$$\bar{\tau}^{n+1} = \bar{\tau}_{\text{trial}}^{n+1} - 3\text{G}\Delta\bar{\varepsilon}^{p} \tag{8.31}$$

- Hyperelastic-plastic model

  The stress is updated as follows:

$$\tau^{n+1} = \tau_{\text{trial}}^{n+1} - 2\text{G}\Delta\bar{\varepsilon}^{p} \tag{8.32}$$

where the trial stress is:

$$\tau_{\text{trial}}^{n+1} = \mathcal{L} : \varepsilon_{\text{trial}}^{e^{n+1}} = \varrho\left[\varepsilon_Z + 2\varepsilon_R\right] + 2\text{G}\varepsilon_Z \tag{8.33}$$

where ε_Z and ε_R are the longitudinal and radial strains, respectively. Moreover, the updated equivalent stress takes the form:

$$\bar{\tau}^{n+1} = \bar{\tau}_{\text{trial}}^{n+1} - 3\text{G}\Delta\bar{\varepsilon}^{p} \tag{8.34}$$

Remark 8.3. The definition of the trial stress is the main difference between the integration procedures of the hypoelastic-plastic and hyperelastic-plastic models.

Irrespective of the constitutive model, the equation of temperature evolution, Eq. (8.7), is approximated by the following expression which allows to update the temperature of the material as a function of the Lagrangian coordinate:

$$T_j^{n+1} = \frac{k\Delta t}{\rho C_p}\left[\frac{\left(T_{j+1}^n - 2T_j^n + T_{j-1}^n\right)}{\left(\Delta Z\right)^2}\right] + \frac{\beta}{\rho C_p}\bar{\tau}^{n+1}\Delta\bar{\varepsilon}^p + T_j^n \tag{8.35}$$

In order to obtain the updated stress and temperature, we calculate the equivalent plastic strain increment $\Delta\bar{\varepsilon}^p$ following the radial return algorithm described in section 4.2.2.

8.2 Analysis and results

Remark 8.4. Unless otherwise noted, the results presented in this chapter are obtained using the hypoelastic-plastic model and the material parameters reported in Table 7.1.

First of all, we validate the predictions of the finite difference model and assess the converge of the numerical solution. Fig. 8.3 shows the normalized axial force $\bar{F} = F/\Lambda_0$ as a function of the loading time t for various finite difference computations conducted with four different mesh densities: 200, 300, 400 and 500 nodes. The time step is $\Delta t = 10^9\ s$, the impact velocity $V^{inp} = 5\ m/s$, the specimen gauge length $L_0 = 20\ mm$ and the cross-section diameter $\Phi = 3\ mm$. The values of the gauge length and the applied velocity are consistent with the experiments of chapter 4. A comparison with a finite element calculation performed under the same loading conditions is presented. Those results indicate that:

1. The predictions of the finite differences scheme are largely insensitive to the mesh density during the process of homogeneous deformation (constant force). On the contrary, the difference becomes noticeable if we focus on the necking growth rate (rate of decay of the force). In this regard, we note that increasing the number of nodes from 200 to 500 seems to lead to a gradual convergence of the results such that the disagreement between $M = 400$ and $M = 500$ turns to be very small. Thus, we take 500 nodes as the reference mesh density for this sample size. Note that this combination of mesh density and time step fulfils the stability condition given by Eq. (8.27).

2. The predictions of the finite difference scheme (from now on we focus the attention on the reference configuration $M = 500$) are largely similar to the finite element calculation during the process of homogeneous deformation. This validates our finite difference model. On the other hand, the rate of decay of the force is much steeper in the case of the finite difference computation. The finite difference scheme is not able to capture the mechanisms which control the post-uniform elongation of the rod. Our belief is that this behaviour is caused by the one-dimensional nature of the numerical model which does not consider the stabilizing effect of stress triaxiality in the necking development.

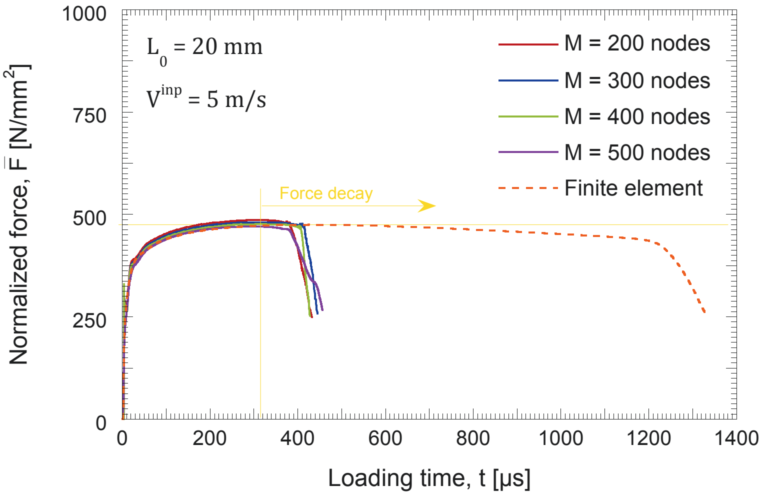

Figure 8.3: Normalized axial force $\bar{F}$ as a function of the loading time t. The gauge length is $L_0 = 20\ mm$ and the impact velocity $V^{inp} = 5\ m/s$. The cross-section diameter is $\Phi = 3\ mm$. The nominal strain rate is $\dot{\varepsilon}_0 = 250\ s^{-1}$. Finite difference results for various mesh densities: $M = 200$, $M = 300$, $M = 400$, $M = 500$. Comparison with a finite element simulation.

Next, we show some additional results obtained from the finite difference model. The goal is to illustrate the ability of our numerical approach to capture the intervention of stress wave propagation within the sample. Figs. 8.4, 8.5 and 8.6 show various field variables along the normalized axial coordinate $\bar{Z} = Z/L_0$ for three different loading times.

Fig. 8.4 corresponds to an early time of the loading process $t = 2.5\ \mu s$. The normalized force $\bar{F}$, the Cauchy stress σ, the axial velocity V, the axial elastic strain ε_Z^e, the axial plastic strain ε_Z^p and the axial plastic strain rate $\dot{\varepsilon}_Z^p$ are shown in Figs. 8.4(a), 8.4(b), 8.4(c), 8.4(d), 8.4(e) and 8.4(f), respectively. The stress wave induced by the sudden application of the impact velocity travels along the bar from the right (impacted end) to the left side (clamped end). A portion of the rod is still unloaded. Since $\rho_0 c_0 V^{inp} < A$ the impact initially induces only elastic strains in the bar. The axial plastic strain ε_Z^p and the axial plastic strain rate $\dot{\varepsilon}_Z^p$ are zero.

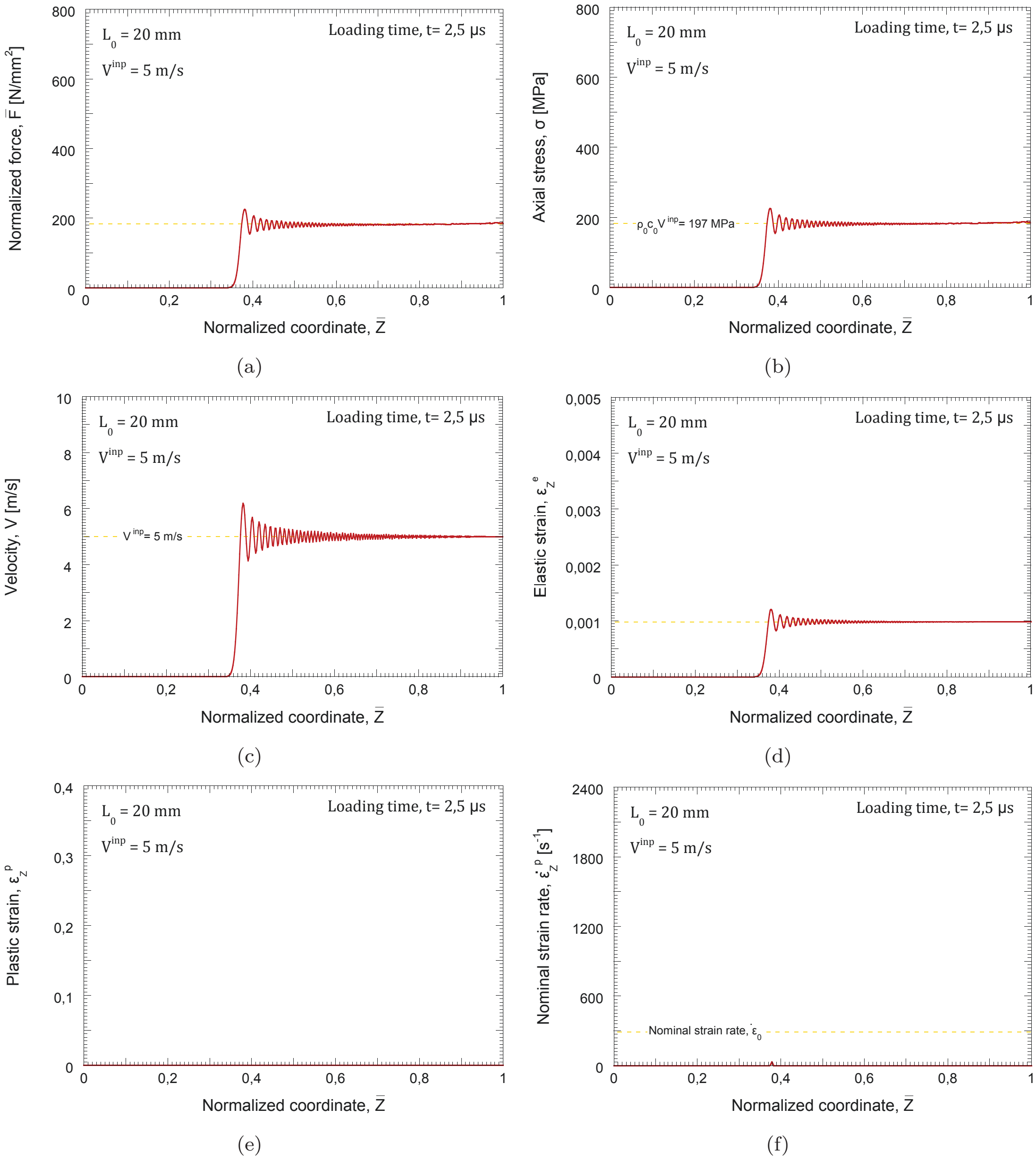

(a) (b) (c) (d) (e) (f)

Figure 8.4: Various field variables as a function of the normalized coordinate $\bar{Z} = \frac{Z}{L_0}$. The impact velocity is $V^{inp} = 5\ m/s$ and the gauge length $L_0 = 20\ mm$. A loading time of $t = 2.5\ \mu s$ is selected.

Fig. 8.5 corresponds to $t = 97\ \mu s$. The stress waves have already travelled along the entire bar several times. Nevertheless, in Figs. 8.5(a) and 8.5(b) we observe that the force and the stress are not uniform. In addition, in Fig. 8.5(c) we illustrate that the velocity does not have a linear profile. These *perturbations* in the field variables caused by the wave propagation phenomena are responsible for necking inception. While the profile of the elastic strain shown in Fig. 8.5(d) is largely constant, we observe incipient plastic strain and plastic strain rate localizations in Figs. 8.5(e) and 8.5(f).

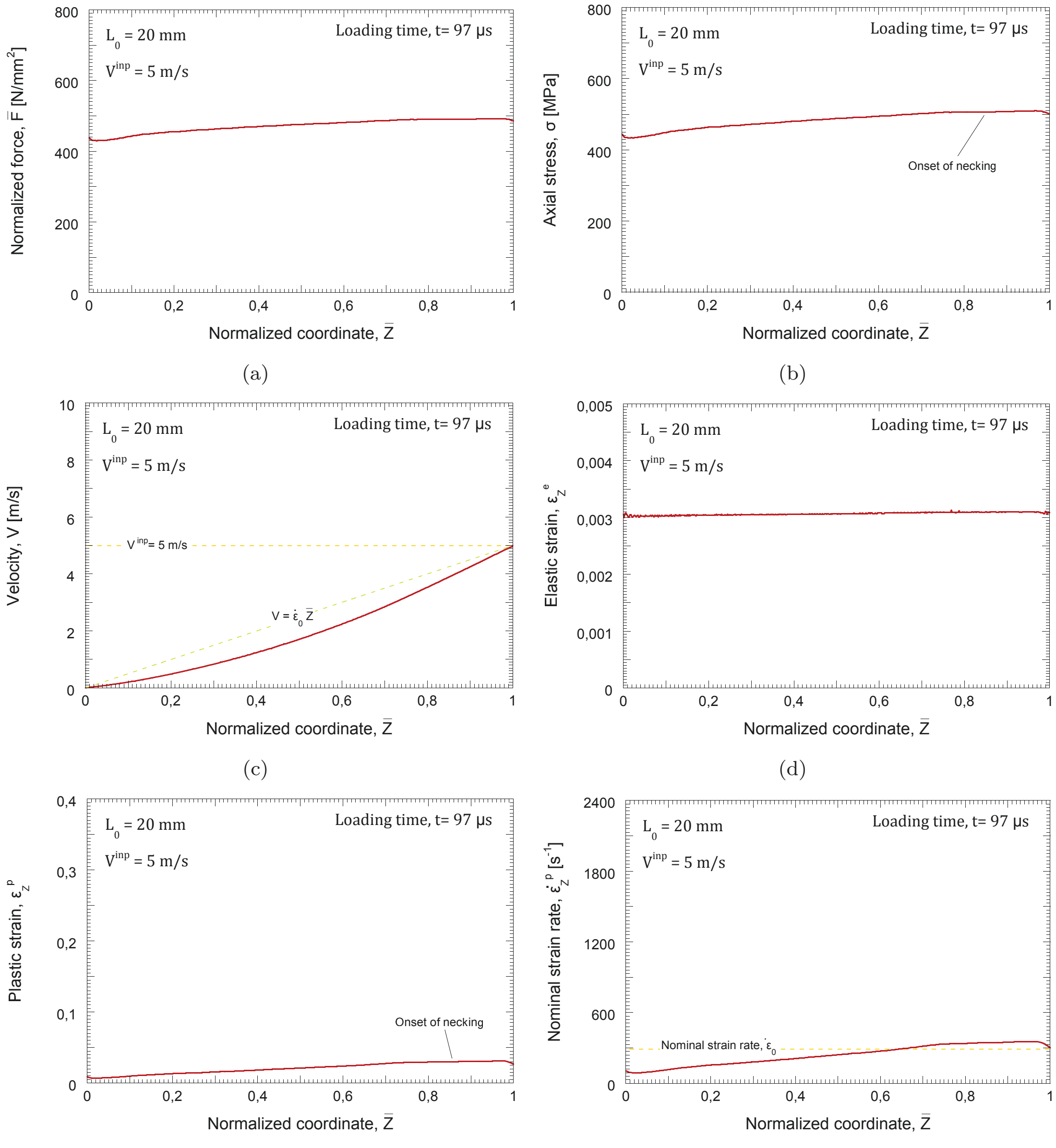

(a) (b)

(c) (d)

(e) (f)

Figure 8.5: Various field variables as a function of the normalized coordinate $\bar{Z} = \frac{Z}{L_0}$. The impact velocity is $V^{inp} = 5\ m/s$ and the gauge length $L_0 = 20\ mm$. A loading time of $t = 97\ \mu s$ is selected.

Fig. 8.6 corresponds to $t = 369.5\ \mu s$. This is a late time of the loading process which shows a *fully developed* neck. In Figs. 8.6(a) and 8.6(b) we observe excursions of force and stress which evidence the flow localization process. Outside the localized area, the model predicts (according to the experimental evidence reported in the literature, see Wang and Tong [117]) an incipient drop in the force. Fig. 8.6(c) shows a discontinuity in the velocity profile induced by the necking development. As discussed by Bonnet-Lebouvier et al. [118] and Rodríguez-Martínez et al. [119], the flow localization is accompanied by a significant variation of the kinetic energy of the solid. The discontinuity in the velocity profile, i.e. the variation of the kinetic energy, reflects the intrinsic dynamic nature of the flow localization process. The elastic strain profile shown in Fig. 8.6(d) also evidences traces of the localization process. The inception of the neck is accompanied by a significant increase of ε^e_Z. Moreover, Figs. 8.6(e) and 8.6(f) show, very clearly, the strong gradients of plastic strain and plastic strain rate which develop due to the localization process. Note that, outside the localization area, the strain rates tends to zero. In other words, outside the necked region the rod is unloading.

Remark 8.5. We should be careful in the analysis of the localization area. According to Needleman and Tvergaard [120], predictions of the shape and size of a necked region are outside the scope of a one-dimensional analysis.

All in all, the series of Figs. 8.4, 8.5 and 8.6 reveal that our simple finite differences model captures the key mechanisms which trigger flow localization. In comparison with *regular* computations carried out using commercial codes, we are able to provide further insights into the intervention of stress waves within the specimen and the kinetics of necking development. This is a salient feature of this Doctoral Research which opens new routes for the analysis of flow localization in elastoplastic rods subjected to dynamic loading.

Next, we develop a comprehensive parametric analysis to assess the influence of loading velocity (section 8.2.1), specimen gauge length (section 8.2.2), material properties (section 8.2.3), material flaws (section 8.2.4) and initial conditions (section 8.2.5) in the location of flow localization. In addition, in section 8.2.6, we develop a comparison between hypoelastic and hyperelastic-based models.

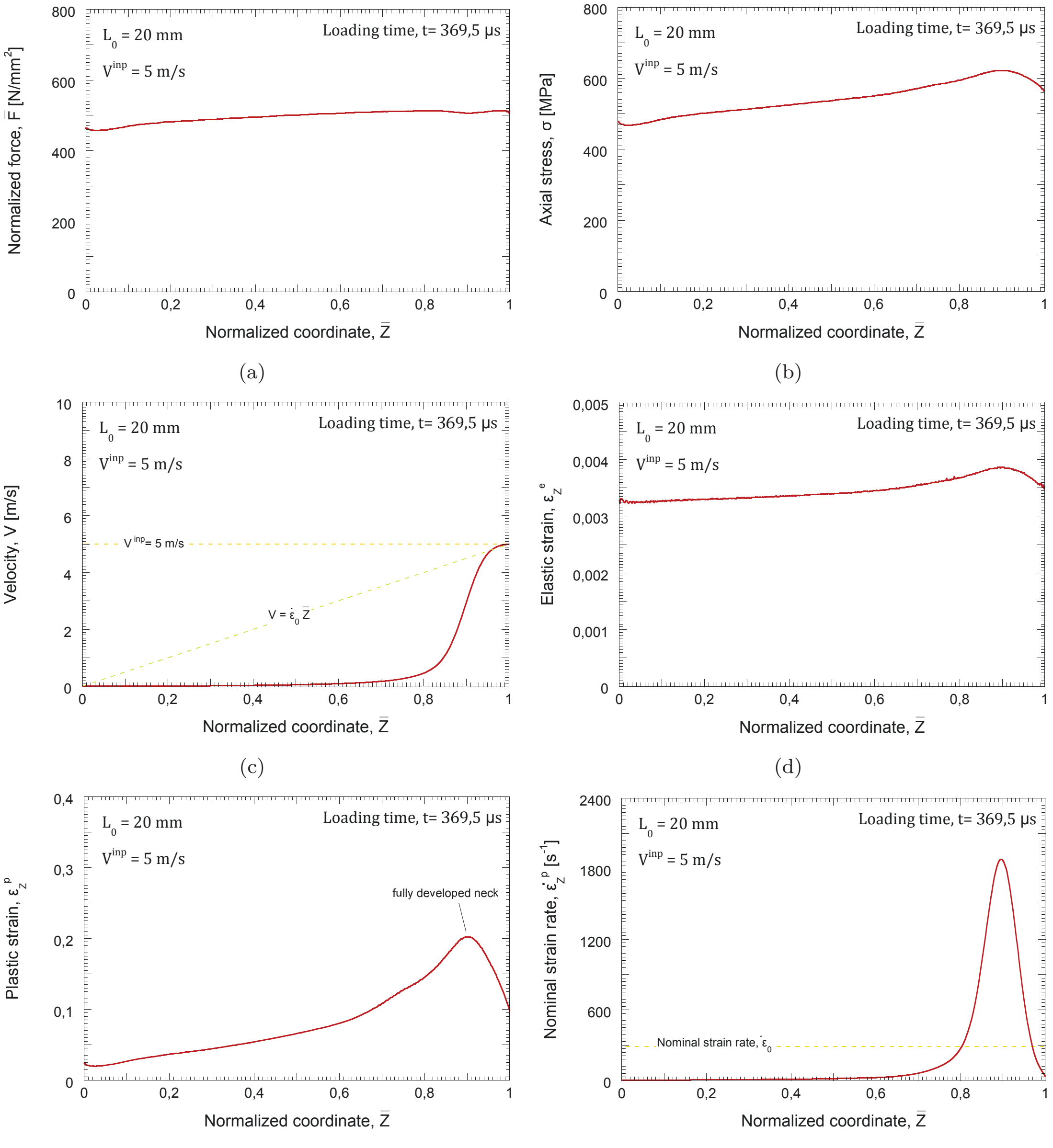

(a) (b)

(c) (d)

(e) (f)

Figure 8.6: Various field variables as a function of the normalized coordinate $\bar{Z} = \frac{Z}{L_0}$. The impact velocity is $V^{inp} = 5\, m/s$ and the gauge length $L_0 = 20\, mm$. A loading time of $t = 369.5\ \mu s$ is selected.

8.2.1 Influence of loading velocity on the location of flow localization

In order to complement our experimental and finite element results presented in chapters 6 and 7, in this section we use the finite difference model to illustrate the influence of the impact velocity in the location of flow localization. We have selected the sample dimensions used in previous section: $L_0 = 20\ mm$ and $\Phi = 3\ mm$. The number of nodes also is $M = 500$. We analyse three impact velocities: $2.5\ m/s$, $5\ m/s$ and $12\ m/s$. These values of V^{inp} are specifically selected to show *(to the full extent)* the role played by the impact velocity in the necking location.

Fig. 8.10 shows the axial plastic strain rate $\dot{\varepsilon}_Z^p$ as a function of the normalized coordinate $\bar{Z}$. For each impact velocity we illustrate the $\dot{\varepsilon}_Z^p - \bar{Z}$ curve at the time of flow localization. This is (roughly) taken as the loading time for which the strain rate outside the necked area goes to zero. According to the experiments and the finite elements presented in chapters 6 and 7, we observe that the necking location (represented by the excursion of strain rate) varies with the impact velocity.

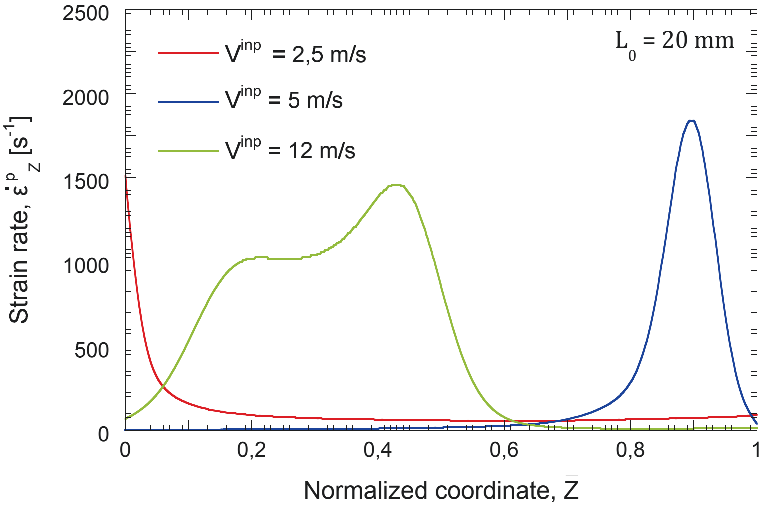

Figure 8.7: Finite difference results. Axial plastic strain rate $\dot{\varepsilon}_Z^p$ as a function of the normalized coordinate $\bar{Z}$. The gauge length is $L_0 = 20\ mm$ and the cross-section diameter $\Phi = 3\ mm$. Three different impact velocities are considered: $V^{inp} = 2.5\ m/s$, $V^{inp} = 5\ m/s$ and $V^{inp} = 12\ m/s$. The mesh density is $M = 500$.

In order to strengthen our idea that the necking location is dictated by the wave propagation phenomena, Fig. 8.10 shows the Cauchy stress σ versus the normalized coordinate $\bar{Z}$ for two different loading times: 2 μs in Fig. 8.10(a) and 262 μs in Fig. 8.10(b).

- The loading time 2 μs corresponds to an early stage of the loading process. The stress wave travels from the impacted side to the clamped end. The impact at 2.5 m/s induce, initially, only elastic strains in the bar. The value of the stress, which depends on the applied velocity, is given by the expression $\rho_0 c_0 V^{inp}$. Note that the stress behind the front wave is largely constant. Same behavior is observed in the impact at 5 m/s, because the induced stress, calculated by means of the previous expression, is close to the initial yield strength. Finally, the impact at 12 m/s generates instantaneous plastic deformation in the material. The stress behind the elastic precursor is not constant but it depends, non-linearly, on the normalized coordinate $\bar{Z}$. It is apparent that the impact velocity determines the stress waves intervention within the specimen.
- The loading time 262 μs corresponds to a late stage of the loading process. Despite the stress waves have travelled several times along the bar, the stress profiles are not uniform. This non-uniformity is the perturbation of the tress field required to trigger the flow localization. The fact that the $\sigma - \bar{Z}$ curve is sensitive to the impact velocity necessarily implies that the necking location is sensitive to the impact velocity.

We highlight the coherence and robustness of our combined experimental-numerical methodology which has revealed (and explained) using three different approaches the interplay between impact velocity and necking location in the dynamic tensile test.

8.2.2 Influence of specimen gauge length on the location of flow localization

This section aims at further deepen into the relationship between the gauge length and the location of flow localization that was presented in chapters 6 and 7. We have selected the specimen cross section used in previous section $\Phi = 3$ mm. The impact velocity is $V^{inp} = 7.5$ m/s. This loading velocity, which induces instantaneous plastic strains in the rod, is representative of the experiments presented in chapter 6. We analyse three gauge lengths: 20 mm, 40 mm and 60 mm. These

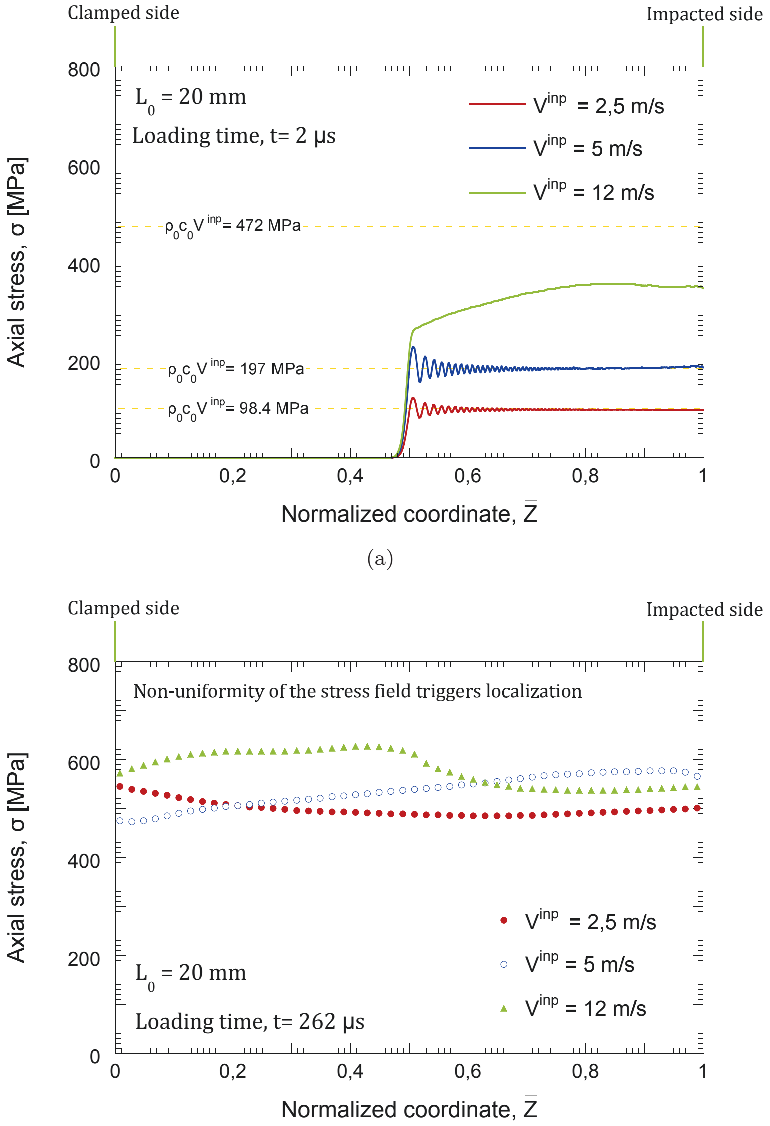

(a)

(b)

Figure 8.8: Finite difference results. Cauchy stress σ as a function of the normalized coordinate $\bar{Z}$. The gauge length is $L_0 = 20\ mm$ and the cross-section diameter $\Phi = 3\ mm$. Three different impact velocities are considered: $V^{inp} = 2.5\ m/s$, $V^{inp} = 5\ m/s$ and $V^{inp} = 12\ m/s$. The mesh density is $M = 500$. Two different loading times are explored: (a) $t = 2\ \mu s$ and (b) $t = 262\ \mu s$.

values of L_0 are within the range used in the experiments of chapter 6. The number of nodes is $M = 500$ and the time step $\Delta t = 10^{-9}\ s$.

Fig. 8.9 shows the axial plastic strain rate $\dot{\varepsilon}_Z^p$ versus the normalized coordinate $\bar{Z}$. The $\dot{\varepsilon}_Z^p - \bar{Z}$ curves are taken at the time corresponding to flow localization (zero strain rate outside the localization area). In agreement with the experimental and numerical evidence reported in chapters 6 and 7, the necking location depends on L_0. In the case of $L_0 = 60\ mm$ there is a single neck located close to the clamped end (left side). On the contrary, in the case of $L_0 = 20\ mm$ we observe the development of two localized regions. The main one is located at the clamped side while the secondary one is located at the impacted end (right side). It has to be highlighted that the case $L_0 = 40\ mm$ is halfway between the localization patterns of $L_0 = 20\ mm$ and $L_0 = 60\ mm$ (similar behaviour was observed in the finite element calculations, see Fig. 7.3 in chapter 7). As shown below, the interplay between gauge length and necking location is caused by the effect of the gauge length in the intervention of stress waves within the sample.

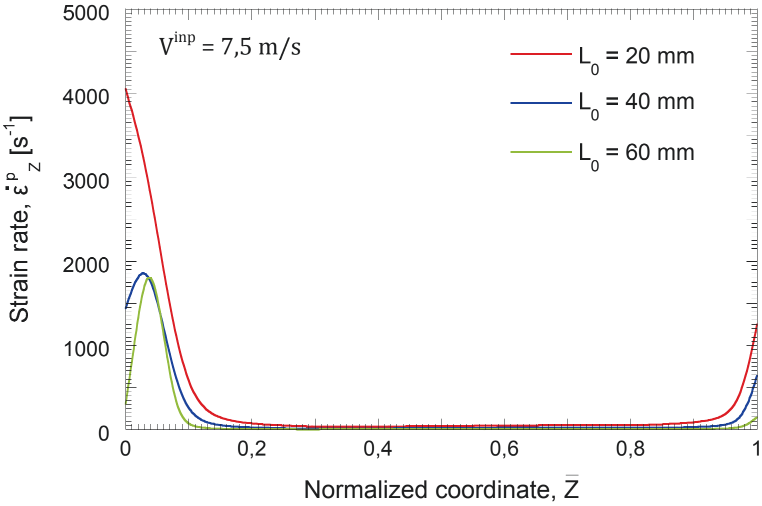

Figure 8.9: Finite difference results. Axial plastic strain rate $\dot{\varepsilon}_Z^p$ as a function of the normalized coordinate $\bar{Z}$. The impact velocity is $V^{inp} = 7.5\ m/s$ and the cross-section diameter $\Phi = 3\ mm$. Three different gauge lengths are considered: $L_0 = 20\ mm$, $L_0 = 40\ mm$ and $L_0 = 60\ mm$. The mesh density is $M = 500$.

Fig. 8.10 shows the Cauchy stress σ versus the normalized coordinate $\bar{Z}$ for two different loading times: 2 μs in Fig. 8.10(a) and 124 μs in Fig. 8.10(b).

- The loading time 2 μs corresponds to an early stage of the loading process. The stress wave induced by the impact has not yet reached the clamped side. Nevertheless, it is apparent that the time remaining for the wave to reach the clamped end is shorter as L_0 is smaller. Different gauge lengths imply different times for the wave to travel along the entire bar, which alters the processes of reflection and interaction of waves.

- The loading time 124 μs corresponds to a late stage of the loading process. The stress waves have travelled along the entire specimen several times. Perturbations of the stress field are observed for the three gauge lengths investigated. We observe that the shape of the $\sigma - \bar{Z}$ curve is sensitive to the gauge length (look at the excursion of the stress at the clamped end of $L_0 = 20\ mm$) which implies that the necking location is sensitive to the gauge length.

We point out that the experiments, the finite elements and the finite differences have shown the relationship between gauge length and the necking location. In addition, the finite difference model has confirmed that the interaction and reflection of stress waves is responsible for such behaviour.

8.2.3 Influence of selected material properties on the location of flow localization

We take advantage of the large flexibility of the finite difference scheme to extend our analysis and investigate the role of selected material properties in the location of flow localization. We develop a parametric study which includes variations of the work hardening exponent n, the strain rate sensitivity exponent m and the initial density ρ_0. We select these specific properties because they markedly affect the dynamic response of the material. On the one hand, n and m enter into the yield stress and affect the visco-plastic response of the solid. On the other hand, ρ_0 determines the elastic wave speed and the instantaneous stress level induced in the bar by the impact. The specimen length is 8 mm, the cross-section diameter 3 mm and the impact velocity 12 m/s. These values of L_0, Φ and V^{inp} are representative of a typical experimental arrangement, see [52, 60]. Note that this impact velocity induces instantaneous plastic deformation in the rod. For all the calculations included in this section the mesh density is $M = 300$ and the time step $\Delta t = 10^{-9}\ s$.

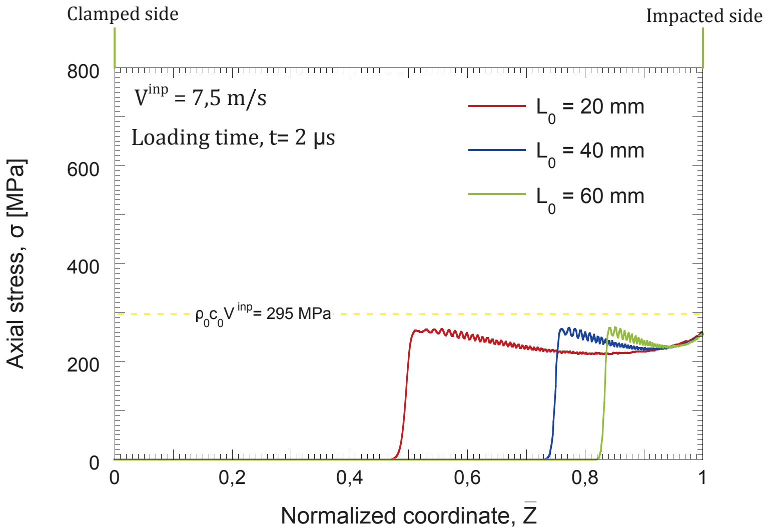

(a)

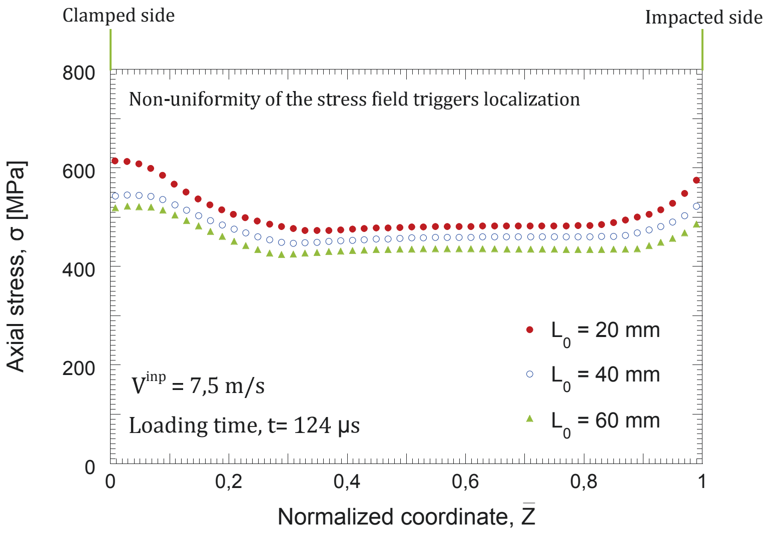

(b)

Figure 8.10: Finite difference results. Cauchy stress σ as a function of the normalized coordinate $\bar{Z}$. The impact velocity is $V^{inp} = 7.5\ m/s$ and the cross-section diameter $\Phi = 3\ mm$. Three different gauge lengths are considered: $L_0 = 20\ mm$, $L_0 = 40\ mm$ and $L_0 = 60\ mm$. The mesh density is $M = 500$. Two different loading times are explored: (a) $t = 2\ \mu s$ and (b) $t = 124\ \mu s$.

8.2.3.1 Influence of work hardening exponent

Three values of the work hardening exponent are investigated: $n = 0.067$, $n = 0.167$ (reference value, Table 7.1) and $n = 0.267$. These values are representative of *typical* metallic alloys.

Fig. 8.11 shows the axial plastic strain rate $\dot{\varepsilon}_Z^p$ versus the normalized coordinate $\bar{Z}$. The $\dot{\varepsilon}_Z^p - \bar{Z}$ curves correspond to the time of flow localization. We observe that the necking location varies with the strain hardening exponent. We have two necks at both ends of the sample for $n = 0.067$, a single neck roughly located at the middle of the specimen for $n = 0.0167$ and a single neck at the clamped side for $n = 0.0267$. This behaviour is attributed to the role played by the coefficient n in the wave propagation phenomena. Fig. 8.12 shows the Cauchy stress σ as a function of the normalized coordinate $\bar{Z}$ for two different loading times: 1 μs in Fig. 8.12(a) and 14 μs in Fig. 8.12(b).

- The loading time 1 μs corresponds to an early stage of the loading process such that the stress wave has not yet reach the clamped end (left end). The stress behind the front wave strongly depends on the value of n. It becomes apparent that the material work hardening plays a key role in the stress waves intervention within the specimen.
- The loading time 14 μs corresponds to a late stage of the loading process. The stress waves have reflected at the boundaries several times. The non-uniformity of the stress field is evident. In the case of $n = 0.067$ we (already) observe the inception of two necks at both ends of the specimen. The dependence of the $\sigma - \bar{Z}$ curves with n explains the role played by the strain hardening exponent in the location of flow localization.

8.2.3.2 Influence of strain rate sensitivity exponent

Three values of the strain rate sensitivity exponent are investigated: $m = 0.0018$, $m = 0.0118$ (reference value, Table 7.1) and $m = 0.0318$. These values are representative of *typical* metallic alloys.

Fig. 8.13 illustrates the axial plastic strain rate $\dot{\varepsilon}_Z^p$ as a function of $\bar{Z}$. The $\dot{\varepsilon}_Z^p - \bar{Z}$ curves correspond to the time of flow localization. The necking location depends

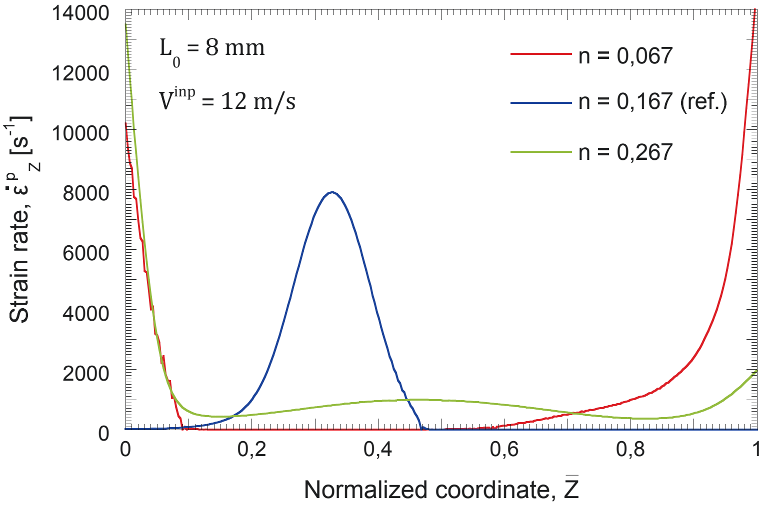

Figure 8.11: Finite difference results. Axial plastic strain rate $\dot{\varepsilon}^p_Z$ as a function of the normalized coordinate $\bar{Z}$. The impact velocity is $V^{inp} = 12\ m/s$, the gauge length $L_0 = 8\ mm$ and the cross-section diameter $\Phi = 3\ mm$. Three different work hardening exponents are considered: $n = 0.067$, $n = 0.167$ (reference value) and $n = 0.267$. The mesh density is $M = 300$.

on the value of m selected. The role played by the strain rate sensitivity on the stress waves propagation is responsible for this behaviour. Fig. 8.14 shows the Cauchy stress σ as a function of the normalized coordinate $\bar{Z}$ for two different loading times: 1 μs in Fig. 8.14(a) and 79 μs in Fig. 8.14(b).

- The loading time 1 μs corresponds to an early stage of the loading process. The stress waves induced by the impact travel from the loaded side to the clamped end. The shape of the $\sigma - \bar{Z}$ curves depends on the value of m. This reveals how the material rate sensitivity influences the stress waves phenomena which develop within the specimen.

- The loading time 79 μs defines a late stage of the loading process such that the stress waves have travelled along the sample several times. Nevertheless, the stress field is non-uniform and dependent on the strain rate sensitivity exponent. Recall that different stress profiles lead to different necking locations.

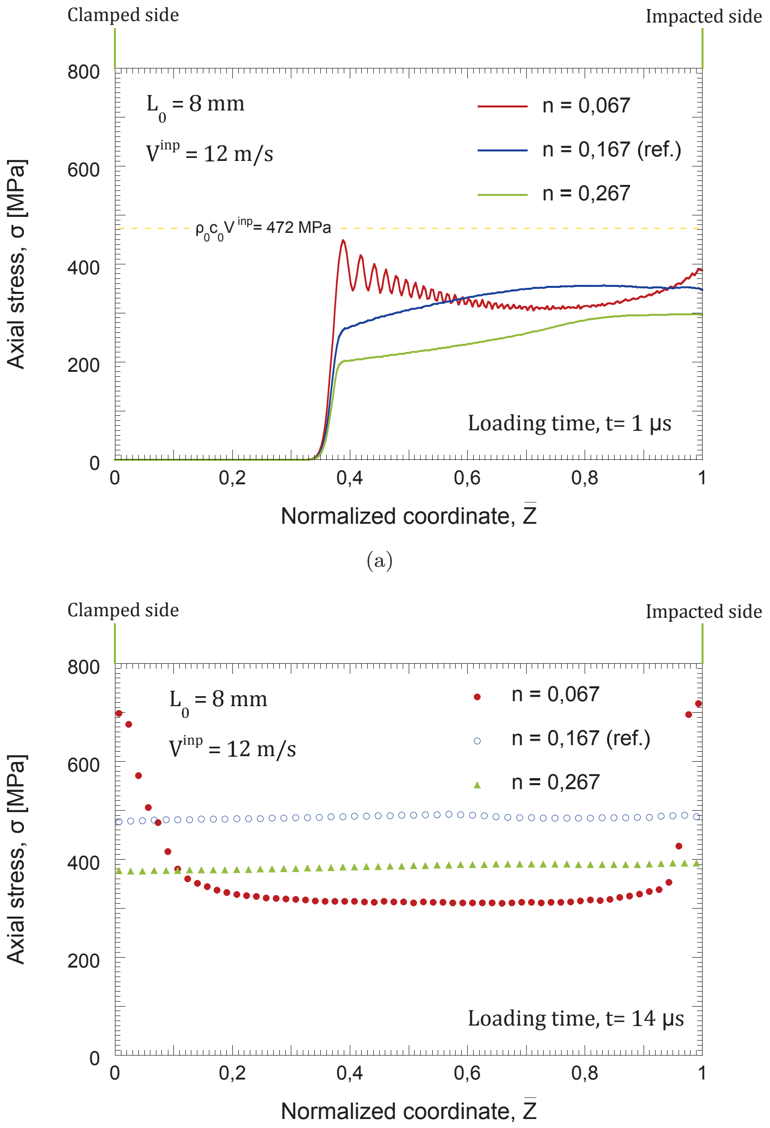

(a)

(b)

Figure 8.12: Finite difference results. Cauchy stress σ as a function of the normalized coordinate $\bar{Z}$. The impact velocity is $V^{inp} = 12\ m/s$, the gauge length $L_0 = 8\ mm$ and the cross-section diameter $\Phi = 3\ mm$. Three different work hardening exponents are considered: $n = 0.067$, $n = 0.167$ (reference value) and $n = 0.267$. The mesh density is $M = 300$. Two different loading times are explored: (a) $t = 1\ \mu s$ and (b) $t = 14\ \mu s$.

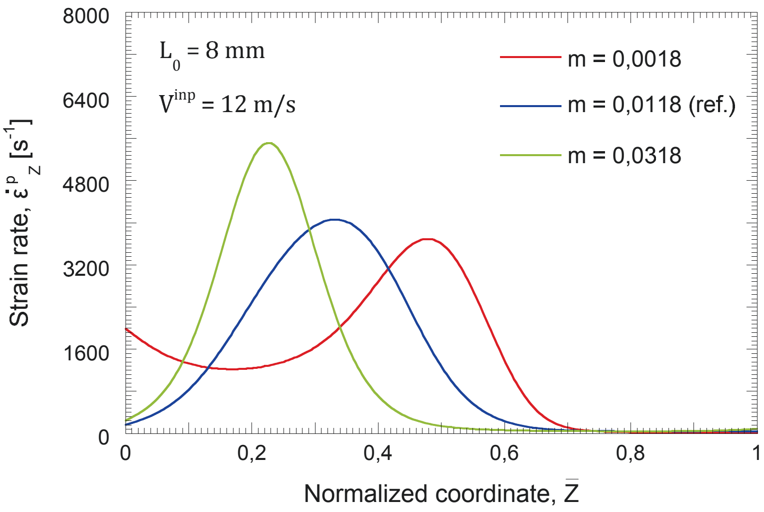

Figure 8.13: Finite difference results. Axial plastic strain rate $\dot{\varepsilon}^p_Z$ as a function of the normalized coordinate $\bar{Z}$. The impact velocity is $V^{inp} = 12\ m/s$, the gauge length $L_0 = 8\ mm$ and the cross-section diameter $\Phi = 3\ mm$. Three different strain rate sensitivity exponents are considered: $m = 0.0018$, $m = 0.0118$ (reference value) and $m = 0.0318$. The mesh density is $M = 300$.

8.2.3.3 Influence of material density

Three values of the initial material density are investigated: $\rho_0 = 2700\ kg/m^3$, $\rho_0 = 7740\ kg/m^3$ (reference value, Table 7.1) and $\rho_0 = 16650\ kg/m^3$. These values are representative of aluminium, steel and tantalum, respectively.

We apply the same analysis procedure developed in sections 8.2.3.1 and 8.2.3.2. Fig. 8.15 shows the axial plastic strain rate $\dot{\varepsilon}^p_Z$ as a function of $\bar{Z}$ at the time of flow localization. This graph reveals that the location of flow localization depends on the value of ρ_0. The case of $\rho_0 = 2700\ kg/m^3$ shows a main necking at the clamped end and a secondary one at the impacted end. The case of $\rho_0 = 16650\ kg/m^3$ shows a single neck at the impacted side. The role played by the material density in (1) the velocity of the elastic waves and (2) the instantaneous stress level induced by the impact is responsible for this behaviour. Fig. 8.16 shows the Cauchy stress σ versus the normalized coordinate $\bar{Z}$ for two different loading times: 0.5 μs in Fig. 8.16(a) and 28 μs in Fig. 8.16(b).

- The loading time 0.5 μs illustrates the first moments of the loading process. The stress waves generated by the impact have not yet reached the clamped end. The shape of the $\sigma - \bar{Z}$ curves depends on the value of ρ_0 and the unloaded portion of the bar is shorter as material density is smaller. It is

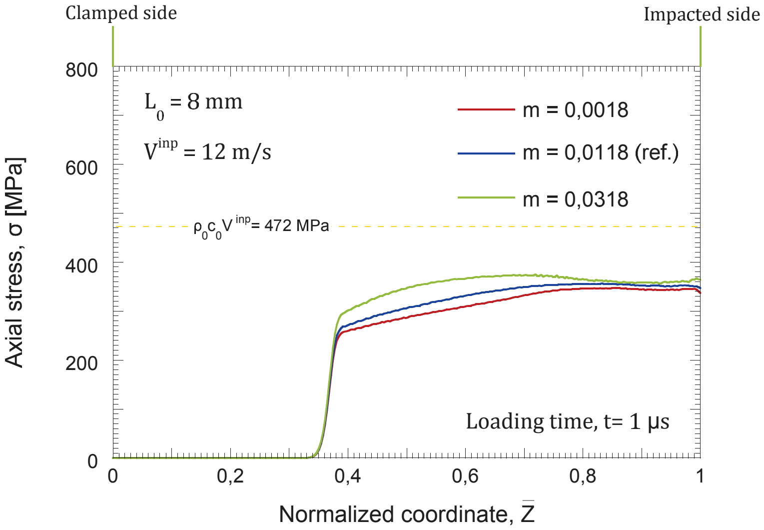

(a)

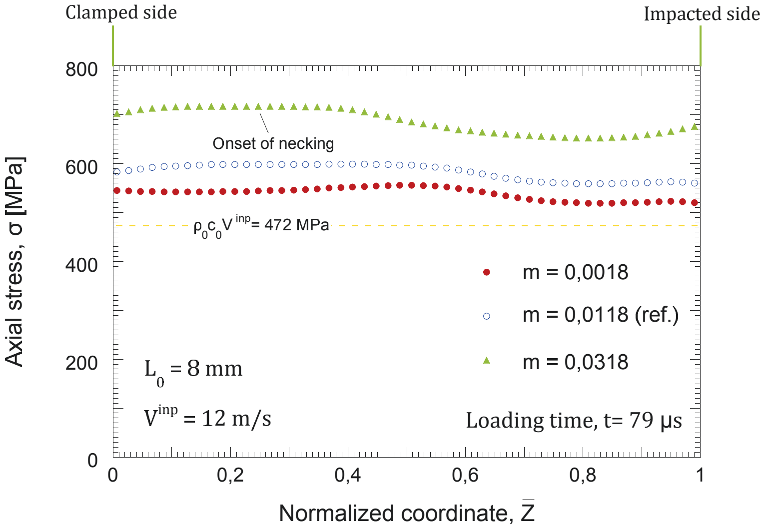

(b)

Figure 8.14: Finite difference results. Cauchy stress σ as a function of the normalized coordinate $\bar{Z}$. The impact velocity is $V^{inp} = 12\ m/s$, the gauge length $L_0 = 8\ mm$ and the cross-section diameter $\Phi = 3\ mm$. Three different strain rate sensitivity exponents are considered: $m = 0.0018$, $m = 0.0118$ (reference value) and $m = 0.0318$. The mesh density is $M = 300$. Two different loading times are explored: (a) $t = 1\ \mu s$ and (b) $t = 79\ \mu s$.

apparent that the material density influences the reflection and interaction of waves within the specimen.

- The loading time 28 μs corresponds to a late stage of the loading process for which the stress waves have already travelled along the specimen several times. The stress field shows fluctuations which reveal the lack of equilibrium of the specimen. These fluctuations are dependent on the value of ρ_0. In the case of $\rho = 2700\ kg/m^3$ we (already) observe incipient necks at both ends of the sample.

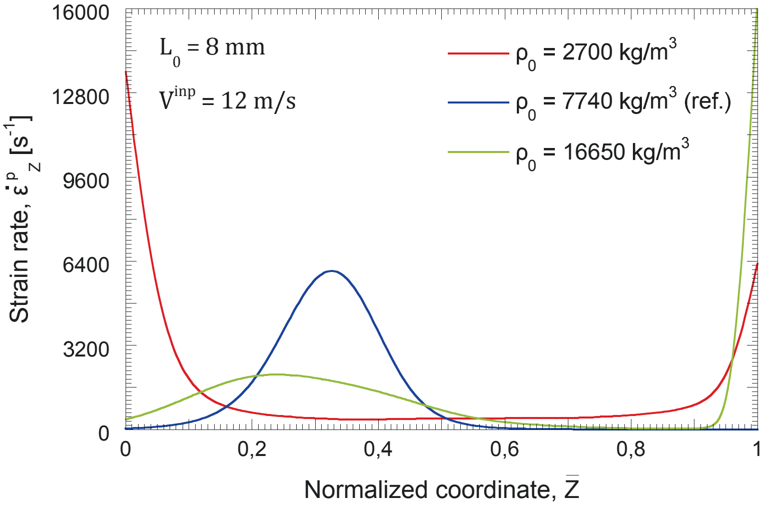

Figure 8.15: Finite difference results. Axial plastic strain rate $\dot{\varepsilon}^p_Z$ as a function of the normalized coordinate $\bar{Z}$. The impact velocity is $V^{inp} = 12\ m/s$, the gauge length $L_0 = 8\ mm$ and the cross-section diameter $\Phi = 3\ mm$. Three different initial material densities are considered: $\rho = 2700\ kg/m^3$, $\rho = 7740\ kg/m^3$ (reference value) and $\rho = 16650\ kg/m^3$. The mesh density is $M = 300$.

The versatility and reliability of our finite difference scheme has allowed us to explore the influence of selected material properties in the necking location. We have observed that strain hardening, strain rate hardening and material density control, to a large extent, the processes of interaction and reflection of stress waves which take place within the rod. In this regard, our finite difference scheme could be used to asses the *equilibrium* (or lack of it) in cylindrical tensile specimens used, for instance, in Split Hopkinson Tensile Bar experiments. This is salient feature of this Doctoral Research and a potential application for our scientific developments.

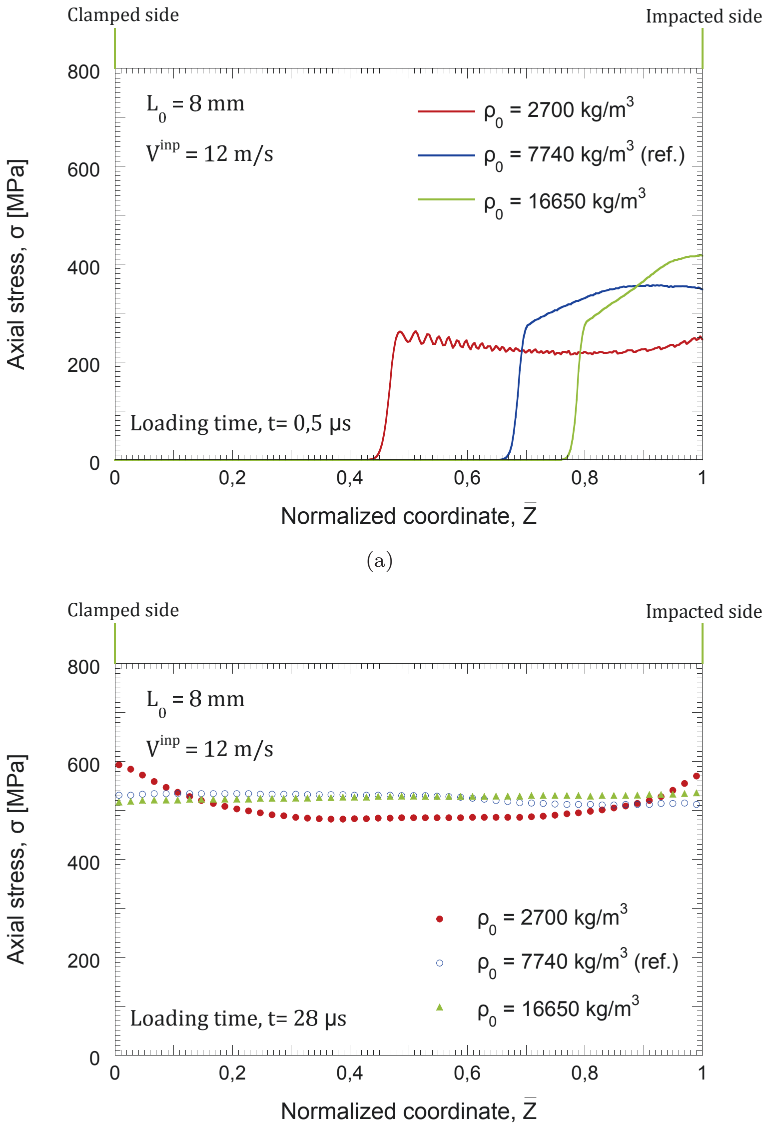

(a)

(b)

Figure 8.16: Finite difference results. Cauchy stress σ as a function of the normalized coordinate $\bar{Z}$. The impact velocity is $V^{inp} = 12\ m/s$, the gauge length $L_0 = 8\ mm$ and the cross-section diameter $\Phi = 3\ mm$. Three different initial material densities are considered: $\rho = 2700\ kg/m^3$, $\rho = 7740\ kg/m^3$ (reference value) and $\rho = 16650\ kg/m^3$. The mesh density is $M = 300$. Two different loading times are explored: (a) $t = 0.5\ \mu s$ and (b) $t = 28\ \mu s$.

8.2.4 Influence of material flaws on the location of flow localization

In this section we develop one of the most innovative analysis of this Doctoral Thesis. We use the finite difference scheme to explore the role played by material defects on necking inception. To this day, whether the material defects may trigger flow localization remains as an open question subjected to strong debates in the literature, see Ravi-Chandar and Triantafyllidis [121].

We model the material flaws introducing, for each node of the spatial grid, a perturbation in the initial yield stress. This procedure is based on the approach of Ravi-Chandar and Triantafyllidis [121]. Firstly, we establish a maximum percentage of variation for the initial yield stress. Secondly, we assign to each node a random value within the interval defined by this percentage. The mean value corresponds to the unaltered initial yield stress of the material given in Table 7.1 by the parameter A. Note that the random values of the perturbed initial yield stress are obtained from a normal distribution with mean parameter $\mu \equiv A = 176$ MPa. The standard deviation parameter σ [1] is determined through an iterative process in order to ensure that the maximum and minimum values in the distribution are inside the interval defined by the selected percentage of variation.

In Fig. 8.17 we show, as an illustrative example, the statistical distributions corresponding to a maximum percentage of variation of ± 5%. Fig. 8.17(a) represents the distribution of values along the coordinate Z of the bar. It can be seen that the maximum and minimum values are inside the limits (red lines) defined by this percentage. In Fig. 8.17(b) we depict the normal probability density function. This normal distribution has a mean value of $\mu \equiv A = 176$ MPa and a standard deviation of $\sigma = 3.54$ MPa. The normal probability and the cumulative distribution function are shown in Fig. 8.17(c) and Fig. 8.17(d), respectively. It is clear that most of the yield stress values assigned to the nodes are surrounding the initial yield stress corresponding to the baseline material given in Table 7.1. Our belief is that this procedure is a suitable tool to model the typical flaws *randomly* generated in metallic materials during, for instance, the manufacturing process.

In the analysis below we use several percentages of variation (± 5 %, ± 10 % and ± 15 %) of the yield stress to simulate defects with different *degrees of severity.*

---

[1] The standard deviation parameter σ should not be confused with the Cauchy stress σ.

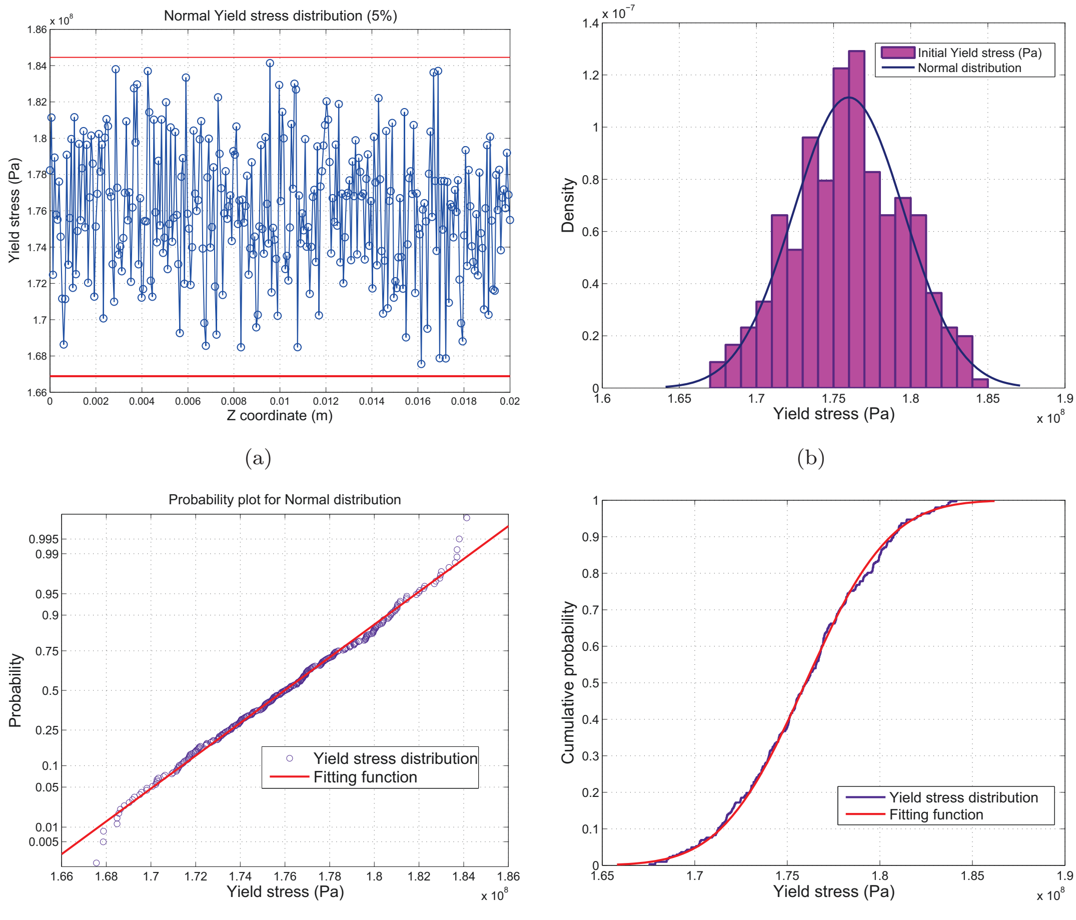

(a) (b)

(c) (d)

Figure 8.17: Yield stress distribution statistics for a maximum percentage variation of ± 5%. (a) Yield stress distribution along the bar. (b) Normal probability density function. (c) Normal probability plot. (d) Cumulative distribution function.

It is apparent that as the percentage of variation increases the variations in the initial yield stress of the material are greater, i.e. the material defects are more important. A comparison is conducted with the baseline material free of defects. The sample length is 8 mm and the cross-section diameter 3 mm. Two different impact velocities are explored: 5 m/s and 12 m/s. For all the calculations we show in this section the mesh density is $M = 300$ and the time step $\Delta t = 10^{-9}$ s.

Fig. 8.18 shows the axial plastic strain rate $\dot{\varepsilon}_Z^p$ as a function of $\bar{Z}$ at the time of flow localization for $V^{inp} = 5$ m/s. We observe that the strain rate profiles for the intact material and ± 5 % are practically coincident. These results suggest that, up to yield stress variations of ± 5 %, the flow localization is not influenced by the material defects. The specimen behaviour is mostly controlled by the stress waves induced by the impact. On the other hand, for ± 10 % and ± 15 % the necking location has moved to the impacted end. Such large defects seem to affect the deformation behaviour of the rod. These conclusions are further rationalized in Fig. 8.19 where the Cauchy stress σ is depicted as a function of $\bar{Z}$ for two different loading times: $t = 20\ \mu s$ in Fig. 8.21(a) and $t = 114\ \mu s$ in Fig. 8.21(b). These loading times are such that the stress waves have travelled along the samples several times. The stress profiles for the intact material and ± 5 % are largely similar. The difference emerges for ± 10 % and, specially, for ± 15 %. Only when we consider such a large defects the stress distribution in the specimens (and therefore the necking location) is affected by the material flaws.

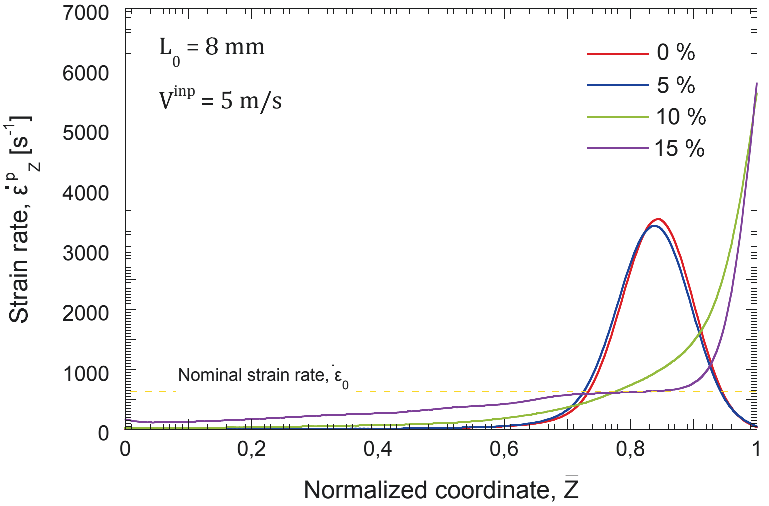

Figure 8.18: Finite difference results. Axial plastic strain rate $\dot{\varepsilon}^p_Z$ as a function of the normalized coordinate $\bar{Z}$. The impact velocity is $V^{inp} = 5\ m/s$, the gauge length $L_0 = 8\ mm$ and the cross-section diameter $\Phi = 3\ mm$. Three different degrees of material flaws are considered: ± 5 %, ± 10 % and ± 15 %. A comparison with the intact material is conducted. The mesh density is $M = 300$.

Similar analysis is performed for the case of $V^{inp} = 12\ m/s$. Figs. 8.20 shows that the necking location is *practically* identical for all the configurations investigated. The strain rate profiles at the time of flow localization for the intact material, ± 5 %, ± 10 % and ± 15 % are very similar. These findings are consistent with the results of Fig. 8.21 where the Cauchy stress σ is depicted versus the normalized coordinate $\bar{Z}$ for two different loading times: $t = 20\ \mu s$ and $t = 94.5\ \mu s$. The stress profiles (specially for the intact material, ± 5 % and ± 10 %) are similar to each other. Only in the case of ± 15 % we observe some excursions in stress. The role of defects in the deformation of the specimen at 15 m/s seems to be smaller than at 5 m/s. We hold that, according to Rodríguez-Martínez et al. [95], this behaviour is caused by the increasing influence of material inertia in the sample

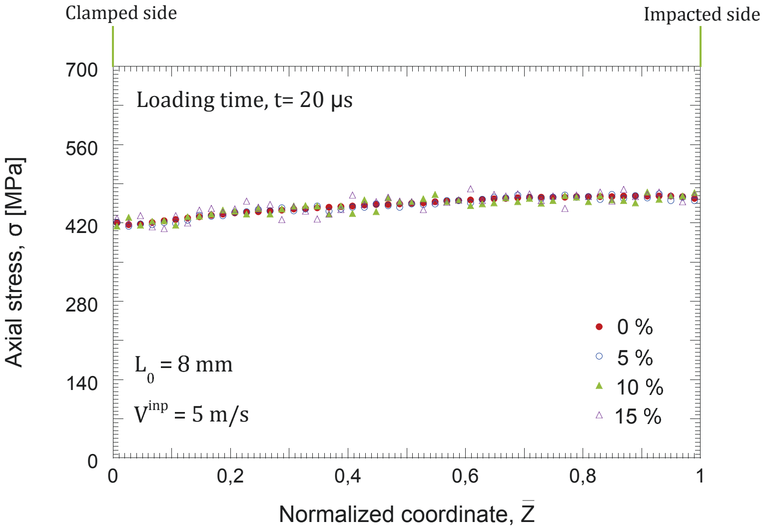

(a)

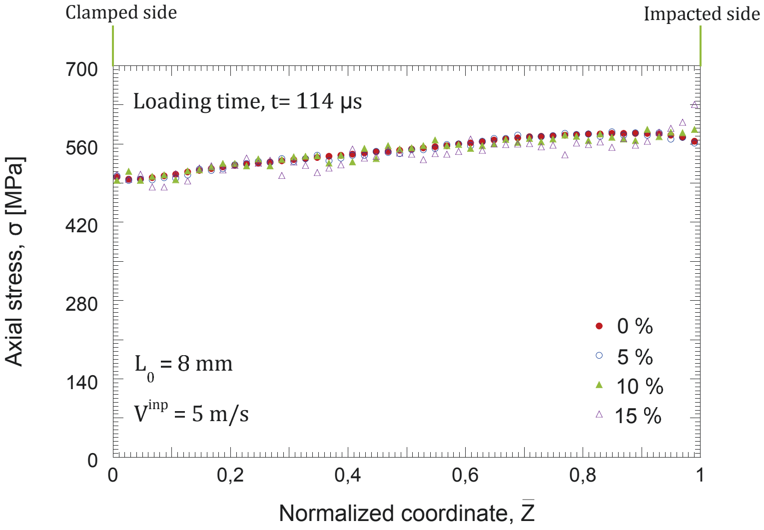

(b)

Figure 8.19: Finite difference results. Cauchy stress σ as a function of the normalized coordinate $\bar{Z}$. The impact velocity is $V^{inp} = 5\ m/s$, the gauge length $L_0 = 8\ mm$ and the cross-section diameter $\Phi = 3\ mm$. Three different degrees of material flaws are considered: ± 5 %, ± 10 % and ± 15 %. A comparison with the intact material is conducted. The mesh density is $M = 300$. Two different loading times are explored: (a) $t = 20\ \mu s$ and (b) $t = 114\ \mu s$.

response. Nevertheless, we acknowledge that further investigations are required to confirm this hypothesis.

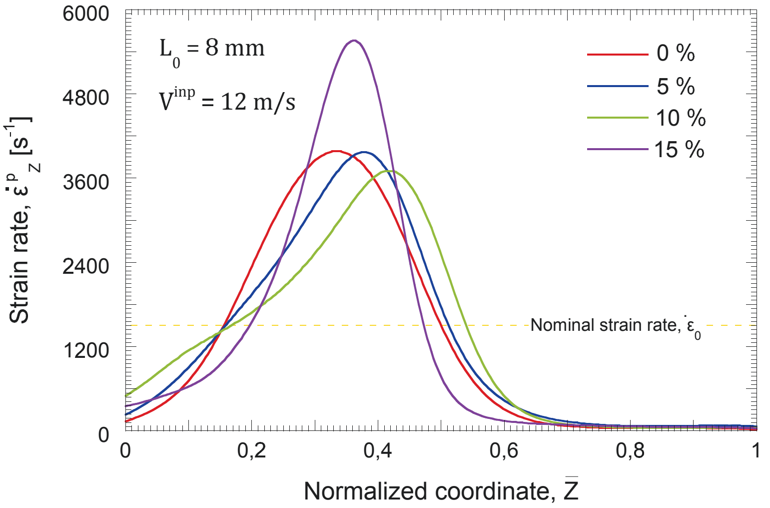

Figure 8.20: Finite difference results. Axial plastic strain rate $\dot{\varepsilon}^p_Z$ as a function of the normalized coordinate $\bar{Z}$. The impact velocity is $V^{inp} = 12\ m/s$, the gauge length $L_0 = 8\ mm$ and the cross-section diameter $\Phi = 3\ mm$. Three different degrees of material flaws are considered: ± 5 %, ± 10 % and ± 15 %. A comparison with the intact material is conducted. The mesh density is $M = 300$.

The findings of this chapter are within the most original and relevant contributions of this Thesis. We have developed a methodology to analyse the role of material flaws in the flow localization. For the geometrical, loading and material configurations that we have investigated, the amplitude of the material defects required to affect the deformation of the specimen is ± 10 % of the initial yield stress. On these basis, we suggest that the material defects play a secondary role within the mechanisms responsible for flow localization in the dynamic tension test. This conclusion agrees with the experimental evidence reported by Rittel et al. [61] and Rotbaum et al. [52].

8.2.5 Influence of initial conditions on the location of flow localization

In this section we use the finite difference scheme in order to asses the influence of initial conditions on flow localization. In this regard, the idea is to complement the results shown in section 7.2.3 of chapter 7. We have initialized the field variables

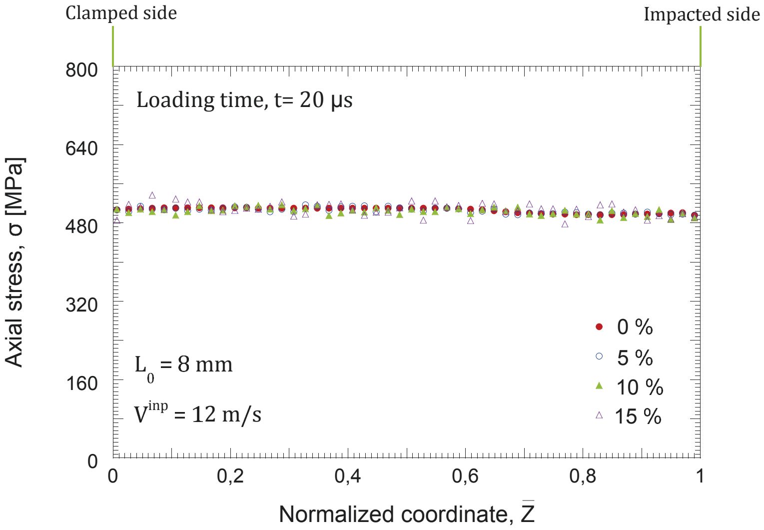

(a)

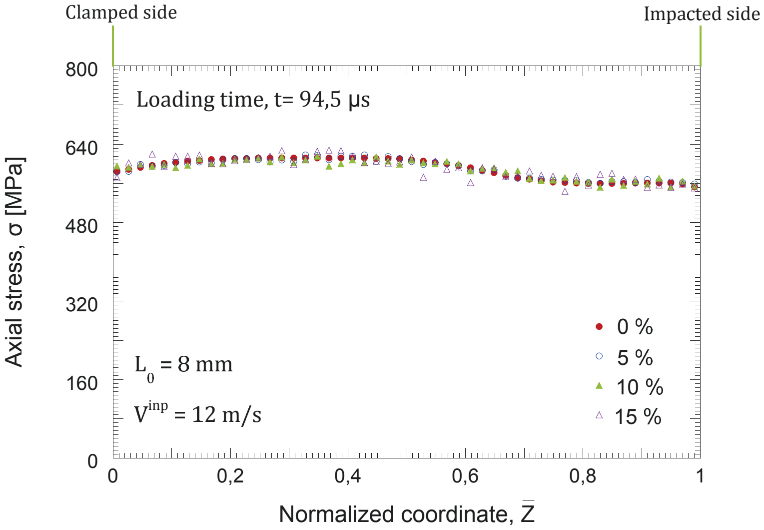

(b)

Figure 8.21: Finite difference results. Cauchy stress σ as a function of the normalized coordinate $\bar{Z}$. The impact velocities is $V^{inp} = 12\ m/s$, the gauge length $L_0 = 8\ mm$ and the cross-section diameter $\Phi = 3\ mm$. Three different grades of material flaws are considered: ± 5 %, ± 10 % and ± 15 %. A comparison with the intact material is conducted. The mesh density is $M = 300$. Two different loading times are explored: (a) $t = 20\ \mu s$ and (b) $t = 94.5\ \mu s$.

of the finite difference model in order to obtain an initial equilibrium configuration for the imposed boundary conditions. The initial values of the field variables are calculated following the procedure detailed in section 7.2.3. Unlike the finite element simulations, the finite difference scheme with the initialized field variables does not develop flow localization. Interestingly, our code is free of the numerical perturbations which are responsible for the necking inception in the **field calculations** of chapter 7. Thus, in order to trigger localization in the initialized finite difference computations we introduce material flaws, following the procedure described in section 8.2.4 of this chapter. A very slight variation of the initial yield stress is introduced in the nodes: 0.001 %. The impact velocity is $V^{inp} = 12\ m/s$ and the gauge length $L_0 = 8\ mm$. Moreover, the mesh density is $M = 300$ and the time step $\Delta t = 10^{-9}\ s$. Figs. 8.22, 8.23 and 8.24 show various field variables (σ, V, ε_Z^p, $\dot{\varepsilon}_Z^p$) along the normalized axial coordinate $\bar{Z} = Z/L_0$ for three different loading times.

- Fig. 8.22 corresponds to an early time of the loading process $t = 5\ \mu s$. The results for the intact and flawed materials are largely similar. The difference is only visible in Fig. 8.22(d) where some slight perturbations in the profile of the axial plastic strain rate are observed in the case of the flawed material.
- Fig. 8.23 corresponds to $t = 12.5\ \mu s$. The specimen has deformed ~ 2 %. The difference between the stress and plastic strain profiles (Figs. 8.22(a) and 8.22(c)) of the intact and flawed materials are negligible. However, we observe that the material flaws generate significant perturbations in the velocity and plastic strain rate fields, Figs. 8.22(b) and 8.22(d).
- Fig. 8.24 corresponds to $t = 101.5\ \mu s$. This a late time in the loading process which induces structural deformations of ~ 15 %. While the intact specimen is in equilibrium, the flawed sample has developed flow localization. We show that minimal variations of the yield stress (minimal material defects) are sufficient to trigger wave propagation phenomena and thus plastic localization.

While largely logical, the results shown in this section are innovative in the sense that reveal, explicitly, that minimal deviations from equilibrium are enough to trigger flow localization. For that task we have developed a simple methodology

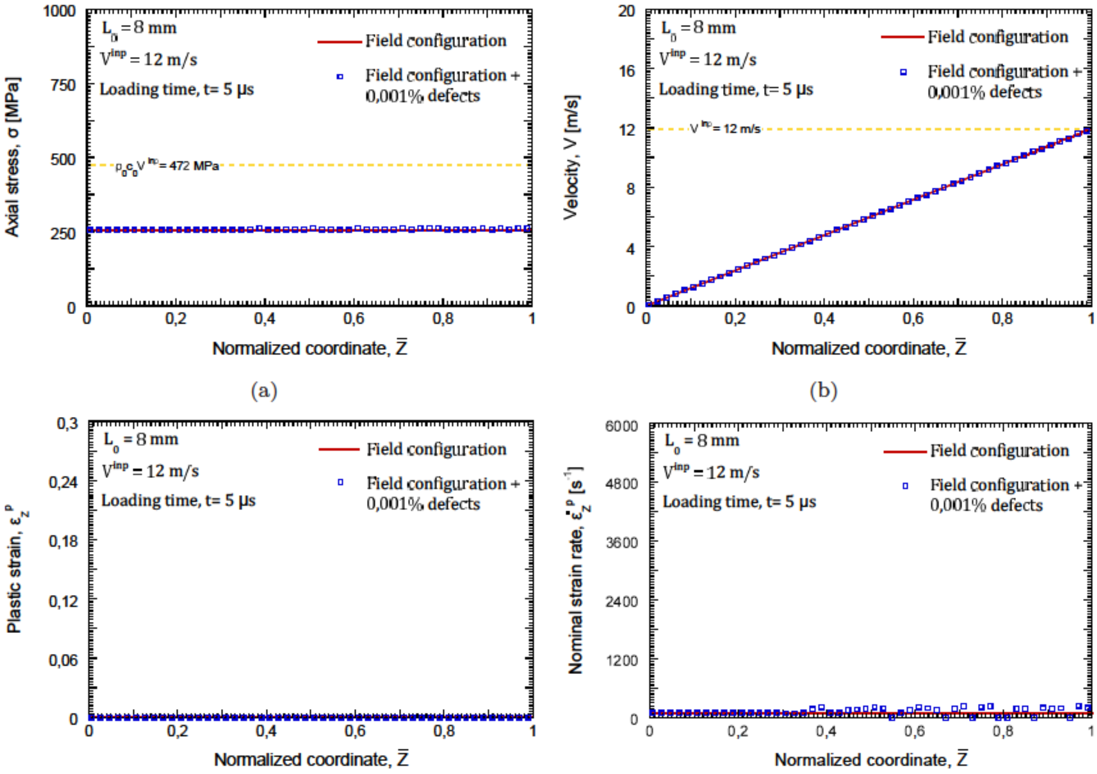

(a) (b) (c) (d)

Figure 8.22: Various field variables as a function of the normalized coordinate $\bar{Z}$. The impact velocity is $V^{inp} = 12\ m/s$, the gauge length $L_0 = 8\ mm$ and the cross-section diameter $\Phi = 3\ mm$. A loading time of $t = 5\ \mu s$ is selected. The field variables are initialized. A comparison between intact and flawed materials is conducted.

that allows to asses the influence of initial conditions in the inception of dynamic necks.

8.2.6 Comparison between hypoelastic and hyperelastic based models

In this section we develop a comparison between the hypoelastic and hyperelastic-based models. Recall that all the previous results shown in this chapter correspond to the hypoelastic-plastic model.

Fig. 8.25 shows the axial plastic strain rate $\dot{\varepsilon}_Z^p$ as a function of $\bar{Z}$ at the time of flow localization. Interestingly, the necking location is sensitive to the constitutive model. While the hyperelastic model predicts the necking at the clamped end, the hypoelastic-based approach predicts the necking at the center of the specimen. The

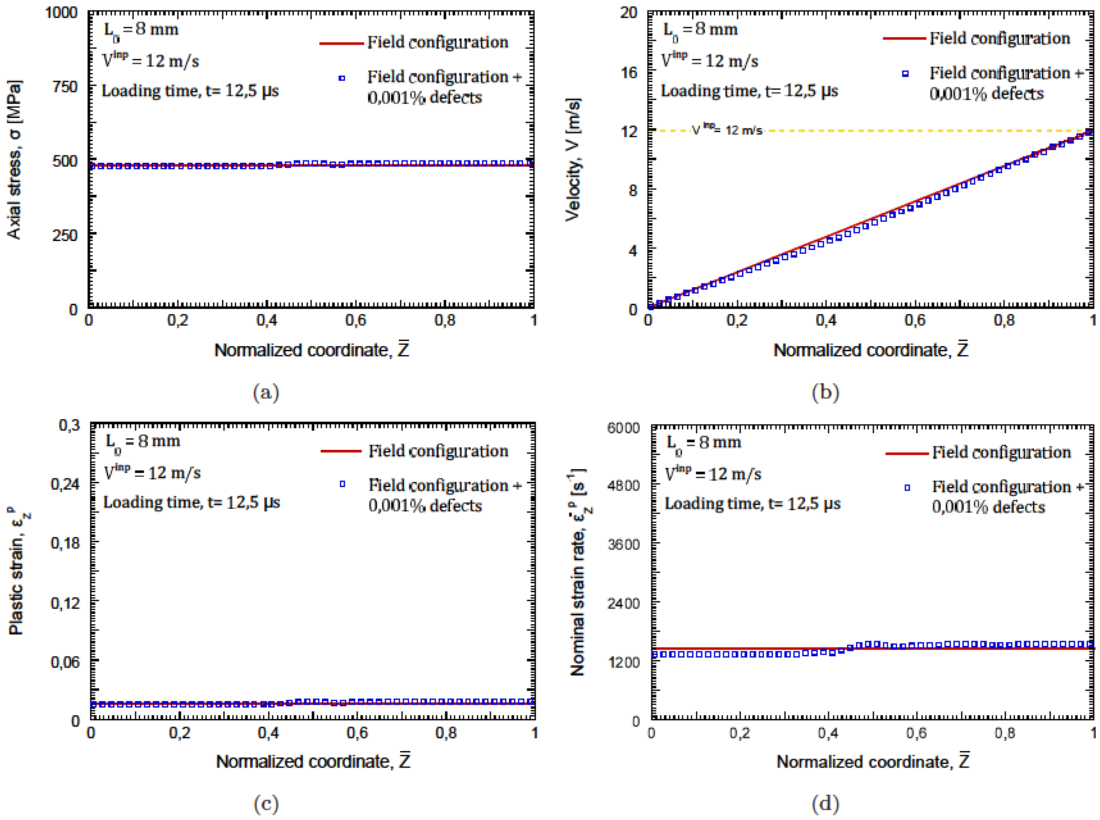

Figure 8.23: Various field variables as a function of the normalized coordinate $\bar{Z}$. The impact velocity is $V^{inp} = 12\ m/s$, the gauge length $L_0 = 8\ mm$ and the cross-section diameter $\Phi = 3\ mm$. A loading time of $t = 12.5\ \mu s$ is selected. The field variables are initialized. A comparison between intact and flawed materials is conducted.

influence of the constitutive model on the stress wave propagation phenomena is responsible for this behaviour.

Fig. 8.26 depicts the Cauchy stress σ as function of the normalized coordinate $\bar{Z}$ for two different loading times: 1 μs in Fig. 8.16(a) and 42 μs in Fig. 8.16(b).

- The loading time 1 μs illustrates an early stage of the loading process. The stress waves generated by the impact have not yet reached the clamped end. The shape of the $\sigma - \bar{Z}$ hypoelastic and hyperelastic curves is very similar, however we observe a slight difference in the stress level at the loaded end.
- The loading time 42 μs corresponds to an stage of the loading process for which the stress waves have already travelled along the specimen several times. As reported for 1 μs, the stress profiles predicted by the hypoelastic and hyperelastic models are slightly different. This slight difference is sufficient to trigger localization in different places of the rod.

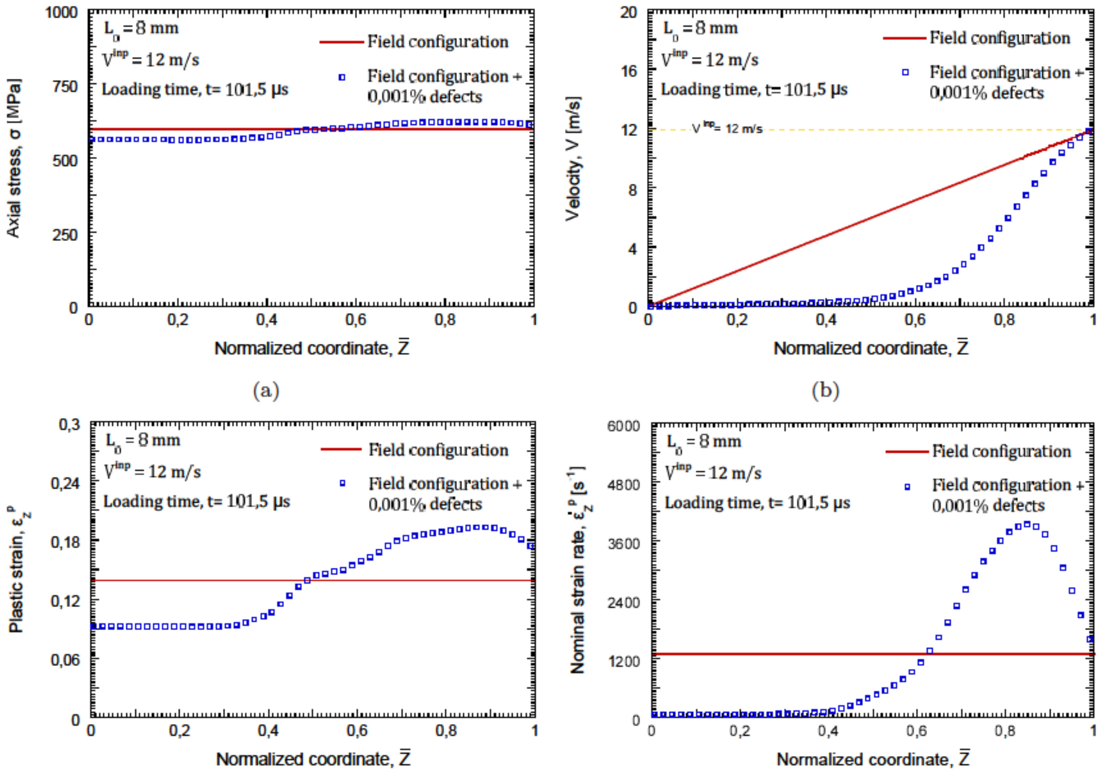

(a) (b)

(c) (d)

Figure 8.24: Various field variables as a function of the normalized coordinate $\bar{Z}$. The impact velocity is $V^{inp} = 12\ m/s$, the gauge length $L_0 = 8\ mm$ and the cross-section diameter $\Phi = 3\ mm$. A loading time of $t = 101.5\ \mu s$ is selected. The field variables are initialized. A comparison between intact and flawed materials is conducted.

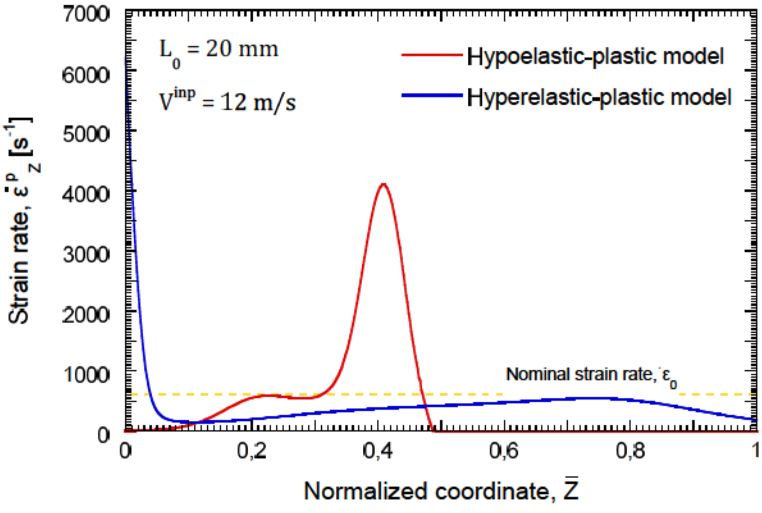

Figure 8.25: Finite difference results. We show a comparison between hypoelastic and hyperelastic-based models. Axial plastic strain rate $\dot{\varepsilon}^p_Z$ as a function of the normalized coordinate $\bar{Z}$. The impact velocity is $V^{inp} = 12\ m/s$, the gauge length $L_0 = 20\ mm$ and the cross-section diameter $\Phi = 3\ mm$. The mesh density is $M = 500$.

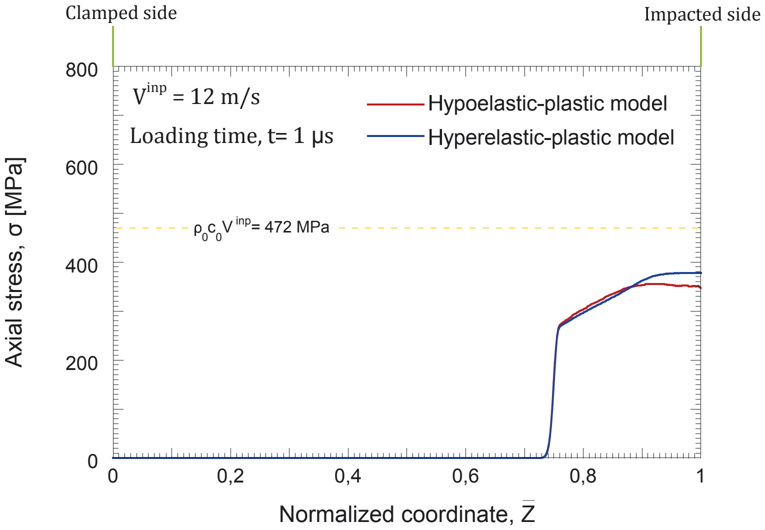

(a)

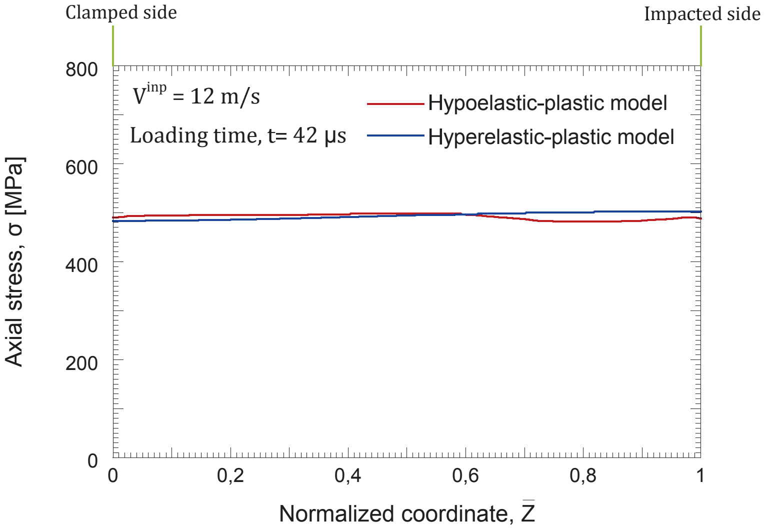

(b)

Figure 8.26: Finite difference results. We show a comparison between hypoelastic and hyperelastic-based models. Cauchy stress σ as a function of the normalized coordinate $\bar{Z}$. The impact velocity is $V^{inp} = 12\ m/s$, the gauge length $L_0 = 20\ mm$ and the cross-section diameter $\Phi = 3\ mm$. The mesh density is $M = 500$. Two different loading times are explored: (a) $t = 1\ \mu s$ and (b) $t = 42\ \mu s$.

The sensitivity of the necking localization to the constitutive model is a key finding of this chapter. Nevertheless, we acknowledge that further investigation are required. We still need to uncover the specific features of the hypoelastic and hyperelastic-based formulations which trigger the difference in the numerical predictions. While we have already carried you some progresses on this issue, we still have a long way to go before understanding all the physical and mathematical concepts involved in this problem. Unfortunately, it is too early for us to draw further conclusions.

8.3 Discussion and conclusions

In this chapter we have developed a simple one-dimensional finite difference model in MATLAB to analyse flow localization in elastoplastic rods subjected to dynamic stretching. The goal is to complement and extend the experimental and finite element results presented in chapters 6 and 7. The key point of our finite difference computations is that, unlike the finite element calculations of chapter 7, we solve the kinematics. This allows for a complete control of the problem at hand.

Taking advantage of the large flexibility of our finite difference model, we have explored the role played by impact velocity, specimen length, material properties, material defects and initial conditions on flow localization. We have shown the stress waves intervention within the specimen and explained the mechanics of flow localization. We have revealed the effect of strain hardening, strain rate hardening and material density in the deformation behaviour of the rod. In this regard, we claim that our finite difference model is a promising tool to analyse the equilibrium *(or lack of it)* in dynamic tensile specimens used, for instance, is Split Hopkinson Tensile Bar experiments. On the one hand, we have rationalized that material flaws (may) play a secondary role within the mechanisms which control dynamic necking inception. On the other hand, we have shown that defects are required to generate stress waves, and thus localization, in fully equilibrated specimens. Finally, we have investigated the constitutive sensitivity of the dynamic tensile problem. We have shown that hypoelastic and hyperelastic-based models provide different predictions for the necking location. This key finding still deserves further research.

All in all, in this chapter of the Thesis we provide a comprehensive analysis of the key factors which control necking inception in cylindrical bars subjected to dynamic tension.

9 Summary and conclusions

In this chapter we summarize the research conducted in this Doctoral Thesis and highlight the main scientific achievements. On the one hand we emphasize the solid foundations of the Continuum Mechanics theory which served as a basis for our research. On the other hand we show that this research meets the requirements of originality and creativity that are demanded to any doctoral work.

9.1 Summary and conclusions

This Doctoral Research have yield to new experimental and numerical results within the context of elastoplastic solids subjected to dynamic tension. A key point is that our original scientific contributions are supported by a strong theoretical background which is founded on the fundamental principles of the Continuum Mechanics theory. Another critical issue is our innovative methodology in which the numerical findings are backed by a comprehensive, and reliable, set of experiments.

We summarize below the main outcomes derived from experiments, finite elements and finite differences:

- **Experiments**. We have developed a thorough experimental campaign that leaves no doubt about the deterministic nature of the flow localization in the dynamic tensile test.

Dynamic tensile experiments have been conducted at several impact velocities using specimens with various gauge lengths. We have shown that the location of flow localization strongly depends on the sample dimensions and the applied velocity. The experiments show remarkable repeatability. Moreover, we have observed that multiple and largely regular necking bands emerge in many of the shortest specimens tested at high loading rates. We have highlighted the critical role played by the sample dimensions on the localization pattern of tensile specimens.

- **Finite elements**. We have conducted 3D finite element computations to uncover the role played by the initial and boundary conditions in the failure pattern of dynamic tensile specimens.

  The computations are devised to complement and rationalize the experimental findings. According to the experimental evidence, the finite element simulations show that variations in the applied velocity and the gauge length lead to the systematic motion of the plastic localization along the gauge. The qualitative agreement between experiments and numerics is understood as an additional proof of the deterministic character of flow localization. The finite element results demonstrated that the specimen ductility, instead of being a material property, is highly dependent on the sample size, the initial conditions and the boundary conditions.

- **Finite differences**. We have developed a 1D finite difference model which shows that the wave propagation phenomena is the critical factor which controls flow localization in dynamic tensile specimens.

  The finite difference model is derived from the basic principles of the Continuum Mechanics theory and, unlike the finite element calculations, allows to have complete control over the kinematic variables involved in the problem at hand. The computations illustrated the processes of reflection and interaction of waves that occur within the sample during loading. We have revealed important details on the propagation of strains along the specimen which serve to analyse the kinetics of flow localization. It has been shown that, in comparison with the wave propagation phenomena, material defects may play a secondary role in the formation of dynamic necks.

While much still needs to be done, our belief is that this Doctoral Thesis has provided new knowledge on the mechanics which control specimen failure in the dynamic tensile test.

[This page is intentionally left blank]

10

Future work

In this chapter we present a number of scientific matters that will be addressed in the near future in order to continue the research conducted in this Doctoral Thesis. On the basis of the scientific methodology that we have developed in this work, we identify experimental and numerical issues.

10.1 Future work

The formation and development of dynamic instabilities in elastopalstic solids subjected to impact loading is a fundamental problem poorly understood by the Continuum Mechanics community. While this Doctoral Thesis provides new ideas on the critical factors which control flow localization in dynamic tensile specimens, there is still much to be done in this field. The following is a list of specific issues that we are planning to address in a near future. The list is short on purpose, with the aim of highlighting the scientific matters that we will approach *right after* the PhD defence. We identify experimental and numerical issues:

Experimental issues:

- Record dynamic tensile tests using a digital image correlation technique in order to obtain experimental evidence of the gradients of strain and strain rate which develop inside a necked region.

- Perform dynamic tensile experiments using metallic samples with different thicknesses and widths in order to uncover the mechanisms which dictate the neck spacing in specimens which show multiple localization patterns.
- Carry out impact tensile tests using anisotropic metallic samples in order to show the role played by material properties on the orientation of the necking bands which preclude failure.
- Conduct impact tensile experiments using printed metallic specimens in order to asses the influence of material porosity in the localization of plastic deformations.

Numerical issues:

- Include in the current 1D finite differences scheme the Bridgman correction factor in order to reveal the stabilizing role played by stress mutiaxiality in the development of dynamic necks.
- Develop a 2D finite differences model in order to capture the formation and development of necking bands in metallic sheets subjected to dynamic stretching.
- Derive and integrate the constitutive equations of anisotropic elastoplastic solids in order to assess the role played by material anisotropy in the formation and development of dynamic necks.
- Formulate and integrate a constitutive framework for porous elastoplastic solids in order to analyse the role played by material porosity in the inception and evolution of necking instabilities.

To our knowledge, all these points are still open questions. On the other hand, the solid knowledge that we have gained during this Doctoral Research give us an excellent opportunity to solve them.

Appendices

[This page is intentionally left blank]

A

Mathematical preliminaries

In this appendix we present the main mathematical operations required to build the Continuum Mechanics framework. These are required to develop the theoretical structure presented in chapters 2, 3 and 4.

A.1 Algebra of vectors

In this section the basic definitions to operate with vectors are presented. The structure of this section is partially based on the works of Hashiguchi and Yamakawa [63] and Holzapfel [1].

A.1.1 Scalar product

The *inner product* or *scalar product* of the vectors **a** and **b** is defined by:

$$\mathbf{a} \cdot \mathbf{b} = \parallel \mathbf{a} \parallel \parallel \mathbf{b} \parallel \cos(\theta) = a_i b_i \tag{A.1}$$

where θ is the angle between the vectors **a** and **b**, and $\parallel\parallel$ defines the magnitude such that:

$$\parallel \mathbf{v} \parallel = \sqrt{v_i v_i} = \sqrt{\mathbf{v} \cdot \mathbf{v}} \tag{A.2}$$

The scalar product presents the following mathematical properties:

$$\mathbf{a} \cdot \mathbf{b} = \mathbf{b} \cdot \mathbf{a} \tag{A.3}$$

$$\mathbf{a} \cdot (\mathbf{b} + \mathbf{c}) = \mathbf{a} \cdot \mathbf{b} + \mathbf{a} \cdot \mathbf{c} \tag{A.4}$$

$$s(\mathbf{a} \cdot \mathbf{b}) = (s\mathbf{a} \cdot \mathbf{b}) = \mathbf{a} \cdot (s\mathbf{b}) = (\mathbf{a} \cdot \mathbf{b})s \tag{A.5}$$

$$(a\mathbf{a} + b\mathbf{b}) \cdot \mathbf{c} = a\mathbf{a} \cdot \mathbf{c} + b\mathbf{b} \cdot \mathbf{c} \tag{A.6}$$

The vector $\mathbf{v}$ is represented in terms of its components and the base vectors as follows:

$$\mathbf{v} = v_i \cdot \mathbf{e}_i, \tag{A.7}$$

where the components v_i are obtained if the projection of $\mathbf{v}$ onto the base vector $\mathbf{e}_i$ is made:

$$v_i = \mathbf{v} \cdot \mathbf{e}_i, \mathbf{v} = (\mathbf{v} \cdot \mathbf{e}_i)\, \mathbf{e}_i. \tag{A.8}$$

A.1.2 Vector product

The *vector* or *cross product* produces a new vector and is not commutative. It is defined as:

$$\mathbf{a} \times \mathbf{b} = \| \mathbf{a} \| \| \mathbf{b} \| \sin(\theta)\, \mathbf{n} = a_i \mathbf{e}_i \times b_j \mathbf{e}_j \tag{A.9}$$

where $\mathbf{n}$ is the unit vector which forms a right-handed base $(\mathbf{a}, \mathbf{b}, \mathbf{n})$ in this order.

Some of the main properties of the vector product are:

$$\mathbf{a} \times \mathbf{a} = 0 \tag{A.10}$$

$$\mathbf{a} \times \mathbf{b} = -\mathbf{b} \times \mathbf{a} \tag{A.11}$$

$$\mathbf{a} \times (\mathbf{b} + \mathbf{c}) = \mathbf{a} \times \mathbf{b} + \mathbf{a} \times \mathbf{c} \tag{A.12}$$

$$\| \mathbf{a} \times \mathbf{b} \|^2 + (\mathbf{a} \cdot \mathbf{b})^2 = (\| \mathbf{a} \| \| \mathbf{b} \|)^2 \tag{A.13}$$

A.1.3 Triple scalar product

The triple scalar (or box) product represents the volume V of the paralelepiped created from the triad $\mathbf{u}$, $\mathbf{v}$ and $\mathbf{w}$. It is defined by:

$$V = [\mathbf{abc}] \equiv \mathbf{a} \cdot (\mathbf{b} \times \mathbf{c}) = [\mathbf{bca}] \equiv \mathbf{b} \cdot (\mathbf{c} \times \mathbf{a}) = [\mathbf{cab}] \equiv \mathbf{c} \cdot (\mathbf{a} \times \mathbf{b}) \tag{A.14}$$

The triple scalar product can be also written using the determinant form as follows [1]:

$$(\mathbf{a} \times \mathbf{b}) \cdot \mathbf{w} = \begin{vmatrix} a_1 & b_1 & c_1 \\ a_2 & b_2 & c_2 \\ a_3 & b_3 & c_3 \end{vmatrix} \tag{A.15}$$

If the triple scalar product is zero, then the vectors $\mathbf{a}$, $\mathbf{b}$ and $\mathbf{c}$ are linearly dependent, that is, the parallelepiped has no volume.

A.1.4 Triple vector product

The product $\mathbf{a} \times (\mathbf{b} \times \mathbf{c})$ is called the **triple vector product**. The formulae of the vector product is described as follows, using the scalar product in section A.1.1:

$$\mathbf{a} \times (\mathbf{b} \times \mathbf{c}) = (\mathbf{a} \cdot \mathbf{c})\, \mathbf{b} - (\mathbf{b} \cdot \mathbf{c})\, \mathbf{a} \tag{A.16}$$

In a similar way

$$(\mathbf{a} \times \mathbf{b}) \times \mathbf{c} = (\mathbf{a} \cdot \mathbf{c})\, \mathbf{b} - (\mathbf{b} \cdot \mathbf{c})\, \mathbf{a} \tag{A.17}$$

Note that, in general, this operation is not associative, i.e. $(\mathbf{a} \times \mathbf{b}) \times \mathbf{c} \neq \mathbf{a} \times (\mathbf{b} \times \mathbf{c})$. The expressions (A.16) and (A.17) are called *back-cab* rule from vector algebra.

A.1.5 Tensor product

The tensor product (o dyadic product) of two vectors leads to a second-order tensor defined as $\mathbf{a} \otimes \mathbf{b}$. The main properties of this operator are:

$$\mathbf{a} \otimes \mathbf{b}\mathbf{c} = \mathbf{a}\left(\mathbf{b} \cdot \mathbf{c}\right) \tag{A.18}$$

$$\left(\mathbf{a} \otimes \mathbf{b}\right)^T = \mathbf{b} \otimes \mathbf{a} \tag{A.19}$$

$$\mathbf{a} \otimes \left(\mathbf{b} + \mathbf{c}\right) = \mathbf{a} \otimes \mathbf{b} + \mathbf{a} \otimes \mathbf{c} \tag{A.20}$$

$$\left(\mathbf{b} \otimes \mathbf{c} - \mathbf{c} \otimes \mathbf{b}\right)\mathbf{a} = \mathbf{a} \otimes \left(\mathbf{b} \otimes \mathbf{c}\right) = \left(\mathbf{a} \cdot \mathbf{c}\right)\mathbf{b} - \left(\mathbf{a} \cdot \mathbf{b}\right)\mathbf{c} \tag{A.21}$$

A.2 Algebra of tensors

A second-order tensor $\mathbf{A}$ can be defined as a linear operator that acts on a vector $\mathbf{u}$ generating a vector $\mathbf{v}$ following the next linear transformation [1]:

$$\mathbf{v} = \mathbf{A}\mathbf{u} \tag{A.22}$$

Any second-order tensor may be expressed as a dyadic, using the tensor product described in section A.1.5. For instance, if we consider the second-order tensor $\mathbf{A}$, it can be represented as a linear combination of dyads formed by the Cartesian basis $\{\mathbf{e}_i\}$, see Holzapfel [1]:

$$\mathbf{A} = A_{ij}\mathbf{e}_i \otimes \mathbf{e}_j \tag{A.23}$$

and tensor $\mathbf{A}$ can be also represented by its components A_{ij} with respect to $\{\mathbf{e}_i\}$, i.e:

$$[\mathbf{A}] = \begin{pmatrix} A_{11} & A_{12} & A_{13} \\ A_{21} & A_{22} & A_{23} \\ A_{31} & A_{32} & A_{33} \end{pmatrix} \tag{A.24}$$

or, using the Kronecker delta δ_{ij}:

$$A_{ij}\delta_{jk} = A_{ik} \tag{A.25}$$

The Kronecker delta allow us to express the unit tensor **I** in terms of its Cartesian components:

$$\mathbf{I} = \delta_{ij}\mathbf{e}_i \otimes \mathbf{e}_j = \mathbf{e}_j \otimes \mathbf{e}_j \tag{A.26}$$

A.2.1 Scalar product

The scalar (dot) product **AB** of two second-order tensors **A** and **B** is a second-order tensor whose components along an orthonormal basis $\mathbf{e}_i$ are, see Holzapfel [1]:

$$(\mathbf{AB})_{ij} = A_{ik}B_{kj} \tag{A.27}$$

The dot product of second-order tensors is not commutative, that is, $\mathbf{AB} \neq \mathbf{BA}$.

A.2.2 Transpose of a tensor

The transpose of a tensor **A** is $\mathbf{A}^T$ and fulfils the following equation:

$$\mathbf{a} \cdot \mathbf{A}\mathbf{b} = \mathbf{b} \cdot \mathbf{A}^T\mathbf{a} \tag{A.28}$$

for all generic vectors **a** and **b**.

Some properties of the tensor transpose are:

$$\left(\mathbf{A}^T\right)^T = \mathbf{A} \tag{A.29}$$

$$(\mathbf{AB})^T = \mathbf{B}^T\mathbf{A}^T \tag{A.30}$$

$$(\alpha\mathbf{A} + \beta\mathbf{B})^T = \alpha\mathbf{A}^T + \beta\mathbf{B}^T \tag{A.31}$$

$$(\mathbf{a} \otimes \mathbf{b})^T = \mathbf{a} \otimes \mathbf{b} \tag{A.32}$$

In the rectangular Cartesian coordinate system, selecting $\mathbf{a} = \mathbf{e}_i$ and $\mathbf{b} = \mathbf{e}_j$ in Eq. (A.28) leads to:

$$A_{ij}^T = A_{ij} \tag{A.33}$$

or, equivalently:

$$\mathbf{A}^T = \left(A_{ij}\mathbf{e}_i \otimes \mathbf{e}_j\right)^T = A_{ij}\mathbf{e}_j \otimes \mathbf{e}_i \tag{A.34}$$

A.2.3 Trace and contraction

The trace of a tensor $\mathbf{A}$ is a scalar denoted by $\mathrm{tr}\mathbf{A}$. If we sum up the diagonal terms of the second-order tensor $\mathbf{a} \otimes \mathbf{b}$, we get the dot product $\mathbf{a} \cdot \mathbf{b} = a_i b_i$ which is called the trace of $\mathbf{a} \otimes \mathbf{b}$:

$$\mathrm{tr}\left(\mathbf{a} \otimes \mathbf{b}\right) = \mathbf{a} \cdot \mathbf{b} = a_i b_i \tag{A.35}$$

The trace of a generic tensor $\mathbf{A}$ with respect to the orthonormal basis $\{\mathbf{e}_i\}$ is given by:

$$\begin{aligned}\mathrm{tr}\mathbf{A} &= \mathrm{tr}\left(A_{ij}\mathbf{e}_i \otimes \mathbf{e}_j\right) = A_{ij}\mathrm{tr}\left(\mathbf{e}_i \otimes \mathbf{e}_j\right) \\ &= A_{ij}\left(\mathbf{e}_i \cdot \mathbf{e}_j\right) = A_{ij}\delta_{ji} \\ &= A_{ii} = A_{11} + A_{22} + A_{33}\end{aligned} \tag{A.36}$$

The following properties hold for the trace of a tensor:

$$\mathrm{tr}\mathbf{A}^T = \mathrm{tr}\mathbf{A} \tag{A.37}$$

$$\mathrm{tr}\left(\mathbf{AB}\right) = \mathrm{tr}\left(\mathbf{BA}\right) \tag{A.38}$$

$$\mathrm{tr}\left(\mathbf{A} + \mathbf{B}\right) = \mathrm{tr}\mathbf{A} + \mathrm{tr}\mathbf{B} \tag{A.39}$$

$$\mathrm{tr}\left(\alpha\mathbf{A}\right) = \alpha\mathrm{tr}\mathbf{A} \tag{A.40}$$

The double dot product of two tensors **A** and **B** is a contraction operation which produces a scalar result. In index notation, a contraction means to identify two indices and sum over them as dummy indices. In symbolic notation a contraction is characterized by a dot, see Holzapfel [1]. A double contraction is represented by two dots as $\mathbf{A} : \mathbf{B}$. Using the tensor components with respect to the orthonormal basis $\{\mathbf{e}_i\}$, the double contraction is defined by:

$$\mathbf{A} : \mathbf{B} = A_{ij} B_{ij} \tag{A.41}$$

Since the i and j subscripts appear in both factors, they are both summed to give:

$$\begin{aligned} \mathbf{A} : \mathbf{B} = A_{ij} B_{ij} = A_{11} \cdot B_{11} + A_{12} \cdot B_{12} + A_{13} \cdot B_{13} + \\ A_{21} \cdot B_{21} + A_{22} \cdot B_{22} + A_{23} \cdot B_{23} + A_{31} \cdot B_{31} + A_{32} \cdot B_{32} + A_{33} \cdot B_{33} \end{aligned} \tag{A.42}$$

considering that **A** and **B** are second order tensors.

The double contraction of two tensors **A** and **B** can be also defined in terms of the trace as:

$$\begin{aligned} \mathbf{A} : \mathbf{B} = \mathrm{tr}\left(\mathbf{A}^T \mathbf{B}\right) = \mathrm{tr}\left(\mathbf{B}^T \mathbf{A}\right) \\ = \mathrm{tr}\left(\mathbf{A} \mathbf{B}^T\right) = \mathrm{tr}\left(\mathbf{B} \mathbf{A}^T\right) = \mathbf{B} : \mathbf{A} \end{aligned} \tag{A.43}$$

Some of the properties of double contraction are now listed [1]:

$$\mathbf{I} : \mathbf{A} = \mathrm{tr}\mathbf{A} = \mathbf{A} : \mathbf{I} \tag{A.44}$$

$$\mathbf{A} : (\mathbf{B}\mathbf{C}) = \left(\mathbf{B}^T \mathbf{A}\right) : \mathbf{C} = \left(\mathbf{A}\mathbf{C}^T\right) : \mathbf{B} \tag{A.45}$$

$$\mathbf{A} : (\mathbf{a} \otimes \mathbf{b}) = \mathbf{a} \cdot \mathbf{A}\mathbf{b} = (\mathbf{a} \otimes \mathbf{b}) : \mathbf{A} \tag{A.46}$$

$$(\mathbf{a} \otimes \mathbf{b}) : (\mathbf{c} \otimes \mathbf{d}) = (\mathbf{a} \cdot \mathbf{c})(\mathbf{b} \cdot \mathbf{d}) \tag{A.47}$$

$$(\mathbf{e}_i \otimes \mathbf{e}_j) : (\mathbf{e}_k \otimes \mathbf{e}_l) = (\mathbf{e}_i \cdot \mathbf{e}_k)(\mathbf{e}_j \cdot \mathbf{e}_l) \tag{A.48}$$

A.2.4 Orthogonal tensor

An orthogonal tensor $\mathbf{Q}$ is a linear transformation which fulfils the condition:

$$\mathbf{Qa} \cdot \mathbf{Qb} = \mathbf{a} \cdot \mathbf{b} \tag{A.49}$$

for all vectors $\mathbf{a}$ and $\mathbf{b}$. As can be seen in Eq. (A.49), the orthogonal transformation does not affect to the dot product $\mathbf{a} \cdot \mathbf{b}$. This means that both the magnitude of the vectors $\| \mathbf{u} \|$ and $\| \mathbf{v} \|$ and the angle θ formed by the vectors are unchanged.

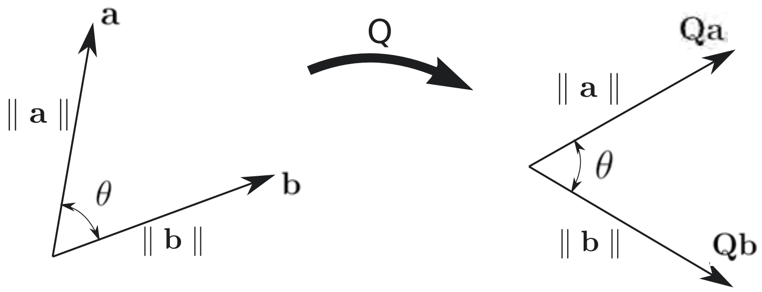

Figure A.1: Orthogonal tensor [1].

Combining the left-hand side in Eq. (A.49) with the transponse property given by Eq. (A.28), the equation becomes:

$$\mathbf{Qa} \cdot \mathbf{Qb} = \mathbf{a} \cdot \left(\mathbf{Q}^T \mathbf{Qb} \right). \tag{A.50}$$

Comparing Eqs. (A.49) and (A.50) we have that an orthogonal tensor must fulfil the following condition:

$$\mathbf{QQ}^T = \mathbf{Q}^T \mathbf{Q} = \mathbf{I} \tag{A.51}$$

which implies that:

$$\mathbf{Q}^{-1} = \mathbf{Q}^T \tag{A.52}$$

Another property is that:

$$\det\left(\mathbf{Q}^T\mathbf{Q}\right) = \left(\det\mathbf{Q}\right)^2. \tag{A.53}$$

where $\det\mathbf{Q} = \pm 1$. If $\det\mathbf{Q} = +1(-1)$, then $\mathbf{Q}$ is said to be proper (improper) orthogonal corresponding to a **rotation** (**reflection**), respectively.

Note that the orthogonal transformation also leaves the trace of two tensors unchanged:

$$\mathrm{tr}\left\{\left(\mathbf{QAQ}^T\right)\left(\mathbf{QBQ}^T\right)\right\} = \mathrm{tr}\left(\mathbf{AB}\right) \tag{A.54}$$

In addition, the magnitude of a tensor is unchanged under this transformation:

$$\| \mathbf{QTQ}^T \| = \| \mathbf{T} \| \tag{A.55}$$

A.2.5 Tensor decompositions

In this section are listed the main tensor decompositions.

A.2.5.1 Symmetric and skew-symmetric tensors

Any tensor $\mathbf{A}$ can always be uniquely decomposed into a **symmetric tensor S** and a **skew** or **antisymmetric** tensor $\mathbf{W}$ as follows [1]:

$$\mathbf{A} = \mathbf{S} + \mathbf{W} \tag{A.56}$$

where:

$$\mathbf{S} = \frac{1}{2}\left(\mathbf{A} + \mathbf{A}^T\right), \quad \mathbf{W} = \frac{1}{2}\left(\mathbf{A} - \mathbf{A}^T\right) \tag{A.57}$$

In matrix notation, $\mathbf{S}$ and $\mathbf{W}$ are:

$$[\mathbf{S}] = \begin{bmatrix} S_{11} & S_{12} & S_{13} \\ S_{12} & S_{22} & S_{23} \\ S_{13} & S_{23} & S_{33} \end{bmatrix}, \qquad [\mathbf{W}] = \begin{bmatrix} 0 & W_{12} & W_{13} \\ -W_{12} & 0 & W_{23} \\ -W_{13} & -W_{23} & 0 \end{bmatrix} \tag{A.58}$$

This decomposition is called the *Cartesian decomposition.* Tensors **S** and **W** satisfy:

$$\mathbf{S} = \mathbf{S}^T, \quad \mathbf{W} = -\mathbf{W}^T \tag{A.59}$$

$$\mathbf{a} \cdot \mathbf{S}\mathbf{b} = \mathbf{b} \cdot \mathbf{S}\mathbf{a} \tag{A.60}$$

$$\mathbf{a} \cdot (\mathbf{W}\mathbf{b}) = -\mathbf{b} \cdot (\mathbf{W}\mathbf{a}) \tag{A.61}$$

In addition we have that:

$$\mathbf{S}\mathbf{S}^T = \mathbf{S}^2, \tag{A.62}$$

$$\mathrm{tr}\,(\mathbf{S}\mathbf{W}) = \mathrm{tr}\left(\mathbf{S}\mathbf{W}^{\mathbf{T}}\right) = 0 \tag{A.63}$$

Using the double dot contraction in Eq. (A.41), the following properties arise:

$$\mathbf{S} : \mathbf{B} = \mathbf{S} : \mathbf{B}^T = \mathbf{S} : \frac{1}{2}\left(\mathbf{B} + \mathbf{B}^T\right) \tag{A.64}$$

$$\mathbf{W} : \mathbf{B} = -\mathbf{W} : \mathbf{B}^T = \mathbf{W} : \frac{1}{2}\left(\mathbf{B} - \mathbf{B}^T\right) \tag{A.65}$$

$$\mathbf{S} : \mathbf{W} = 0 \tag{A.66}$$

where **B** is any second-order tensor.

A.2.5.2 Spherical and deviatoric tensors

Any generic tensor **A** can be decomposed into a *spherical part* and a *deviatoric part* [1]:

$$\mathbf{A} = \alpha \mathbf{I} + \mathrm{dev}\mathbf{A} \tag{A.67}$$

$$\alpha = \frac{1}{3}\mathrm{tr}\mathbf{A} = \frac{1}{3}\left(\mathbf{I} : \mathbf{A}\right) \tag{A.68}$$

The first term in Eq. (A.67), in which α is a scalar, is known as a **spherical tensor**, while the second term in Eq. (A.67) is the **deviatoric** part of tensor **A**.

If the trace of the deviatoric part of tensor **A** is computed, we have that:

$$\mathrm{tr}\left(\mathrm{dev}\mathbf{A}\right) = 0 \tag{A.69}$$

A.2.6 Higher-order tensors

Any tensor of order n may be expressed in the form:

$$A_{i_1 i_2 \ldots i_n} \mathbf{e}_{i_1} \otimes \mathbf{e}_{i_2} \otimes \ldots \otimes \mathbf{e}_{i_n} \tag{A.70}$$

where a tensor of order n has 3^n components $A_{i_1 i_2 \ldots i_n}$ provided with n indices $i_1, i_2, \ldots, i_n$.

Let $\boldsymbol{\mathcal{E}}$ denote the third-order **permutation tensor** expressed as:

$$\boldsymbol{\mathcal{E}} = \varepsilon_{ijk} \mathbf{e}_i \otimes \mathbf{e}_j \otimes \otimes \mathbf{e}_k \tag{A.71}$$

Then, the following expression arises:

$$\boldsymbol{\mathcal{E}} : (\mathbf{u} \otimes \mathbf{v}) = \mathbf{v} \times \mathbf{u} \tag{A.72}$$

A.3 General bases

A.3.1 General basis vectors

Consider the fixed set $\{\mathbf{g}_i\}_{i\in\{1,2,3\}}$ of basis vectors. Vectors $\mathbf{g}_1$, $\mathbf{g}_2$, $\mathbf{g}_3$ of this basis are the **covariant basis vectors**. Despite they may not fulfil the orthogonality condition to each other or to be unit vectors, they must be non-zero and non-parallel. Thus, the vectors in the basis are linearly independent, that is, $(\mathbf{g}_1 \otimes \mathbf{g}_s) \cdot \mathbf{g}_3 \neq 0$.

Following the same assumptions, a new basis called **reciprocal or dual basis** of $\{\mathbf{g}_i\}$ is the fixed set $\{\mathbf{g}^i\}_{i\in\{1,2,3\}}$. Each component $\mathbf{g}^1$, $\mathbf{g}^2$, $\mathbf{g}^3$ of this basis are called **contravariant basis vectors** or **reciprocal basis vectors**.

The covariant $\{\mathbf{g}_i\}$ and contravariant $\{\mathbf{g}^i\}$ basis fulfill the following condition:

$$\mathbf{g}^i \cdot \mathbf{g}_j = \delta^i_j \tag{A.73}$$

where δ^i_j is the **Kronecker delta**. Eq. (A.73) means that each vector of a basis is orthogonal to the two vectors of the other basis whose indices are different, see Fig. (A.2).

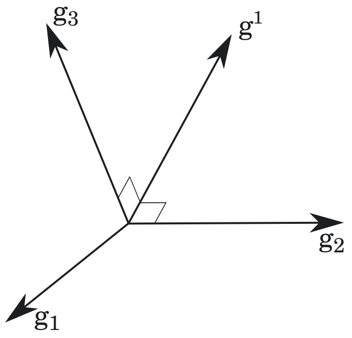

Figure A.2: General basis $\{\mathbf{g}_i\}$, $\mathbf{g}^1$ is orthogonal to $\mathbf{g}_2$ and $\mathbf{g}_3$. Adapted from Holzapfel [1].

The following property of the vectors in both basis arise:

$$\mathbf{g}^i \cdot \mathbf{g}^j = g^{ij}, \qquad \mathbf{g}_i \cdot \mathbf{g}_j = g_{ij} \tag{A.74}$$

or g^{ji} and g_{ji} because the dot product is commutative. For the particular cases in which $i = j$, it can be obtained the square of the length of the basis vector, i.e, $g_{11} =\mid \mathbf{g}_1 \mid^2$. This quantity determine the geometrical characteristic or **metric** of a basis. These values are also called g^{ij} and g_{ij} **metric coefficients**.

Some additional properties can be attained:

$$\mathbf{g}^i = g^{ij}\mathbf{g}_j, \qquad \mathbf{g}_i = g_{ij}\mathbf{g}^j \tag{A.75}$$

and the reciprocal property:

$$g^{ij}g_{kj} = \delta^i_k \tag{A.76}$$

which can be expressed as $[g_{ij}] = [g^{ij}]^{-1}$.

Remark A.1. It has to be noted that, if the basis is orthonormal, then $g^i = g_i$ and it is not necessary to distinguish between covariant and contravariant vector in the basis, as it happens in the Cartesian basis.

A.3.2 Covariant and contravariant components of a vector

Using the basis described in the section A.3.1, a generic vector **u** can be expressed as a linear combination of the contravariant or covariant basis vectors as follows:

$$\mathbf{u} = u_i\mathbf{g}^i = u^i\mathbf{g}_i \tag{A.77}$$

in which the components with the subscript u_i are the covariant components of **u** in the basis $\{\mathbf{g}^i\}$ and the components with the superscript u^i are the contravariant components of **u** in the basis $\{\mathbf{g}_i\}$. The covariant vector is the one described in covariant components. If the contravariant components are used, then it is a contravariant vector.

A.3.3 Covariant, contravariant and mixed components of a tensor

A generic tensor **A** can be represented with respect to a basis consisting of tensor products of the covariant and contravariant vectors:

$$\mathbf{A} = A^{ij}\mathbf{g}_i \otimes \mathbf{g}_j = A_{ij}\mathbf{g}^i \otimes \mathbf{g}^j = A^i_j\mathbf{g}_i \otimes \mathbf{g}^j = A^j_i\mathbf{g}^i \otimes \mathbf{g}_j \tag{A.78}$$

where A^{ij} and A_{ij} are the contravariant and covariant components and A^i_j and A^j_i are the mixed components of the tensor **A**. If a tensor **A** is symmetric ($A^{ij} = A^{ji}$ and $A_{ij} = A_{ji}$), and only under this assumption, mixed components A^i_j and A^i_j are equal.

A.3.4 Scalar, vector, tensor functions

A **tensor function** is a function whose arguments are *one* or *more* tensor variables and whose values are *scalars*, *vectors* or *tensors*. The functions $\Phi\left(\mathbf{B}\right)$,$\mathbf{u}\left(\mathbf{B}\right)$ and $\mathbf{A}\left(\mathbf{B}\right)$ are examples of so-called **scalar-valued**, **vector-valued** and **tensor-valued tensor functions** of *one* tensor variable **B**, respectively. In a similar way, $\Phi\left(\mathbf{u}\right)$, $\mathbf{v}\left(\mathbf{u}\right)$ and $\mathbf{A}\left(\mathbf{u}\right)$ are **vector functions** of *one* vector variable **u** with the value of a scalar, vector and tensor, respectively.

Finally, we can consider **scalar functions** of *one* scalar variable, i.e. time t, in such a way that $\Phi = \Phi(t)$, $\mathbf{u} = \mathbf{u}(t)$ and $\mathbf{A} = \mathbf{A}(t)$ be scalar-valued, vector-valued and tensor-valued scalar functions.

The first derivative of **u** and **A** with respect to t is

$$\dot{\mathbf{u}} = \frac{\mathrm{d}\mathbf{u}}{\mathrm{d}t}, \quad \dot{\mathbf{A}} = \frac{\mathrm{d}\mathbf{A}}{\mathrm{d}t}, \quad \dot{\Phi} = \frac{\mathrm{d}\Phi(t)}{\mathrm{d}t} \tag{A.79}$$

Making use of the rules of differentiation, we can obtain the following list of useful expressions:

$$\overset{\cdot}{\overline{\mathbf{u} \pm \mathbf{v}}} = \dot{\mathbf{u}} \pm \dot{\mathbf{v}} \tag{A.80}$$

$$\overset{\cdot}{\overline{\Phi \mathbf{u}}} = \dot{\Phi} \mathbf{u} + \Phi \dot{\mathbf{u}} \tag{A.81}$$

$$\overset{\cdot}{\overline{\mathbf{u} \otimes \mathbf{v}}} = \dot{\mathbf{u}} \otimes \mathbf{v} + \mathbf{u} \otimes \dot{\mathbf{v}} \tag{A.82}$$

$$\overset{\cdot}{\overline{\mathbf{A} \pm \mathbf{B}}} = \dot{\mathbf{A}} \pm \dot{\mathbf{B}} \tag{A.83}$$

$$\overset{\cdot}{\overline{\mathbf{A}^T}} = \dot{\mathbf{A}}^T \tag{A.84}$$

$$\overset{\cdot}{\overline{\mathrm{tr}\mathbf{A}}} = \mathrm{tr}\dot{\mathbf{A}} \tag{A.85}$$

$$\overset{\cdot}{\overline{\mathbf{A}^{-1}}} = -\mathbf{A}^{-1} \dot{\mathbf{A}} \mathbf{A}^{-1} \tag{A.86}$$

A.3.4.1 Gradient of a scalar-valued function

Considering the nonlinear scalar-valued function $\Phi(\mathbf{A})$ of the second-order tensor variable $\mathbf{A}$, the total differential $\mathrm{d}\Phi$ is:

$$\mathrm{d}\Phi = \frac{\partial \Phi(\mathbf{A})}{\partial \mathbf{A}} : \mathrm{d}\mathbf{A} = \mathrm{tr}\left[\left(\frac{\partial \Phi(\mathbf{A})}{\partial \mathbf{A}}\right)^T \mathrm{d}\mathbf{A}\right] \tag{A.87}$$

and the first term of the right-hand side is the **gradient** of the function Φ at $\mathbf{A}$. This function can be approximated by a first-order Taylor's expansion:

$$\Phi(\mathbf{A} + \mathrm{d}\mathbf{A}) = \Phi(\mathbf{A}) + \mathrm{d}\Phi + o(\mathrm{d}\mathbf{A}) \tag{A.88}$$

Now we derive an important relation which is useful to obtain material derivatives. Considering the property of determinant $\det(\mathbf{AB}) = \det\mathbf{A}\det\mathbf{B}$, we can find (assuming that tensor $\mathbf{A}$ is invertible) that:

$$\det(\mathbf{A} + \mathrm{d}\mathbf{A}) = \det\left[\mathbf{A}\left(\mathbf{I} + \mathbf{A}^{-1}\mathrm{d}\mathbf{A}\right)\right] = \det\mathbf{A}\det\left(\mathbf{I} + \mathbf{A}^{-1}\mathrm{d}\mathbf{A}\right) \tag{A.89}$$

Using the description of determinant product in terms of the invariants, the last term in previous equation can be rewritten as follows:

$$\det\left(\mathbf{A}^{-1}\mathrm{d}\mathbf{A} + \mathbf{I}\right) = 1 + \mathrm{tr}\left(\mathbf{A}^{-1}\mathrm{d}\mathbf{A}\right) + o(\mathrm{d}\mathbf{A}) \tag{A.90}$$

where we consider just the first invariant because the second and third one are in fact functions of higher order of d**A**. Replacing this expression in Eq. (A.89) we obtain:

$$\det\left(\mathbf{A}+\mathrm{d}\mathbf{A}\right)=\det\mathbf{A}\left[1+\operatorname{tr}\left(\mathbf{A}^{-1}\mathrm{d}\mathbf{A}\right)\right]+o\left(\mathrm{d}\mathbf{A}\right) \tag{A.91}$$

Using Eqs. (A.87) and (A.88) we have:

$$\begin{aligned}\det\left(\mathbf{A}+\mathrm{d}\mathbf{A}\right)&=\det\mathbf{A}+\operatorname{tr}\left[\left(\frac{\partial\det\mathbf{A}}{\partial\mathbf{A}}\right)^{T}\mathrm{d}\mathbf{A}\right]+o\left(\mathrm{d}\mathbf{A}\right)\\&=\mathrm{d}\mathbf{A}+\operatorname{tr}\left(\det\mathbf{A}\mathbf{A}^{-1}\mathrm{d}\mathbf{A}\right)+o\left(\mathrm{d}\mathbf{A}\right)\end{aligned} \tag{A.92}$$

Comparing previous expressions and using the transpose properties, we have that:

$$\begin{aligned}&\frac{\partial\det\mathbf{A}}{\partial\mathbf{A}}:\mathrm{d}\mathbf{A}=\left(\det\mathbf{A}\mathbf{A}^{-1}\right)^{T}:\mathrm{d}\mathbf{A}=\det\mathbf{A}\mathbf{A}^{T}:\mathrm{d}\mathbf{A}\\&\Longrightarrow\frac{\partial\det\mathbf{A}}{\partial\mathbf{A}}=\det\mathbf{A}\mathbf{A}^{-T}\end{aligned} \tag{A.93}$$

A.4 Gradients and related operators

Consider the **tensor field** $\mathbf{A}(\mathbf{x})$ and the **vector field** $\mathbf{u}(\mathbf{x})$ expressed in Cartersian coordinates x_i. Moreover, note that a **scalar field** $\Phi(\mathbf{x})$ of a body is defined as a function that assigns a scalar value Φ to each material point $\mathbf{x}$.

Thus, we can introduce the **Nabla vector operator** ∇, represented in index notation as ∂_i:

$$\nabla(\bullet)\equiv\partial_i\equiv\frac{\partial}{\partial x_i}\equiv\left(\frac{\partial}{\partial x_1},\frac{\partial}{\partial x_2},\frac{\partial}{\partial x_3}\right) \tag{A.94}$$

The nabla operator has the following properties:

- It follows the conventional rules of a derivative of a product and it operates on the tensors to their right.
- It behaves like any other vector in algebraic operations.

The dot product, cross product and tensor product of the vector operator ∇ with a smooth vector or tensor field $(\bullet)$ is governed by the rules:

$$\nabla \cdot (\bullet) = \frac{\partial(\bullet)}{\partial x_i} \cdot \mathbf{e_i}, \qquad \nabla \times (\bullet) = \mathbf{e_i} \times \frac{\partial(\bullet)}{\partial x_i}, \qquad \nabla \otimes (\bullet) = \frac{\partial(\bullet)}{\partial x_i} \otimes \mathbf{e_i} \tag{A.95}$$

in which $\mathbf{e}_i$ is the set of basis vectors of the Cartesian coordinate system.

A.4.1 Gradient of a scalar field

If we consider a smooth scalar field $\Phi(\mathbf{x})$ continuously differentiable, then the gradient of Φ is the following vector field:

$$\mathrm{grad}\Phi = \nabla\Phi = \left(\frac{\partial\Phi}{\partial x_1}, \frac{\partial\Phi}{\partial x_2}, \frac{\partial\Phi}{\partial x_3}\right) \tag{A.96}$$

A.4.2 Gradient of a vector field

The gradient of a smooth *vector field* $\mathbf{u}(\mathbf{x})$ turns into a second-order *tensor field* and is given as:

$$\mathrm{grad}\mathbf{u} = \nabla \otimes \mathbf{u} = \frac{\partial u_i}{\partial x_j}\mathbf{e}_i \otimes \mathbf{e}_j \tag{A.97}$$

or, in matrix notation:

$$[\mathrm{grad}\mathbf{u}] = \begin{bmatrix} \frac{\partial u_1}{\partial x_1} & \frac{\partial u_1}{\partial x_2} & \frac{\partial u_1}{\partial x_3} \\ \frac{\partial u_2}{\partial x_1} & \frac{\partial u_2}{\partial x_2} & \frac{\partial u_2}{\partial x_3} \\ \frac{\partial u_3}{\partial x_1} & \frac{\partial u_3}{\partial x_2} & \frac{\partial u_3}{\partial x_3} \end{bmatrix} \tag{A.98}$$

A.4.3 Gradient of a second-order tensor field

The gradient of a smooth second-order tensor field $\mathbf{A}(\mathbf{x})$ leads to a third-order tensor field:

$$\mathrm{A} = \nabla \otimes \mathbf{A} = \frac{\partial A_{ij}}{\partial x_k} \mathbf{e}_i \otimes \mathbf{e}_j \otimes \mathbf{e}_k \tag{A.99}$$

A.4.4 Divergence of a vector field

The divergence of a smooth vector field $\mathbf{u}(\mathbf{x})$ is a scalar field expressed as follows:

$$\mathrm{div}\mathbf{u} = \nabla \cdot \mathbf{u} = \frac{\partial u_j}{\partial x_i} \mathbf{e}_j \cdot \mathbf{e}_i = \frac{\partial u_1}{\partial x_1} + \frac{\partial u_2}{\partial x_2} + \frac{\partial u_3}{\partial x_3} \tag{A.100}$$

A.4.5 Divergence of a second-order tensor field

The divergence of a smooth second-order tensor field $\mathbf{A}(\mathbf{x})$ is the following vector field:

$$\mathrm{div}\mathbf{A} = \nabla \cdot \mathbf{A} = \frac{\partial A_{ik}}{\partial x_j} \left(\mathbf{e}_i \otimes \mathbf{e}_k \right) \cdot \mathbf{e}_j = \frac{\partial A_{ik}}{\partial x_j} \delta_{kj} \mathbf{e}_i = \frac{\partial A_{ij}}{\partial x_j} \mathbf{e}_i \tag{A.101}$$

A.4.6 Laplacian

The Laplacian is an operation defined using the divergence and gradient operators in one operation:

$$\nabla^2(\bullet) = \nabla \cdot \nabla(\bullet) = \nabla \cdot \frac{\partial(\bullet)}{\partial x_i} \mathbf{e}_i = \frac{\partial^2(\bullet)}{\partial x_i \partial x_j} \mathbf{e}_i \cdot \mathbf{e}_j = \frac{\partial^2(\bullet)}{\partial x_i \partial x_j} \delta_{ij} = \frac{\partial^2(\bullet)}{\partial x_i^2} \tag{A.102}$$

The Laplacian ∇^2 of a scalar field Φ results in the following scalar field:

$$\nabla^2(\Phi) = \frac{\partial^2 \Phi}{\partial x_1^2} + \frac{\partial^2 \Phi}{\partial x_2^2} + \frac{\partial^2 \Phi}{\partial x_3^2} \tag{A.103}$$

Various identities are included below:

$$\begin{aligned}
\mathrm{div}(\Phi\mathbf{u}) &= \Phi\mathrm{div}\mathbf{u} + \mathbf{u}\cdot\mathrm{grad}\Phi \\
\mathrm{div}(\Phi\mathbf{A}) &= \Phi\mathrm{div}\mathbf{A} + \mathbf{A}\mathrm{grad}\Phi \\
\mathrm{div}(\mathbf{A}^T\mathbf{u}) &= \mathrm{div}\mathbf{A}\cdot\mathbf{u} + \mathbf{A}:\mathrm{grad}\mathbf{u} \\
\mathrm{div}(\mathbf{u}\otimes\mathbf{v}) &= (\mathrm{grad}\mathbf{u})\mathbf{v} + \mathbf{u}\mathrm{div}\mathbf{v} \\
\mathrm{grad}(\Phi\Psi) &= (\mathrm{grad}\Phi)\Psi + \Phi\mathrm{grad}\Psi \\
\mathrm{grad}(\Phi\mathbf{u}) &= \mathbf{u}\otimes\mathrm{grad}\Phi + \Phi\mathrm{grad}\mathbf{u} \\
\mathrm{grad}(\mathbf{u}\cdot\mathbf{v}) &= (\mathrm{grad}^T\mathbf{u})\mathbf{v} + (\mathrm{grad}^T\mathbf{v})\mathbf{u}
\end{aligned} \tag{A.104}$$

A.5 Integral theorems

This section is adapted from Holzapfel [1].

A.5.1 Divergence theorem

The divergence theorem, also known as **Gauss's theorem** or **Ortrogradsky's theorem**, states that the density, in absence of creation or destruction of matter within a region of space, only changes if exists a flow crossing the boundary of that region. Consider $\mathbf{u}(\mathbf{x})$ a smooth vector field and $\mathbf{A}(\mathbf{x})$ a smooth tensor field defined on a three-dimensional region in space with volume v. Then, the divergence theorem states that:

$$\int_s \mathbf{u}\cdot\mathbf{n}ds = \int_v \mathrm{div}\mathbf{u}dv \tag{A.105}$$

$$\int_s \mathbf{A}\cdot\mathbf{n}ds = \int_v \mathrm{div}\mathbf{A}dv \tag{A.106}$$

where $\mathbf{n}$ is the outward unit normal field acting along the surface s and dv is the infinitesimal volume elements at $\mathbf{x}$.

A.5.2 Reynolds transport theorem

Reynolds transport theorem or Leibniz-Reynolds transport theorem, is a three-dimensional generalization of the Leibniz integral rule. It is used to compute derivatives of integrals. Reynolds theorem is used to formulate the basic conservation laws of continuum mechanics and specifically large-deformation solid mechanics (see chapter 3). The Reynolds' transport theorem allows us to compute the material time derivative of a volume integral for a spatial scalar field $\Phi = \Phi(\mathbf{x}, t)$ describing some physical quantity:

$$I(t) = \int_{\Omega} \Phi(\mathbf{x}, t) dv \tag{A.107}$$

Since the current region Ω depends on time t, integration and time differentiation do not commute; so $I(t)$ must be transformed to the reference configuration. Using the motion $\mathbf{x} = \chi(\mathbf{X}, t)$ and the expression of the volume ratio $dv = J(\mathbf{X}, t) dV$, the time rate of change of $I(t)$ is:

$$\dot{I}(t) = \frac{D}{Dt} \int_{\Omega} \Phi(\mathbf{x}, t) dv = \frac{D}{Dt} \int_{\Omega_0} \Phi\left(\chi(\mathbf{X}, t), t\right) J(\mathbf{X}, t) dV \tag{A.108}$$

Using the product rule of differentiation and rearranging this expression we have that:

$$\begin{aligned}
\frac{D}{Dt} \int_{\Omega} \Phi(\mathbf{x}, t) dv &= \int_{\Omega_0} \left[\dot{\Phi}\left(\chi(\mathbf{X}, t), t\right) J(\mathbf{X}, t) + \Phi\left(\chi(\mathbf{X}, t), t\right) \dot{J}(\mathbf{X}, t)\right] dV \\
&= \int_{\Omega_0} \left[\dot{\Phi}\left(\chi(\mathbf{X}, t), t\right) + \Phi\left(\chi(\mathbf{X}, t), t\right) \frac{\dot{J}(\mathbf{X}, t)}{J(\mathbf{X}, t)}\right] J(\mathbf{X}, t) dV \\
&= \int_{\Omega} \left[\dot{\Phi}(\mathbf{x}, t) + \Phi(\mathbf{x}, t) \frac{\dot{J}(\mathbf{X}, t)}{J(\mathbf{X}, t)}\right] dv \\
&= \int_{\Omega} \left[\dot{\Phi}(\mathbf{x}, t) + \Phi(\mathbf{x}, t) \mathrm{div} \mathbf{v}(\mathbf{x}, t)\right] dv
\end{aligned}$$

Which finally leads to:

$$\frac{D}{Dt} \int_{\Omega} \Phi(\mathbf{x}, t) dv = \int_{\Omega} \left[\dot{\Phi}(\mathbf{x}, t) + \Phi(\mathbf{x}, t) \mathrm{div} \mathbf{v}(\mathbf{x}, t)\right] dv \tag{A.109}$$

Applying the material time derivative we obtain an expression for the time rate of change of the integral $I(t)$:

$$\begin{aligned}\frac{D}{Dt}\int_{\Omega}\Phi(\mathbf{x},t)dv &= \int_{\Omega}\left[\frac{\partial\Phi}{\partial t} + \mathrm{grad}\Phi\cdot\mathbf{v} + \Phi\mathrm{div}\mathbf{v}\right]dv\\ &= \int_{\Omega}\left[\mathrm{div}(\Phi\mathbf{v}) + \frac{\partial\Phi}{\partial t}\right]dv\end{aligned}$$

An equivalent expression can be obtained using the divergence theorem developed in section A.5.1:

$$\frac{D}{Dt}\int_{\Omega}\Phi(\mathbf{x},t)dv = \int_{\partial\Omega}\Phi\mathbf{v}\cdot\mathbf{n}\mathrm{d}s + \int_{\Omega}\frac{\partial\Phi}{\partial t}dv \tag{A.110}$$

where the first term characterizes the rate of transport and the second term denotes the local time rate of change of the spatial scalar field Φ within region Ω. This relation is the Reynolds' transport theorem.

It can be obtained another useful expression of Reynolds' transport theorem if we consider the following scalar-valued function:

$$\overline{I}(t) = \int_{\Omega}\rho(\mathbf{x},t)\Psi(\mathbf{x},t)dv \tag{A.111}$$

where the expression (A.107) is modified using $\Phi = \rho\Psi$, where Φ is a generic spatial scalar field describing some physical quantity in space per unit *mass* and time t. Thus, we have the time rate of change of $\overline{I}(t)$ given by:

$$\frac{D}{Dt}\int_{\Omega}\rho\Psi dv = \int_{\Omega}\left(\dot{\overline{\rho\Psi}} + \rho\Psi\mathrm{div}\mathrm{v}\right)dv \tag{A.112}$$

Using the chain rule of the time derivative and the continuity mass equation $\dot{\rho} = -\rho\mathrm{div}\mathbf{v}$ we have that:

$$\dot{\overline{\rho\Psi}} = \rho\dot{\Psi} + \dot{\rho}\Psi = \rho\dot{\Psi} - \rho\Psi\mathrm{div}\mathbf{v} \tag{A.113}$$

Finally, we obtain:

$$\frac{D}{Dt}\int_{\Omega}\rho(\mathbf{x},t)\Psi(\mathbf{x},t)dv=\int_{\Omega}\rho(\mathbf{x},t)\dot{\Psi}(\mathbf{x},t)dv \tag{A.114}$$

A.6 Stoke's heat flux theorem

The counterpart of Cauchy's stress theorem (see section C.1.1) in continuum mechanics is the **Stoke's heat flux theorem** in thermodynamics.

It postulates that scalar functions q_n and Q_N are linear functions of the outward unit normals so that:

$$q_n\left(\mathbf{x},t,\mathbf{n}\right)=-\mathbf{q}\left(\mathbf{x},t\right)\cdot\mathbf{n} \tag{A.115}$$

$$Q_N\left(\mathbf{X},t,\mathbf{N}\right)=-\mathbf{Q}\left(\mathbf{X},t\right)\cdot\mathbf{N} \tag{A.116}$$

where $\mathbf{q}=\mathbf{q}\left(\mathbf{x},t\right)$ is the so-called **Cauchy heat flux** defined per unit surface area and $\mathbf{n}$ is the outward unit normal to an infinitesimal spatial surface area $\mathrm{d}s$ at the current position $\mathbf{x}$. Vector $\mathbf{Q}=\mathbf{Q}\left(\mathbf{X},t\right)$ is the **Piola-Kirchhoff heat flux** and $\mathbf{N}$ is the outward unit normal to an infinitesimal material surface element $\mathrm{d}S$ at $\mathbf{X}$.

A.7 The tensor exponential

This section is adapted from de Souza Neto et al. [67].

A.7.1 The tensor exponential function

Considering the following initial value problem [67]:

$$\dot{\mathbf{Y}}(t)=\mathbf{A}\mathbf{Y}(t) \tag{A.117}$$

with the initial condition:

$$\mathbf{Y}(t_0) = \mathbf{Y}_0 \tag{A.118}$$

where $\mathbf{A}$ and $\mathbf{Y}_0$ are constant tensors. The solution to this ordinary differential equation is the so-called *tensor exponential function*:

$$\mathbf{Y}(t) = \exp\left[(t - t_0)\,\mathbf{A}\right]\mathbf{Y}_0 \tag{A.119}$$

The exponential map for a generic tensor $\mathbf{X}$ can be expressed using a series representation:

$$\exp\left[\mathbf{X}\right] = \sum_{n=0}^{\infty} \frac{1}{n!}\mathbf{X}^n \tag{A.120}$$

Some properties of the tensor exponential function are briefly summarized here:

- The determinant of the exponential of a tensor satisfies:

  $$\det\left[\exp\left[\mathbf{X}\right]\right] = \exp\left[\mathrm{tr}\left[\mathbf{X}\right]\right] \tag{A.121}$$

  So it immediately implies that

  $$\mathrm{tr}\left[\mathbf{X}\right] = 0 \Longleftrightarrow \det\left[\exp\left[\mathbf{X}\right]\right] = 1 \tag{A.122}$$

- For any orthogonal tensor $\mathbf{Q}$:

  $$\exp\left[\mathbf{Q}\mathbf{X}\mathbf{Q}^T\right] = \mathbf{Q}\exp\left[\mathbf{X}\right]\mathbf{Q}^T \tag{A.123}$$

- For any generic tensor $\mathbf{X}$:

  $$\exp\left[-\mathbf{X}\right] = \left(\exp\left[\mathbf{X}\right]\right)^{-1} \tag{A.124}$$

- For any generic tensors $\mathbf{C}$ and $\mathbf{D}$, if the relation $\mathbf{C}\mathbf{D} = \mathbf{D}\mathbf{C}$ is fulfilled, then we have that:

$$\exp\left[\mathbf{C}+\mathbf{D}\right]=\exp\left[\mathbf{C}\right]\exp\left[\mathbf{D}\right]=\exp\left[\mathbf{D}\right]\exp\left[\mathbf{C}\right] \tag{A.125}$$

Previous expression implies that:

$$\exp\left[n\mathbf{X}\right]=\left(\exp\left[\mathbf{X}\right]\right)^{n} \tag{A.126}$$

A.7.2 Exponential map integrators

The exponential map can be used to solve various types of initial value problems similar to that defined by Eqs. (A.117) and (A.118):

$$\dot{\mathbf{Y}}(t)=\mathbf{A}(t)\mathbf{Y}(t) \tag{A.127}$$

with initial condition:

$$\mathbf{Y}(t_0)=\mathbf{Y}_0 \tag{A.128}$$

where tensor $\mathbf{A}$ depends on time t. This type of initial value problem plays an important role in finite computational mechanics (see chapter 4).

A.7.2.1 Generalised Exponential map midpoint rule

The exact solution given by Eq. (A.119) is useful to obtain approximations to the initial value problem defined by Eqs. (A.127) and (A.128). For that task a *generalised exponential map midpoint rule* can be used. If the time interval $[t_n, t_{n+1}]$ is considered, then an approximate solution is the exact solution at t_{n+1} considering $\mathbf{A}$ as a constant tensor. That is:

$$\mathbf{Y}_{n+1}=\exp\left[\Delta t\mathbf{A}\left(t_{n+\theta}\right)\right]\mathbf{Y}_n \tag{A.129}$$

where:

$$\Delta t\equiv t_{n+1}-t_n, \quad t_{n+\theta}\equiv t_n+\theta\Delta t \tag{A.130}$$

The parameter θ satisfies $0 \leq \theta \leq 1$. It is known that the *explicit* exponential map integrator is obtained if $\theta = 0$ is selected. $\theta = 1$ implies an *implicit* (or *backward*) exponential map integrator, and the general *midpoint* rule is derived if $\theta = \frac{1}{2}$ is taken.

[This page is intentionally left blank]

B

Material and spatial descriptions

In this appendix we present the main physical concepts and mathematical operations associated to the material (Lagrangian) and spatial (Eulerian) descriptions. These are needed to develop the theoretical structure presented in chapters 2, 3 and 4.

B.1 Material and spatial descriptions

This appendix is adapted from Hashiguchi and Yamakawa [63] and Holzapfel [1]. The **material description** characterizes any quantity (including the motion) with respect to the material coordinates (X_1, X_2, X_3) and time t. The salient feature of this description is that the material particles are observed as they move. This description is commonly called **Lagrangian configuration** (or **Lagrangian form**). On the contrary, if we focus on a specific point in space and analyze the evolution of the field variables at this point over time, then the mathematical description is known as the **Eulerian** (or **spatial**) **configuration** (or **Eulerian form**). It characterizes any quantity (including the motion) with respect to the spatial coordinates (x_1, x_2, x_3) and time t.

The Eulerian description is widely used in Fluid Mechanics, referring all quantities in spatial coordinates because material coordinates are usually not known. In Solid Mechanics, both descriptions are used, but the Lagrangian description is more frequently applied since the constitutive behaviour of deformable solids is given in terms of material coordinates.

B.2 Material derivatives

On one hand, a **material field** can be defined using the independent variables $(\mathbf{X}, t)$, in which $\mathbf{X}$ is the referential position and t the time. On the other hand, in a **spatial field** the independent variables are $(\mathbf{x}, t)$, that is, the current position $\mathbf{x}$ and the time t [1]. If we define a smooth **material field** $\mathcal{F} = \mathcal{F}(\mathbf{X}, t)$ and a **spatial field** $f = f(\mathbf{x}, t)$ of some physical scalar, vector o tensor associated with the motion χ, then the derivatives described in the following sections hold:

B.2.1 Material time derivative of a material field

The **material time derivative** represents the rate at which the material field $\mathcal{F}$ changes with time as monitored by an observer which follows the path line of a particle [1].

The material time derivative is denoted by:

$$\dot{\mathcal{F}}(\mathbf{X}, t) = \frac{\mathrm{D}\mathcal{F}(\mathbf{X}, t)}{\mathrm{D}t} = \left(\frac{\partial \mathcal{F}(\mathbf{X}, t)}{\partial t}\right)_X \tag{B.1}$$

Following the definition of directional derivative, another useful expression arises:

$$\frac{\mathrm{D}\mathcal{F}(\mathbf{X}, t)}{\mathrm{D}t} = D_v \mathcal{F}(\mathbf{X}, t) \tag{B.2}$$

where D_v is the directional derivative of $\mathcal{F}$ in the direction of the velocity vector $\mathbf{v}$.

The **material velocity field** and the **material acceleration field** are, respectively:

$$\mathbf{V}(\mathbf{X}, t) = \left(\frac{\partial \mathbf{U}(\mathbf{X}, t)}{\partial t}\right)_{\mathbf{X}} = \dot{\mathbf{U}} \tag{B.3}$$

$$\mathbf{A}(\mathbf{X}, t) = \left(\frac{\partial \mathbf{V}(\mathbf{X}, t)}{\partial t}\right)_{\mathbf{X}} = \dot{\mathbf{V}} \tag{B.4}$$

We consider that:

$$\dot{\mathbf{V}}\left(\mathbf{X},t\right)=\frac{\partial^{2}\mathbf{U}\left(\mathbf{X},t\right)}{\partial t^{2}}=\ddot{\mathbf{U}} \tag{B.5}$$

in order to define the material description of the material velocity **V** and the acceleration field **A** of a particle at time **t** using the time derivative of the displacement [1]:

$$\mathbf{A}=\dot{\mathbf{V}}=\ddot{\mathbf{U}} \tag{B.6}$$

B.2.1.1 Material gradient of a material field

Following Holzapfel [1], we define the **material gradient** of a smooth material field $\mathcal{F}\left(\mathbf{X},t\right)$ as:

$$\mathrm{Grad}\mathcal{F}\left(\mathbf{X},t\right)=\frac{\partial\mathcal{F}\left(\mathbf{X},t\right)}{\partial\mathbf{X}} \tag{B.7}$$

Similarly, the divergence operator can be used to calculate the **material divergence** of $\mathcal{F}$.

B.2.1.2 Spatial time derivative and spatial gradient of a spatial field

The **spatial time derivative** of a smoooth spatial field $f\left(\mathbf{x},t\right)$ is denoted by:

$$\frac{\partial f\left(\mathbf{x},t\right)}{\partial t} \tag{B.8}$$

Following the procedure of section B.2.1.1, the **spatial gradient** of f is:

$$\mathrm{grad}f\left(\mathbf{x},t\right)=\frac{\partial f\left(\mathbf{x},t\right)}{\partial\mathbf{x}} \tag{B.9}$$

and so on for the **spatial divergence**, see Holzapfel [1].

B.2.1.3 Material time derivative of a spatial field

The **material time derivative**, denoted by $\dot{f}\left(\mathbf{x},t\right)$, is the time derivative of the spatial field f holding $\mathbf{X}$ fixed. To compute the material time derivative is necessary to map f in the material description, operate to calculate the material time derivative and then go back to the spatial description:

$$\dot{f}\left(\mathbf{x},t\right)=\frac{\mathrm{D}f\left(\mathbf{x},t\right)}{\mathrm{D}t}=\left(\frac{\partial f\left[\mathcal{X}\left(\mathbf{X},t\right),t\right]}{\partial t}\right)_{\mathbf{X}=\mathcal{X}^{-1}(\mathbf{x},t)} \tag{B.10}$$

If Φ is a smooth spatial field which assigns a scalar $\Phi\left(\mathbf{x},t\right)$ to each point $\mathbf{x}$ at time t, then the time derivative is:

$$\dot{\Phi}\left(\mathbf{x},t\right)=\left(\frac{\partial\Phi(\mathbf{x},t)}{\partial t}\right)_{\mathbf{x}}+\left(\frac{\partial\Phi\left(\mathbf{x},t\right)}{\partial\mathbf{x}}\right)_{t}\cdot\left(\frac{\partial\mathcal{X}\left(\mathbf{X},t\right)}{\partial t}\right)_{\mathbf{X}=\mathcal{X}^{-1}(\mathbf{x},t)} \tag{B.11}$$

Using Eqs. (B.9) and (B.3) we have that:

$$\dot{\Phi}\left(\mathbf{x},t\right)=\frac{D\Phi(\mathbf{x},t)}{Dt}=\frac{\partial\Phi(\mathbf{x},t)}{\partial t}+\mathrm{grad}\Phi(\mathbf{x},t)\cdot\mathbf{v}\left(\mathbf{x},t\right) \tag{B.12}$$

The first term on the right-hand side of Eq. (B.12) is the spatial time derivative of the spatial scalar field Φ and the second term is called the **convective rate of change** of Φ, which describes the change of position of a particle.

Consider a specific spatial field, for instance, the spatial description of a velocity field $\mathbf{v}(\mathbf{x},t)$, which is vector-valued; then the material time derivative $\dot{\mathbf{v}}=\dot{\mathbf{v}}(\mathbf{x},t)$ is given by:

$$\dot{\mathbf{v}}\left(\mathbf{x},t\right)=\frac{\mathrm{D}\mathbf{v}\left(\mathbf{x},t\right)}{\mathrm{D}t}=\frac{\partial\mathbf{v}\left(\mathbf{x},t\right)}{\partial t}+\mathrm{grad}\mathbf{v}\left(\mathbf{x},t\right)\mathbf{v}\left(\mathbf{x},t\right) \tag{B.13}$$

The expression (B.13) is interpreted as the spatial acceleration field $\mathbf{a}=\dot{\mathbf{v}}$:

$$\mathbf{a}\left(\mathbf{x},t\right)=\frac{\partial\mathbf{v}}{\partial t}+\mathrm{grad}\mathbf{v}\mathbf{v} \tag{B.14}$$

The first term is the spatial acceleration or local rate of change of the velocity field, while the second term is called the **convective acceleration field**.

The spatial velocity field $\mathbf{v}(\mathbf{x}, t)$ can be expressed as the material time derivative of the motion $\mathbf{x} = \mathcal{X}(\mathbf{X}, t)$:

$$\mathbf{v} = \dot{\mathbf{x}} = \frac{\partial \mathbf{x}}{\partial t} = \dot{\mathbf{u}} \tag{B.15}$$

and the spatial acceleration field:

$$\mathbf{a} = \dot{\mathbf{v}} = \ddot{\mathbf{u}} \tag{B.16}$$

[This page is intentionally left blank]

C

Traction vectors, stress tensors and work conjugacy

In this appendix we develop and discuss the basic ideas related to the concept of stress. The fundamental theory associated to the traction vectors, the stress tensors and the work conjugacy is developed. This is required to build the Continuum Mechanics framework presented in chapters 2, 3 and 4.

C.1 Traction vectors and stress tensors

This section is adapted from Holzapfel [1]. We consider a deformable continuum body occupying a region Ω in space with a boundary surface $\partial\Omega$ at time t. We postulate that this solid is subjected to a set of arbitrary forces acting at the boundary surface and on a surface within the interior of this body.

We cut this body by a plane surface and consider the interaction between two resultant parts of the body. Force are transmitted across this plane surface. We consider the infinitesimal resultant force acting on a surface element as $\mathrm{d}\mathbf{f}$. For every surface element we have that:

$$\mathrm{d}\mathbf{f} = \mathbf{t}\mathrm{d}s = \mathbf{T}\mathrm{d}S \tag{C.1}$$

Vector $\mathbf{t} = \mathbf{t}\left(\mathbf{x}, t, \mathbf{n}\right)$ represents the **Cauchy** or true traction vector in the current configuration, exerted on $\mathrm{d}s$ with outward normal $\mathbf{n}$. Vector $\mathbf{T} = \mathbf{T}\left(\mathbf{X}, t, \mathbf{N}\right)$ represents the **first Piola-Kirchhoff** or nominal traction vector pointing in the same direction as $\mathbf{t}$. These tractions are commonly referred as **surface tractions**.

C.1.1 Cauchy's stress theorem

There exist unique second-order tensor fields $\boldsymbol{\sigma}$ and $\mathbf{P}$ so that:

$$\mathbf{t}\left(\mathbf{x}, t, \mathbf{n}\right) = \boldsymbol{\sigma}\left(\mathbf{x}, t\right)\mathbf{n} \tag{C.2}$$

$$\mathbf{T}\left(\mathbf{X}, t, \mathbf{N}\right) = \mathbf{P}\left(\mathbf{X}, t\right)\mathbf{N} \tag{C.3}$$

where $\boldsymbol{\sigma}$ is the symmetric spatial tensor field called the **Cauchy stress tensor** while $\mathbf{P}$ is the **first Piola-Kirchhoff stress tensor**. Eqs. (C.2) and (C.3) conform the well-known **Cauchy's stress theorem**.

Moreover, we combine Eq. (C.1) with Eqs. (C.2) and (C.3) to obtain the following transformation:

$$\mathbf{t}\left(\mathbf{x}, t, \mathbf{n}\right)\mathrm{d}s = \mathbf{T}\left(\mathbf{X}, t, \mathbf{N}\right)\mathrm{d}S \tag{C.4}$$

which leads to:

$$\boldsymbol{\sigma}\left(\mathbf{x}, t\right)\mathbf{n}\mathrm{d}s = \mathbf{P}\left(\mathbf{X}, t\right)\mathbf{N}\mathrm{d}S \tag{C.5}$$

Using Nanson's formula, i.e. Eq. (2.19), $\mathbf{P}$ can be written in the form:

$$\mathbf{P} = J\boldsymbol{\sigma}\mathbf{F}^{-T} \tag{C.6}$$

Previous expression is known as the *Piola transformation*. The inverse or this relation is:

$$\boldsymbol{\sigma} = J^{-1}\mathbf{P}\mathbf{F}^{T} = \sigma^{T} \tag{C.7}$$

which implies that the Cauchy stress tensor is symmetric but tensor $\mathbf{P}$ is, in general, not symmetric.

$$\mathbf{P}\mathbf{F}^{T} = \mathbf{F}\mathbf{P}^{T} \tag{C.8}$$

C.1.2 Alternative stress tensors

The first alternative stress tensor presented here is the so-called **Kirchhoff stress tensor $\boldsymbol{\tau}$**, which is a spatial tensor field related with the Cauchy stress tensor $\boldsymbol{\sigma}$ by the Jacobian determinant J as follows:

$$\boldsymbol{\tau} = J\boldsymbol{\sigma} \tag{C.9}$$

The **second Piola-Kirchhoff stress tensor S**, often used in computational mechanics, is defined as:

$$\mathbf{S} = \mathbf{F}^{-1}\boldsymbol{\tau}\mathbf{F}^{-T} \tag{C.10}$$

or, equivalently, in terms of the Cauchy stress tensor as:

$$\mathbf{S} = J\mathbf{F}^{-1}\boldsymbol{\sigma}\mathbf{F}^{-T} = \mathbf{F}^{-1}\mathbf{P} \tag{C.11}$$

From previous expression a fundamental relation arises:

$$\mathbf{P} = \mathbf{F}\mathbf{S} \tag{C.12}$$

C.2 Work conjugacy

It has been shown that the strain-stress pair is coupled in constitutive structure via an unified concept called work-conjugacy. This means that, independently of any material behaviour for selected strain measure, the corresponding stress measure has to be taken and vice versa [65].

The rate of internal mechanical work $\mathcal{P}_{int}$ in the balance of mechanical energy can be described using a series of alternative expressions that define the same stress power and allow us to determine the correct stress-strain conjugate pair:

$$\mathcal{P}_{int} = J\boldsymbol{\sigma} : \mathbf{d} = \mathbf{P} : \dot{\mathbf{F}} = \mathbf{S} : \dot{\mathbf{E}} \tag{C.13}$$

The double contraction of a stress tensor and its associated rate of deformation tensor describes the real physical power during a dynamical process or the rate of internal mechanical work. In this sense, the stress fields $J\boldsymbol{\sigma}$, $\mathbf{P}$, $\mathbf{S}$ are the **work conjugate** to the strain fields $\mathbf{d}$, $\dot{\mathbf{F}}$, $\dot{\mathbf{E}}$.

D

Remarks on the hyperelastic-plastic model

This appendix describes some salient features of the elastic predictor and the return mapping algorithm used in the hyperelastic-plastic model developed in chapter 4. We provide some computational details, following the procedure described by de Souza Neto et al. [67], that allow to obtain an extension to the finite range of the integration algorithm characteristic of the small-strains theory. In particular, we discuss the application of the logarithmic strain measure and the exponential integrator of the flow rule in the formulation of the constitutive equations.

D.1 Exponential map backward discretisation

The main difference between the discretisation of the finite strain problem and the infinitesimal one lies on the numerical approximation of the flow rule:

$$\mathbf{L}^p \equiv \dot{\mathbf{F}}^p \left(\mathbf{F}^p\right)^{-1} = \dot{\bar{\varepsilon}}^p \left(\mathbf{R}^e\right)^T \frac{\partial \Psi}{\partial \boldsymbol{\tau}} \mathbf{R}^e \tag{D.1}$$

Using a backward *exponential map integrator* (see section A.7.2 for further details), the following discretization of the plastic flow rule is obtained:

$$\mathbf{F}^{p^{n+1}} = \exp\left[\Delta\bar{\varepsilon}^p (\mathbf{R}^{e^{n+1}})^T \left.\frac{\partial \Psi}{\partial \boldsymbol{\tau}}\right|^{n+1} \mathbf{R}^{e^{n+1}}\right] \mathbf{F}^{p^n} \tag{D.2}$$

Considering the isotropy of the tensor exponential function, see section A.7.1, we have that:

$$\mathbf{F}^{p^{n+1}} = (\mathbf{R}^{e^{n+1}})^T \exp\left[\Delta\bar{\varepsilon}^p \left.\frac{\partial\Psi}{\partial\tau}\right|^{n+1}\right]\mathbf{R}^{e^{n+1}}\mathbf{F}^{p^n} \tag{D.3}$$

If we had adopted a standard backward Euler difference scheme to discretise the plastic flow equation (4.55), a different updating expression for the deformation gradient arises:

$$\mathbf{F}^{p^{n+1}} = \left(\mathbf{I} - \Delta\bar{\varepsilon}^p\mathbf{R}^{e^{n+1}})^T \left.\frac{\partial\Psi}{\partial\boldsymbol{\tau}}\right|^{n+1}\mathbf{R}^{e^{n+1}}\right)^{-1}\mathbf{F}^{p^n} \tag{D.4}$$

Remark D.1. The latter formula is not volume-preserving, i.e. given $\mathbf{F}^{p^n}$ such that $\det\mathbf{F}^{p^n} = 1$ and a traceless $\partial\Psi/\partial\boldsymbol{\tau}$, we obtain a $\mathbf{F}^{p^{n+1}}$ which $\det\mathbf{F}^{p^{n+1}} \neq 1$.

D.2 Logarithmic strains and infinitesimal return mapping scheme

We apply a multiplicative split to Eq. (D.3) and obtain the following expression to update the elastic deformation gradient:

$$\mathbf{F}^{e^{n+1}} = \mathbf{F}_\Delta\mathbf{F}^{e^n}(\mathbf{R}^{e^{n+1}})^T \exp\left[-\Delta\bar{\varepsilon}^p \left.\frac{\partial\Psi}{\partial\tau}\right|^{n+1}\right]\mathbf{R}^{e^{n+1}} \tag{D.5}$$

where $\mathbf{F}_\Delta$ is the incremental deformation gradient defined in Eq. (4.57).

The key point of this formulation is that the return-mapping scheme can be converted into the classical one if the logarithmic elastic strain measure is used (see section 4.3).

We multiply the equation (D.5) at both sides by $(\mathbf{R}^{e^{n+1}})^T$ to obtain:

$$\mathbf{V}^{e^{n+1}} = \mathbf{F}^{e^{n+1}}_{\text{trial}}(\mathbf{R}^{e^{n+1}})^T \exp\left[-\Delta\bar{\varepsilon}^p \left.\frac{\partial\Psi}{\partial\boldsymbol{\tau}}\right|^{n+1}\right] \tag{D.6}$$

An equivalent expression is derived using the exponential inversion:

$$\mathbf{V}^{e^{n+1}} \exp\left[\Delta\bar{\varepsilon}^p \left.\frac{\partial\Psi}{\partial\tau}\right|^{n+1}\right] = \mathbf{F}^{e^{n+1}}_{\text{trial}}(\mathbf{R}^{e^{n+1}})^T \tag{D.7}$$

Making use of the polar decomposition $\mathbf{V}^{e^{n+1}}_{\text{trial}} = \mathbf{F}^{e^{n+1}}_{\text{trial}}(\mathbf{R}^{e^{n+1}})^T$, equation (D.6) is reduced to:

$$\mathbf{V}^{e^{n+1}} = \mathbf{V}^{e^{n+1}}_{\text{trial}} \exp\left[-\Delta\bar{\varepsilon}^p \left.\frac{\partial\Psi}{\partial\tau}\right|^{n+1}\right] \tag{D.8}$$

We take the tensor logarithm at both sides of Eq. (D.8) to obtain the following expression in terms of the logarithmic strain tensor:

$$\varepsilon^{e^{n+1}} = \varepsilon^{e^{n+1}}_{\text{trial}} - \Delta\bar{\varepsilon}^p \left.\frac{\partial\Psi}{\partial\tau}\right|^{n+1} \tag{D.9}$$

Remark D.2. Note that the last expression has the mathematical structure of the elastic strain update formula in the backward return-mapping algorithm of the infinitesimal theory. This is a fundamental feature of the model and allows to retrieve the algorithm developed for the hypoelastic-plastic constitutive equations.

[This page is intentionally left blank]

E

Complete set of dynamic experiments

In this appendix we show a table with the complete set of dynamic experiments, providing the fracture location in each case. These results complement the selected experiments shown in chapter 6.

E.1 Complete set of dynamic experiments

The complete set of dynamic experiments is shown in Table E.1.

		Fracture location					
Velocity (m/s)	**Specimen**	$\mathbf{L_2 = 20}$ **mm**	$\mathbf{L_2 = 40}$ **mm**	$\mathbf{L_2 = 60}$ **mm**	$\mathbf{L_2 = 80}$ **mm**	$\mathbf{L_2 = 100}$ **mm**	$\mathbf{L_2 = 140}$ **mm**
1	**1**	*Centre*	*Impact*	*Impact*	*Impact*	*Clamped*	*Clamped*
	2	*Centre*	*Impact*	*Impact*	*Clamped*	*Clamped*	*Clamped*
	3	*Centre*	*Impact*	*Impact*	*Clamped*	*Clamped*	*Clamped*
	4	*N/A*	*N/A*	*N/A*	*Clamped*	*N/A*	*N/A*
1,75	**1**	*Centre*	*Impact*	*Clamped*	*Impact*	*Impact*	*Centre*
	2	*Centre*	*Impact*	*Clamped*	*Impact*	*Impact*	*Centre*
	3	*Centre*	*Clamped*	*Clamped*	*Impact*	*Impact*	*Centre*
	4	*N/A*	*Impact*	*N/A*	*N/A*	*N/A*	*N/A*
2,5	**1**	*Centre*	*Impact*	*Impact*	*Impact*	*Clamped*	*Centre*
	2	*Centre*	*Impact*	*Clamped*	*Clamped*	*Clamped*	*Centre*
	3	*Centre*	*Impact*	*Clamped*	*Clamped*	*Clamped*	*Centre*
	4	*Centre*	*N/A*	*Clamped*	*Clamped*	*N/A*	*N/A*
3,75	**1**	*Centre*	*Impact*	*Clamped*	*Clamped*	*Impact*	*Clamped*
	2	*Centre*	*Impact*	*Clamped*	*Centre*	*Impact*	*Impact*
	3	*Centre*	*Impact*	*Clamped*	*Clamped*	*Impact*	*Clamped*
	4	*N/A*	*N/A*	*Clamped*	*Clamped*	*N/A*	*Clamped*
5	**1**	*Centre*	*Impact*	*Clamped*	*Clamped*	*Clamped*	*Centre*
	2	*Centre*	*Impact*	*Clamped*	*Clamped*	*Clamped*	*Clamped*
	3	*Centre*	*Impact*	*Clamped*	*Clamped*	*Clamped*	*Centre*
	4	*N/A*	*N/A*	*N/A*	*N/A*	*N/A*	*Centre*
6,25	**1**	*Centre*	*Impact*	*Clamped*	*Clamped*	*Impact*	*Clamped*
	2	*Centre*	*Impact*	*Clamped*	*Clamped*	*Clamped*	*Clamped*
	3	*Centre*	*Impact*	*Clamped*	*Clamped*	*Impact*	*Clamped*
	4	*Centre*	*N/A*	*N/A*	*N/A*	*Impact*	*N/A*
7,5	**1**	*Centre*	*Impact*	*Impact*	*Clamped*	*Impact*	*Clamped*
	2	*Centre*	*Impact*	*Impact*	*Clamped*	*Clamped*	*Clamped*
	3	*Centre*	*Impact*	*Impact*	*Clamped*	*Clamped*	*Clamped*
	4	*N/A*	*N/A*	*N/A*	*N/A*	*Clamped*	*N/A*

Table E.1: Complete set of dynamic experiments. For each test we indicate the fracture location.

F

Finite difference method

In this appendix we present the salient features of the finite difference method, with emphasis in the mathematical concepts and operations used in the one-dimensional scheme developed in chapter 8.

F.1 Discretization

The physical systems are (usually) described using continuous mathematical functions, $f(x, t)$, and their derivatives is space and time. In order to represent or solve the (non-linear) partial differential equations defined by those functions, the continuous systems use to be discretized in space and time. The discretization methods can be divided into grid and gridless methods.

Within the **gridless** methods we highlight those which represent the function $f(x, t)$ as a superposition of continuous functions expressed in terms of sines and cosines. This technique is, for instance, the key point of the spectral methods. Another gridless method is the so-called smoothed particle hydrodynamics (SPH), which uses discrete particles to represent the mass distribution and generate continuous functions integrating over these particles with a kernel.

Within the **grid** methods we highlight the finite element, the finite difference and the finite volume methods. The finite-element method has become very popular in Solid Mechanics to face (material and geometrical) non-linear problems. The finite difference method is the *classical* procedure to solve (numerically) the differential form of the evolution equations which govern the initial boundary value problems of the Continuum Mechanics (see chapter 3). On the other hand, the finite volume method uses the integral form of the evolution equations.

F.2 Grid basics

The derivatives are represented numerically by discretizing the domain into a finite number of regions, transforming the continuous space into a discrete one. Although there are various grid methods, for instance those mentioned above, here we only deal with the finite difference format.

Fig. F.1 shows the two possible configurations in the finite difference method. The upper one displays the *common* finite difference grid, in which the function values f_i are evaluated in the points x_i regularly distributed in the mesh grid: $x_i = i\Delta X, \quad i = 0, \dots, N-1$. The other approach is the bottom grid shown in Fig. F.1. This grid is called a cell-centred finite difference grid. In this case, we also divide the region in an uniform grid but the function evaluation is conducted in the middle of each segment. The physical coordinate of the centres of each segment is $x_i = \left(i + \frac{1}{2}\right)\Delta X, \quad i = 0, \dots N-1$. Therefore, unlike the first configuration, in the second one the spatial coordinates are not located at the physical boundary of each end.

F.3 1-D differences on a uniform mesh

F.3.1 Finite difference approximations

Let us first address the discretized expressions for the continuous functions f which are sampled at discrete grid points X_i such as: $f\left(X_i\right) \equiv f_i$. For the simplest case, the discrete points in the grid are assumed to be ordered in a natural way from left to right as the figure below:

In the finite difference method, the partial differential equations are approximated by discrete equations. Note that for a given first-order partial derivative, there are several difference formats [122]. For instance, assuming a constant mesh spacing $\Delta X \equiv X_{i+1} - X_i \quad \forall i$, we can derive the following Taylor series [123]:

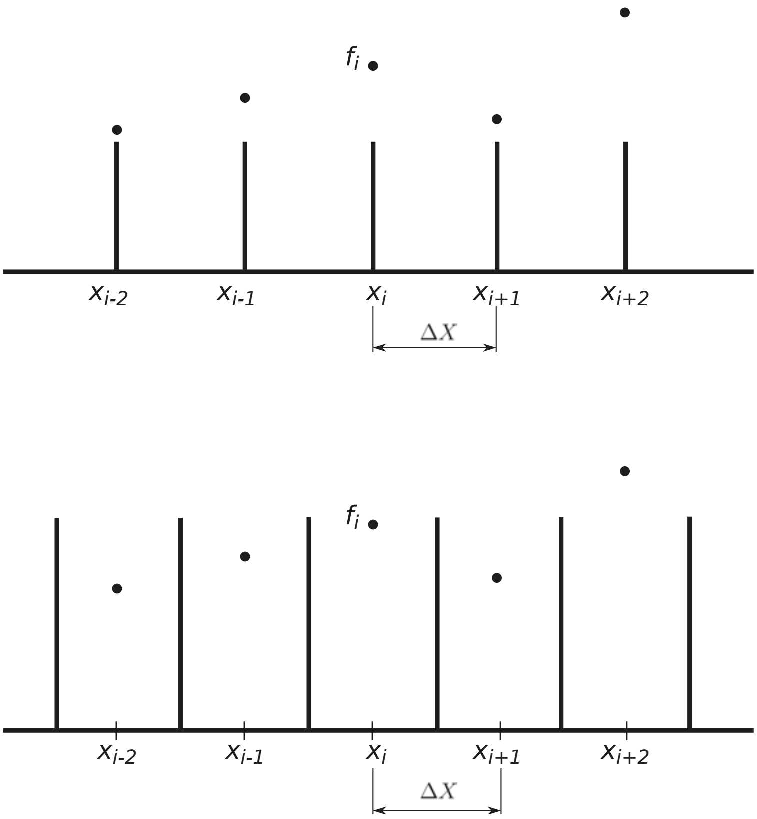

Figure F.1: Different types of structured grids. Top: a *common* finite difference grid. Bottom: cell centered finite difference grid.

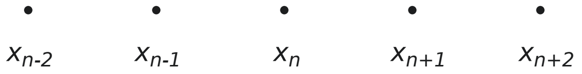

Figure F.2: Grid in space.

$$f_{i+1} = f_i + \Delta X \frac{\partial f_i}{\partial X} + \frac{(\Delta X)^2}{2!} \frac{\partial^2 f_i}{\partial X^2} + \mathcal{O}\left(\Delta X^3\right) \tag{F.1}$$

The first derivative is:

$$\frac{\partial f_i}{\partial X} = \frac{f_{i+1} - f_i}{\Delta X} - \frac{\Delta X}{2!} \frac{\partial^2 f_i}{\partial x^2} + \mathcal{O}\left(\Delta X^2\right) = \frac{\Delta f_i}{\Delta X} + \mathcal{O}\left(h\right) \tag{F.2}$$

At this stage is necessary to analyse whether the difference format is suitable to the specific partial differential equations to be solved [122]. We need to assess the accuracy of the solution evaluating the so called truncation errors. For instance, for the scheme above, the leading error is of the order of ΔX. Whether this error is acceptable or not, depends on the user and application requirements.

The second order derivative can be computed in a similar manner writing the corresponding Taylor series as:

$$f_{i+2} = f_i + 2\Delta X \frac{\partial f_i}{\partial X} + \frac{(2\Delta X)^2}{2!} \frac{\partial^2 f_i}{\partial X^2} + \frac{(2\Delta X)^3}{3!} \frac{\partial^3 f_i}{\partial X^3} + \ldots \tag{F.3}$$

We replace in the formula above the expression given by Eq. (F.2) in order to obtain:

$$\frac{\partial^2 f_i}{\partial X^2} = \frac{f_{i+2} - 2f_{i+1} + f_i}{(\Delta X)^2} - \Delta X \frac{\partial^3 f_i}{\partial X^3} + \ldots \equiv \frac{\Delta^2 f_i}{(\Delta X)^2} + \mathcal{O}(\Delta X) \tag{F.4}$$

This expression can be expressed using the following notation:

$$\frac{\partial^n f_i}{\partial x^n} = \frac{\Delta^n f_i}{(\Delta X)^n} + \mathcal{O}(\Delta X) \tag{F.5}$$

where $\Delta^n f_i$ indicates the difference between f_i and f_{i+1}. This approach is called the *forward difference* scheme. It has the following recursive property:

$$\Delta^n f_i = \Delta\left(\Delta^{n-1} f_i\right) \tag{F.6}$$

where the operator Δ describes the first forward difference.

In a similar manner, we define the so-called *backward difference* scheme:

$$f_{i-1} = f_i - \Delta X \frac{\partial f_i}{\partial X} + \frac{(\Delta X)^2}{2!} \frac{\partial^2 f_i}{\partial X^2} + \ldots \tag{F.7}$$

$$\frac{\partial^n f_i}{\partial X^n} = \frac{\nabla^n f_i}{(\Delta X)^n} + \mathcal{O}(\Delta X) \tag{F.8}$$

$$\nabla^n f_i = \nabla\left(\nabla^{n-1} f_i\right) \tag{F.9}$$

These two approximations are first-order in the mesh spacing ΔX. Nevertheless, it is possible to obtain higher order approximations raising the order in the Taylor series to have:

$$f_{i+1} = f_i + (\Delta X)\frac{\partial f_i}{\partial X} + \frac{(\Delta X)^2}{2!}\frac{\partial^2 f_i}{\partial X^2} + \frac{(\Delta X)^3}{3!}\frac{\partial^3 f_i}{\partial X^3} + \dots \tag{F.10}$$

$$f_{i+2} = f_i + 2(\Delta X)\frac{\partial f_i}{\partial X} + \frac{(2\Delta X)^2}{2!}\frac{\partial^2 f_i}{\partial X^2} + \frac{(2\Delta X)^3}{3!}\frac{\partial^3 f_i}{\partial X^3} + \dots \tag{F.11}$$

We perform a linear combination of last two equations and select the corresponding coefficient such that the second derivative term vanishes. Then, we obtain the following higher order expression for the first derivative:

$$\frac{\partial f_i}{\partial X} = \frac{-f_{i+2} + 4f_{i+1} - 3f_i}{2\Delta X} - \frac{(\Delta X)^2}{3!}\frac{\partial^3 f_i}{\partial X^3} + \mathcal{O}\left(\Delta X^3\right) \tag{F.12}$$

Moreover, a (commonly used) scheme with a higher order accuracy than the *forward* and *backward* format is the *central difference* approximation shown below:

$$\frac{\partial f_i}{\partial X} = \frac{\Delta f_i}{\Delta X} - \frac{\Delta X}{2!}\frac{\partial^2 f_i}{\partial X^2} + \mathcal{O}\left(\Delta X^2\right) \tag{F.13}$$

$$\frac{\partial f_i}{\partial X} = \frac{\nabla f_i}{\Delta X} - \frac{\Delta X}{2!}\frac{\partial^2 f_i}{\partial X^2} + \mathcal{O}\left(\Delta X^2\right) \tag{F.14}$$

We combine these two expressions to obtain:

$$\frac{\partial f_i}{\partial X} = \frac{\nabla f_i + \Delta f_i}{2\Delta X} + \mathcal{O}\left(\Delta X^2\right) \tag{F.15}$$

where

$$\nabla f_i + \Delta f_i = f_{i+1} - f_{i-1} \equiv \iota f_i \tag{F.16}$$

where ι represents the central difference operator. This scheme has a second order accuracy in ΔX.

F.3.1.1 Difference formulas with cross-derivatives

It may be the case that a mixed derivative with respect to two or more dimensions needs to be faced. A suitable approach to solve this problem is to apply the 2-D Taylor series such that:

$$f\left(X+\Delta X, y+\Delta y\right)=f\mid_{X,Y}+\left(\Delta X\frac{\partial}{\partial X}+\Delta Y\frac{\partial}{\partial Y}\right)f\mid_{X,Y}+ \tag{F.17}$$
$$+\frac{1}{2!}\left(\Delta X\frac{\partial}{\partial X}+\Delta Y\frac{\partial}{\partial Y}\right)^2 f\mid_{X,Y}+\frac{1}{3!}\left(\Delta X\frac{\partial}{\partial X}+\Delta Y\frac{\partial}{\partial Y}\right)^3 f\mid_{X,Y}+\dots$$

where:

$$\left(\Delta X\frac{\partial}{\partial X}+\Delta Y\frac{\partial}{\partial Y}\right)^2=\Delta X^2\frac{\partial^2}{\partial X^2}+2\Delta X\Delta Y\frac{\partial^2}{\partial X\partial Y}+\Delta Y^2\frac{\partial^2}{\partial Y^2} \tag{F.18}$$

An identical procedure shall be applied to obtain the rest of potential terms.

An alternative approach is to operate with the 1-D formula developed before. For instance, using an uniform (i,j) mesh spacing grid $(\Delta X, \Delta Y)$ we have that:

$$\frac{\partial^2 f}{\partial X\partial Y}=\frac{\partial}{\partial X}\left(\frac{\partial f}{\partial Y}\right)\simeq\frac{\left[\frac{f_{j+1}-f_{j-1}}{2\Delta Y}\right]_{i+1}-\left[\frac{f_{j+1}-f_{j-1}}{2\Delta Y}\right]_{i-1}}{2\Delta X} \tag{F.19}$$

F.3.2 Explicit scheme

We pay attention to the discretization of the $X-t$ plane and we include the time t as a variable to be discretized. This plane is meshed using a rectangular grid which defined by two groups of isometric straight lines parallel to the corresponding axes, see [123]:

$$\begin{aligned} X = X_k = k\Delta X \qquad & k = 0, \pm 1, \pm 2, \ldots \\ t = t_j = t_0 + j\Delta t \qquad & j = 0, 1, 2, \ldots \end{aligned} \tag{F.20}$$

where, as anticipated, ΔX and Δt are the steps (lengths) in the X and t directions, respectively. We consider that the node coordinate (X_k, t_j) is defined by (k, j) and $f(X_k, t_j)$ is defined by $f(k, j)$. Then, the following schemes are derived:

- *Forward difference* quotient:

$$\begin{aligned} \frac{\partial f}{\partial t}\,|_{(k,j)} &= \frac{f(k,j+1) - f(k,j)}{\Delta t} - \frac{\Delta t}{2}\frac{\partial^2 f(k,t_1)}{\partial t^2} \\ \frac{\partial f}{\partial X}\,|_{(k,j)} &= \frac{f(k+1,j) - f(k,j)}{\Delta X} - \frac{\Delta X}{2}\frac{\partial^2 f(X_1,j)}{\partial X^2} \end{aligned} \tag{F.21}$$

- *Backward difference* quotient:

$$\begin{aligned} \frac{\partial f}{\partial t}\,|_{(k,j)} &= \frac{f(k,j) - f(k,j-1)}{\Delta t} - \frac{\Delta t}{2}\frac{\partial^2 f(k,t_2)}{\partial t^2} \\ \frac{\partial f}{\partial X}\,|_{(k,j)} &= \frac{f(k,j) - f(k-1,j)}{\Delta X} - \frac{\Delta X}{2}\frac{\partial^2 f(X_2,j)}{\partial X^2} \end{aligned} \tag{F.22}$$

- *Central difference* quotient:

$$\begin{aligned} \frac{\partial f}{\partial t}\,|_{(k,j)} &= \frac{f(k,j+1) - f(k,j-1)}{2\Delta t} - \frac{\Delta t^2}{6}\frac{\partial^3 f(k,t_3)}{\partial t^3} \\ \frac{\partial f}{\partial X}\,|_{(k,j)} &= \frac{f(k+1,j) - f(k-1,j)}{2\Delta X} - \frac{\Delta X^2}{6}\frac{\partial^3 f(X_3,j)}{\partial X^3} \end{aligned} \tag{F.23}$$

where $t_j \leq t_1 \leq t_{j+1}$, $X_k \leq X_1 \leq X_{k+1}$, $t_{j-1} \leq t_2 \leq t_j$, $X_{k-1} \leq X_2 \leq X_k$, $t_{j-1} \leq t_3 \leq t_{j+1}$ and $X_{k-1} \leq X_3 \leq X_{k+1}$.

In the previous schemes, the partial derivative with respect to t is approximated by a forward difference. This means that, once the initial condition is given, the $f(k,1)$ of grid nodes on the first layer can be calculated [123]. In general, as soon as we know the $f(k,j)$ of the layer j the $f(k,j+1)$ of the layer $j+1$ can be calculated. This finite difference scheme is known as **explicit format**. Fig. (F.3) illustrates a representative scheme of the explicit format.

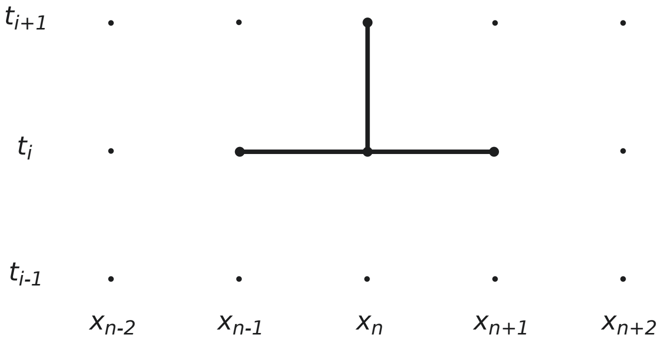

Figure F.3: Illustration of a explicit scheme of first order in time and second order in space.

Bibliography

[This page is intentionally left blank]

Bibliography

[1] G.A. Holzapfel. *Nonlinear solid mechanics. A continuum approach for engineering.* John Wiley and Sons, LTD, 2000.

[2] P. Kelly. Foundations of continuum mechanics, Part III. 2015. URL http://homepages.engineering.auckland.ac.nz/~pkel015.

[3] AK steel corporation. Product Data Sheet: 430 stainless steel. 9227 Centre Pointe Drive. West Chester, OH 45069, 2007.

[4] A.G. Considère. Mémoire sur l'emploi du fer et de l'acier dans les constructions. *Annales des ponts et chaussées*, 9:574–775, 1885.

[5] A. Nadai and M.J. Manjoine. High-speed tension tests at elevated temperatures. Parts II and III. *Journal of applied mechanics*, 63:A–77, A–91, 1941.

[6] A.V. De Forest, C.W. MacGregor, and A.R. Anderson. *Rapid tension tests using the two-load method*, chapter Institute of metals division (In metals technology), pages 1–9. American Institute of Mining and Metallurgical Engineers, 1941.

[7] D.S. Clark. The influence of impact velocity on the tensile characteristics of some aircraft metals and alloys. Technical report, Nationa1 Advisory Committee for Aeronautics, 1942.

[8] E.R. Parker and C. Ferguson. The effect of strain rate upon the tensile impact strength of some metals. *Transactions of the american society for metals*, 30:68–80, 1942.

[9] M.J. Manjoine. Influence of rate of strain and temperature on yield stress of mild steel. *Journal of applied mechanics. Transactions of the ASME*, 11: 211–218, 1944.

[10] H.C. Mann. High-velocity tension-impact tests. *Proceedings american society of testing materials*, 36:85–109, 1936.

[11] H.C. Mann. Fundamental study of the design of impact test specimens. *Proceedings american society of testing materials*, 37:102–130, 1937.

[12] D.S. Clark and G. Datwyler. Stress–strain relations under tension impact loading. *Proceedings–American society of testing materials*, 38:98–111, 1938.

[13] G.F. Beardsley and L.D. Coates. A study of the effect of repeated tension impact loads upon certain metals used in aircraft construction. Master's thesis, California Institute of Technology, 1939.

[14] Wm. E. Jr. Genter and J. O. Biglow. A study of the effect of repeated tension impact loads upon certain metals used in aircraft construction. Master's thesis, California Institute of Technology, 1940.

[15] C.B. Olsen and S.W. Brown. A study of the effect of repeated tension impact loads upon certain metals used in aircraft construction. Master's thesis, California Institute of Technology, 1942.

[16] P.E. Duwez and P.E. Clark. An experimental study of the propagation of plastic deformation under conditions of longitudinal impact. *Proceedings–American society of testing materials*, 47:502–532, 1947.

[17] P.E. Clark and P.E. Duwez. Discussion of the forces acting in tension impact test of materials. *Journal of applied mechanics*, 15:243–247, 1948.

[18] P.E. Clark and P.E. Duwez. The influence of strain rate of some tensile properties of steel. *Proceedings of the american society for testing materials*, pages 560–575, 1950.

[19] P.E. Clark and D.S. Wood. The tensile impact properties of some metals and alloys transactions. *American society of metals*, 42:45–74, 1950.

[20] T. Von Kármán. On the propagation of plastic deformation in solids. Technical report, National Defense Research Committee. Office of Scientific Research and Development N°365, 1942.

[21] Kh.A. Rakhmatulin. Mechanics of unloading waves. *Prikladnaya matematika i mekhanika*, 9:191–100, 1945.

[22] G.I. Taylor. The testing of materials at high rates of loading. *Journal of the institution of civil engineers*, 26:486–519, 1946.

[23] M.P. White and L. Griffis. The permanent strain in a uniform bar due to longitudinal impact. *Journal of applied mechanics*, 14:337–343, 1947.

[24] L.E. Malvern. Plastic wave propagation in a bar of material exhibiting a strain rate effect. *Quarterly of applied mathematics*, 8:405–411, 1951.

[25] J. Harding, E.O. Wood, and J.D. Campbell. Tensile testing of materials at impact rates of strain. *Journal of mechanical engineering science*, 2:488–96, 1960.

[26] S.A. Simmons, E. Hauserf, and J. Dorn. *Response of metals to high velocity deformation*, pages 1–14. Interscience, 1961.

[27] U.S. Lindholm. Some experiments with the Split Hopkinson Pressure bar. *Journal of the mechanics and physics of solids*, 12:317–335, 1964.

[28] T. Nicholas. Mechanical properties of structural grades of beryllium at high strain rates. Technical report, Air Force Materials Laboratory, 1975.

[29] T. Nicholas. Dynamic tensile testing of structural materials using a split hopkinson bar apparatus. Technical report, Air Force Wright Aeronautical Laboratories, 1980.

[30] T. Nicholas. Tensile testing of materials at high rates of strain. *Experimental mechanics*, 21:177–185, 1981.

[31] C. Fressengeas and A. Molinari. Inertia and thermal effects on the localization of plastic flow. *Acta metallurgica*, 33:387–396, 1985.

[32] C. Fressengeas and A. Molinari. Fragmentation of rapidly stretching sheets. *European journal of mechanics A/Solids*, 13:251–268, 1994.

[33] R. Hill and J.W. Hutchinson. Bifurcation phenomena in the plane tension test. *Journal of the mechanics and physics of solids*, 23:239–264, 1975.

[34] J. Hutchinson, K. Neale, and A. Needleman. *Mechanics of sheet metal forming*, pages 269–285. Plenum Press, New York/London, 1978.

[35] V.B. Shenoy and L.B. Freund. Necking bifurcations during high strain rate extension. *Journal of the mechanics and physics of solids*, 47:2209–2233, 1999.

[36] S. Mercier and A. Molinari. Predictions of bifurcations and instabilities during dynamic extensions. *International journal of solids and structures*, 40:1995–2016, 2003.

[37] S. Mercier and A. Molinari. Analysis of multiple necking in rings under rapid radial expansion. *International journal of impact engineering*, 30:403–419, 2004.

[38] F. Zhou, J.F. Molinari, and K. T. Ramesh. An elasto-visco-plastic analysis of ductile expanding ring. *International journal of impact engineering*, 33: 880–891, 2006.

[39] J. Lubliner. A generalized theory of strain-rate-dependent plastic wave propagation in bars. *Journal of the mechanics and physics of solids*, 12:59–65, 1964.

[40] R. Botte, T. Rousseau, P. Peguin, and P. Gobin. Calculation of the behaviour of a bar during a high-strain-rate tensile test. *Journal of physics D: Applied physics*, 18:663–670, 1967.

[41] R. Botte, T. Rousseau, and P. Gobin. A theoretical and experimental analysis of high strain-rate test using Malvernś theory. *Journal of physics D: Applied physics*, 2:1235–1243, 1969.

[42] G. Regazzoni, J. N. Johnson, and P.S. Follansbee. Theoretical study of the dynamic tensile test. *Journal of applied mechanics*, 53:519–528, 1986.

[43] V.R. Tvergaard and A. Needleman. *Damage mechanics in engineering materials*, volume 109, chapter Ductile failure modes in dynamically loaded notched bars, pages 117–128. ASME, 1990.

[44] A. Needleman. The effect of material inertia on neck development. Topics in Plasticity, pages 151–160. AM Press, Ann Arbor, MI, 1991.

[45] P. Knoche and A. Needleman. The effect of size on the ductility of dynamically loaded tensile bars. *European journal of mechanics A/Solids*, 12: 585–601, 1993.

[46] J.A. Nemes and J. Eftis. Constitutive modelling on the dynamic fracture of smooth tensile bars. *International journal of plasticity*, 9:243–270, 1993.

[47] A.K. Noor, A. Needleman, and J.M. Peters. Sensitivity analysis for failure and damage in dynamically loaded tensile bars. *Computer methods in applied mechanics and engineering*, 151:461–478, 1998.

[48] N.J. Sørensen and L.B. Freund. Dynamic bifurcation during high-rate planar extension of a thin rectangular block. *European journal of mechanics A/Solids*, 17:709–724, 1998.

[49] A. Glema, T. Łodygowski, and P. Perzyna. Interaction of deformation waves and localization phenomena in inelastic solids. *Computers methods in applied mechanics and engineering*, 183:123–140, 2000.

[50] P.R. Guduru and L.B. Freund. The dynamics of multiple neck formation and fragmentation in high rate extension of ductile materials. *International journal of solids and structures*, 39:5615–5632, 2002.

[51] Z. Xue, A. Vaziri, and J.W. Hutchinson. Material aspects of dynamic neck retardation. *Journal of the mechanics and physics of solids*, 56:93–113, 2008.

[52] Y. Rotbaum, S. Osovski, and D. Rittel. Why does necking ignore notches in dynamic tension? *Experimental mechanics*, 78:173–185, 2015.

[53] A. Rusinek, R. Cheriguene, P. Baümer, J.R. Klepaczko, and P. Larour. Dynamic behaviour of high-strength sheet steel in dynamic tension: experimental and numerical analyses. *Journal of strain analysis for engineering design*, 43:37–43, 2008.

[54] H. Huh, S.B. Kim, J.H. Song, and J.H. Lim. Dynamic tensile characteristics of TRIP-type and DP-type steel sheets for an auto-body. *International journal of mechanical sciences*, 50:918–931, 2008.

[55] G. Mirone. The dynamic effect of necking in Hopkinson bar tension tests. *Mechanics of materials*, 58:84–96, 2013.

[56] A. Rusinek, R. Zaera, J.R. Klepaczko, and R. Cheriguene. Analysis of inertia and scale effects on dynamic neck formation during tension of sheet steel. *Acta materialia*, 53:5387–5400, 2005.

[57] W.W. Wood. Experimental mechanics at velocity extremes-very high strain rates. *Experimental mechanics*, 5:361–371, 1965.

[58] G. Besnard, F. Hild, J.M. Lagrange, P. Martinuzzi, and S. Roux. Analysis of necking in high speed experiments by stereocorrelation. *International journal of impact engineering*, 49:179–191, 2012.

[59] J.A. Rodríguez-Martínez, D. Rittel, R. Zaera, and S. Osovski. Finite element analysis of AISI 304 steel sheets subjected to dynamic tension: the effects of martensitic transformation and plastic strain development on flow localization. *International journal of impact engineering*, 53:206–216, 2013.

[60] S. Osovski, D. Rittel, J.A. Rodríguez-Martínez, and R. Zaera. Dynamic tensile necking: Influence of specimen geometry and boundary conditions. *Mechanics of materials*, 62:1–13, 2013.

[61] D. Rittel, Y. Rotbaum, J.A. Rodríguez-Martínez, D. Sory, and R. Zaera. Dynamic necking of notched tensile bars: An experimental study. *Experimental mechanics*, 54:1099–1109, 2014.

[62] Simulia. *ABAQUS/Explicit User's Manual*. Dassault Systèmes, Providence, USA, version 6.10 edition, 2010.

[63] K. Hashiguchi and Y. Yamakawa. *Introduction to finite strain theory for continuum elasto-plasticity*. John Wiley and Sons, Ltd, 2012.

[64] J. Bonet and R.D. Wood. *Nonlinear continuum mechanics for finite element analysis*. Cambridge University Press, 1997.

[65] W. Sumelka. *The constitutive model of the anisotropy evolution for metals with microstructural defects*. PhD thesis, Poznan University of Technology. Faculty of Civil and Environmental Engineering, 2009.

[66] Liu I-Shih and R. Sampaio. On objectivity and the principle of material frame-indifference. *Mecanica computacional*, XXXI:1553–1569, 2012.

[67] E.A de Souza Neto, D. Peric, and D.R.J. Owen. *Computational methods for plasticity: Theory and applications*. John Wiley and Sons, Ltd, 2008.

[68] J.C. Simo and K.S. Pister. Remarks on the rate constitutive equations for finite deformation problems: Computational implications. *Computer methods in applied mechanics and engineering*, 46:201–215, 1984.

[69] S. Nemat-Nasser. On finite deformation elasto-plasticity. *International journal of solids and structures*, 18:857–872, 1982.

[70] J.C. Nagtegaal and J.E. Jong. *Some aspects of non-isotropic work-hardening in finite strain plasticity. Plasticity of metals at finite strain: Theory, experiment and computation.* Division of Applied mechanics, Stanford University and Department of Engineering and Mechanics, Rensselaer Polytechnic Institute., 1982.

[71] J.C. Simo. On the computational significance of the intermediate configuration and hyperelastic stress relations in finite deformation elastoplasticity. *Mechanics of materials*, 4:439–451, 1985.

[72] J.C. Simo and M. Ortiz. A Unified approach to finite deformation plasticity based on the use of hyperelastic constitutive equations. *Computer methods in applied mechanics and engineering*, 49:221–245, 1985.

[73] R. Zaera and J. Fernández-Sáez. An implicit consistent algorithm for the integration of thermoviscoplastic constitutive equations in adiabatic conditions and finite deformations. *International journal of solids and structures*, 43:1594–1612, 2006.

[74] J.C. Simó and T.J.R. Hughes. *Computational inelasticity.* Springer, New York, 1998.

[75] I. Doghri. *Mechanics of deformable solids: linear and nonlinear, analytical and computational aspects.* Springer, Berlin, 2000.

[76] L. Anand. On H. Hencky's approximate strain-energy function for moderate deformations. *Journal of applied mechanics*, 46:78–82, 1979.

[77] L. Anand. Moderate deformations in extension-torsion of incompressible isotropic elastic materials. *Journal of the mechanics and physics of solids*, 34:293–304, 1986.

[78] S. Gomaa. *Computational procedures for finite deformation rate-independent plasticity and visco-plasticity based on overstress.* PhD thesis, Faculty of Rensselaer Polytechnic Institute, Troy, New York, 2000.

[79] E.H. Lee. Elastic-plastic deformation at finite strains. *Journal of applied mechanics*, 36:1–6, 1969.

[80] P. Perzyna. Application of the thermodynamical theory of elasto-viscoplasticity in modern manufacturing processes. In *Damage mechanics and micromechanics of localized fracture phenomena in inelastic solids*, volume 525 of *CISM Courses and Lectures*, pages 227–376. Springer Vienna, 2011. ISBN 978-3-7091-0426-2. doi: 10.1007/978-3-7091-0427-9_3.

[81] C. Truesdell. Hypoelasticity. *Journal of rational mechanics*, 4:83–133, 1955.

[82] W. Noll. On the continuity of the solid and fluid states. *Journal of rational mechanics*, 4:3–81, 1955.

[83] B. Bernstein and K. Rajagopal. Thermodynamics of hypoelasticity. *Zeitschrift fÃijr angewandte mathematik und physik*, 59:537–553, 2008.

[84] J.L. Ericksen. Hypo-elastic potentials. *Quarterly journal of mechanics and applied mathematics*, XI:67–72, 1958.

[85] B. Bernstein. Hypo-elasticity and elasticity. *Archive for rational mechanics and analysis*, 2:89–104, 1960.

[86] B. Bernstein. A unified thermodynamic theory of elasticity and plasticity. *Journal of elasticity*, 13:411–427, 1983.

[87] E.T. Olsen and B. Bernstein. A class of hypo-elastic non-elastic materials and their thermodynamics. *Archive for rational mechanics and analysis*, 86: 291–303, 1984.

[88] A. Vaz-Romero, J.A. Rodríguez-Martínez, and A. Arias. The deterministic nature of the fracture location in the dynamic tensile testing of steel sheets. *International journal of impact engineering*, 86:318–335, 2015. doi: http://dx.doi.org/10.1016/j.ijimpeng.2015.08.005.

[89] J.A. Rodríguez-Martínez, R. Pesci, and A. Rusinek. Experimental study on the martensitic transformation in AISI 304 steel sheets subjected to tension under wide ranges of strain rate at room temperature. *Materials science and engineering: A*, 528:5974–5982, 2011.

[90] G. Battams. *The use of optical techniques to asses the damage tolerance of composite materials.* PhD thesis, University of Southampton, 2014.

[91] S. Storen and J.R. Rice. Localized necking in thin sheets. *Journal of the mechanics and physics of solids*, 23:421–441, 1975.

[92] H. Zhang and K. Ravi-Chandar. On the dynamics of necking and fragmentation - II. Effect of material properties geometrical constraints and absolute size. *International journal of fracture*, 150:3–36, 2008.

[93] J.A. Rodríguez-Martínez, A. Rusinek, and A. Arias. Relation between strain hardening of steel and critical impact velocity. *Journal of theoretical and applied mechanics*, 47:645–665, 2009.

[94] U.S. Lindholm. Review of dynamic testing techniques and material behaviour. In Oxford, editor, *Conference on mechanical properties of materials at high rates of strain*, pages 3–21. Institute of Physics, 1974.

[95] J.A. Rodríguez-Martínez, G. Vadillo, J. Fernández-Sáez, and A. Molinari. Identification of the critical wavelength responsible for the fragmentation of ductile rings expanding at very high strain rates. *Journal of the mechanics and physics of solids*, 61:1357–1376, 2013.

[96] D.E. Grady and D.A. Benson. Fragmentation of metal rings by electromagnetic loading. *Experimental mechanics*, 12:393–400, 1983.

[97] H. Gourdin. Analysis and assessment of electromagnetic ring expansion as a high-strain-rate test. *Journal of applied physics*, 65:411–422, 1989.

[98] M. Altynova, X. Hu, and G.S. Daehn. Increased ductility in high velocity electromagnetic ring expansion. *Metallurgical and materials transactions A*, 27:1837–1844, 1996.

[99] D.E. Grady and M.L. Olsen. A statistics and energy based theory of dynamic fragmentation. *International journal of impact engineering*, 29:293–306, 2003.

[100] H. Zhang and K. Ravi-Chandar. On the dynamics of necking and fragmentation - I. Real-time and post-mortem observations in Al 6061-O. *International journal of fracture*, 142:183–217, 2006.

[101] J. Janiszewski. Ductility of selected metals under electromagnetic ring test loading conditions. *International journal of solids and structures*, 49:1001–1008, 2012.

[102] T. Hiroe, K. Fujiwara, H. Hata, and H. Takahashi. Deformation and fragmentation behaviour of exploded metal cylinders and the effects of wall materials, configuration,explosive energy and initiated locations. *International journal of impact engineering*, 35:1578–1586, 2008.

[103] D. Goto, R. Becker, T. Orzechowski, H. Springer, A. Sunwoo, and C. Syn. Investigation of the fracture and fragmentation of explosively driven rings and cylinders. *International journal of impact engineering*, 35:1547–1556, 2008.

[104] S. Mercier, N. Granier, A. Molinari, F. Llorca, and F. Buy. Multiple necking during the dynamic expansion of hemispherical metallic shells, from experiments to modelling. *Journal of the mechanics and physics of solids*, 58: 955–982, 2010.

[105] R. Zaera, J.A. Rodríguez-Martínez, G. Vadillo, and J. Fernández-Sáez. Dynamic necking in materials with strain induced martensitic transformation. *Journal of the mechanics and physics of solids*, 64:316–337, 2014.

[106] J.R. Klepaczko. *Introduction to experimental techniques for material testing at high strain rates*. Scientific Library. Warszawa Institute of Aviation, 2007.

[107] A. Rusinek and R. Zaera. Finite element simulation of steel ring fragmentation under radial expansion. *International journal of impact engineering*, 34:799–822, 2007.

[108] J.A. Zukas and D.R. Scheffer. Practical aspects of numerical simulations of dynamic events: effects of meshing. *International journal of impact engineering*, 24:925–945, 2000.

[109] A. Needleman. Material rate dependence and mesh sensitivity in localization problems. *Computer methods in applied mechanics and engineering*, 67:69–85, 2008.

[110] A. Molinari. Collective behaviour and spacing of adiabatic shear bands. *Journal of the mechanics and physics of solids*, 45:1551–1575, 1997.

[111] J.R. Klepaczko. Review on critical impact velocities in tension and shear. *International journal of impact engineering*, 32:188–209, 2005.

[112] R. Zaera, J.A. Rodríguez-Martínez, G. Vadillo, J. Fernández-Sáez, and A. Molinari. Collective behaviour and spacing of necks in ductile plates subjected to dynamic biaxial loading. *Journal of the mechanics and physics of solids*, Submitted for Publication, 2015.

[113] N. Triantafyllidis and J.R. Waldenmyer. Onset of necking in electromagnetically formed rings. *Journal of the mechanics and physics of solids*, 52:2127–2148, 2004.

[114] X. Hu and G.S. Daehn. Effect of velocity on flow localization in tension. *Acta materialia*, 44:1021–1033, 1996.

[115] G. Vadillo, J.A. Rodríguez-Martínez, and J. Fernández-Sáez. On the interplay between strain rate and strain rate sensitivity on flow localization in the dynamic expansion of ductile rings. *International journal of solids and structures*, 49:481–491, 2012.

[116] N.A. Kudryashov, P.N. Ryabov, and A.S. Zakharchenko. Self-organization of adiabatic shear bands in OFHC copper and HY-100 steel. *Journal of the mechanics and physics of solids*, 76:180–192, 2015.

[117] L. Wang and W. Tong. Identification of post-necking strain hardening behavior of thin sheet metals from image-based surface strain data in uniaxial tension tests. *International journal of solids and structures*, In press, 2015.

[118] A.S. Bonnet-Lebouvier, A. Molinari, and P. Lipinski. Analysis of the dynamic propagation of adiabatic shear bands. *International journal of solids and structures*, 39:4249–4269, 2002.

[119] J.A. Rodríguez-Martínez, A. Molinari, R. Zaera, G. Vadillo, and J. Fernández-Sáez. The critical neck spacing in ductile plates subjected to dynamic biaxial loading: On the interplay between loading path and inertia effects. *International journal of solids and structures*, Submitted for Publication, 2015.

[120] A. Needleman and V. Tvergaard. Analyses of plastic flow localization in metals. *Applied mechanics reviews*, 45:S3–S18, 1992.

[121] K. Ravi-Chandar and N. Triantafyllidis. Dynamic stability of a bar under high loading rate: Response to local perturbations. *International journal of solids and structures*, 58:301–308, 2015.

[122] W. Li-li, Y. Li-ming, and Z. Feng-hua. *Foundations of stress waves*. Elsevier, 2007.

[123] Finite difference calculus. In *Numerical partial differential equations for environmental scientists and engineers*, pages 11–19. Springer US, 2005. ISBN 978-0-387-23619-3.